Développement d'un nouveau concept de cible pour faisceau de protons au CERN/ISOLDE

Mélanie Delonca

SPIM

Thèse de Doctorat

école doctorale **sciences pour l'ingénieur et microtechniques**

UNIVERSITÉ DE TECHNOLOGIE BELFORT-MONTBÉLIARD

Développement d'un nouveau concept de cible pour faisceau de protons au CERN/ISOLDE

Development of new target concepts for proton beams at CERN/ISOLDE

MELANIE DELONCA

SPIM

Thèse de Doctorat

école doctorale **sciences pour l'ingénieur et microtechniques**

UNIVERSITÉ DE TECHNOLOGIE BELFORT-MONTBÉLIARD

N° 2 7 8

THÈSE présentée par

MELANIE DELONCA

pour obtenir le

Grade de Docteur de
l'Université de Technologie de Belfort-Montbéliard

Spécialité : **Mécanique**

Développement d'un nouveau concept de cible pour faisceau de protons au CERN/ISOLDE

Development of new target concepts for proton beams at CERN/ISOLDE

Unité de Recherche :
Laboratoire IRTES-M3M et IRTES-LERMPS

Soutenue publiquement le 14 decembre 2015 devant le Jury composé de :

ZHI-QIANG FENG	Rapporteur	Professeur à l'Université d'Evry
DANIEL MORVAN	Rapporteur	Professeur à l'École Nationale Supérieure de Chimie de Paris
MANUEL FRANÇOIS	Examinateur	Professeur à l'Université de Technologie de Troyes
CHRISTIAN LATGÉ	Examinateur	Docteur au Commissariat à l'énergie atomique et aux énergies alternatives (CEA)
FRANÇOIS PEYRAUT	Directeur de thèse	Professeur à l'Université de Technologie de Belfort-Montbéliard
GHISLAIN MONTAVON	Co-Directeur de thèse	Professeur à l'Université de Technologie de Belfort-Montbéliard
THIERRY STORA	Co-Directeur de thèse	Docteur au Centre Europeen de Recherche Nucléaire (CERN)

Acknowledgements

La vie est jalonnée de projets et de choix qui conduisent à des moments importants. Le chemin qu'a été ce doctorat est l'un d'eux, un projet que je n'avais pas prévu et qui m'a enrichi au-delà de ce que j'aurais pu prévoir.

Durant ce voyage, j'ai eu la chance de travailler avec différentes personnes qui m'ont permis de grandir, tant professionnellement que personnellement, et que je souhaite ici remercier.

Tout d'abord, je voudrais remercier mes différents superviseurs: Mr François Peyraut (UTBM - M3M) pour son soutien et sa présence, ses conseils et sa patience avec moi; Mr Ghislain Montavon (UTBM - LERMPS) qui a toujours su trouver le temps pour m'épauler ainsi que Mr Thierry Stora (CERN) qui a accepté de prendre en charge la supervision de mon doctorat sur la dernière année et qui a donc hérité de toute la partie intense de lecture et correction de thèse, et de tout le stress associé à une telle tâche.

Je souhaiterais également remercier tout spécialement Mr Cesare Maglioni, mon "premier" superviseur CERN, qui m'a permis de réaliser ce doctorat en me proposant un sujet en or et qui m'a permis de me réaliser et d'apprécier pleinement la carrière que j'ai choisi. Grâce à toi, je suis aujourd'hui plus assurée, plus ouverte qu'à mes débuts et je t'en remercie.

Viennent ensuite mes remerciements à tous les membres du jury. Premièrement, je remercie Mr Daniel Morvan qui a accepté d'être à la fois rapporteur et président du jury. Un merci tout particulier également à Mr Zhi-Qiang Feng, pour avoir accepté d'être rapporteur. Merci enfin à Mr Christian Latgé et Mr François Manuel qui ont acceptés de faire partie de mon jury de thèse alors même que leur emploi du temps chargé leur donne peu de temps à consacrer à ce genre de tâche.

Merci à tous mes collègues, de mes deux sections, mes deux familles d'accueil: Valentina, Florian, Alexandre O., Oliver, Dawid, Edouard, Alexandre P. pour TCD; Camille, Vincent, Stefano, Matteo pour RBS. Merci pour leur rire, merci pour leur écoute, merci pour créer chaque jour ce climat de bonheur.

Un grand merci également à tous les partenaires du projet: Ana Paula et Tania au sein du CERN, qui m'ont soutenue dans les moments difficiles; Mr Paul Schuurmans, de SCK-CEN, qui a su nous donner de précieux conseils et qui est sans nul doute une personne clé dans la réussite de ce projet, Donald et Lucia pour leur précieuse collaboration. Merci à Kalvis et Raimonds pour avoir toujours répondu présent à toutes les questions que j'avais; Susanta et Moumita, pour leurs sourires.

Je souhaiterais également remercier tout particulièrement Mr Ramon Folch sans qui ce projet n'aurait pu progresser de la sorte.

Merci à mes amis, Aurélie, Lorelle, Vincent, pour m'avoir soutenu, écouté, avoir su trouver les mots quand il le fallait. Merci de faire partie de ma vie tout simplement. Merci à Marco pour ses missions de soutien intense, pour m'avoir redonné le sourire quand necessaire et pour toujours croire en moi, inconditionnellement.

Merci à ma sœur, ma moitié. Déjà, pour avoir ouvert la voie de ce projet insensé, d'avoir "testé avant, pour moi", et d'avoir ensuite signalé les difficultés. Merci d'avoir toujours été la, de me

soutenir contre vents et marrées, peu importe ce qu'il se passe. Merci de toute l'énergie que tu m'envoies tous les jours, de toute la force qui me vient de toi.

Pour terminer, je souhaiterais remercier mes parents, qui m'ont soutenus tout au long de ces années de travail, qui ont su se montrer intéressés et curieux même si ce domaine leur était inconnu, qui ont su poser les bonnes questions à certains moment cruciaux (et faire avancer de manière significative ma vision du projet). Merci pour le cocon familial qu'ils ont su créer et au sein duquel j'ai toujours pu me ressourcer quand nécessaire. Merci pour les mots, merci pour les silences et merci pour tout cet amour.

Ce moment important se termine, voilà la fin d'une aventure. Merci à vous tous car grâce à vous, je me lance dans la nouvelle le sourire aux lèvres.

‘Science is bound, by the everlasting vow of honour, to face fearlessly every problem which can be fairly presented to it.’

Lord Kelvin

Contents

List of Tables

List of Figures

Acronyms

SC Synchrocyclotron

CEA Commissariat à l'énergie atomique et aux énergies alternatives

CERN European Organization for Nuclear Research

CFD Computational Fluid Dynamics

DPA Displacement Per Atoms

EM Electro Magnetic

EOS Equation Of State

EPDM Ethylene Propylene Diene Monomer

EURISOL European ISOL facility

FEBIAD Force Electron Beam Induced Arc Discharge

FOM Figure Of Merit

HEX Heat Exchanger

IPUL Institute of Physics of University of Latvia

ISOL Isotopes Separator On Line

LBE Lead Bismuth Eutectic

LIEBE Liquid Eutectic Lead Bismuth Loop Target for EURISOL

LiLiT Liquid Lithium Target

MEGAPIE MegaWatt Pilot Target Experiment

NPSH Net Positive Suction Head

PMP Permanent Magnet Pump

PSB Proton Synchrotron Booster

PSI Paul Scherrer Institute

RIBs Radioactive Ion Beams

SCK-CEN StudieCentrum voor Kernenergie ou Centre d'étude de l'énergie nucléaire

SINP Saha Institute of Nuclear Physics

SPH Smoothed Particle Hydrodynamics

SS Stainless Steel

TISS Target Ion Source System

VADIS Versatile Arc Discharge Ion Source

WP Work Package

Introduction

Particle physics always fascinated and questioned at the same time. What is it really use for? What is the application behind? It is not always simple and this scientific field is usually thought as being the matter of a very small group of scientist, fascinated by this very specific field. Since the fundamentals laws of the quantum mechanic in the 20's, physicists have been using these laws in order to explore the world of the nucleus. At the beginning of the 1930's, models to describe their structures as well as their nuclear forces linking protons and neutrons are proposed [19]. The theoretical basics of the nuclear physics are then posed by Heisenberg, Majorana, Fermi, Gamow and Yukawa [19]. However, particle physics is not done by scientist in their office. Indeed, in order to study and push further the limits of the nuclear physics knowledge, that evolve every day, specific tool are required. This is when the pure nuclear physics world meet with the engineering one, and where the limit between those two worlds stop to be that clearly defined. Indeed, more and more, specific objects need to be developed for the study of this scientific field. It can be either detection tools, measurements tools, or production tools to only cite a few. Engineer worked more and more in close collaboration with physicist in order to open the door to new possibility and new discoveries.

In this context, many facilities have been developed all around the world over the past last 100 years. In the late 60's, Isotopes Separator On Line (ISOL) facilities were built and linked to accelerators, mainly in Europe. More specifically, at CERN-ISOLDE (Geneva, Switzerland), this concept has proved its efficiency to produce, control and study high intensity beams of Radioactive Ion Beams (RIBs). Nowadays, the technique to produce RIBs is well known: a primary beam is sent on a production target, from which the isotopes are created and are then ionized thanks to an ion source before to be accelerated and separated in mass. However, the need for more intense beams and for more intense exotics beams (beams of isotopes having a half-life under 300 ms) is well present and leads to the development of more intense primary beam. By increasing the power of the primary beam and thus, the number of secondary particles that will be created, new studies can be done. However, this comes with the need of new engineering development. Indeed, higher beam power induces new challenges to be faced, and new engineering development to address them. Focusing on the targets part, the usually standard solid target design evolved toward liquid targets [20]. One specific liquid loop target design has been proposed during the EURISOL Design Study [12] and could handle the very high primary beam power by circulating the liquid target material and possibly by using an heat exchanger.

Nowadays, mainly solid targets are used. To extract the high power sent, specific shapes are used like for example pellets forms, that are easier to cooled down as they have a higher surface able to radiate while being actively cool down by the use of air or water flow on the external surface. This is the case in Triumf, Canada [21]. Liquid loop targets are already existing as for

example in SARAF (Soreq Applied Research Accelerator Facility), Israel, where a loop making use of Lithium has been developed [22]. In this design, both a pump and a heat exchanger are used. This is also the case for the MEGAPIE target, developed at PSI (Paul Scherrer Institute), Switzerland [11], on which Lead Bismuth Eutectic (LBE) is circulating thanks to a pump while being cooled down with a heat exchanger.

The research works presented in this manuscript was mainly performed at Geneva (Switzerland), in the Engineering department of the CERN facility, and more specifically in the EN-STI (Sources, Targets and Interactions) group. This group has as common ground the study of beam interactions with matter, aiming to apply its know-how to particle generation and to particle interception. In this context, CERN launched in 2012 a R&D project grouping different institutes, called LIEBE (Liquid Eutectic Lead Bismuth Loop Target for Eurisol) to investigate the feasibility of testing on line a LBE loop target compatible with the present installations at ISOLDE. My direct contribution to the LIEBE project has been to coordinate the work-package WP3 "construction, assembly" but worked closely for the work-package WP2 "conceptual design and simulation". The target design is currently being manufactured and will be tested at CERN-ISOLDE during the year 2016.

The proposed thesis presents the development and design of a liquid loop target aiming at the increase of the production of short-lived species while handling high primary beam power. This requires different elements that must be integrated in the target design: a pump for the circulation of the liquid, an heat exchanger for the extraction of the power brought by the primary beam, but also a diffusion chamber, where droplets of liquid are created through a grid in order to help the diffusion of the isotopes out of the liquid and thus, increase the final production of these isotopes. These different elements are not standard in classical target design and induces many parameters to take into account, these parameters being linked to each other on some extent. For the design of such a target, many different fields must be taken into account and the presented thesis touches many different engineering subjects such as thermo-mechanics, thermal analyses, thermodynamics (pressure losses), fluid dynamics, shock-waves and physics (release efficiency of short-lived species). Considering the complex multi-physics framework for designing liquid loop target dedicated to high power beams, up to 19 design parameters were investigated (Table 1). Some of these parameters are concerned by different topics as the temperature of the loop for example which is related to the pump as well as to the thermal equilibrium. In order to find the best balance between all these parameters (with sometimes opposite objectives), we have developed and combined several analytical, numerical and experimental approaches.

The **Chapter 1** of this thesis presents the principle of Radioactive Ion Beams (RIBs) production and the nuclear reactions involved when sending a proton beam onto target materials. A specification of the different type of RIBs production method is presented, leading to the definition of Isotope Separation On Line (ISOL) method. The different elements constituting ISOL facilities are explained while an overview of the different facilities around the world is given. The different parameters involved in the production of RIBs are presented leading to the presentation of possible improvement in order to obtain higher production rate. The different challenges related to the design of high power targets are also presented while proposing a general overview of high power target and a list of current high power target principle around the world. Finally, the problematic and context of this thesis are explained.

The **Chapter 2** aims to provide a handy tool to use when developing a high power target similar to the one presented, meaning a liquid loop target using a pump and an heat exchanger, and

having a droplets shower used to increase the total release efficiency of short half-life species. It can also be used if the new design groups only one or few of these elements. More specifically, an exhaustive list of the different design parameters studied in this part are presented hereunder (Table 1):

Target element	Parameters
Pump	Flow rate of the loop
	Temperature of the loop
	Pressure losses inside the loop
	Diameter of the pipes of the loop
Thermal equilibrium	Temperature of the loop
	Diameter of the pipes of the loop
	Thickness of the pipes
	Thickness of the insulation
	Emissivity of the insulation
	Thermal conductivity of the insulation
Heat Exchanger (HEX)	Flow rate of the water
	Surface area of the water channels
	Shape of the water channels
	Thermal conductivity of the HEX material
Shower formation	Velocity of the formed droplets
	Diameters of the grid holes
	Thickness of the grid
	Inter axis distance between holes
Optimization for release efficiency	Velocity of the formed droplets
	Volume of the irradiation chamber
	Height of the diffusion chamber
	Time of the irradiated liquid in the irradiation chamber
	Time of the droplets in the diffusion chamber

Table 1: Parameters to take into account for the design of a high power liquid loop target improving the release efficiency of short-lived species

Each of these parameters are considered and put in highlight compared to others in order to show the different links between each of them in order to propose a design as optimized as possible. They are developed and linked to each other when possible thanks to analytical analyses which give the general trend-lines of the impact of each of these parameters while being put in perspective for the developed target application.

In the **Chapter 3**, the presented tools are applied in order to develop the LIEBE (**Li**quid **E**utectic Lead **B**ismuth Loop Target for **E**urisol) target. The final design retained is presented and validated thanks to numerical tools (Fluid analysis, thermo-mechanical analyses and shock-waves analyses done with the software ANSYS [23], mathematical calculation done with the mathematical software MathCad [24]) and the analytical tools developed in the Chapter 2. The detailed development of the different constituting elements is shown. This Chapter shows how this target has been developed and how the various constraints related to the ISOLDE environment have been taken into account. Particularly, a complete thermal equilibrium analysis has been conducted in order to develop an Heat Exchanger making use of water in order to

extract power out of Lead Bismuth Eutectic (LBE) operated between 200 and 600 °C. Considering the complexity of this part, it will be manufactured using additive manufacturing. The dimensioning of the grid used to create a shower, as well as the flow rate of the loop, are fixed thanks to analytical analysis on the shower formation regimes [25]. This is done by taking into account the different parameters impacting on the final release efficiency for short-lived species and optimizing them to achieve the highest final release.

Finally, the **Chapter 4** presents the experimental results of a test conducted in order to assess the shower formation feasibility. In this test, a fixed volume of LBE is forced by gravity through different grids, with a fixed holes diameter but with different inter-axis distance between the holes. The test bench used for the experiment is presented while giving the main components and the procedure of the tests. Starting from existing theoretical models in fluid dynamics [26], a numerical approach adapted to the specific context of our study has been proposed. This numerical approach allows:

- to take into account the oxidation occurring in time and blocking some of the holes of the grids,
- to define and study some key parameters by comparison with some of the holes of the grids. This model is then applied to the experimental results in order to:
  - obtain the velocity of the created droplets versus the time,
  - assess the minimum velocity necessary in order to create droplets as small as possible,
  - highlight a velocity number at which a change in droplets formation occurs,
  - validate the Weber number of the transition between two regimes in the very specific case of LBE.

To summarize, this Chapter presents the different parameters related to the formation of LBE droplets passing through a shower and explains how these parameters interact between them.

Chapter 1

Background Theory

1.1 Introduction

1.1.1 Nuclear reaction

In nuclear physics, a nuclear reaction is a process in which nucleus or nuclear particles disintegrate or collide with another particle, to produce products different than the initial particles. In principle a reaction can involve more than two particles colliding, but such an event is exceptionally rare. Most nuclear reactions are studied by inducing a collision between two nuclei where one of the reacting nuclei is at rest (the *target* nuclei) while the other nucleus (the *projectile* nucleus) is in motion or where both are in motion. Such nuclear reactions can be described as:

$projectile\ P + target\ T \longrightarrow emitted\ particle\ X + residual\ nucleus\ R$

In nuclear reaction, there is conservation of the number of protons (or atomic number Z) and neutrons (and thus the number of nucleons or mass number A) as in the following example:

${}^{6}_{3}Li + {}^{2}_{1}H \longrightarrow {}^{4}_{2}He + {}^{4}_{2}He$

In this example, Lithium (Li) in reaction with Hydrogen (H) will produce two atoms of Helium (He) by keeping conservation in the total number of nucleons (here it is 8) and the number of protons (4 in this example).

1.1.2 Product reaction

The production of radioactive isotopes can happen through a multitude of reaction classes. However, the reaction types of more generic use in order to cover a large parts of the nuclei chart are: fragmentation, spallation and fission as shown in Figure 1.1. The different product reactions can be summarized as follow:

- Spallation: the spallation reactions are nuclear reactions in which several nucleons are released from the nucleus of an atom [27].

- Fragmentation: the fragmentation is a process during which a beam of nuclei is accelerated and sent onto a target. The primary nuclei are then fragmented into smaller nuclei with many nucleons (protons or neutrons) that are knocked out of the beam nucleus [28].

- Fission: the nuclear fission can be expressed as a nuclear reaction or a radioactive decay process in which the nucleus of an atom splits into smaller parts (lighter nuclei) [29].

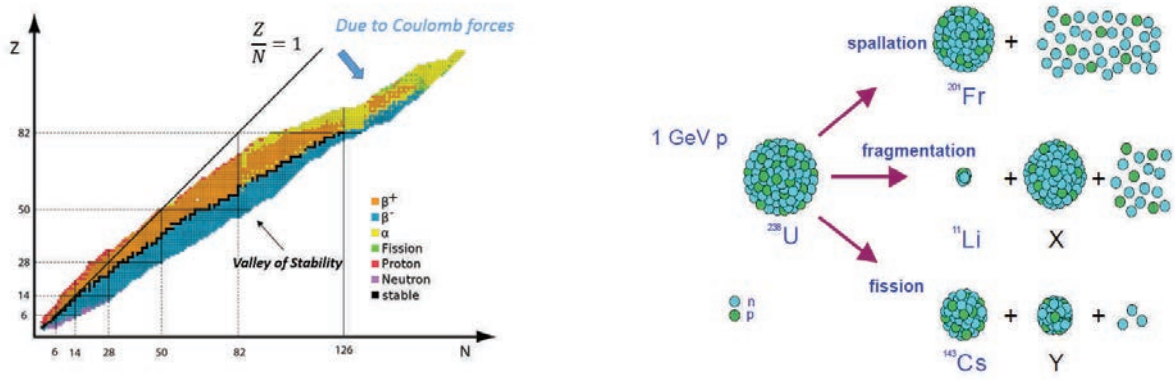

(a) Nuclei chart [4]

(b) Reaction products [7]

Figure 1.1: Nuclei chart and reaction products

1.1.3 Nuclear decay

Nuclear decay or radioactive decay is the emission of **energy** and **matter** (photon, electron, positron, neutrino, ...) inducing changes in the "mother" nucleus. Such unstable isotopes are known as radioactive element and the process is called radioactivity. The nuclear decay often involves the emission of ionizing particles or ionizing radiation. This decay will continue until a new stable isotope is formed which cannot further disintegrate. Hence by using nuclear decay, all unstable elements will evolve toward the neutron to proton ratio of one to 1.5, meaning reaching the valley of stability.

Regardless of the mode of decay, the total number of nucleons is conserved in all nuclear reactions.

There are six fundamentally different kinds of nuclear decay schemes, and each of them releases a different kind of particle and/or radiation energy. The essential features of each decay are shown in Figure 1.2. The most common are alpha and beta decay and gamma emission, but the others are essential to an understanding of nuclear decay reactions.

Alpha particles may be completely stopped by a sheet of paper, beta particles by Aluminum shielding. Gamma rays can only be reduced by much more substantial mass, such as a very thick layer of lead (see Figure 1.3). This is used for the nuclei detection as the different radiation (gamma, beta, alpha) will interact on a different way with the matter. All the detectors are based on the interaction between the radiation and the detector material.

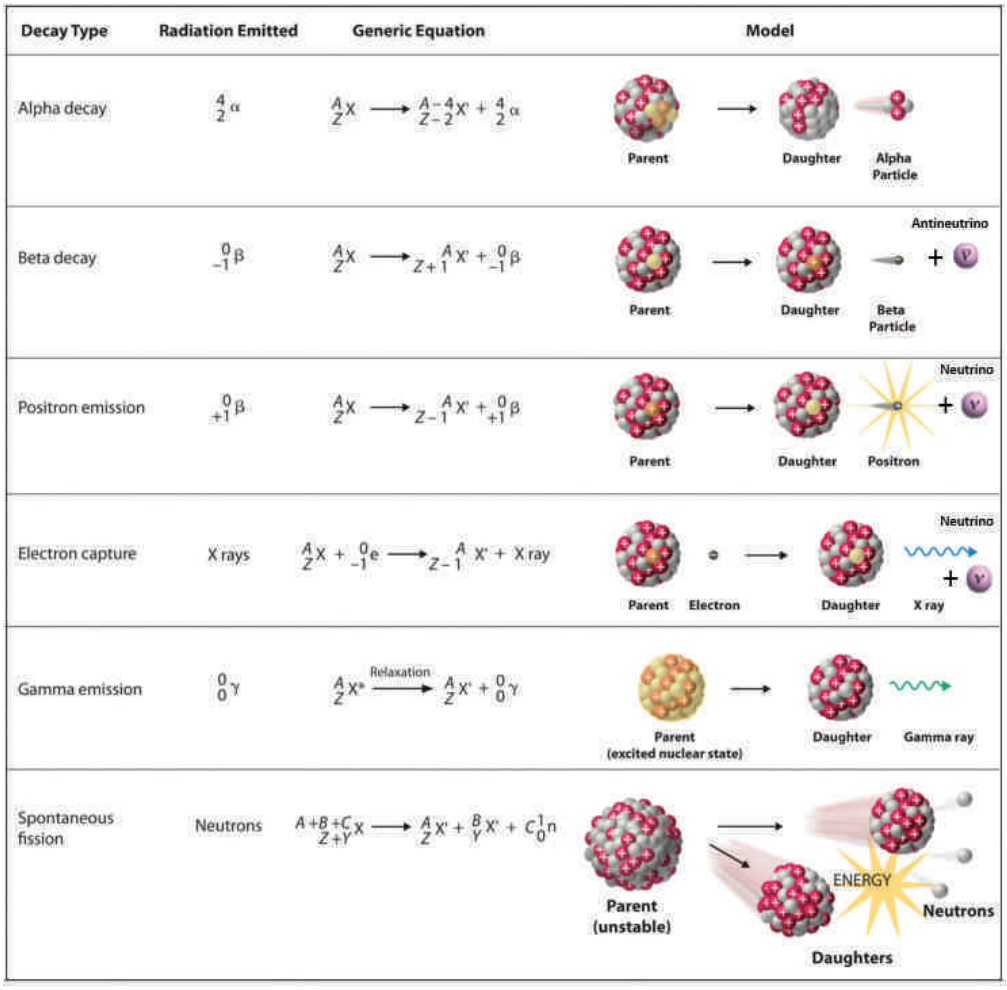

Figure 1.2: Nuclear decay [2]

1.1.3.0.1 ***An example of decay*** The nuclei of all elements with atomic numbers greater than 83 are unstable. Consequently, all isotopes of all elements beyond Bismuth in the periodic table are radioactive. Because alpha decay decreases the number of proton Z by only 2, and positron emission or electron capture decreases Z by only 1, it is impossible for any nuclei with $Z > 85$ to decay to a stable daughter nuclei in a single step, except via nuclear fission. Thus, radioactive isotopes with $Z > 85$ usually decay to a daughter nucleus that is radiaoctive, which then decays to a second radioactive daughter nucleus, and so on, until a stable nucleus is finally reached (cf Figure 1.4a). These series of sequential alpha- and beta-decay reactions are called a radioactive decay series.

The Figure 1.4 shows the process in details. Uranium-238 has an alpha decay (see Figure 1.4b) so it will turn into an isotope with a mass number of 234 (238-4 for alpha decay) and an atomic number of 90 (92-2 for alpha decay). After alpha decay, Uranium-238 becomes Thorium-234. This isotope will decay through the Beta decay. It will thus become Thorium-233.

1.1.4 Introduction to radioactive ion beams (RIBs)

Pure and intense radioactive ion beams (RIBs) are of great demand in numerous fields such as nuclear physics, astrophysics, studies on weak interactions, solid state physics and life science.

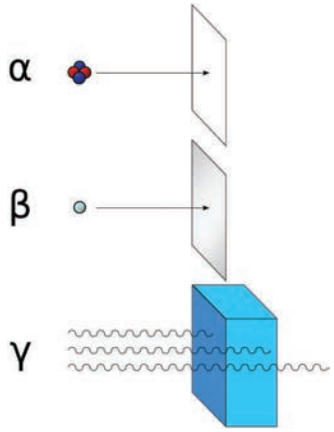

Figure 1.3: Stopping of decay emissions [3]

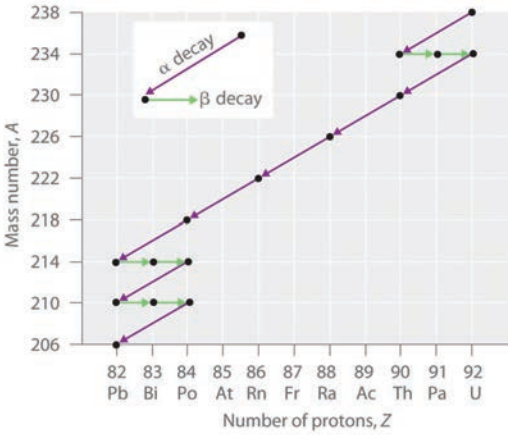

(a) Process of decay in case of Uranium-238 [3]

(b) Periodic table of elements

Figure 1.4: Process of decay of Uranium-238 and nuclei chart correspondence

The isotopes of interest are produced in a nuclear reaction between an accelerated primary beam or by neutrons in case of nuclear reactors and a stationary target. Not only this process allows the production of stable nuclei (from the valley of stability) but also of unstable species approaching the valley boundaries (cf Figure 1.5). Each color in the nuclei chart corresponds to a decay mode. Each nucleus is expressed by its decay mode (that can be a combination of different decay modes like for example the 236Np that tends to decay 13.50 % in alpha decay, the rest being electron capture - see Figure 1.4b).

These unstable species tend to decay more or less quickly, sometimes within milliseconds. This decay time is defined by the radioactive half-life, also specified in the nuclei chart.

The radioactive half-life $T_{1/2}$ for a given radioisotope is a measure of the tendency of the nucleus to decay of half its staring level. This means that after this period of time, half of the initial number of nuclei already decays.

This measure is purely based on probability. The tiny nuclear size compared to the atom and the enormity of the forces which act within it make it almost totally impervious to the

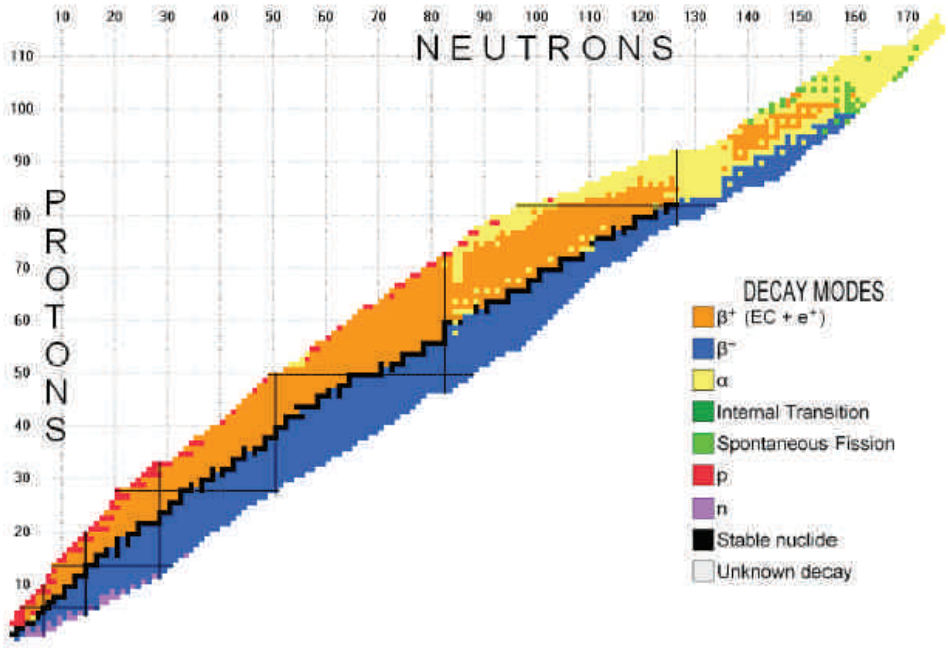

Figure 1.5: Nuclear chart with possible decay modes [4]

outside world. The half-life is independent of the physical state (solid, liquid, gas), temperature, pressure, the chemical compound in which the nucleus finds itself, and essentially any other outside influence. It is independent of the chemistry of the atomic surface, and independent of the ordinary physical factors of the outside world. The only thing which can alter the half-life is direct nuclear interaction with a particle from outside, e.g., a high energy collision in an accelerator.

Due to their fast decay, it is very challenging to produce short-lived species in high beam intensity and obviously depend upon the method used to create and extract them.

Over the years, two main methods have been developed in order to obtain pure and intense RIBs: the Isotope Separator On-Line (ISOL) technique and the in-flight separation technique which will be fully described in the next sections .

1.2 Radioactive ion beams (RIBs): a tool to study unstable nuclei

Developments over the last decades for the production and study of radioactive ion beams (RIBs) have resulted in techniques used to explore the properties of isotopes far from the valley of stability. However, by moving away from the valley of beta stability, the production of these so-called exotic nuclei is confronted to several difficulties [5]:

- extremely low production cross section,
- overwhelming production of unwanted species in the same nuclear reaction,
- very short half lives of the nuclei of interest.

Originally, two complementary ways to make good quality RIBs were developed: the isotope separation on line (ISOL) technique and the in-flight separation technique .

The final aim is the production of exotic nuclei that are intense and pure.

1.2.1 RIBs production methods and facilities

1.2.1.1 In-flight and ISOL methods

In the in-flight method, the constituting elements are a accelerator complex for heavy-ion, a thin production target followed by a separation device and optional further beam manipulation devices like range bunchers, stopping cells or storage rings [5]. This method uses fragmentation of intense heavy-ion beams.

The different steps involved in an ISOL system include production of the radioactive isotopes, thermalization in a gas, liquid or in the thick target itself, ionization, extraction from the target-ion source system (TISS) and acceleration, mass separation and post-acceleration. The TISS can be considered as the heart of an ISOL system.

The ISOL method requires a high-intensity primary beam of light particles from a driver accelerator (or a reactor) and a thick target. The radioisotopes are produced via spallation, fragmentation or fission. Figure 1.6 shows the two different production methods.

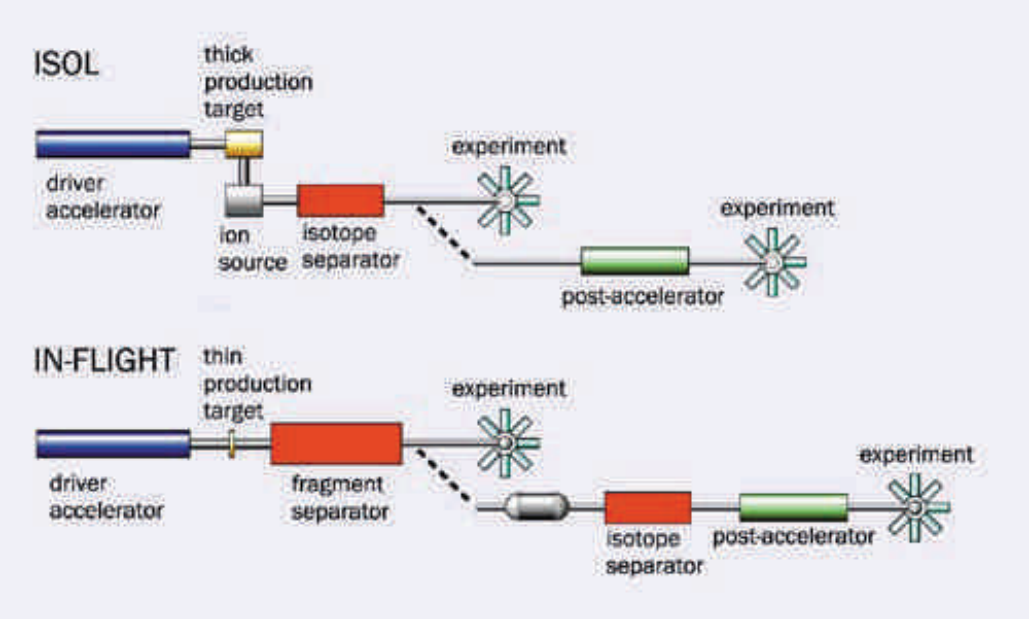

Figure 1.6: Schematic drawing of the ISOL and in-flight based production methods for RIBs [5]

The ISOL method, which was the first one developed, produces fragment almost at rest which can be used for experiments at low energy (a few tens to a few hundreds of keV) or may be re-accelerated by a post-accelerator [5]. Radioactive beams at energies greater than 30 MeV have been produced so far at heavy-ion accelerators by using the in-flight separation method.

1.2.1.2 In-flight and ISOL facilities around the world

1.2.1.2.1 Current facilities The first isotope separator was developed at the Copenhagen Cyclotron by Bohr and co-workers using the principle of electromagnetic separation [30]. Today, there are many laboratories around the world which supply beams of radioactive ions.

For the in-flight method, the pioneering work was performed at the bevalac at Berkeley, CA [31]. The Super-HILAC was initially a low energy heavy ion linear accelerator set on the hillside at the Lawrence Berkeley laboratory and the Bevatron a proton synchrotron for particle physics located over a half mile away. In order to produce the first relativistic heavy ion machine, both accelerators were connected by a beam line descending from the hill through the laboratory and transforming the HILAC into a heavy ion injector for the Bevalac [31].

A map of the different RIBs facilities as from 2003 is presented in the Figure 1.7. In blue and green are presented the existing facilities while the red ones are future facilities planned.

Figure 1.7: RIB facilities - 2012 [6]

Nowadays, three major ISOL facilities can be counted in the world: CERN-ISOLDE and GANIL-SPIRAL in Europe and TRIUMF in North America. The oldest and the precursor of other ISOL installations worldwide, is ISOLDE at CERN. They all deliver a large variety of beams. Regarding to the in-flight method facilities, NSCL-MSU in America, GANIL and GSI in EUrope and RIKEN in Japan can be considered as the leaders.

Upgrades in existing facilities are being planned and would lead to an increase in RIB intensity: HIE-ISOLDE that should be operational in 2016, SPIRAL 2 in 2017 and SPES in 2017.

From Figure 1.7, it is obvious than a worldwide effort is put to produce always more intense and pure RIBs.

1.2.1.2.2 Future facilities This effort can be seen as well in the desire to develop new facilities, weither in America, Europe or Asia. Indeed, future RIB facilities are currently under study in each one of these part of the world:

- **EURISOL** in Europe [12]. The EURISOL project is aimed at the design and subsequent construction of the next-generation European ISOL radioactive ion beam (RIB) facility. The ion yields delivered by the current ISOL facilities, or those under construction (HIE-ISOLDE, SPES, SPIRAL2) will be exceeded by at least a factor 100. This will open a wide field of research for physicists. A design study has been done from 2005 to 2009 and lead to a design proposal. Two over the twelve tasks of the design study phase proposed new targets designs to deal with the 100 KiloWatts and MegaWatts beams power that will be delivered by the facility (see Section 1.5.2.1). The location of the future EURISOL facility is not yet defined. So far, CERN in Switzerland or GANIL in France are possible site but no decision has been made and all possible candidate will be considered in the future.
- **FAIR** in Europe. FAIR, located in Darmstadt, Germany is a very ambitious Nuclear Physics project under construction [32]. The scientific research foreseen at FAIR includes physics of hadrons and quarks in compressed nuclear matter (CBM experiment); atomic and plasma physics, and applied sciences in the bio, medical, and materials sciences (APPA); hadron structure and spectroscopy, strange and charm physics, hypernuclear physics with antiproton beams (PANDA) and of most interest, the structure of nuclei, physics of nuclear reactions, and nuclear astrophysics with RIBs (NUSTAR).
- **FRIB** in North America [33]. This facility will provide a combination of ISOL and In-flight techniques. The driver linac will deliver ion from protons to uranium with a beam power of 400 kW or more, and a beam energy of 900 MeV for protons or 400 MeV per nucleon for primary heavy ions. The production method can be optimized for a given nuclei.

Other projects such as HIE-ISOLDE in Switzerland, ISOL@MYRRHA in Belgium, MAFF in Germany and JHF E-ARENA at KEK-Tanashi in Japan are also planned or under study. A more complete overview of the existing and planned facilities can be found in different proceedings from the European Particle Accelerator Conference (EPAC) [34], [35].

1.2.2 Components of ISOL facilities

1.2.2.1 Introduction

As explained previously and shown in the Figure 1.8, three main steps can be identified in the ISOL method:

- TISS: target-ion source system, which is the heart of the ISOL method. At that step, the RIBs are created from the impact of a primary beam impact onto a thick target and extracted from the target material. It is then ionized in the ion source.
- Isotope separation: done by mass separation, depending on the particle mass selected.
- Post acceleration phase: phase during which the beam from the selected isotopes is post accelerated.

Each of these steps will now be presented in details.

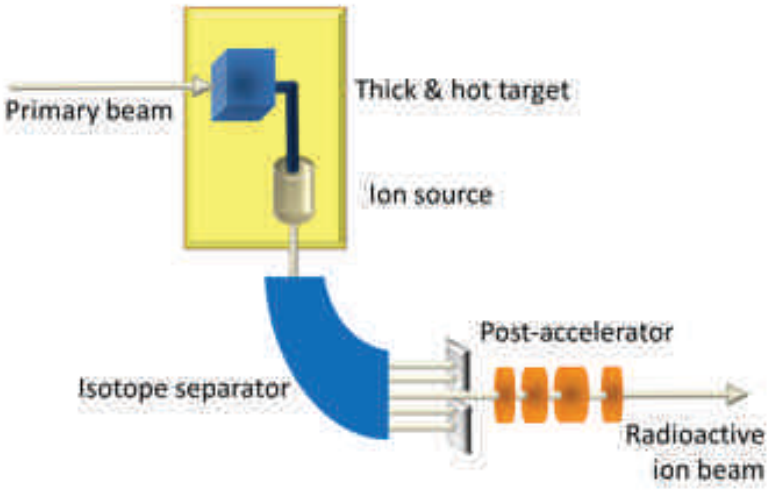

Figure 1.8: Schematic drawing of the ISOL methods for RIBs [5]

1.2.2.2 Target-ion source system (TISS)

The TISS is the system that allows the creation and ionization of the radioactive ion beams.

1.2.2.2.1 *Targets*

Different production reactions are used depending on the isotope of interest. Intense primary beams impinge on different target materials and configurations. Thin targets are mainly used for light and heavy-ion fusion evaporation reactions (in-flight method) while thick targets are mainly used for spallation, fragmentation and fission reactions produced with proton or neutron (ISOL method) [5]. In some cases, liquid target materials can be used. Indeed, continuous efforts to increase the primary beam intensity is pursued, leading to new target development as it will be seen in Section 1.4. Liquid target is an answer to this increase of beam intensity since liquid usually handle better the shock waves due to impact of the high beam intensity if the beam is pulsed. They represent the innovative solution currently developed. It forms the core of this PhD thesis where the complete design of a liquid lead bismuth target is fully studied, from the modeling and manufacturing of the target to its off-line experimentation.

1.2.2.2.2 *Transfer line*

Between the thick target and the ion source operated in an ISOL facility, a transfer line is needed (see Figure 1.9). This tube is in general kept at high temperature to avoid sticking of the atoms to the walls. The tube can also be used for purification depending on the secondary beam required. By cooling the tube, only atoms from volatile elements will be transferred if needed. The non-volatile elements will stick to the walls of the transfer tube where they will undergo radioactive decay and will then be lost [36]. A quartz tube can also be inserted in the transfer tube to specifically absorb alkali elements such as Rb [37].

1.2.2.2.3 *Ion source*

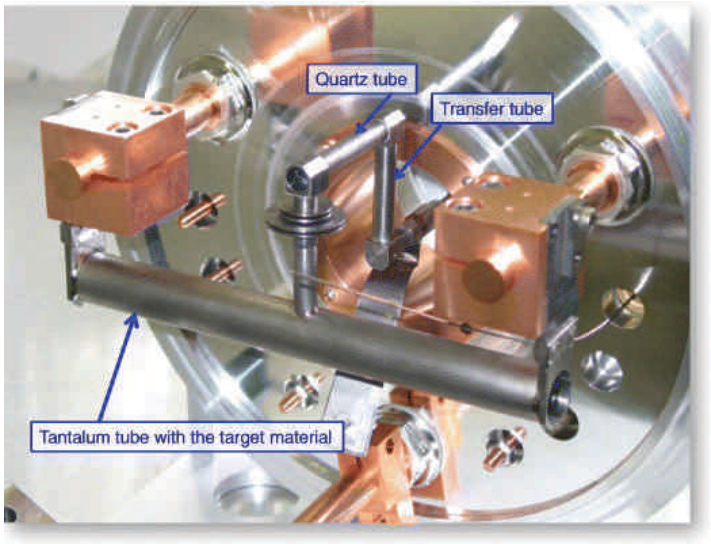

Figure 1.9: ISOLDE target unit - visualisation of transfer line and quartz tube [7]

The development of ion source is a combination of chemistry, mass-transport, electromagnetism, plasma, radio-frequency and material physics. The function of an ion source is to ionize (i.e. acquiring a negative or positive charge by gaining or losing electrons) the radioactive nuclei coming from the target material and to release them with the maximum efficiency and as fast as possible. The type of ion source used will depend upon the resulting beam created (low or high ionization potential, highly pure beam, ...). The different types of ion sources typically used in ISOL facilities are presented hereunder.

Surface ion sources The surface ion source is the simplest ionization method. The set-up consists in a line which has a higher work function than the atom that should be ionized (see Figure 1.10), i.e. a higher need of energy to remove an electron from a bulk material (solid or liquid). In surface ionization, atoms of elements with low ionization potential are converted to singly charged ions after they had impacted a metal surface of high work function.

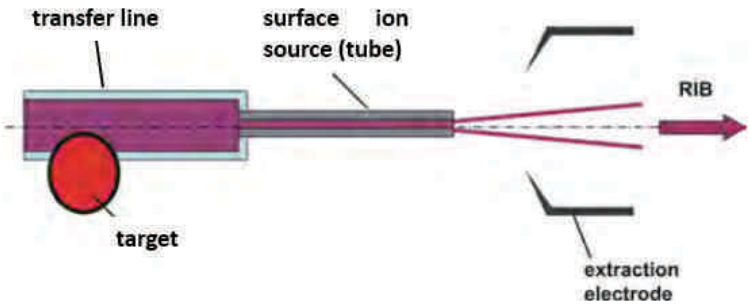

Figure 1.10: Scheme of a surface ion source [8]

The line and the surface ion source can be heated up to 2400° C, the maximum temperature depending on the construction material.

After the source, an extraction electrode accelerates the ions up to the desired energy trying to maximize the efficiency. This ion source has been demonstrated to be an efficient method and

it is used in combination with most of the different target materials.

FEBIAD ion sources Forced electron beam-induced arc discharge (FEBIAD) ions sources are widely used in ISOL facilities due to its versatility. In FEBIAD ion sources, a heated cathode emits electrons which are accelerated in a chamber by an anode. The atoms or molecules in this chamber, coming from the target or injected via a dedicated gas system, are ionized by electron impact ionization. The transfer line can be both hot or cold [8].

Laser ion sources There are some isotopes that cannot be ionized efficiently with any of the previously presented ion sources (surface and FEBIAD ion sources). Indeed, the beam obtained with these methods may contain an important load of impurities. The laser ion source has been developed to obtain a purified beam since it works only on the element for which the laser wavelength is tuned for. Consequently, the isobaric contamination is reduced. The layout of a laser ion source is presented in Figure 1.11. Furthermore, more information about this technique can be found in [8].

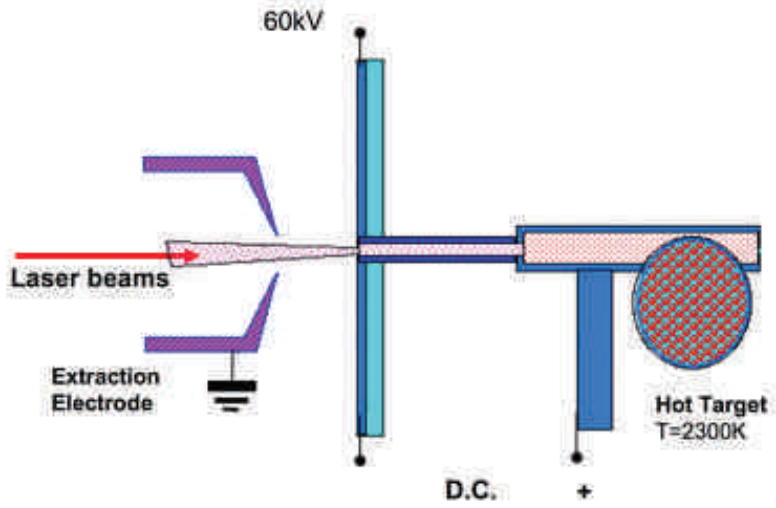

Figure 1.11: Scheme of a laser ion source [7]

RIBs and ion sources Figure 1.12 shows the periodic table with a superimposed color code to indicate the different ion source types used nowadays at the ISOL-based RIB facilities. Surface ionization is used for the alkaline and alkaline-earth elements. The 'plus' and 'minus' sign indicate the creation of a positive respectively negative ion. Electron impact ionization (plasma sources with a 'hot' or 'cooled' transfer tube) can in principle be used for all elements but focuses on the volatile elements. Laser ionization can in principle also be used for all elements but efficient schemes are difficult to realize for the noble gases and some light elements with a high ionization potential [5].

1.2.2.3 Mass separator

The beam produced at the target-ion source is then accelerated by an electrostatic potential of several kV. But it does not usually fit the requirements for the experiments in terms of purity

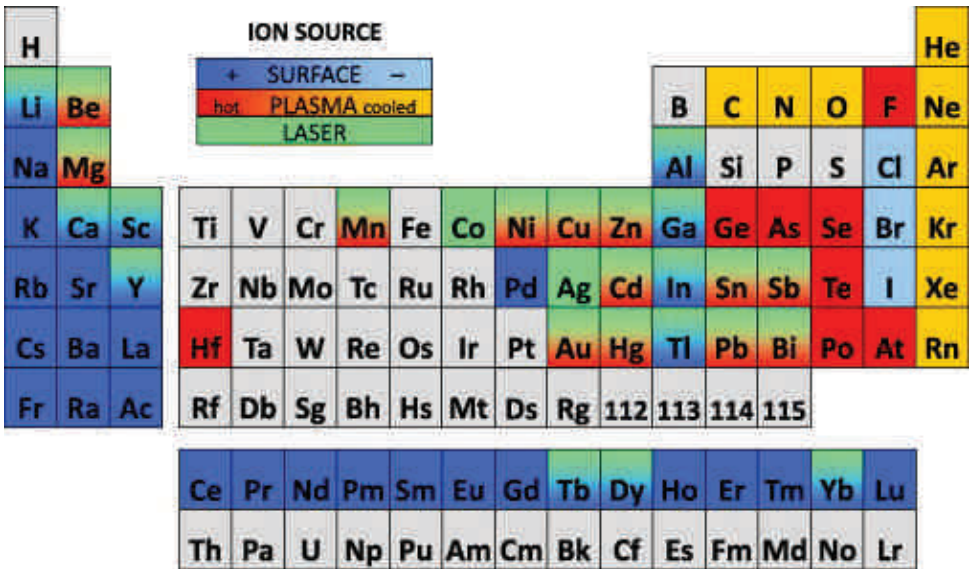

Figure 1.12: Periodic table showing the differents RIBs created with the different ion sources type [5]

or optical quality. Consequently, the beam is then transported to a mass separator as shown on Figure 1.13a.

Magnetic mass separator are implemented in the beam line to get the required purity. These devices use a magnetic field perpendicular to the beam axis to bend the ion trajectories. Since the curvature radius is different for different masses, a specific isotope can be selected out. For example, an isotope of mass 15.9994 would correspond to the stable element O (Oxygen) in the periodic table (see Figure 1.13b). Isobaric masses can be separated with the magnetic mass separators. It also could be an association of two or more isotopes. For example, a mass 27 could correspond to the stable element Co (Cobalt) but also to the stable element O (Oxygen) with a unstable nucleus of mass 11 (for example 11C).

1.2.2.4 Post-acceleration

Different post-accelerators are used for the production of energetic RIB. Three type of accelerators are used for post-acceleration: cyclotrons (GANIL), linear accelerators (ISOLDE and TRIUMF) and tandems (HRIBF). The combined charge-breeding and post-accelerator system have their own characteristic timing and can also be used for further purification of the RIB [39][4].

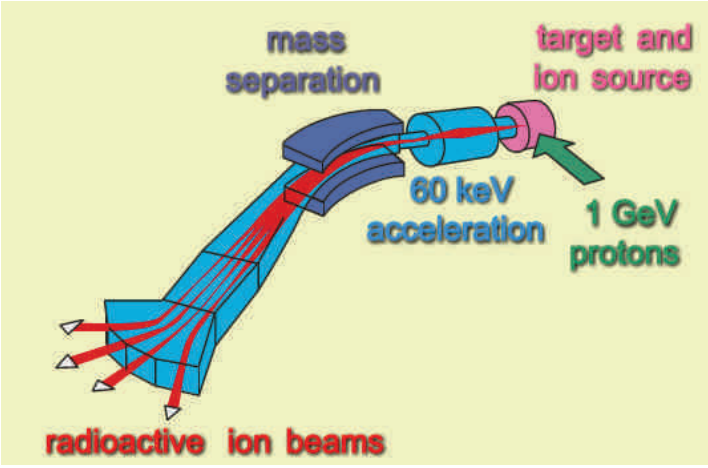

(a) ISOLDE post TISS layout [7]

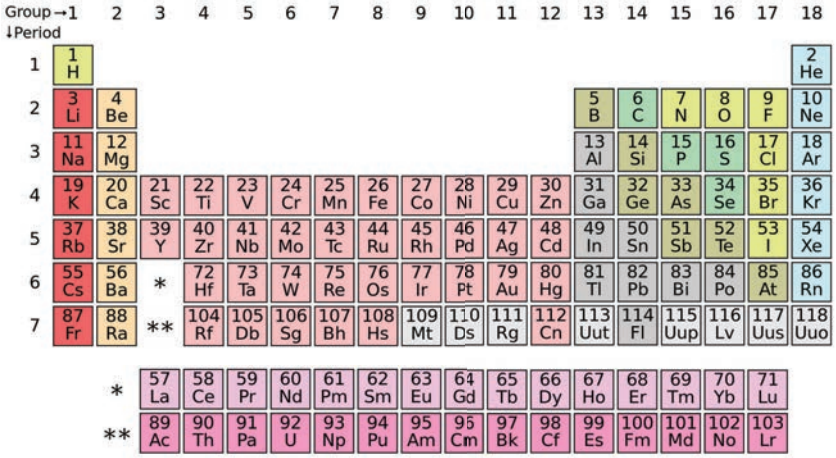

(b) Periodic table of elements [38]

Figure 1.13: Mass separator (a) and corresponding Isotopes depending on the mass (b)

1.3 Production of Radioactive Ion Beam (RIBs)

1.3.1 Primary beam definitions

1.3.2 Factor determining the RIBs intensity

As specified before, the decisive figure of merit for any RIB facility is the intensity i expressed in Ampere (Coulomb per second) and the purity of its beams. The yield of the same produced beam is then the fraction of produced beam (in ion/second) per proton intensity (in Ampere). The yield is expressed in $\boldsymbol{ion/\mu C}$. For an ISOL facility, the beam intensity in ions per seconds provided to the user is given by [40]:

$$i = \Phi.\sigma.N.\varepsilon_{target}.\varepsilon_{source}.\varepsilon_{sep}.\varepsilon_{transport} \tag{1.1}$$

The production in the target is determined by $\Phi.\sigma.N.$, i.e. the flux Φ (s^{-1}) of primary particle, the cross section σ (cm^2) to produce the desired isotope and the number N of target nuclei per

square cm. The final RIB intensity is then obtained by taking into account different efficiencies inherent to the system. The coefficients $\varepsilon_{target}, \varepsilon_{source}, \varepsilon_{sep}$ and $\varepsilon_{transport}$ respectively represent the efficiencies of the release from the target, the ionization in the ion source, the transmission through the mass separator and the transport trhough the beam lines. The values for the different efficiencies depend strongly on the isotopes studied and the systems used. The decay losses are taken into account in each individual release efficiencies. As a matter of fact, the goal is to achieve a total efficiency close to 1 to get the highest yield of beam. The difficulty to reach this goal increases in case of short-lived species, which tend to decay before to be delivered for physics experiments. The different efficiencies are described with more details below.

1.3.2.1 Target release efficiency

The target release efficiency expresses the amount of ions that survive from the moment of their production in the target to the moment of their extraction from the ion source. The two principal processes that affect the release efficiency are diffusion in a solid or liquid state and effusion to the ion source. These processes, including the desorption process, are described below.

1.3.2.1.1 Diffusion process The diffusion is the phase during which the created isotopes must diffuse within the target material, meaning reaching the surface of the material. Atoms produced will move through the solid until equilibrium is reached. The net flux J of atoms in atom.m^{-2}.s^{-1} is related to the gradient of concentration ∇n by the first Fick's law:

$$J = -D.\nabla n \tag{1.2}$$

where D is the diffusion coefficient in $m^2.s{-}1$ and the concentration n is expressed in $atom.m^{-3}$. This coefficient is dependent upon the state of the material (solid, liquid or gas) and its evaluation is presented hereunder.

The diffusion coefficient can be described by two different formulas depending on the type of diffusion, namely a solid-state or a liquid-state one.

- **Solid-state diffusion:** For solid-state diffusion, the diffusion coefficient D is dependent on the activation energy H_A required to move the atoms or vacancies from site to site, and on the temperature T of the solid [41]:

  $$D = D_0.exp(-H_A/(kT)) \tag{1.3}$$

  where k is the Boltzmann's constant (k =1.38 10^{-33} J.K^{-1}) and D_0 is the maximum diffusion coefficient constant at infinite temperature in m^2/s. The activation energy H_A is expressed in J. Here, the diffusion coefficient will tend towards D_0 for high value of temperature.

- **Liquid-state diffusion:** For liquid state diffusion, a semi empirical formula suggested by Walls and Upthegrove is proposed for the estimation of the diffusion coefficient D_0 [42]:

$$D = \frac{k.T.\gamma^{-1/3}}{2.\pi.h.b.(2b+1)} \frac{V}{N_0}^{2/3} exp(\frac{-\Delta S^*}{R}) exp(\frac{-\Delta H^*}{R.T}) \quad (1.4)$$

where γ is a dimensionless number equal to 4/3, b is a dimensionless number equal to 0.419, V is the molar volume in m^3/mol, N_0 is the Avogadro's number ($N_0 = 6.022.10^{23} mol^{-1}$), ΔS^* is the entropy of activation for kinematic viscosity in $J.K^{-1}.mol^{-1}$ and ΔH^* is the enthalpy of activation for kinematic viscosity in $J.mol^{-1}$.

- **Desorption process**

  An adsorbed species present on a surface at low temperatures may remain almost indefinitely in that state. As the temperature of the substrate is increased, however, there will come a point at which the thermal energy of the adsorbed species is such that the desorption process can occur. The desorption rate of atoms per unit area *dN'/dt* in thermal equilibrium with a surface at temperature T is given by [41]:

$$\frac{dN'}{dt} = \frac{P(T).N'.k.T}{h}.exp((\Delta S.T - H_{ad})/(kT)) \quad (1.5)$$

where *P(T)* is the temperature-dependant probability that the particle will stick to the surface (or sticking coefficient), *N'* is the number of atoms adsorbed per unit area, h is the Planck's constant ($h = 6.63\ 10^{-34}$ J.s^{-1}), ΔS is the change of entropy of the adsorbed particle in J.K^{-1} and H_{ad} is the heat of adsorption in *J*.

1.3.2.1.2 Effusion process Once a particle has diffused to the surface of the target, the subsequent effusion step is determined by several quantities:

- **the mean number** χ of collision with the surface of the target and its enclosure before leaving the ion source as neutral or ionized particle,
- **the mean sticking time** τ_a per wall collision, which depends essentially on temperature and adsorption enthalpy ΔH_a of the surface of the enclosure,
- **the mean flight time** τ_f between two wall collisions.

The transfer line, also called cold line, can possibly be is kept at a lower temperature than the target in order to condense some volatile elements that could be released as contaminants for the beam of interest. This type of line is usually defined as "cold" lines.

1.3.2.2 Others efficiency

The values for the different efficiencies depend strongly on the isotopes studied and the system used. Typical numbers for ε_{sep} are over 80 % and over 90 % for $\varepsilon_{transport}$. It is not possible to give global number for ε_{source}. However, ionization efficiencies can reach over 50 % for noble gases using electron impact ionization or ECR sources, surface ion sources for elements with a low ionization potential when efficient excitation and ionization steps are known [41].

1.3.3 Primary beam definition

In order to obtain a RIB, a primary beam is sent onto the target. The sent particles will deposit heat onto the material while colliding with the target matter. This primary beam can be made of different particles (protons, heavy ions, ...) and can be either pulsed or continuous. This will have a direct impact onto the target design, operation and lifetime. In all cases, this deposited heat should be extracted either by active or passive cooling.

A pulsed beam is a beam having a frequency which means that it is not a continuous impact of particles but that the particles are produced by packet. The particles are sent all together in a pulse. The time between the first and last particle of the pulse is called pulse length. The pulse length can be as low as few nanoseconds so that during the beam impact onto a target, a high power is deposited in few nanoseconds up to microseconds (see Figure 1.14).

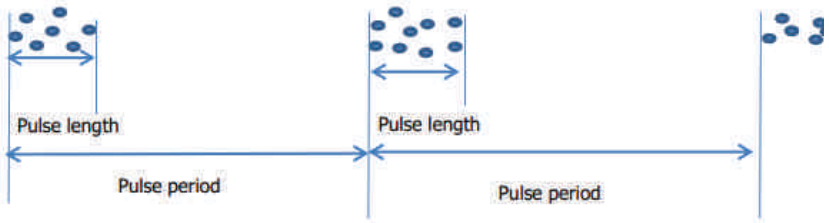

Figure 1.14: Beam structure in case of pulsed beam dynamics

On the contrary, a continuous beam will constantly impinge onto the target.

The primary beam is usually defined by its intensity. It can be either an average intensity in case of both the pulsed and continuous beam, or it can be the peak intensity in case of the pulsed beam as shown in the Figure 1.15.

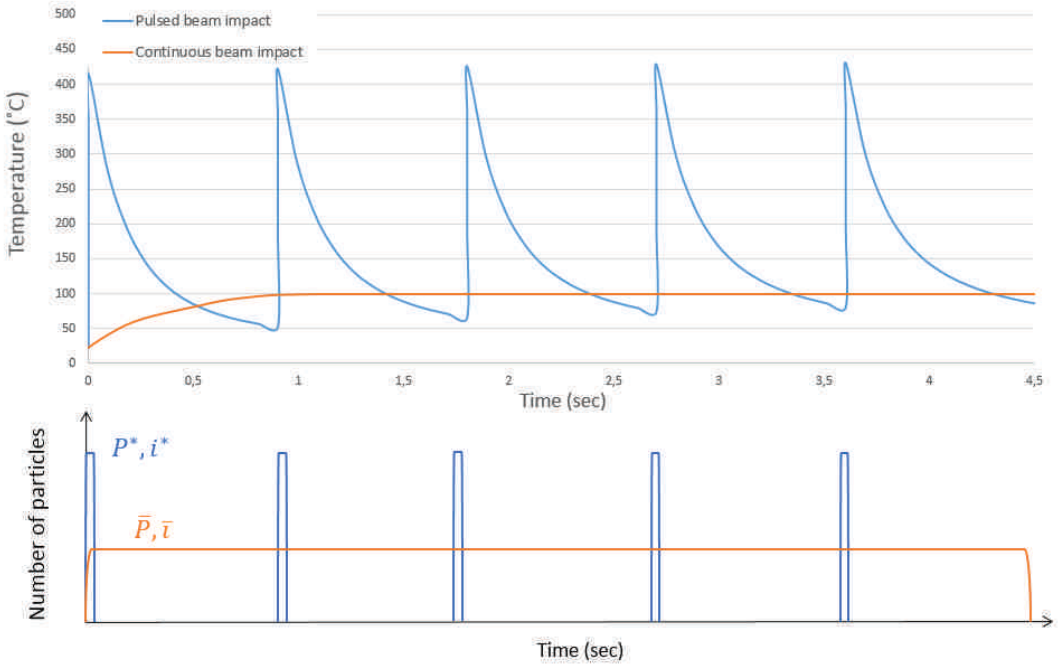

Figure 1.15: Pulsed vs continuous beam - temperature over time

This distinction is quite important. Indeed, in case of a pulsed beam, the target will be submitted to an average current $\bar{i}$ or power $\bar{P}$ that will constantly increase the target temperature until the thermal equilibrium is reached thanks to the target cooling (active or passive cooling). In case of a pulsed beam, the same steady state thermal field will be reached but added to it, a peak of current i^* or power P^* will be deposited at the beam frequency. This will induce high and fast thermal increase in a localized point of the target, inducing high stresses and shock waves as well.

A relation link easily the average or peak power of a pulsed beam to the number of particle and to the time structure of the beam [43]:

$$\bar{P} = \frac{E * C * Np}{pp} \quad \text{and} \quad P^* = \frac{E * C * Np}{pl} \tag{1.6}$$

with E the beam energy in eV, C the charge of one electron *(1.602*10^{-19} C)*, Np the number of particles, pl the pulse length in *sec* and pp the pulse period in *sec*. This usually does not represent the power deposited onto the target as only a certain percent of the primary beam (usually around 50 to 70 %) will enter in collision with the target material.

As well, one can define the average or peak beam intensity by [43]:

$$\bar{i} = \frac{C * Np}{pp} \quad \text{and} \quad i^* = \frac{C * Np}{pl} \tag{1.7}$$

The intensity i is given in Amperes *(A)* and the power P is given in Watts *(W)*.

The general beam intensities and power considered for high power targets are given in Table 1.1.

Parameters	***Unit***	**Value**
Average current $\bar{i}$	μA	$>$ 50 - 20 000
Peak current i^*	A	>0.5 - 1
Average power $\bar{P}$	kW	$>$ 50 - 4 000
Peak power P^*	MW	> 1

Table 1.1: Typical values for high power beams for RIB facilities - power and intensities

This power deposited onto the target will induce an increase of the material temperature. In case of high power target, it is of major importance to properly control this excess of heat for the safe operation of the target.

1.3.4 Proposed improvements to increase the yield of produced RIBs

As previously said, to reach high beam intensity for short-lived species is very challenging. Indeed, it is strongly affected by decay losses due to time delay between in-target production

and ion beam extraction. Consequently, the target and ion source units must be developed in order to shorten diffusion lengths for fast diffusion release and fast transport to the ion source.

Equation 1.1, which looks like a simple product, is actually more complicated since most of the factors are inter dependent. For example, an increase of N by increasing the target length is in principle possible if the energy of the primary beam is high enough to provide a sufficient range but it is obvious that a radioactive particle can get easily trapped and decays before finding its way out to the ion source. Indeed, by trying to increase the target "thickness", the diffusion release efficiency would be decreased.

The development of a new concept of high power liquid target with short diffusion paths is one of the main purpose of this thesis. During the target development phase, different parameters have been optimized. These solutions are listed below:

- Increasing the target material density. Indeed, with a higher density, the number N of target nuclei would be increased and thus, the total beam intensity would be increased as well, all other parameters being preserved.

- Use of a liquid material rather than a solid one: diffusion coefficients for liquids are several orders of magnitude larger than those for their solid-state counterparts and therefore are especially attractive for short-lived species. Unfortunately, few elemental metals have the vapor pressure characteristics adapted to these applications. To take advantage of the fast diffusion properties of liquid-state targets, eutectic alloys can be employed as a means of reducing the melting points of metals of higher melting points [5].

- Increase of the target unit temperature: as seen previously, the diffusion and effusion phases are highly dependent upon the temperature of use. Generally, the higher the temperature, the higher the efficiencies will be. However, limitations can be found due to the vapor pressure of the material (the target is operated in high vacuum ($\approx 10^{-6}$ mbar), and the TISS operation should not be hampered by a vapor pressure).

- Choice of target material: in the ideal case, the radioactive species should possess physical and chemical properties almost opposite to those of the target-material itself. For example, the species should not form refractory compounds within the target-material, rapidly diffuse to the surface, either in elemental or compound form, and upon reaching the surface, be readily desorbed. These idealized differences in chemical and physical properties of the target/species combination are not often realizable, particularly for close lying elements where their physical and chemical properties are often similar [5].

- Modification of liquid geometry: Experimental results exist for static targets ran under different conditions [20]. For yields obtained at ISOLDE with an incident quasi continuous proton beam delivered by the Synchrocyclotron (SC), a liquid Pb target was operated with an electromagnetic shaking which was reported to reduce the release time of Hg to one third of its original value [20]. For yields obtained at ISOLDE with an incident highly pulsed beam delivered by the Proton Synchrotron Booster (PSB), the strong pressure waves generated by the beam lead to violent shaking of the liquid metal target which accelerates the release process [20].

  Theses statements lead to a more complete analysis and a model of fractional release have been used to compare the available data with a calculated release fraction from

a diffusion chamber producing fine showers or droplets of Pb. The model chosen and developed during the EURISOL design study phase, when a comparison between available experimental data and the calculated release fraction has proven the validity of this model, is the one of Fujioka and Arai [9] that gives an evaluation of remaining fraction of isotopes at time t depending on the solid form considered, being foil, fiber and particle [9]:

$$f(\widehat{t}) = \frac{2.n}{\pi^2} \sum_{m=1}^{\infty} \frac{1}{c_m} . exp^{-c_m . \widehat{t}} \tag{1.8}$$

where $\widehat{t}$ is the time divided by a characteristic diffusion time τ_D, n and c_m are coefficients given for each solid form (foil, fiber or particle).

With this model, Fujioka and Arai demonstrated that some improvement in the fraction of remaining isotope and thus in the diffusion release can be reached when using a particle shape rather than a foil or fiber one (see Figure 1.16).

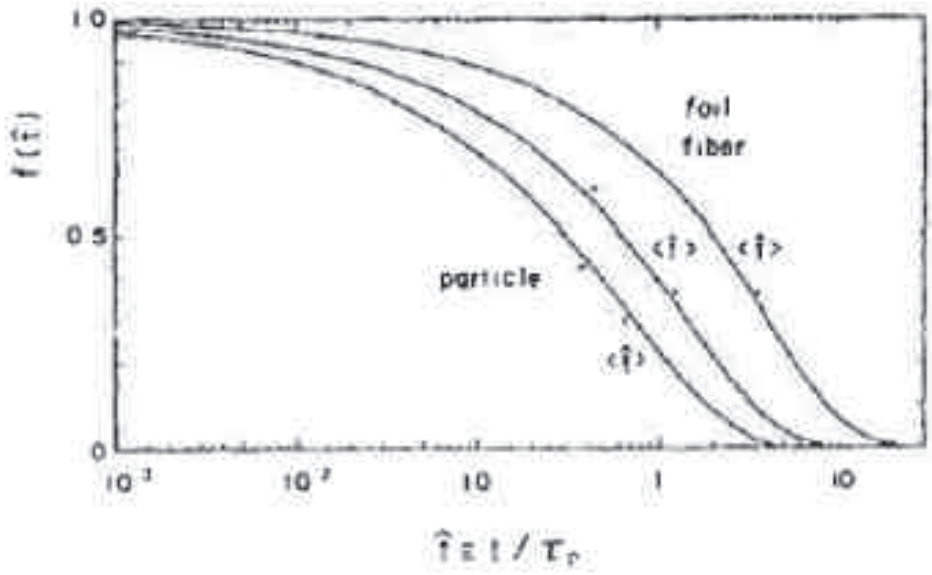

Figure 1.16: Fraction of isotope remaining in the solid [9]

This proposal has not been tested yet under beam irradiation conditions. It is the retained solution for the developed target presented in this manuscript and will be fully described in Chapter 2.

- Increase of the primary beam intensity: it is obvious than if the primary beam intensity is higher (i.e. higher number of primary particles), the created RIBs will be more intense as well since the reactions will increase. However, this leads to new challenges to handle.

All these techniques are used to produce the beam requested by new challenges in this field of physics. However, a lot of proposed improved parameters (target material, temperature, form of target, ...) imply the need of new targetry concept to handle the increase of beam intensity as well as new kind of material.

1.4 High power ISOL targets

This section proposes to give an exhaustive summary of the different types of high power ISOL targets developed around the world as well as the specific challenges of this type of target.

1.4.1 Main high power target challenges

Targets capable of reliable operation with high power particle beams are a crucial component of several future accelerator facilities. There are many factors driving the limits for a specific design, including energy deposition by the beam, cooling, activation and radiation damage. These mains issues can be separated in three parts: the thermal load, the radiation damage and the coolant performances while at all time, the design should allow an optimized maintenance and reduce the activation.

1.4.1.1 Thermal stresses

Induced thermal stresses in target components pose a major challenge particularly in facilities that operate with pulsed beam or continuous beam with poor reliability that causes frequent beam interruptions.

Time-varying energy deposition in the target leads to non-uniform time-dependent heating of the target. This results in different rates of thermal expansion across the target. Furthermore, the frequency of the pulsed beam as well as the sharp temperature rise due to the fast deposition of energy can also leads to thermal shocks. Figure 1.17 shows two examples of what can occur under a pulsed beam of high energy. Figure 1.17a presents a Tantalum rod with the occurrence of a plastic deformation and possibly cracking due to a stress wave moving through the target material. The plastic deformation and the compressive stress wave are created by the fast expansion of the material surrounded by a cooler one. Figure 1.17b presents the rupture of the beam window of an ISOLDE static lead target unit due to a beam impact of about 1 GigaWatt [44].

Many efforts have been done to assess more in detail this phenomena [45]. For example a full study is provided in [45], including fluids dynamics computation, to understand the hydrodynamics behavior of Isolde liquid metal targets. This study relates the pressure waves induced by the beam impact and the possible splashing phenomenon that occurs in such targets (see Figure 1.18).

1.4.1.2 Radiation damage

In high power targets, radiation damage is a result of both displacement damage of lattice atoms and transmutation. Displacement damage is mainly caused by collisions with incident protons, fast spallation neutrons or recoil energy when atoms emit particles. The displaced atom moves inside the lattice until it loses all its energy creating many vacancies and interstitials. This usually leads to a reduction of the thermo-mechanical properties of the material. As shown on

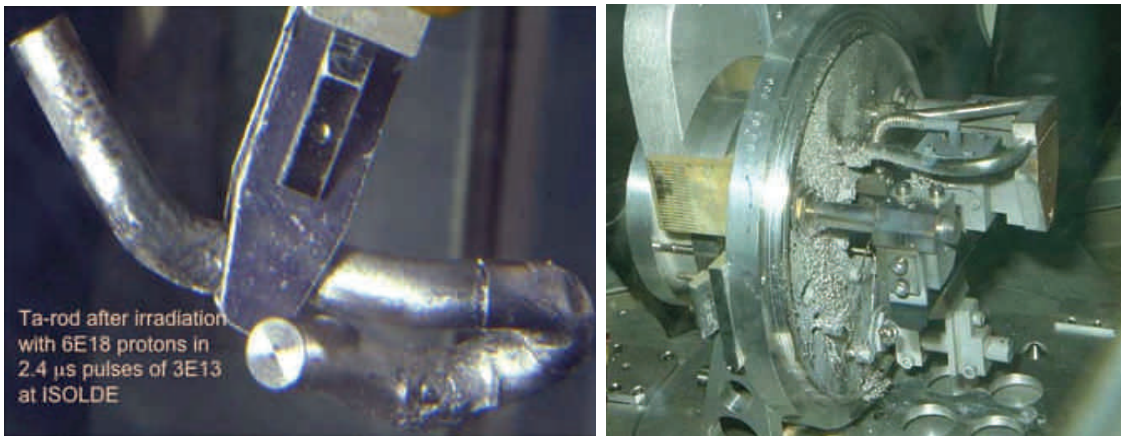

(a) Ta rod after irradiation - plastic deformation [10]

(b) Beam window rupture of a lead static unit in Isolde [44]

Figure 1.17: Thermal stresses example

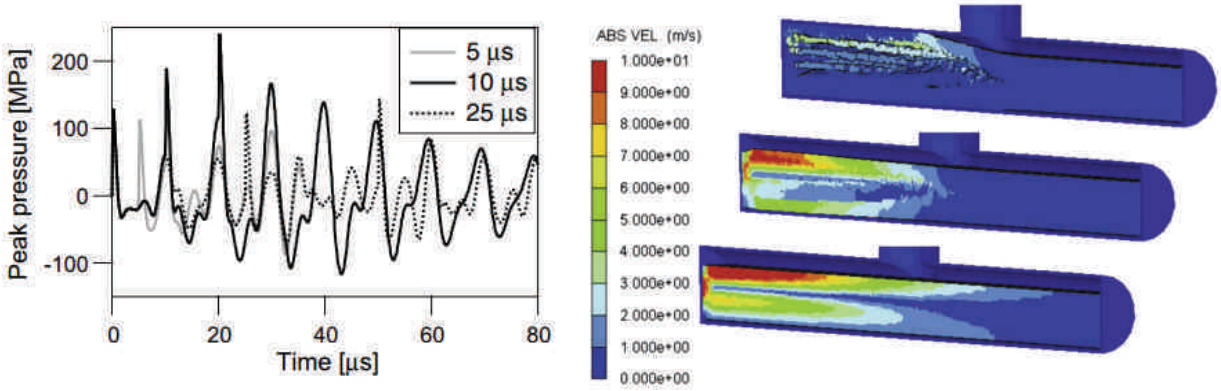

(a) Pressure histories in one location inside the metal liquid [45]

(b) Absolute velocity profile after beam impact - splashing phenomenon [45]

Figure 1.18: Shock waves into metal liquid Isolde targets

Figure 1.19, this can also create a swelling in the material representing the volume change of the material due to the irradiation.

The occurrence of these different phenomena depends on the Displacement Per Atoms (DPA) level in the material. This unit is equivalent to the irradiation level under which the material has been exposed. Usually, to accumulate a high level of DPA (more than a tens of DPA), the object must be irradiated for a long period (several years) under a high beam energy.

1.4.1.3 Cooling performance

Due to the high beam intensities that are expected to be reached in the upcoming years, cooling capacity in the target becomes a key component of such devices. In the current target configuration, the cooling is often done through free convection and radiation toward the ambient. This usually works well for low beam power deposited but for a high beam power, it is not sufficient and new ways for cooling down the target must be considered. The adopted cooling

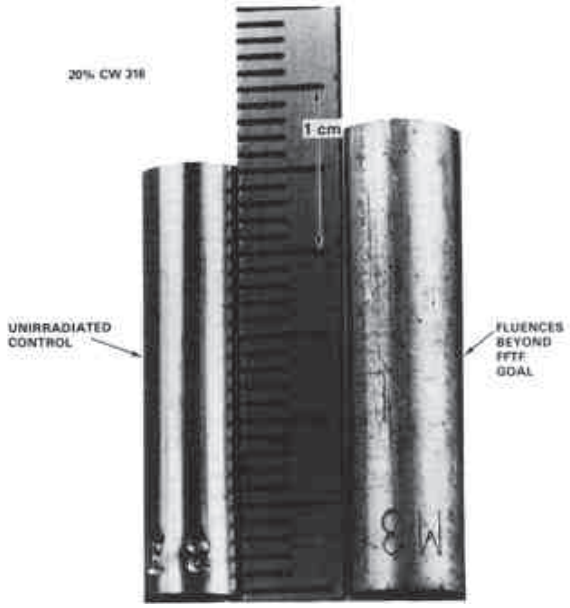

Figure 1.19: Swelling effect on a Stainless Steel sample at 80 DPA [10]

system for high power target is usually a forced convection one. The coolant can be a gas or a liquid. It can also be a liquid metal in some cases. This is new compared to the current target layout and leads to new issues: tightness and pressure of the cooling circuit, thermal equilibrium or possible secondary particle flux and thus increase in radiation level.

1.4.2 General sketch of a high power target

As seen previously, a high power target must comply with a certain number of constraints due to the very high primary beam power impacting on it. More specifically, it should be able to:

- Deal with the possible induced shock waves in case of a pulsed primary beam,
- Extract the additional power brought by the primary beam, either by an passive or active cooling,
- Allow a fast release of isotopes.

Furthermore, the target must be monitored at all time while safety measured must be respected. This means that a double envelope should be found around the target so that in case of target failure of brutal break up, no activated part can pollute the installation.

A general sketch of high power targets can be found in Figure 1.20.

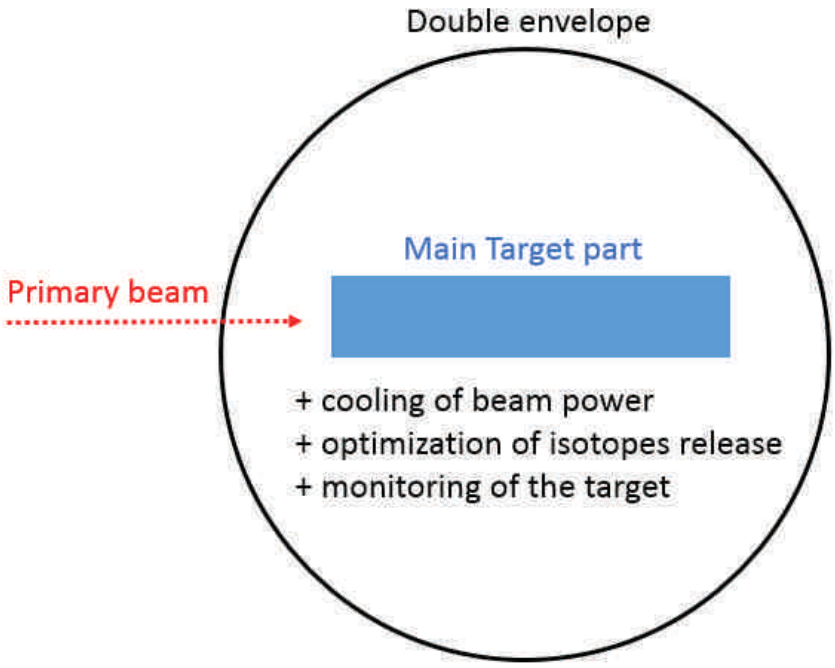

Figure 1.20: General sketch for High Power Targets

1.4.3 Overview of high power ISOL targets

1.4.3.1 Solids targets

As expressed in section 1.2.2, there is many type of targets that have been developed. The type and material of the target depends upon the kind of isotopes that is aimed for. However, some main design constraints must be kept in mind while developing a target, and this, depending of the state of the material used (either solid or liquid).

In case of solid targets, it is important to keep an appropriated configuration so that the diffusion and effusion processes can occur in optimized condition. Different approaches can be developed:

- Having a full cylinder block of a material. In this case, the target material must be chosen carefully as only few target materials can withstand high power deposition. Furthermore, the material should allow a good release of isotopes. Consequently, material with open porosity are preferred.
- Having small disks positioned at a certain distance one from each other. Here again, the material choice is important. However, the release is here increased by the gap positioned between the disks.

Example of solid target can be found at Triumf as shown in the Figure 1.21.

Having spaced pellets also allow a better cooling of the target.

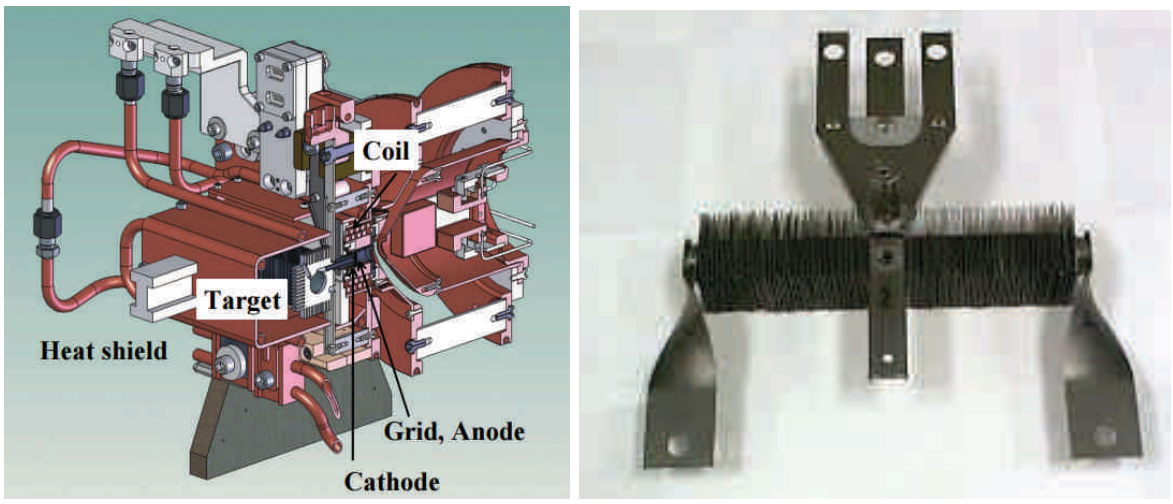

(a) ISAC target and FEBIAD ion source [46] (b) Core of the ISAC target [46]

Figure 1.21: Isac target

1.4.3.2 Static liquids targets

As seen previously (see section 1.3.4), an increase in the material density can significantly increase the yield of the secondary beam intensity. Molten metal is therefore a perfect candidate for target material as it usually has very high material density and does not require open porosity as it would be the case in solid targets. Several materials have been used for liquid targets over the past decades: Lead (Pb), Lanthanum (La) or Tin (Sn) or Sodium Fluorine (NaF). For example, a molten fluoride salt target was tested at the Isolde facility recently [47]. The geometry adopted for molten target and the particular one used for the molten fluoride salt target are presented on Figure 1.22.

Compared to a classical solid target, a chimney has been added in order to condense the possible vapor of molten fluoride salt. Furthermore, the beam window has been upgraded compared to solid target. This allows to cope with the possible shock waves due to the beam impact. These improvements were developed with a Lead target [20]. However, the molten fluoride salt presented a high corrosion and important volatility, which was never handled before.

1.4.3.3 Circulating liquid targets

Today, dynamic liquid metal targets are still sparsely used even though many designs have been proposed. Two dynamic liquid targets can be cited:

- **The LiLiT target**[22]: the Liquid-Lithium target was built and tested "offline" with a high-power electron gun at the Soreq Nuclear Research Center in Israel. It has been used with low energy proton "online" recently. The target, as presented in Figure 1.23, consists in a film of liquid lithium (at 200° C, above the lithium melting temperature of 180.5° C) forced to flow at high velocity onto a concave thin stainless-steel wall. The target is to be bombarded by a high-intensity proton beam impinging directly on the Li-vacuum interface (windowless). A rectangular-shaped nozzle just before the curved wall defines the film width and thickness (18 mm and 1.5 mm, respectively).

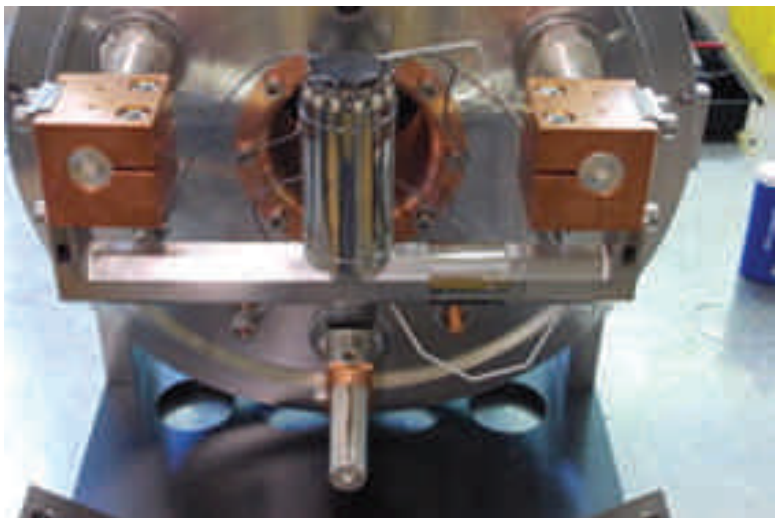

(a) Molten Fluoride Salt target [47]

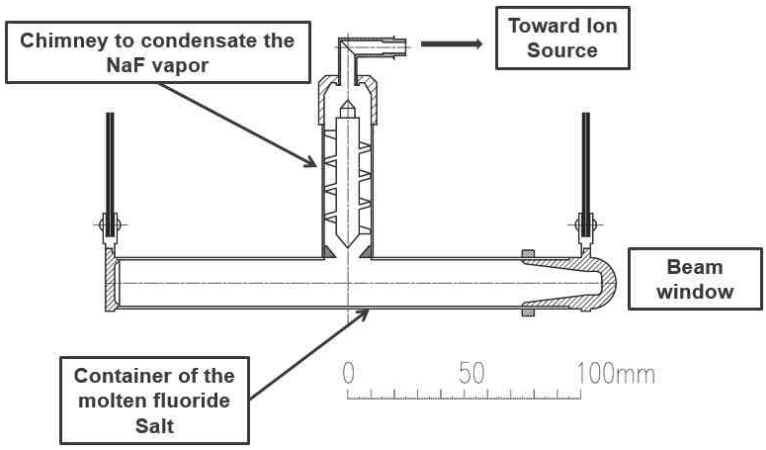

(b) Drawing of usual Isolde molten metal target [47]

Figure 1.22: Molten metal target (a) - general design at Isolde (b)

This target makes use of an heat exchanger with a secondary loop circuit of oil. Two pumps are installed in order to allow the circulation of both liquid (oil and Lithium). The pump for the circulation of Lithium is an electromagnetic one.

- **The MegaPie target** [11]: the Megawatt pilot target experiment (MEGAPIE) was the first target developed worldwide to demonstrate the feasibility of a molten metal liquid (lead bismuth eutectic LBE) target for spallation facilities and Accelerated Driven Systems (ADS) for nuclear waste transmutation at a beam power of 1 MegaWatt, within the frame of an international consortium: PSI ("Paul Scherrer Institute" in Switzerland), CEA ("Commissariat à l'énergie atomique et aux énergies alternatives" in France), KIT ("Karlsruhe Institute of Technology" in Germany), CNRS ("Centre National de la Recherche Scientifique" in France), ENEA ("Agenzia nazionale per le nuove tecnologie, l'energia e lo sviluppo economico sostenibile" in Italy), SCK-CEN ("StudieCentrum voor Kernenergie ou Centre d'étude de l'énergie nucléaire" in Belgium), DOE ("Department of Energy" in the United State), JAEA ("Japan Atomic Energy Agency" in Japan) and KAERI ("Korea Atomic Enery Research Institute" in Korea). The design of the target started in 2000, then it was built in France, Switzerland and Italy (ancillary system) and was successfully operated at SINQ in PSI for almost six months starting in August 2006.

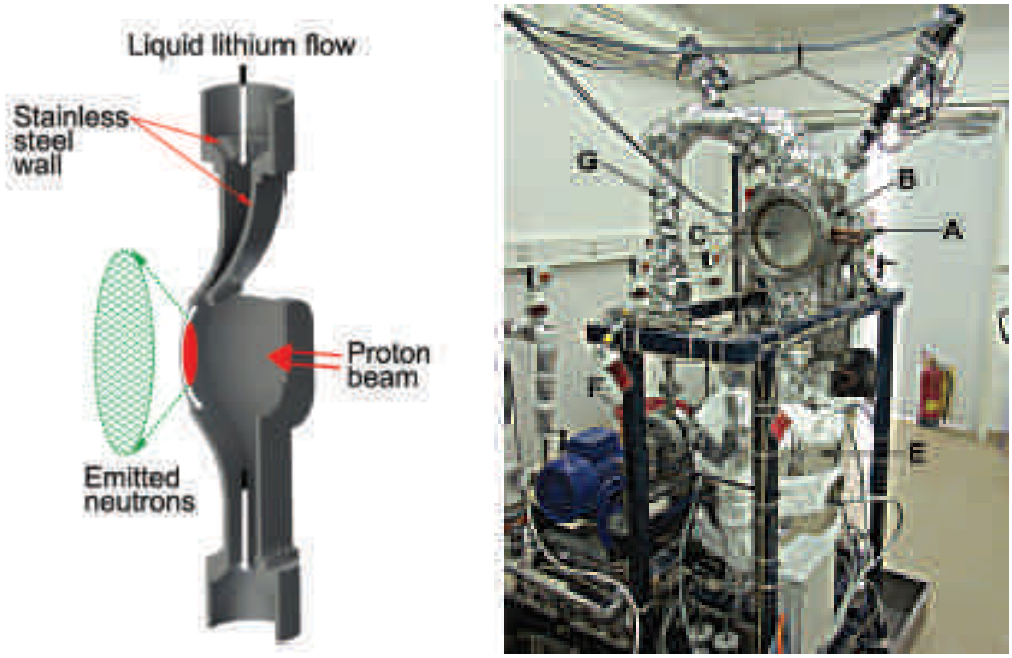

(a) LiLiT system [22] (b) LiLit target [22]

Figure 1.23: LiLit target and principle

The target was dismantled and further Post Irradiation Examination of structural material and LBE was carried out [48]. The main target components are an electromagnetic pump for the circulation of the liquid, a shielding for the radiation to be confined as much as possible and an heat exchanger to control the thermal equilibrium of the target and regulate the 1 MW of power deposited by the beam (see Figure 1.24). The total volume of LBE used for this target is 82 L. It has been operated between 230 and 380° C at a maximum flow velocity of 1.2 m/s. The total height of the target is about 5.35 meters.

After the irradiation of the Megapie target [49], several design feedback have been highlighted for this kind of target:

- The choice of the material i.e. 9Cr martensitic steel (T91) was considered as a good choice,
- The decision to avoid the implementation of oxygen control to avoid significant corrosion was validated, due to the effective operational conditions,
- The decision to perform Integral Tests, with ancillary systems, out of proton beam, is essential to provide answers to the Regulatory Authorities,
- The tightness of the Cover Gas System has been complex, to cope with the overpressure in the target, and to ensure the confinement of all radioactive gases produced by the spallation process and a regular and controlled venting,
- The redundancy of the instrumentation is absolutely necessary,
- The decommissioning phase and the waste management were underestimated with regards to the complexity and consequently duration.

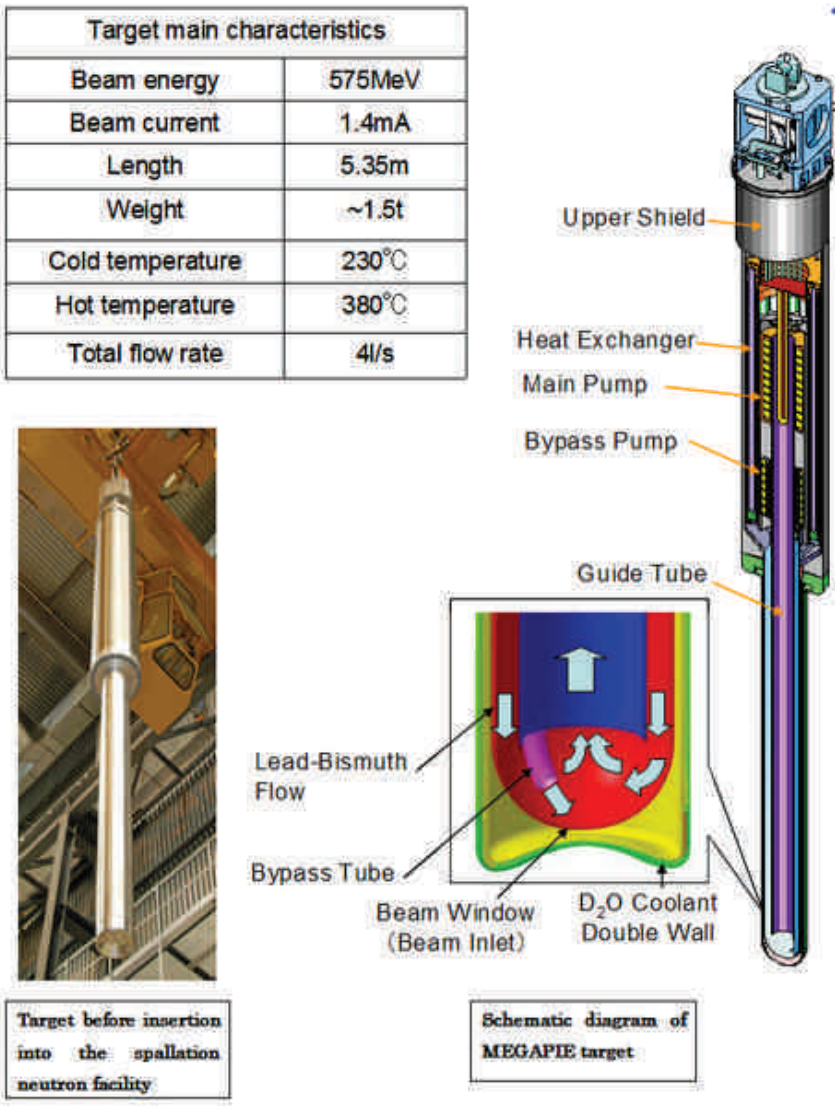

Figure 1.24: Megapie target [11]

These different points must be taken into account for any new design of a target. Megapie remains a reference in the field since it had proven to work successfully at 1 MW.

1.4.4 Summary of ISOL High Power target

The presented targets are a non exhaustive list but allow the overview of the main design proposed over the past decades. A summary is proposed in Table 1.2.

Target name	Facility	Beam characteristics	Cooling system	Isotope release	Innovation	Safety measures	Schematic
ISAC Targets [21]	Triumf	proton beam - up to 25 kW constant power - continuous beam	Radiation from fins	Separated disks Material choice	Use of fins	Double enclosure	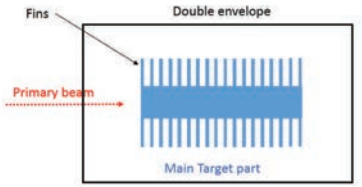
Liquid Lead/Salt Targets [20]	Isolde	Proton beam - 3 kW average power - $11.7.10^6$ kW peak power - 0.8 Hz frequency	Radiation	Material choice (liquid) Splashing from shock waves induces droplets	Beam windows developed / chimney / liquid material	Double enclosure	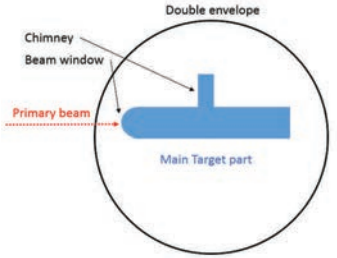
LiLit Target [22]	SARAF	proton beam - 2.3 kW average power - 20 kW peak power - 1 Hz frequency	Heat Exchanger	-	Heat Exchanger / Pump for liquid circulation / Li (metallic) window-less	Double enclosure	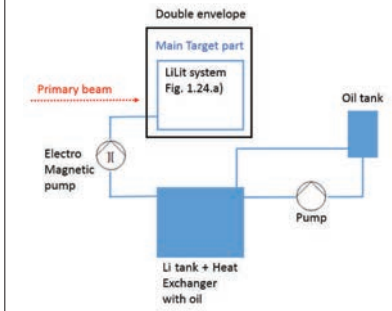
MEGAPIE Target [11]	PSI	neutron beam - up to 66.10^3 kW constant power - continuous beam	Heat Exchanger	-	Heat Exchanger / Pump for liquid circulation	Double enclosure	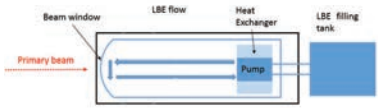

Table 1.2: Summary of High Power Target

1.5 Problematic and context of the project

1.5.1 Problematic of the thesis project

The purpose of the presented thesis is to propose a new target design able to cope with high beam power (range of 100 kW) and to validate the conceptual design proposed during the EURISOL design phase. This target should be operated and thus tested on-line (under beam) at ISOLDE.

1.5.2 Context of the thesis project

As stated previously, the next step for the RIBs production is the increase of the primary beam intensity while the design of the new targets should be carefully developed in order to optimize the isotopes yield production, in particular in the case of short life species. The design study phase of the EURISOL project proposed new conceptual design in order to cope with the different beam power of the facility [12].

1.5.2.1 EURISOL

During the EURISOL feasibility study, it has been stated that a 1 GeV (Giga electron Volt) beam would be suitable for RIB production, with a beam intensity that could reach up to 4 MW. Two different target units have been proposed: a multi-MW mercury converter-uranium target in order to produce a high range of isotopes by fission and a direct molten metal target to produce the elements not available by fission. These direct targets would be impinged by a 100 kW beam of protons [12].

The proposed layout presented in Figure 1.25 can be separated in four main parts:

- **The driver accelerator** where the primary beam is accelerated up to 1 GeV,
- **The target station** where the beam can be sent either on the multi-MW converter target or onto one of the three direct targets,
- **The separation phase** where the isotope of interest is selected,
- **The post accelerator** where the species are post accelerated.

The target facility layout is presented in Figure 1.26:

EURISOL will operate with three 100-kW direct target stations and another station with a 4-MW liquid-metal converter target surrounded by six fission targets.

The target that has been proposed to be tested at CERN-ISOLDE is a first step toward the full scale targets for EURISOL. In the same time, this target would be used for second generation ISOL facilities such as HIE-ISOLDE in order to outperform the production of exotic ions beams of interest presently delivered at CERN-ISOLDE.

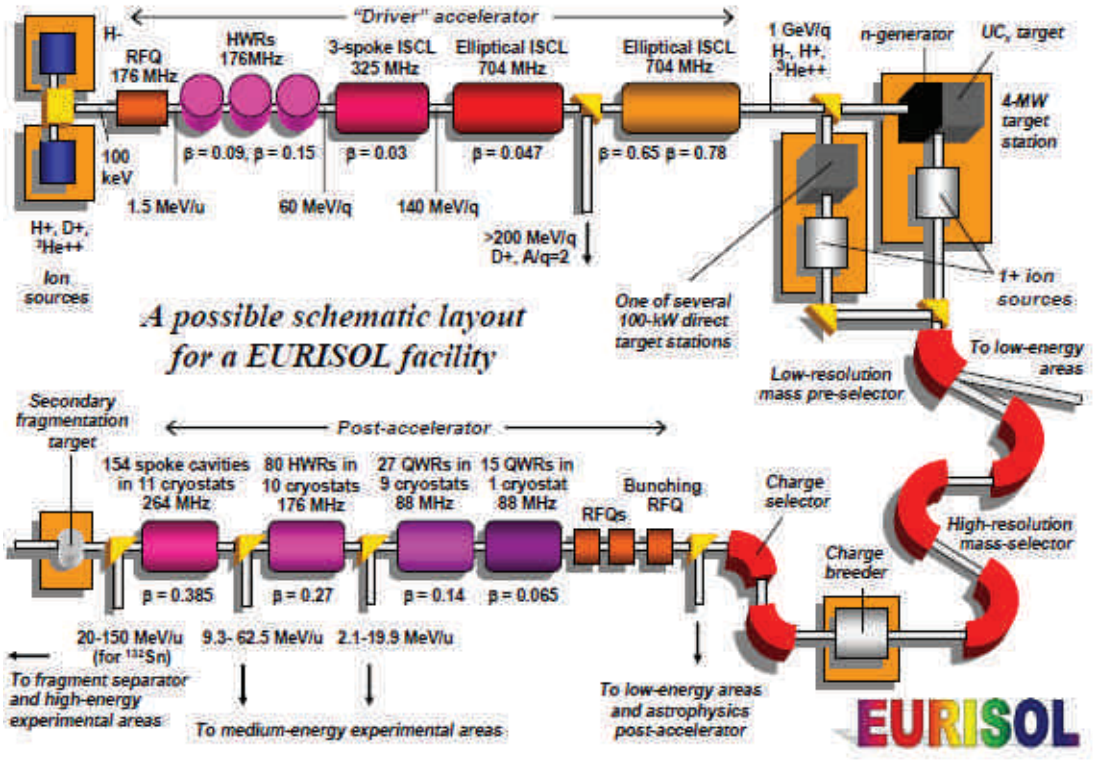

Figure 1.25: Schematic diagram of the envisaged EURISOL facility [12]

The proposed layout for the EURISOL direct target makes use of a lead bismuth eutectic (LBE) metal liquid target material, interesting for its low temperature of fusion but also because it allows the production of various nuclear species of interest such as mercury or astatine. Furthermore, a diffusion chamber is foreseen in the proposed design in order to optimize the diffusion process as seen in section 1.3.2. Indeed, droplets should be formed after the beam impact into this diffusion chamber. This should allow the extraction of short-lived species (see Figure 1.27).

1.5.2.2 The ISOLDE facility

Since the target must be tested at CERN-ISOLDE, the environment of the facility must be taken into account from the initial step of the design in order to provide a fully compatible target. The target will be coupled to the ISOLDE front end, where the secondary beam line is connected as it is presented on Figure 1.28.

1.5.2.3 The LIEBE project

In this context, CERN launched in 2012 a R&D project grouping different institutes, called LIEBE (**Li**quid **E**utectic Lead **B**ismuth Loop Target for **E**urisol) to investigate the feasibility of testing on line a LBE loop target compatible with the present installations at ISOLDE and used for HIE ISOLDE. A collaboration has been started between different institutes over the world:

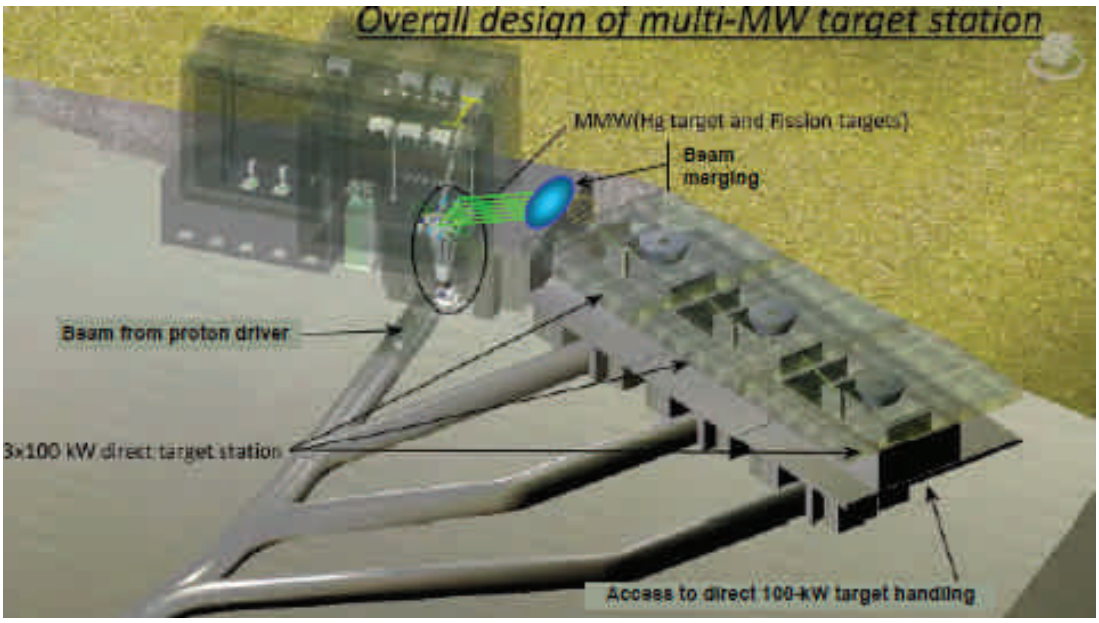

Figure 1.26: Eurisol target facility [12]

- CEA/Saclay: the "Commissariat à l'énergie atomique et aux énergies alternatives" is a french research center on the nuclear and renewable energies. CEA is active in four main areas: low-carbon energies, defense and security, information technologies and health technologies.

- CERN: the European Organization for Nuclear Research is a European research organization whose purpose is to operate the world's largest particle physics laboratory.

- IPUL: the Institute of Physics of University of Latvia is recognized as one of the oldest and largest worldwide centers in the field of fundamental and applied magnetohydrodynamics (MHD) research.

- PSI: the Paul Scherrer Institute is the largest research centre for natural and engineering sciences within Switzerland. They perform world-class research in three main subject areas: Matter and Material, Energy and the Environment, and Human Health.

- SCK-CEN: the " StudieCentrum voor Kernenergie ou Centre d'étude de l'énergie nucléaire" in Belgium is a research center dealing with peaceful applications of radioactivity. They perform forward-looking research and develop sustainable technology.

- SINP: the Saha Institute of Nuclear Physics in India is an institution of basic research and training in physical and biophysical sciences.

Different work-packages have been defined, with coordinators from the various institutes (Table 1.3).

The goal of the LIEBE project is to design, operate safely and collect information during online tests at ISOLDE of a Lead Bismuth Eutectic (LBE) loop target for direct isotope beam production. The conceptual loop design of the target was proposed by E. Noah et al. during the EURISOL Design Study phase [13].

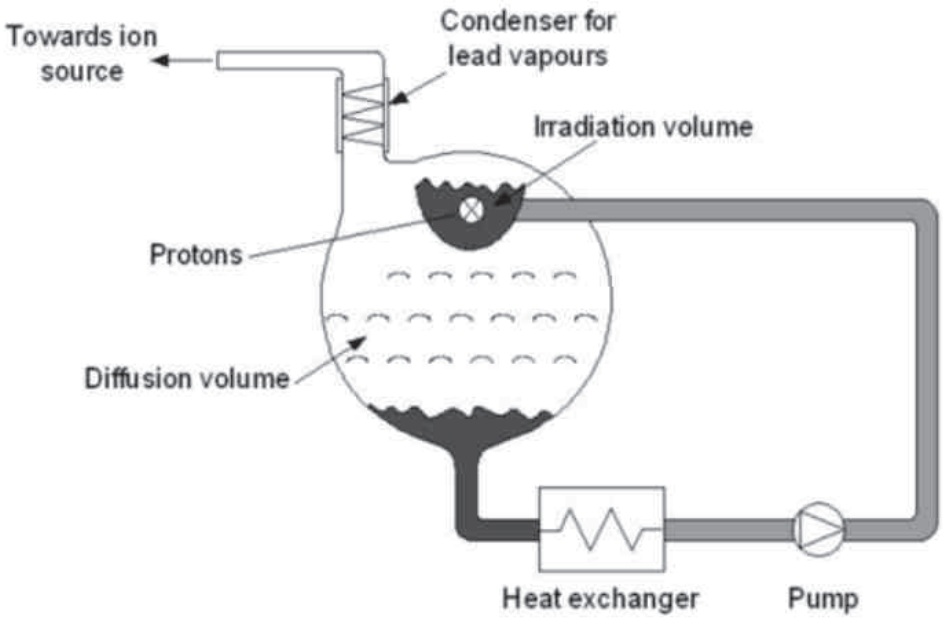

Figure 1.27: Lead Bismuth loop proposed during the Eurisol design study phase [13]

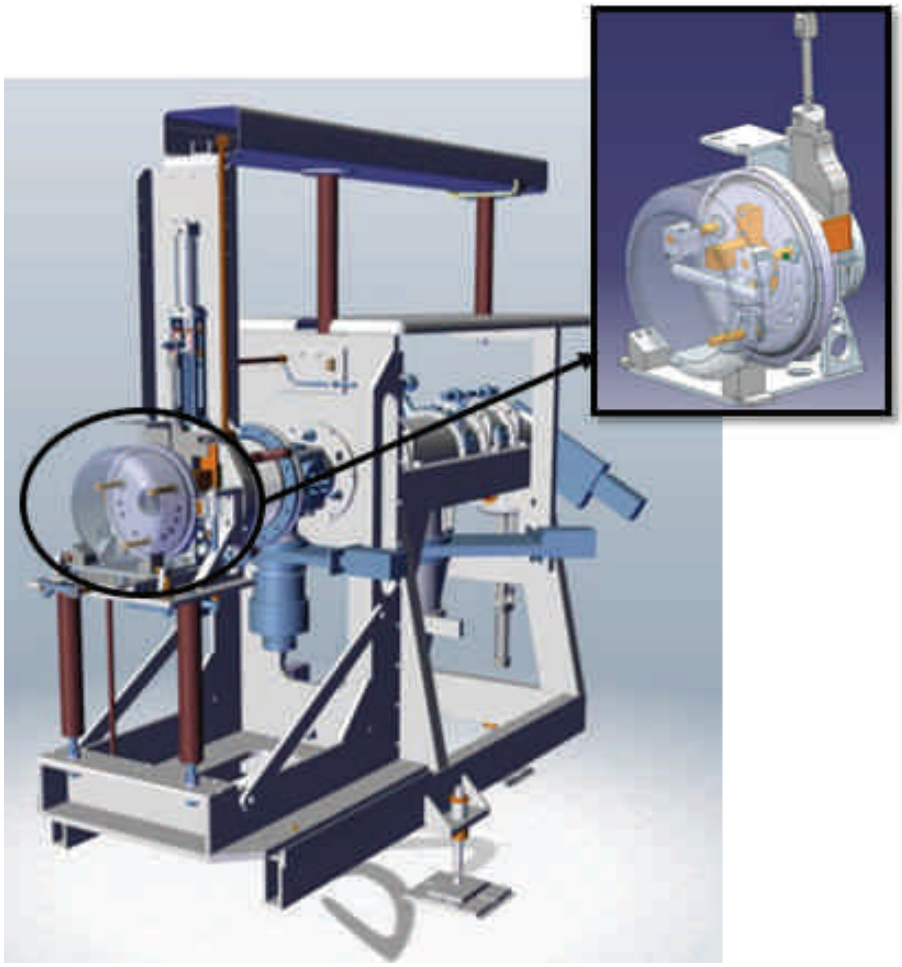

Figure 1.28: ISOLDE front end and standard target unit

WP definition	WP holder	Coordinator
WP1 : Coordination	CERN	T. Stora
WP2 : Conceptual Design and simulations	SCK-CEN	P. Schuurmans
WP3 : Construction, assembly	CERN	M. Delonca
WP4 : Instrumentation	CERN	T. Mendonca
WP5 : Safety and Licensing	CEA	A. Marchix
WP6 : Target characterization and analysis	PSI	D. Schumann
WP7 : Radiochemistry	SINP	S. Lahiri
WP8 : Offline commissioning	IPUL	K. Kravalis
WP9 : Online operation	CERN	T. Mendonca

Table 1.3: LIEBE project: work-package and work-package holders

My direct contribution to the LIEBE project has been to coordinate the work-package WP3 "construction, assembly" and to work within the work-package WP2 "conceptual design and simulation". This task implied the design of this target, including the proposal of pre-designs, the full development and integration of the chosen design and its validation through numerical tools as well as by prototype. However, all the work-package fields have been considered at the early stage of the target design. This work will be presented in this thesis.

1.5.3 Conclusion

As a conclusion to this introductory chapter, in order to cope with high beam power challenges, it is necessary to design, manufacture and test a new target according to the following requirements:

- Estimation of the different design constraints in order to produce a target validating the design proposed during the EURISOL Design Study phase (as seen in Figure 1.27) and being compatible with the Isolde environment while allowing the extraction of new species, specifically the short-lived ones as it will be seen in the Chapter 2,
- Proposal of several pre-designs that cope with these different constraints, and preliminary study in order to assess the most suitable one as it will be explained in the next Chapter 2,
- Choice of the retained design and detailed study as it will be seen in Chapter 3,
- Validation of the target design thanks to several prototyping. This part will be presented in Chapter 4,
- On-line testing of the target and validation of the physic program. Because of the delay and the availability of the accelerator loop, it is planned to proceed the testing after the PhD defense.

Chapter 2

Challenges in the conceptual design of a liquid loop target

Introduction

This chapter focuses on the specific challenges related to the development of a liquid loop target able to cope with high beam power while optimizing the yield of secondary beams of short-lived isotopes. Different pre-designs addressing the technical issues are proposed in a first step while only one of them will be selected and developed more in detail in the following chapter.

Several Figures of Merits have been defined by taking into account different aspects of the design of a high power target. These Figures of Merits lead to different parameters to be optimized in order to develop the most efficient target for short lived species.

First, we particularly address in the part 2.3.1 the pressure losses that will be induced by the circulation of the Lead Bismuth Eutectic (LBE) inside the loop. Indeed, the total pressure delivered by the pump is a fixed parameter and the total pressure losses within the target must remain lower than this design limit. The different pressure losses will depend upon the geometry of the loop (length of the pipe and all changes in geometry) and upon the velocity of the LBE. It will be shown that the general shape of the target loop is already constrained by this parameter.

Secondly, we address the thermal analysis of the pipe in which the LBE is circulating. This analysis is a key point to properly determine the heat losses induced in the loop by the active cooling coming from the convection of the LBE inside the loop, by the conduction through the wall of the pipes, by the conduction through the insulators chosen and finally by the radiative transfer towards the ambient. The determination of the total power losses inside the loop is of major importance to properly design the functional heating and cooling elements required to operate the target at different temperatures. This will directly impact on the selection of the insulating elements and on the piping diameters. This has to be put in perspective with the estimation of the pressure losses and their implications in terms of pipe diameter for example.

In a subsequent part, a full analysis is conducted to estimate the driving parameters of the release of short lived isotopes. As introduced in the first chapter, droplets are preferred to a jet or a foil geometry (cf Figure 1.16). The impact of the diameter, of the time required to fragment the liquid in droplet shape, and of the time before which these droplets collapse

returning to the circulating liquid is assessed. Through the analysis of the different phase of radioisotope release until the ionization phase which are the diffusion and the effusion release, optimized dimensions of some parts of the target have been extracted.

More specifically, an analysis is conducted to study the different regimes of droplets formation. The consequences on the induced velocity and residence time in the diffusion chamber according to the optimum design obtained in Section 2.3.2.2 will be discussed.

2.1 General considerations

This prototype loop target is developped within the LIEBE (**Li**quid **E**utectic Lead **B**ismuth Loop Target for **E**urisol) project to validate the 100 kW direct target conceptual design proposed during the EURISOL Design Study. This metal loop target will make use of LBE. Indeed, to optimize the production of the aimed neutron deficient isotopes (Hg isotopes, A = 177-185), both Lead or LBE could be used but the higher melting point of the Lead (327.5 °C over 125 °C for LBE) limits its use. It has been decided to operate the target from 200° C up to 600° C considering the material melting temperature and its high vapour pressure beyond 600° C. This brings additional constraints as the LBE properties will vary with temperature as presented in Table 2.1 (for additional information, refer to the Appendix A) [1].

	k ***(W/(m.K))***	C_p ***(J/(kg.K))***	ρ ***(kg/m^3)***	μ ***(Pa.s)***	ν ***(m^2/s)***	σ ***(N/m)***
200°**C**	10.4	147.7	10 470	$2.43.10^{-3}$	$2.37.10^{-7}$	0.40
600°**C**	15.5	140.7	9 940	$1.17.10^{-3}$	$1.18.10^{-7}$	0.38

Table 2.1: Main parameters of LBE at 200°C and at 600°C

with k the thermal conductivity, C_p the specific heat capacity at constant pressure, ρ the volumetric mass density, μ the dynamic viscosity, ν the kinematic viscosity and σ the surface tension.

Furthermore, the target will be tested at CERN-ISOLDE. Consequently, it needs to be fully compatible with the layout of the facility, and the full unit must be manipulated remotely: this is because the ISOLDE front end, where the target will be installed and operated, is located in a highly radioactive area. It has also to comply with the safety requirements of the facility, aspect that must be considered at each stage of the development.

2.1.1 Material consideration

LBE is a good candidate for its low melting temperature, its high density and its vapor pressure in temperature. However, it shows high corrosion activity for conventional structural materials. Indeed, materials exposed to liquid metals which undergo corrosion can display a degradation of their mechanical properties.

Consequently, it is important to select a material that combines good corrosion resistance and good mechanical properties. Indeed, no oxygen monitoring of the loop is foreseen. However,

the design should comply with this constraints, meaning that the exposition of LBE to oxygen should be completely impossible at all stage of the target operation.

Several studies have been conducted with different steel materials in contact with LBE [1] (refer to Appendix A for complete results). It has been particularly shown that Stainless Steel 316L (C: $< 0.03\%$, Cr: 16-18.5 %, Ni: 10-14 %, Mo: 2-3 %, Mn < 2 %, Si: $< 1\%$, P: < 0.045 %, S: < 0.03 %, Fe: balance) has good compatibility with LBE and this material has been chosen as a reference material in many laboratories making use of LBE. For these reasons, the full loop of the LIEBE target will be built with Stainless Steel 316L. The main characteristics of this material at 22°C (ambient temperature), at 200°C and at 600°C are reported in Table 2.2 [50].

	k *(W/ (m.K))*	C_p ***(J/ (kg.K))***	α (K^{-1})	ρ (kg/m^3)	**E *(GPa)***	γ	**Yield *(MPa)***	**Ulti. *(MPa)***
22°C	13.3	486	$1.71.10^{-5}$	7 960	194	0.29	302	608
200°C	15.9	554	$1.76.10^{-5}$	7 887	179	0.31	224	481
600°C	21.3	628	$1.86.10^{-5}$	7 710	145	0.35	175	413

Table 2.2: Main parameters of Stainless Steel 316L at 22°C, 200°C and at 600°C

with k the thermal conductivity, C_p the specific heat capacity at constant pressure, α the thermal expansion, ρ the mass density, E the Young Modulus, γ the Poisson ratio, *Yield* the Yield Strength and *Ultimate* the Ultimate Strength.

Knowing the material for the loop, it is already possible to define different possible pipe dimensions. Indeed, in the standard ISOLDE target, the container, where the beam is impacting, has a diameter of 20 mm. Consequently, one can consider in a first approach that the loop target will have similar dimensions and 20 mm can be fixed as maximum internal diameter in a first approach. Considering commercially available tube dimensions for Stainless Steel (SS) 316L, two options have been identified as a first possible baseline for the LIEBE target. Their characteristics are summarized in Table 2.3.

Parameters	**Units**	**Pipe 1**	**Pipe 2**
Internal diameter	*mm*	10	17
External diameter	*mm*	12	19
Wall thickness	*mm*	1	1

Table 2.3: Main characteristics of standard SS 316L pipes

2.1.2 Safety aspects

As seen in the Section 1.4.1.1 in Figure 1.17, previous targets at ISOLDE had failed and safety measure must be taken to protect the installation and the personnel: in no situation, the front end could be polluted by irradiated liquid (LBE in the case of the LIEBE target). To ensure this, it is mandatory to use a double envelop that will surround every part of the loop. This envelop would keep the liquid in case of the primary loop failure. Consequently, it must be dimensioned to handle the worst case failure scenario which means to keep its integrity in case of a full rupture of the main loop when the LBE is at 600 °C. This double enclosure brings additional constraints as the pump must be compatible with it.

2.1.3 ISOLDE Environment constraints

As the ISOLDE environment in the target area is highly radioactive, the manipulation of every target must be done remotely. This is done thanks to a robot as presented in Figure 2.1.

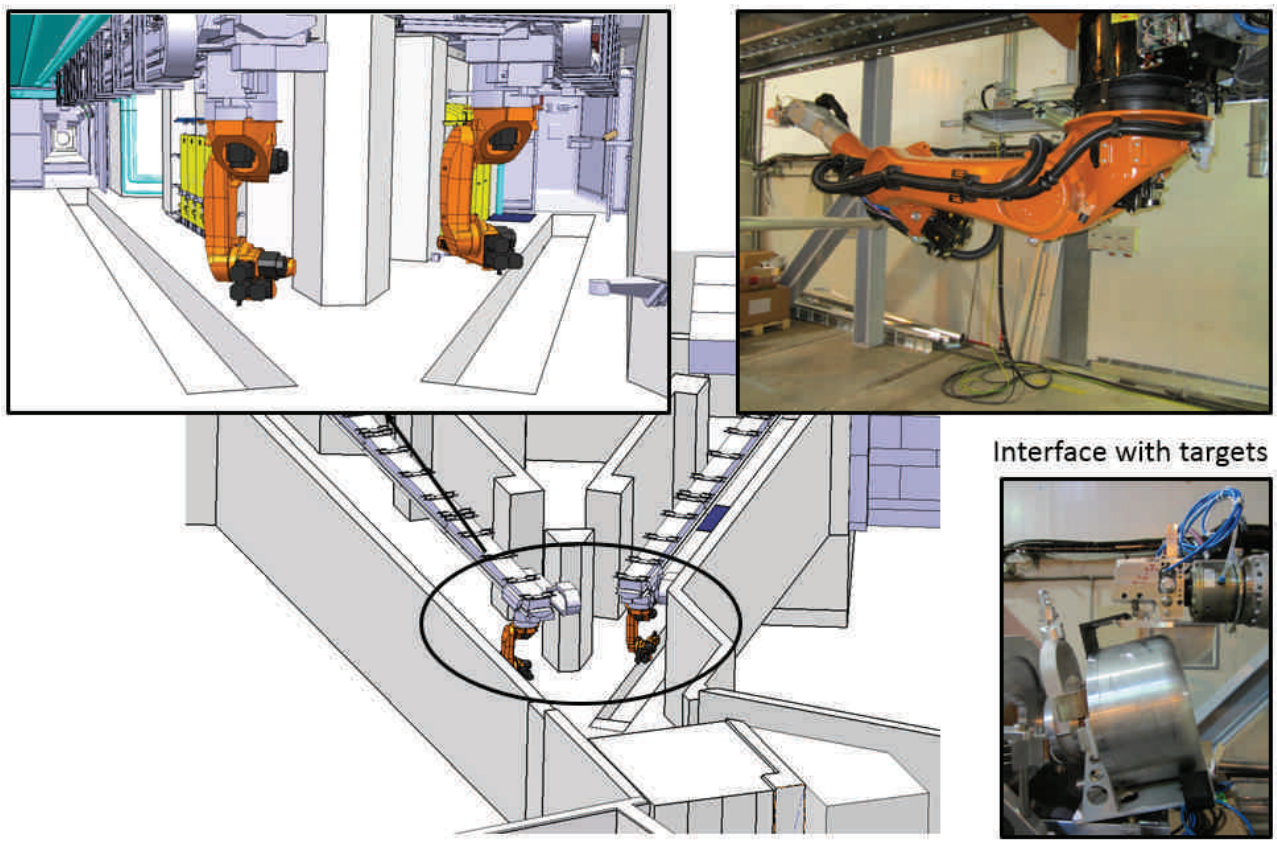

Figure 2.1: Robot handling in the ISOLDE facility and interface with the targets

This robot presents a limit of 65 kg of maximum weight it can carry on. This sets, as design parameter, 65 kg for the maximum weight of the loop.

Furthermore, part of the front end must be polarized at 30 kV to extract a beam (RIB) at 30 keV. This means that a specific care must be taken when designing the target:

- Use of insulators such as ceramics,
- Preserve a minimum distance of 200 mm between two metallic parts at different potentials.

In addition, as the position of the proton beam axis is fixed within $\pm$ 2 cm, the target container where the beam impact will occur has to be positioned within this limit. Furthermore, the prototype target must be fully compatible with the front end table or should require a minimum of changes which should remain transparent for the standards units.

Finally, an heat exchanger is foreseen. To dissipate the heat, only water or air convection is available and can be used in the ISOLDE front end area. This will once again impact drastically on the target design.

2.2 Pre-designs proposals

Some of the key components of the liquid loop must be carefully designed and chosen to cope with the various issues of a high power target design.

During the EURISOL Design Study phase, calculations were done to estimate the released fraction of Hg isotopes diffusing out of Pb (lead) droplets or jets in function of the size of the holes of the grid. It has been shown that sphere-shaped drops are preferred [12] as seen in section 1.3.4 on Figure 1.16.

Tests were carried out at the Institute of physics of the University of Latvia (IPUL) to dimension the diffusion chamber and determine suitable components of the loop [12]. The scheme of the liquid metal test loop is presented in Figure 2.2.

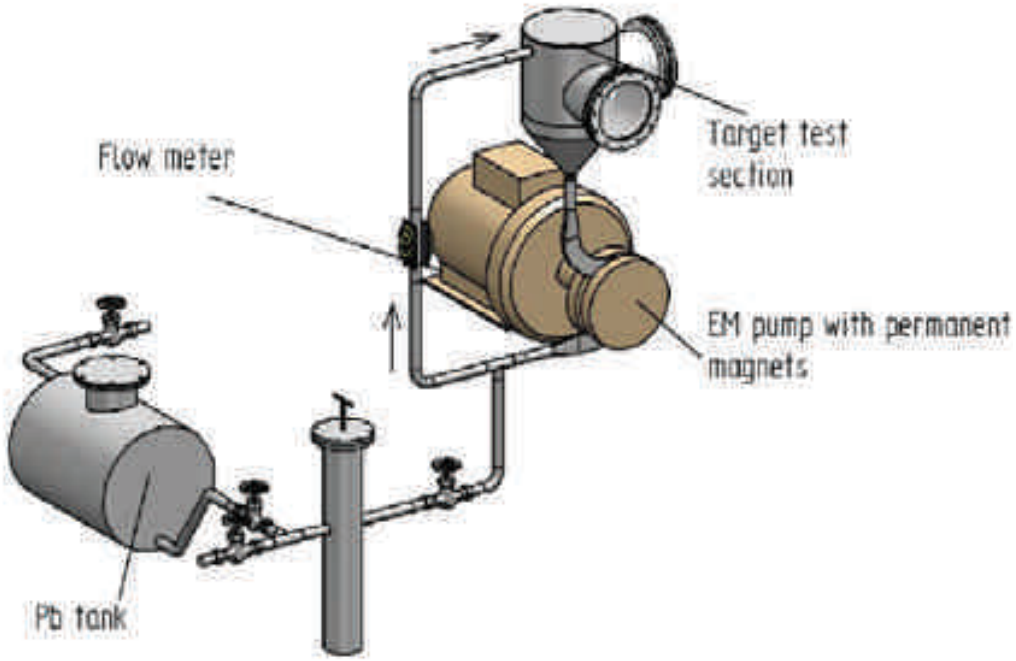

Figure 2.2: Schematic of the liquid metal loop run at IPUL during the EURISOL Design Study phase [12]

Results showed that such a loop is feasible if the flow parameters are appropriately defined and controlled: flow velocity, pump pressure, diameter of the holes of the grid and temperature of the liquid. It has been demonstrated that up to 600° C, with an electromagnetic pump and heaters all along the pipes, it is possible to manage and run a loop of molten Pb through a grid. During the tests, two different grid settings were studied: 164 holes of 500-μm diameter and 1017 holes of 230-μm diameter. This latter option is rather preferred since it is expected to reduce the droplet size and the extraction time of the isotopes [12]. The main loop parameters for the tests done at IPUL are summarized below (Table 2.4):

Parameters	Units	Values
Flow rate	$cm^3.s^{-1}$	60 - 200
Pump pressure	bar	0.1 - 2
Diameter of droplets (jets) obtained	mm	0.5 - 1
Hole diameter	μm	< 500

Table 2.4: Main loop parameters as tested at IPUL during EURISOL-DS for molten lead

2.2.1 Geometrical restrictions from the ISOLDE environment

The proposed LIEBE loop target prototype for its conceptual implementation at ISOLDE is shown on Figure 2.3:

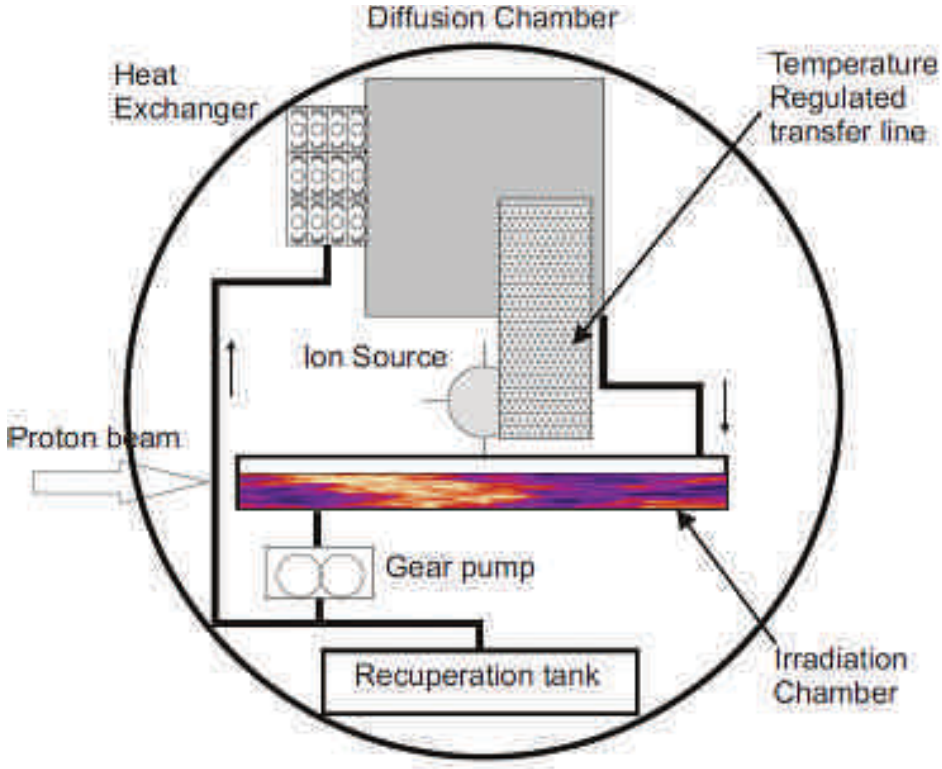

Figure 2.3: Proposed layout for the prototype of a LBE loop target at CERN-ISOLDE [14]

Each of the target constitutive elements must be carefully designed and studied to address the different constraints of a high power target. Furthermore, compatibility with the ISOLDE environment induces additional constraints. That target must:

- Be compatible with the ISOLDE front end for a proper coupling,
- Be installed in the Faraday cage, be polarized at 30kV for beam extraction and respect certain dimensions (a minimum of 200 mm distance should be maintained between two polarized parts) to avoid any electrical arc,
- Be contained in a double confinement to avoid any risk of contamination in case of rupture of the loop,

- Be compatible with the robot handling that should bring and remove the target.

These points have been considered from the very first steps of the design.

2.2.2 Proposed pre-designs

Different pre-designs have been developed combining the parts already introduced in different configurations.

The final design will have to accommodate the full beam impact that creates shock waves within the target container. It should also ensure a constant flow and efficient evacuation of part of the deposited heat. Finally the production and extraction of isotopes have to be facilitated by following the previous recommendation about size and shape of the droplets within the diffusion chamber. Three pre-designs are detailed hereunder, with their main advantages and drawbacks.

2.2.2.1 First concept

In the first concept, the diffusion chamber is together with the target container. In this proposal, the time between the creation of the isotopes in the container and their extraction in the diffusion chamber is reduced to the minimum. The pump and heat exchanger are located after the diffusion chamber (see Figure 2.4).

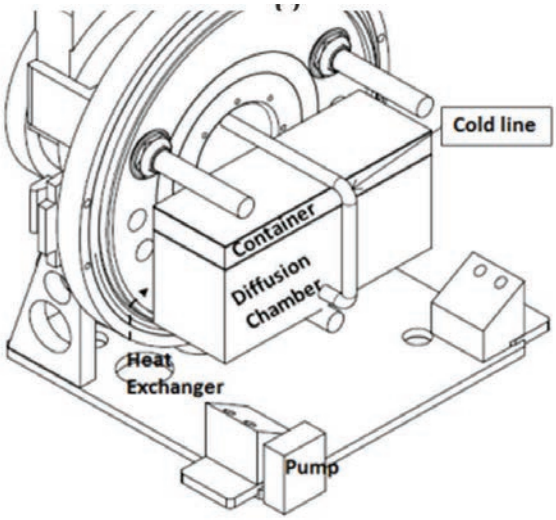

Figure 2.4: Concept 1, container and diffusion chamber together, connection between the different elements of the loop are not shown

2.2.2.2 Second concept

Also with the idea of minimizing the time between the creation and extraction of isotopes, this concept proposes a diffusion chamber separated and directly linked downstream to the

container. In this case, a valve could be positioned in between to control the flow arriving into the diffusion chamber (see Figure 2.5). The beam impact and resulting shock waves are decoupled from the shower. Again, the pump and heat exchanger would be positioned after the diffusion chamber.

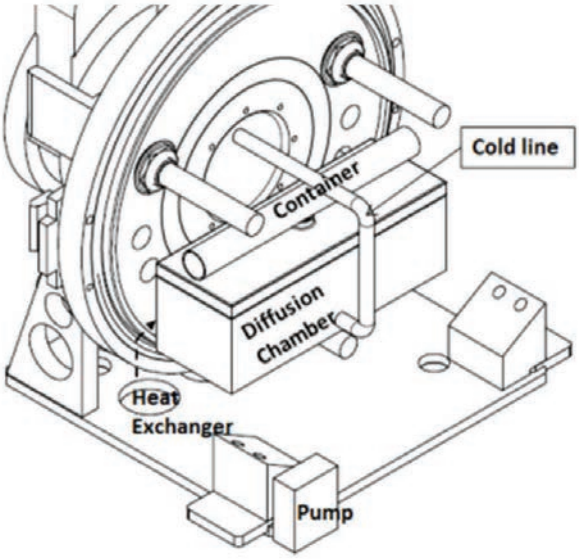

Figure 2.5: Concept 2, container and diffusion chamber linked with a valve or pipe, connection between the different elements of the loop are not shown

2.2.2.3 Third concept

The pump and the heat exchanger are positioned in between the container and the diffusion chamber as seen in the proposed layout (Figure 2.3), the main advantage being the control of the over-pressure created at the entrance of the grid into the diffusion chamber. The geometry of the different elements would be be identical to those of the concept 2, with no direct connection in between the container and the diffusion chamber.

2.2.2.4 Advantages/Drawbacks

The main advantages and drawbacks for each concept are summarized in Table 2.5.

2.3 A high power target for extraction of short-lived species: design considerations

In the development proposed within LIEBE, two new aspects are particularly addressed.

First, the necessity to deal with beam interaction will induce, as seen in part 1.4.1, various issues such as dealing with the power deposited by the beam and the subsequent thermal stresses that can create shock waves, radiation damage or the performances of the cooling scheme.

	Advantages	**Drawbacks**
Concept 1	• Shortest delay between creation and extraction of isotopes • Compact design • Simpler design	• Shock waves from beam impact may disrupt the shower • Difficult control of the loop • Risk that the container becomes empty
Concept 2	• Separation of beam impact from the shower • Flow control facilitated • Delay remain short between creation and extraction of isotopes	• Additional space required • More complex design
Concept 3	• Separation of beam impact from the shower • Part where the shower is created can be in over pressure	• Longer path inducing losses of short-lived isotopes • Transfer of isotopes in the pump and heat exchanger

Table 2.5: Advantages and drawbacks of concepts introduced

Secondly, the goal of extracting short-lived species requires a specific development with respect to the current target design as seen in the part 1.3.4.

These two mains aspects will be fully covered in the upcoming sections.

2.3.1 High-power target: design constraints related to the pressure loss

2.3.1.1 Pump compatibility with LBE

2.3.1.1.1 Design requirements One of the main differences between the three concepts is the path between the container where the isotopes are created and the diffusion chamber where the shower is created. The necessity of using a pump will impact on that path length and thus, possibly drive the final design choice toward one of the proposed concepts.

Indeed, one of the main requirements of the pump operation is to have a minimum height of liquid at the inlet in order to avoid cavitation. This value is called the Net Positive Suction Head (NPSH) [51]. This drastically impacts the design because, with our constraints, the pump needs to be positioned at the lowest point of the loop. In this configuration, the concept 3 is no longer a valid option as it would set a too long path and consequently time between the isotope formation in the container and their release in the diffusion chamber.

This pump is designed by IPUL (WP8:Offline commissioning) which has the relevant expertise. An electromagnetic induction permanent magnets pump allows an operation of the loop without direct contact with the LBE since LBE circulates inside pipes. This means that the double envelope can be confined to the pipes of the pump, and exclude the full pump. For other types of pumps, it is challenging to have reliable seals at high operating temperature with liquid aggressive metal. The main disadvantage of this pump is its low efficiency.

IPUL defined some parameters of the pump based on past developments and of the experience gained from the offline test conducted with Lead during the EURISOL Design Study (Section 2.2). This allowed the definition the parameters of the pump of the LIEBE target. Theses parameters are presented in Table 2.6.

Parameters	Units	Values
Max. Operating Temperature	$°C$	600
Max. Flow rate	l/s	0.5
Max. Pressure	bar	2
Min. Height for NPSH	cm	70

Table 2.6: Main parameters of the proposed electromagnetic pump

These parameters have a direct impact on the design of the loop.

2.3.1.1.2 Hydraulics parameters of the LIEBE loop The maximum flow rate and pressure of 2 bars fixed by the selection of the pump implies that the maximum pressure losses in the loop, dependent of the LBE velocity and thus related to its flow rate, remains under this

limit. While the pump manufactured by IPUL might provide a pressure higher than 2 bars, this figure was selected as a design parameter for the loop. A minimum NSPH of 70 mm has been experimentally defined by IPUL to ensure that no cavitation will occur. To estimate the total pressure losses in the loop, a possible piping of this loop.

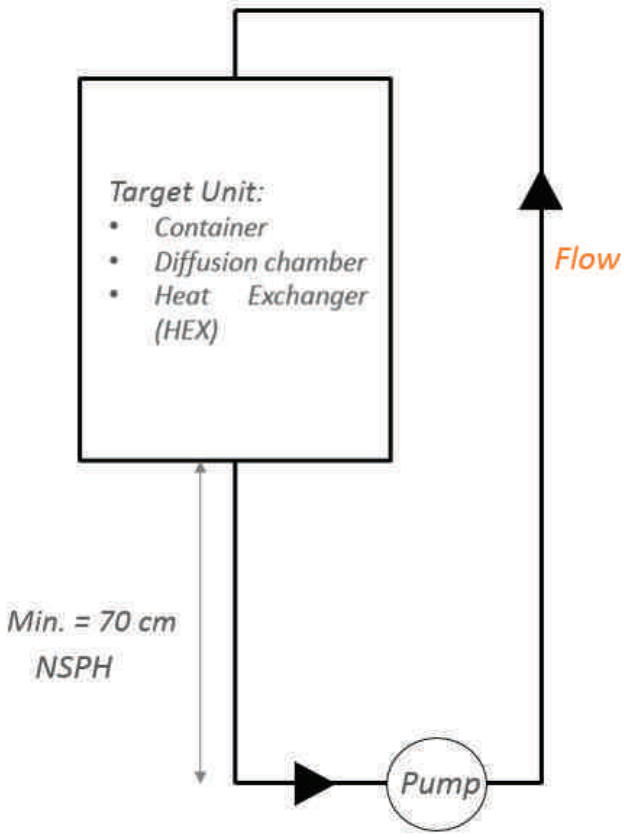

Figure 2.6: Schematic layout of the loop

The "target unit" bloc also includes the container, the diffusion chamber and the heat exchanger (Figure 2.6). It means that it includes the grid used for the droplets formation as well as any possible valves positioned in between the container and diffusion chamber (as proposed in pre-concept 2). There are two sorts of pressure losses: the distributed losses in the pipe and the localized losses at every change of cross-section geometry.

Localized pressure losses

For each change in the geometry, a loss factor ξ is defined [15]. The localized pressure losses can be defined as follow [15]:

$$\Delta P = \Delta h.\rho.g \quad \text{with} \quad \Delta h = \xi.\frac{v^2}{2.g} \tag{2.1}$$

with ρ the density of the fluid in kg/m^3, g the standard gravity of 9.81 m/s^2 and v the velocity of the fluid.

The velocity v can be simply estimated from [26]:

$$Q = v.S \tag{2.2}$$

with Q the flow rate of the flow in m^3/s and S the cross sectional surface in m^2.

Knowing the maximum flow rate of 0.5 l/s provided by the pump and having fixed two possible pipe diameters, one can estimate the maximum velocity in the two defined cases that will directly impact upon the pressure losses in the loop as summarized in Table 2.7.

Flow rate (l/s)	**Internal pipe Diameter (mm)**	**Max. Velocity (m/s)**
0.5	10	6.4
0.5	17	2.2

Table 2.7: Hydraulics parameters in the LIEBE target loop

As a matter of fact, the higher the velocity, the higher the pressure losses will be as presented in Equation 2.1.

- *Pressure losses due to the grid:*

  When flowing through the grid for the droplets formation, the liquid will loose in pressure. The pressure drop at the grid can be expressed as follows [15]:

  $$\Delta P_{grid} = \xi.\rho.\frac{v^2}{2} \quad \text{with} \quad \xi = (1 + \frac{l}{d}.\lambda + 0.5) \tag{2.3}$$

  with d is the hole diameter, l the plate thickness, $\lambda \approx 0.02$ and v the velocity at the grid exit.

  The velocity considered here is the velocity at the grid exit since it takes into account the total number of holes and thus, the total surface area (or cross section) represented by the holes.

  Two holes diameters have been considered, 0.1 mm which is the targeted diameter and 0.23 mm which is the diameter achieved in the tests conducted at IPUL during the EURISOL Design Study (Section 2.2), the pressure losses at the grid have been estimated thanks to Equation 2.3 for a thickness of 0.5 mm and of 1 mm.

  The obtained results will be dependent upon the temperature as the LBE properties, and more particularly the mass density ρ in that case, vary between the two temperature limits of 200 °C and 600 °C (Table 2.1). The results are presented in Figure 2.7. It is obvious that the maximum pressure provided by the pump implies a limit on the maximum velocity of the LBE in the loop.

- *Localized pressure losses in the loop*

  Other localized pressure losses must be added to the pressure losses at the grid. This will happen every time that the geometry is changing compared to a straight circular pipe. At this early stage of the design of the geometry, it is difficult to assess with precision the different geometry changes that will occur in the final loop. However, the most probable geometry change that could occur can be estimated as indicated in Table 2.8 and referenced in [15] and pressure losses for each of them can be calculated. These geometry

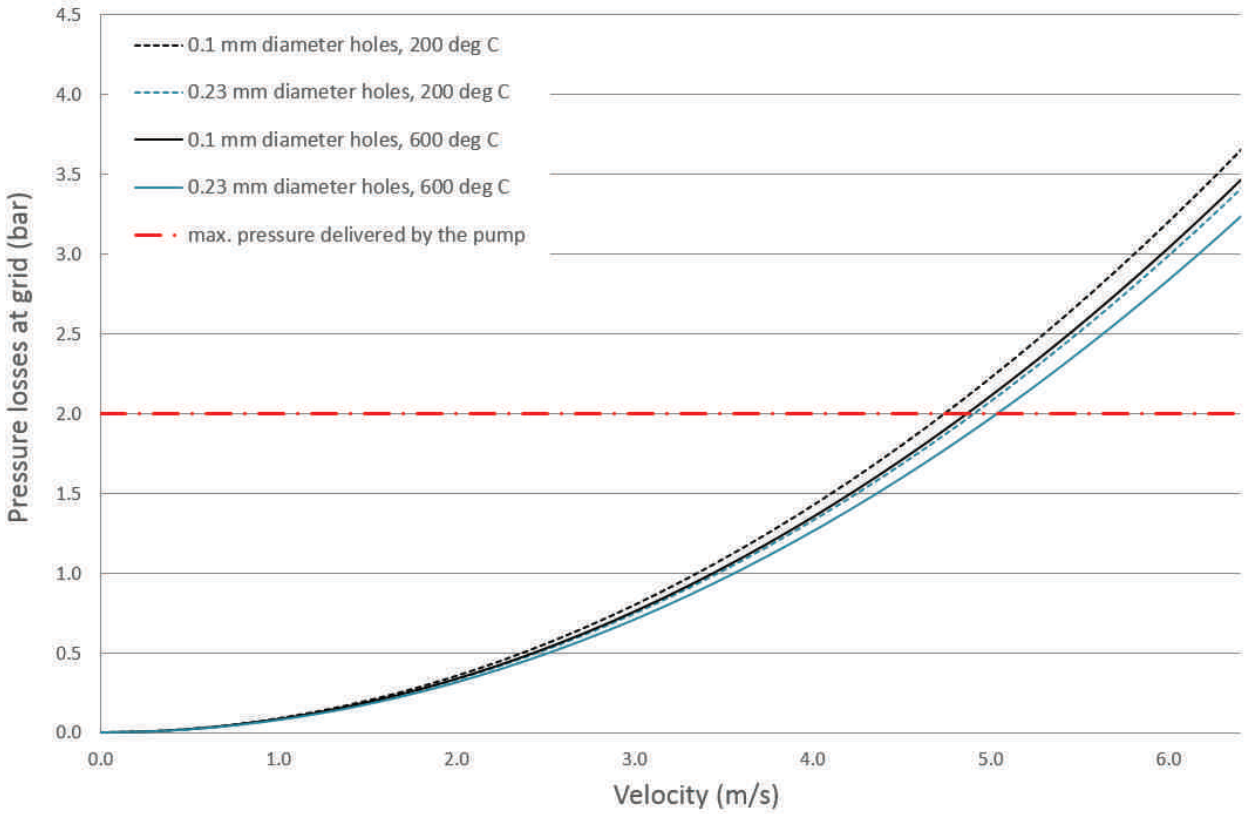

Figure 2.7: Pressure losses due to the grid in function of velocity in the channels for different holes diameters and at 200° C and 600°C.

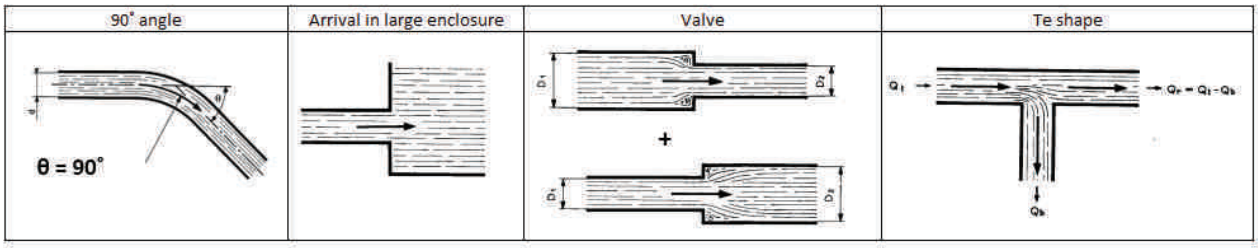

Figure 2.8: Geometry changes representation [15].

changes are shown in Figure 2.8.

The localized pressure losses can be classified in two categories:

- **The pressure losses of constant values** i.e they are not dependent upon the piping diameter such as changes in section (arrival and exit of enclosures),
- **The pressure losses varying with the piping diameter** from which the pressure losses are mainly due to the friction and turbulence created as for example in an angle or a valve.

For the different defined changes of geometry, and considering the two predefined possible pipe diameters, the geometry factors have been defined as follows:

– 90° **angle pipe bent:** in case of a 90° angle pipe bent, the geometry factor can be defined as follows [15]:

$$\xi = x.4.ft \tag{2.4}$$

with x a fixed factor equal to 30 and ft a coefficient depending upon the pipe diameter. In case of a 10 mm diameter pipe, ft is equal to 0.014 and in case of a 17 mm diameter, it is equal to 0.0125.

– **Valve:** for a valve, a reduction followed by an increase of internal pipe diameter of a factor 0.5 (equivalent to an open valve in a conservative diameter situation) has been assumed. The coefficient factor ξ is then defined as follows [15]:

$$\xi = 0.5.(1 - (\frac{D_2}{D_1})^2) \tag{2.5}$$

with D_1 and D_2 the diameter of the pipe before and after the reduction or increase.

– **Te shape in a pipe:** for the Te shape, the most conservative case would be the one where the full flow will turn (in case of further blocking on the straight direction pipe). In that case, the chart would give a coefficient factor ξ of 1.28 [15]. This differs from the 90° angle pipe bent as the angle of bending is here sharp while it is not the case for a bended pipe that has a minimum curvature radius.

Geometry change	**ξ for a 10 mm diameter pipe**	**ξ for a 17 mm diameter pipe**
90° angle pipe bent	0.42	0.38
Arrival in larger enclosure	1	1
Valve	1	1
Te shape in a pipe	1.28	1.28

Table 2.8: Geometry factors for different geometry changes for localized pressure losses calculation

For each of these geometry changes, it is possible to calculate the pressure losses using Equation 2.1 in function of the velocity at the two extreme working temperatures as seen in Figure 2.9. Since the only geometry change on which the diameter has an impact is the 90° angle pipe bent, it is the only one defined in function of the pipe diameter as well. Furthermore, as the geometry factor is the same for the arrival in a larger enclosure and for the valve, the legend in the plot will only indicate the case of the pressure losses for an arrival in the same enclosure.

The possible pressure losses due to other geometry changes such as the presence of the pump and the heat exchanger would be assessed later once the geometry of the target will be better defined.

Here again, the velocity should not be too high in order not to overcome the maximum pressure delivered by the pump, i.e. a pressure of 2 bars represented by an horizontal straight line on Figure 2.9 and 2.10.

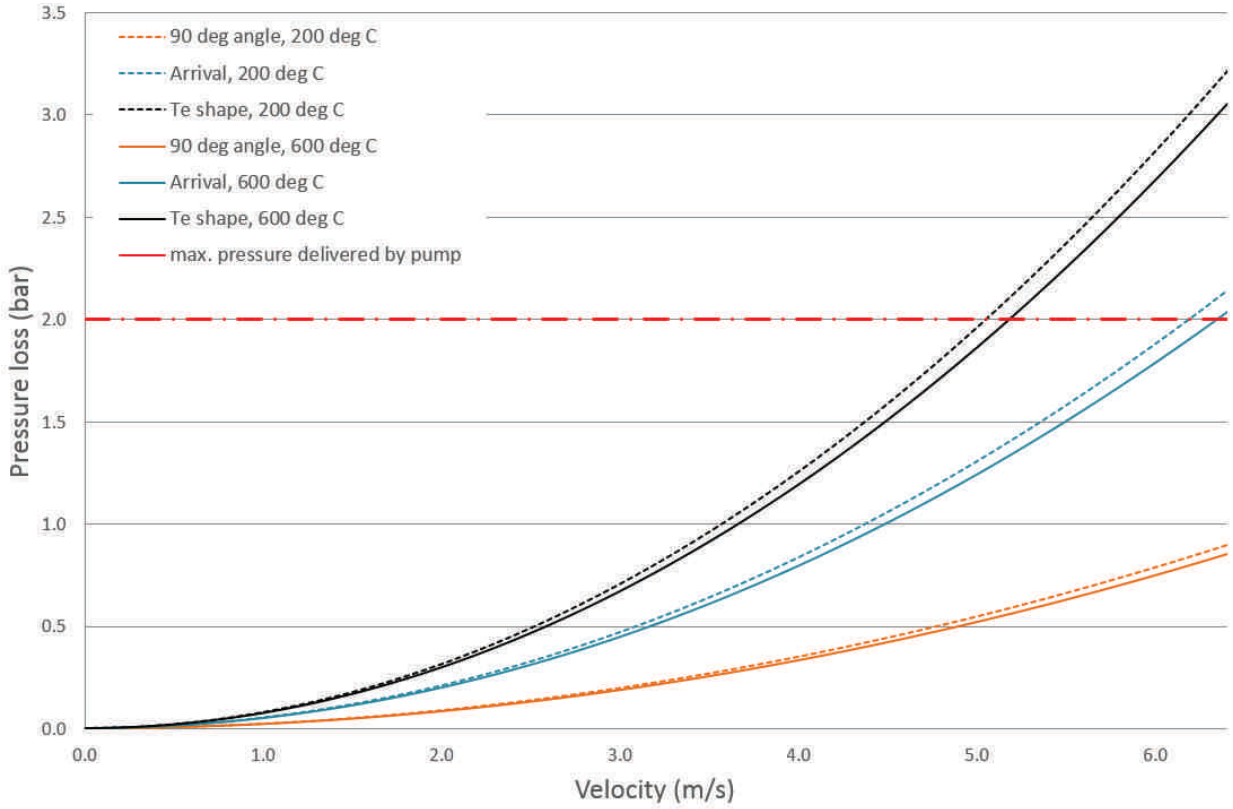

Figure 2.9: Localized pressure losses for different geometry change in function of velocity at 200° C and 600°C for a 10 mm inside diameter pipe.

Distributed pressure losses

The distributed pressure losses are the losses due to the roughness within the pipe and to its length. They are expressed as follows [15]:

$$\Delta P_{distributed} = \Delta h.\rho.g \quad \text{with} \quad \Delta h = f.\frac{L}{D}.\frac{v^2}{2g} \tag{2.6}$$

where L is the total length of the pipe in m and D its diameter in m.

Furthermore, Percorninc and Haaland specified that the expression of the loss coefficient f adopts the following form [52]:

$$f = \frac{0.25}{log(\frac{15}{Re} + \frac{\varepsilon}{3.715.D})^2} \tag{2.7}$$

for $Re = Reynolds\ number = 1.10^3\ to\ 1.10^8$ and $\frac{\varepsilon}{D} = relative\ roughness = 0.01\ to\ 5.10^{-6}$.

It has been shown in [52] that the maximum error on the evaluation of f in these conditions is 6 %.

Considering a roughness of 0.09 mm, which corresponds to an average value for a Stainless Steel pipe, and a total length of 1 m for possible scaling, the distributed pressure losses have

been estimated from Equation 2.6 and 2.7 for the two diameters of pipe considered and at the two extreme working temperature limits (Figure 2.10).

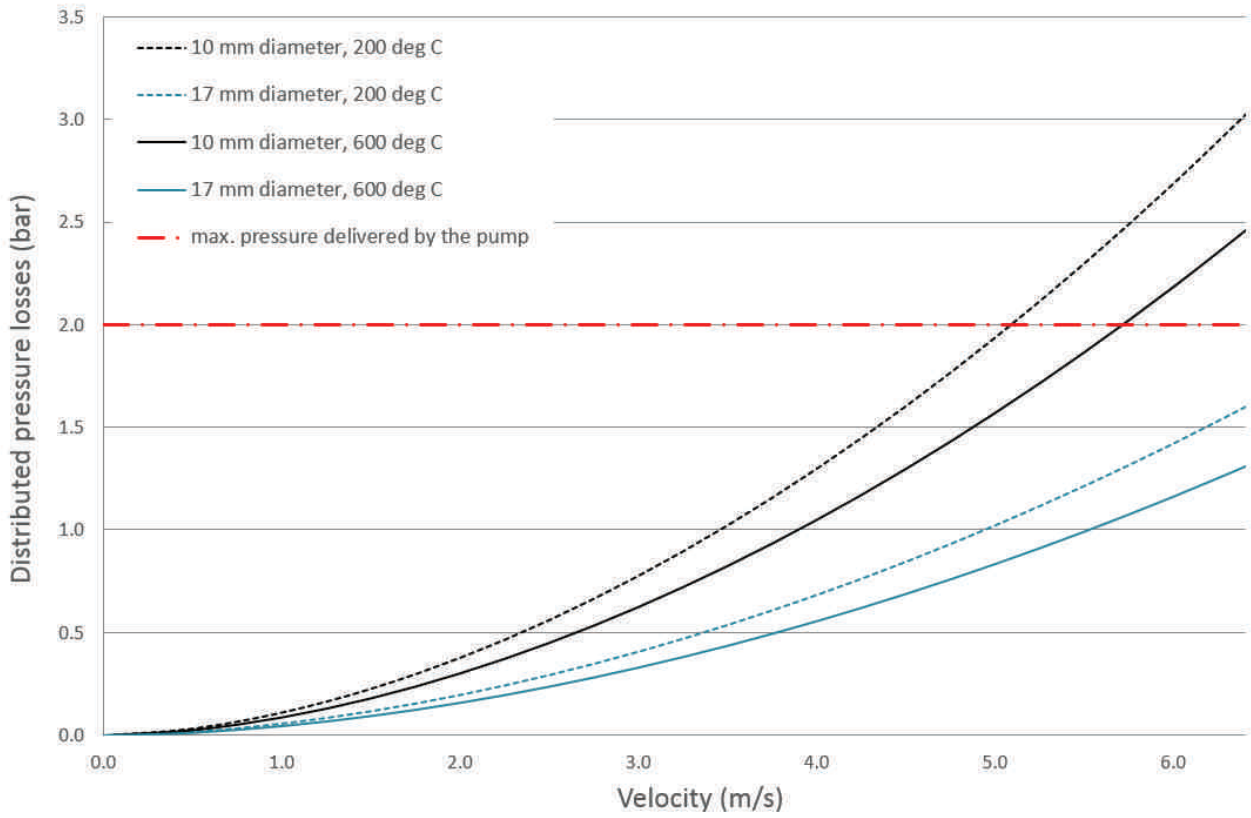

Figure 2.10: Distributed pressure losses in function of velocity for 10 mm and 17 mm diameter pipes and at 200° C and 600°C.

Here again, it is shown that the velocity and consequently flow rate and pipe diameter must be carefully chosen in order to keep the total pressure losses under the maximum pressure delivered by the pump of 2 bar. It is observed on Figure 2.10 that an increase of the temperature is favorable to reduce the pressure loss as it is directly dependent upon the LBE properties. Indeed, the loss coefficient f depends upon the Reynolds number Re, which is about two times higher at 600°C compared to its figure at 200°C. This implies that the loss factor f will be lower at 600°C. Furthermore, even though the density of the LBE will also vary with the temperature, this variation is not high enough to compensate the impact of the Reynolds number.

It is also noticed that the larger the diameter is, the lower the pressure loss is.

Pressure losses: impact on the target geometry

The pressure losses must remain under the value of 2 bars set as limit, with a minimum safety factor of 1.2 in order to have some margin in the pump operation.

In order to reduce the pressure losses, it is preferable to have a bigger pipe diameter as illustrated on Figure 2.10. Furthermore, the analysis must be done for the two temperature limits of 200 °C and 600 °C as differences are expected considering the differences of properties of LBE at those two temperatures.

The Figures of merits that can be defined are the following:

- Maximum pressure losses in the entire loop of 2 bars,
- Diameter of the pipe to be defined consequently (pressure losses generally lower for higher diameter).

2.3.1.2 Thermal equilibrium

The developed LIEBE target will be tested at CERN-ISOLDE, thus, it must be compatible with the beam parameters of the facility as presented on Table 2.9:

Parameters	**Units**	**Proton values**
Energy	GeV	1.4
Average Power deposited	kW	0.99 - 1.22
Peak Power deposited	GW	≈ 1
Total number of particles per pulse	p^+	2.4 e^{13} - 3.2 e^{13}
Max. Pulse Frequency	Hz	0.8
Pulse duration	μs	2.4 - 40
1 σ of the Gaussian beam	mm	2 - 3.5

Table 2.9: General Isolde beam parameters

Assuming a Gaussian proton beam shape, its size is defined in mm. One σ represents 68.2 % while the 99.99 % of the beam are represented by 4 σ. More detail will be presented in the Section 3.2.1.2.

To deal with the additional power deposited by the beam, an heat exchanger is foreseen and must be carefully designed and dimensioned. Its dimensioning should allow a proper thermal equilibrium and thus, an accurate control of the target temperature. Furthermore, the pump must be compatible with the high temperature of use of 600° C. Its possible heat contribution must be considered in the thermal equilibrium of the target.

The heat sinks and heat sources will impact on the thermal equilibrium of this target. They are listed in the following table:

Heat sources	**Heat sinks**
Beam	-
-	radiation
Pump	Pump
-	Heat Exchanger

Table 2.10: Heat contribution in the LIEBE target

The power contribution of the pump has been expressed as both heat source and sink since, depending on the design, it can contribute to both of them. This will be developed later on, when the design will be chosen and further elaborated (see Section 3.3.1.2).

2.3.1.2.1 Proton beam contribution The impact of the proton beam in the target will induce a heat deposition due to the energy lost by the particles. This power directly depends upon the beam parameters.

For this study, two beam modes have been considered: the staggered mode and the normal mode. The beam parameters for the two modes are summarized in Table 2.11.

Parameters	**Units**	**Proton values Staggered mode**	**Proton values Normal mode**
Energy	GeV	1.4	
Frequency	Hz	0.8	
Number of bunch	-	3	4
Bunch spacing	μs	16	
Bunch width	ns	200	
Total number of particles	p^+	2.4 e^{13}	3.2 e^{13}
Average deposited power	W	990	1 220

Table 2.11: Isolde beam parameters

The estimation of the deposited power onto the target has been done using the Monte Carlo code Fluka [53]. From these beam parameters, it is obvious that the staggered mode will deposit less power on the target than the normal one used with the maximum beam intensity. In order to be conservative, the dimensioning of the target will be done considering the higher power deposition, thus, 1 220 W.

2.3.1.2.2 Losses due to thermal radiation The developed target is planned to be operated between 200° C and 600° C thus power losses will happen by radiation toward the ambient environment. In this part, the power losses due to the radiation of the hot target toward the ambient are estimated. This part only considers the radiation of a pipe towards its environment since an inter radiative estimation would required unknown information such as the view factors.

In a steady state operation, the power brought to the system is equal to the power leaving it. This means that the total losses should be compensated by the heating system of the loop. Consequently, it is advised to have a proper insulation to minimize the losses and thus minimize the required heating oven. This insulation is planned to be made with insulation elements such as glass fiber.

For any one-dimensional steady state conduction, an equivalent thermal circuit may be employed to model heat flow in a same way as electrical circuits are used for current flow. The geometry considered in this analysis is presented in Figure 2.11a. The equivalent thermal circuit is presented in Figure 2.11b. The total power P_{losses} lost is then calculated from:

$$P_{losses} = \frac{T_1 - T_{amb}}{R_{tot}} \quad \text{and} \quad R_{tot} = R_{12} + R_{23} + R_{34} + R_{45} \tag{2.8}$$

All the quantities introduced in Figure 3.44b and in Equation 2.8 are now discussed. In the proposed equivalent model, four different phenomena are considered:

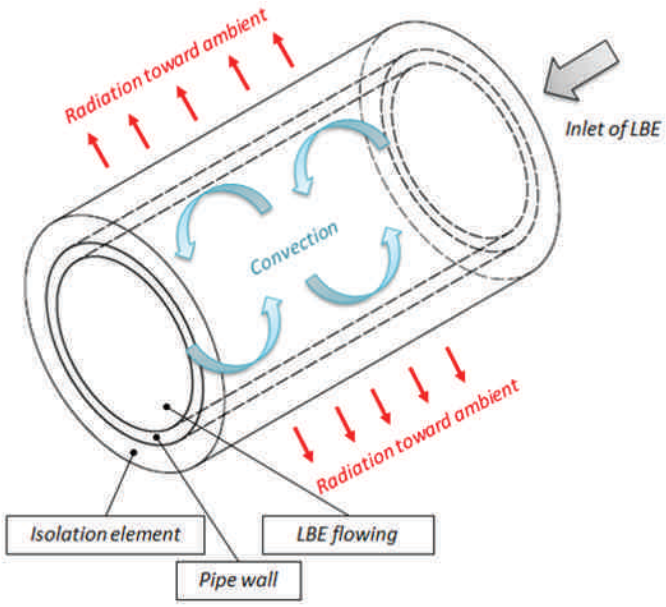

(a) Geometry considered for the power losses

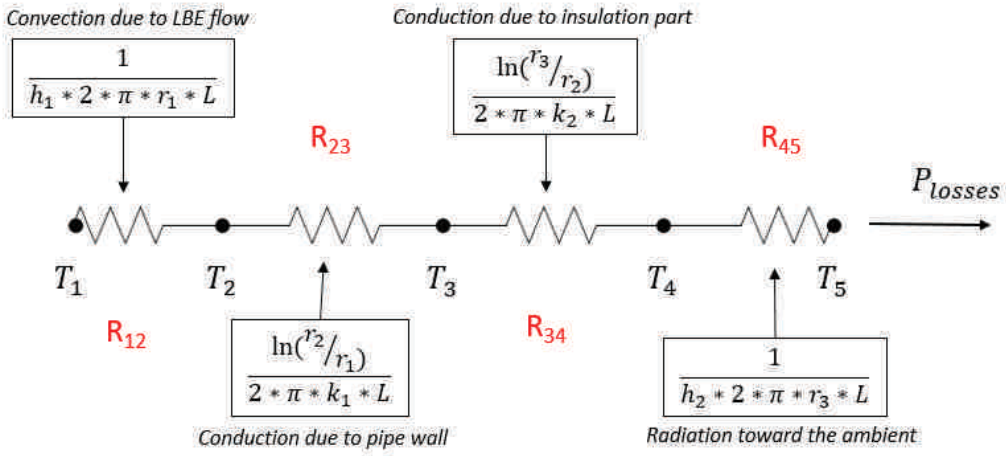

(b) Equivalent thermal circuit

Figure 2.11: Schematic model of the thermal exchange inside and outside the pipe

- The convection of the LBE inside the pipe,
- The conduction through the wall of the pipe in which the LBE is circulating,
- The conduction through the insulating element located around the pipe,
- The radiation of the full set toward the ambient.

For each of these steps, a resistance is estimated.

Heat resistance due to the convection

A heat transfer occurs when a liquid is forced through a pipe. This phenomenon, between a fixed surface and a moving fluid, is called forced convection. In order to estimate the heat

resistance due to the convection induced by the LBE flowing onto the pipe, it is first necessary to evaluate the convection coefficient h. h can be defined thanks to the Nusselt number Nu which corresponds to the ratio of convective to conductive heat transfer across a surface [54]:

$$Nu = \frac{h.D}{k} \tag{2.9}$$

with h the convection heat transfer coefficient in $W/m^2.K$, D the pipe diameter in which the flow occurs in m and k the thermal conductivity of the fluid in $W/(m.K)$.

The evaluation of the Nusselt number depends on different conditions, the first one being the flow regime, defined by its Reynolds number Re. To define the regime of the flow in this case, the Reynolds number Re_D has been calculated for the two considered diameters D (10 and 17 mm) for a flow rate varying from 0 up to 0.5 l/s (the maximum defined) as follows [54]:

$$Re_D = \frac{u.D}{\nu} \tag{2.10}$$

with u the fluid velocity over the tube cross section in m/s and ν the kinematic viscosity in m^2/s.

To estimate the Reynolds number of the LBE flowing into the two pipe diameters considered and at both temperature limits of 200°C and 600°C, the relevant properties defined in Table 2.1 are used.

The results are shown in Figure 2.12.

In a fully developed flow, the critical Reynolds number corresponding to the onset of turbulence is [54]:

$$Re_{D,c} \approx 2300 \tag{2.11}$$

For any flow rate higher than 0.01 l/s, the regime of the LBE will be turbulent.

For liquid metal and in case of fully developed turbulent flow in smooth circular tubes with constant surface temperature, Seban and Shimazaki [54] recommend the following formula for $Re_D.Pr \geq 100$:

$$Nu_D = 5.0 + 0.025(Re_D.Pr)^{0.8} \tag{2.12}$$

with Re_D the Reynolds number and Pr the Prandtl number defined as follows [54]:

$$Pr = \frac{C_p.\mu}{k} \tag{2.13}$$

with C_p is the specific heat capacity in $J.kg.K$, μ is the dynamic viscosity in $Pa.s$ and k is the thermal conductivity in $W/.m.K$.

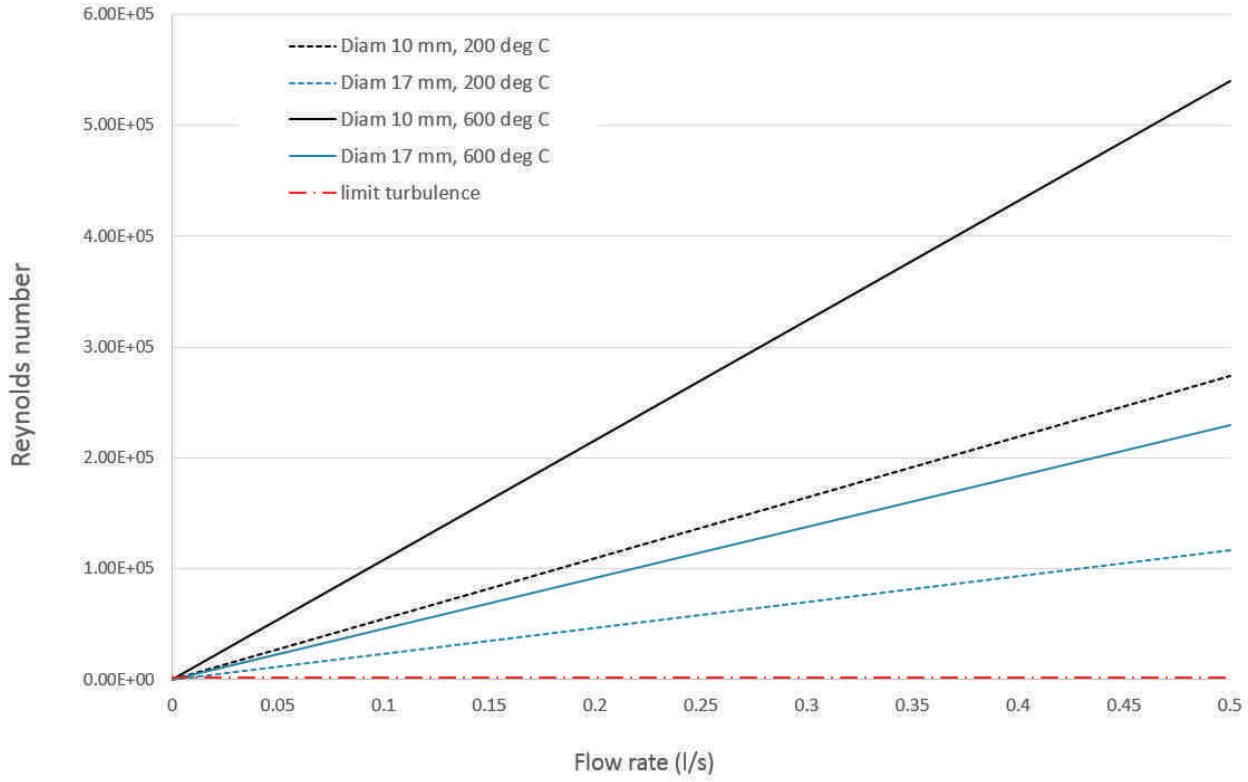

Figure 2.12: Reynolds number in function of flow rate for LBE at 200°C and 600°C and for two pipe diameters (10 mm and 17 mm)

Combining Equations 2.9, 2.10, 2.12 and 2.13 allows to obtain the convection coefficient h as shown in Figure 2.13. The dependence on the temperature is accounted for by using the thermal properties listed in Table 2.1.

From Figure 2.13, it is clear that the smaller the pipe diameter is, the higher the convection coefficient will be. Also, as one could expect, the convection coefficient increases when the flow rate increases. The difference induced by a change of the temperature from 200°C to 600°C is independent of the flow. This means that the impact of a change in temperature is larger for low flow rate compared to high flow rate (the convection coefficient change by 40 % at 600°C between the two diameters at 0.01 l/s while it is about 6 % higher at 0.5 l/s).

In a last step, it is then possible to estimate the heat resistance from the convection due to the LBE circulating inside the pipe knowing that [54]:

$$R_{convectionLBE} = R_{12} = \frac{1}{h.2.\pi.r_{pipe}.L_{pipe}} \tag{2.14}$$

with r_{pipe} is the internal radius of the pipe, also called r_1, in m and L_{pipe} the total length of the pipe in m. For the simplicity of the calculation, the total length of pipe that will be considered is 1 m for a simple scaling once the final length is known.

Figure 2.14 represents the total resistance due to the circulation of the LBE inside the pipe which is calculated from Equation 2.14. According to Equation 2.8, the higher the resistance

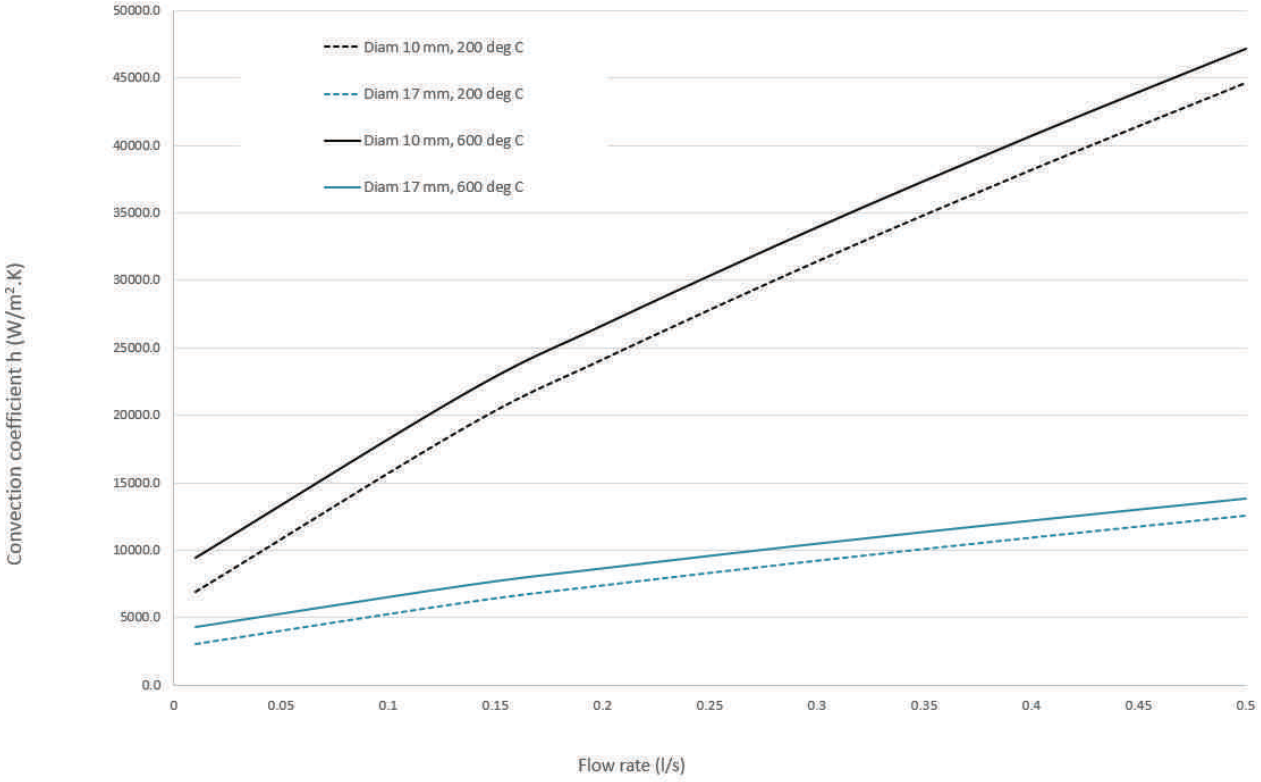

Figure 2.13: Convection heat transfer coefficient in function of flow rate for LBE at 200°C and 600°C and for two diameter of pipe (10 mm and 17 mm)

due to the convection phenomenon is, the lower will be the power losses. On Figure 2.14 that for low flow rate, the resistance will be higher and, consequently, the power loss lower.

Furthermore, it is also noted that the influence of the pipe diameter is lower than the influence of the temperature change, particularly for large values of flow rate. At lower temperature, the power losses are less important (since the resistance is higher) which is consistent with well-known heat transfer phenomena.

Resistance due to the conduction through the wall of the pipe

The second resistance in series will be associated with the the pipe itself. The phenomenon leading to this thermal transfer is the classical heat conduction. In this case, the resistance can be expressed as seen in the Figure 3.44b by:

$$R_{conduction \quad pipe} = R_{23} = \frac{ln(\frac{r_2}{r_1})}{2.\pi * k_1.L} \tag{2.15}$$

where r_1 and r_2 are respectively the inner and outer radius of the pipe in m, k is the thermal conductivity of the pipe material in $W/(m.K)$ and L_{pipe} the total length of the pipe in m. Here again, L will be taken as equal to 1 meter for simplicity in later scaling. r_1 and r_2 are respectively equal to 5 mm and 6 mm in case of the 10 mm-diameter pipe and to 8.5 mm and 9.5 mm in the case of the 17 mm-diameter pipe (see Table 2.3).

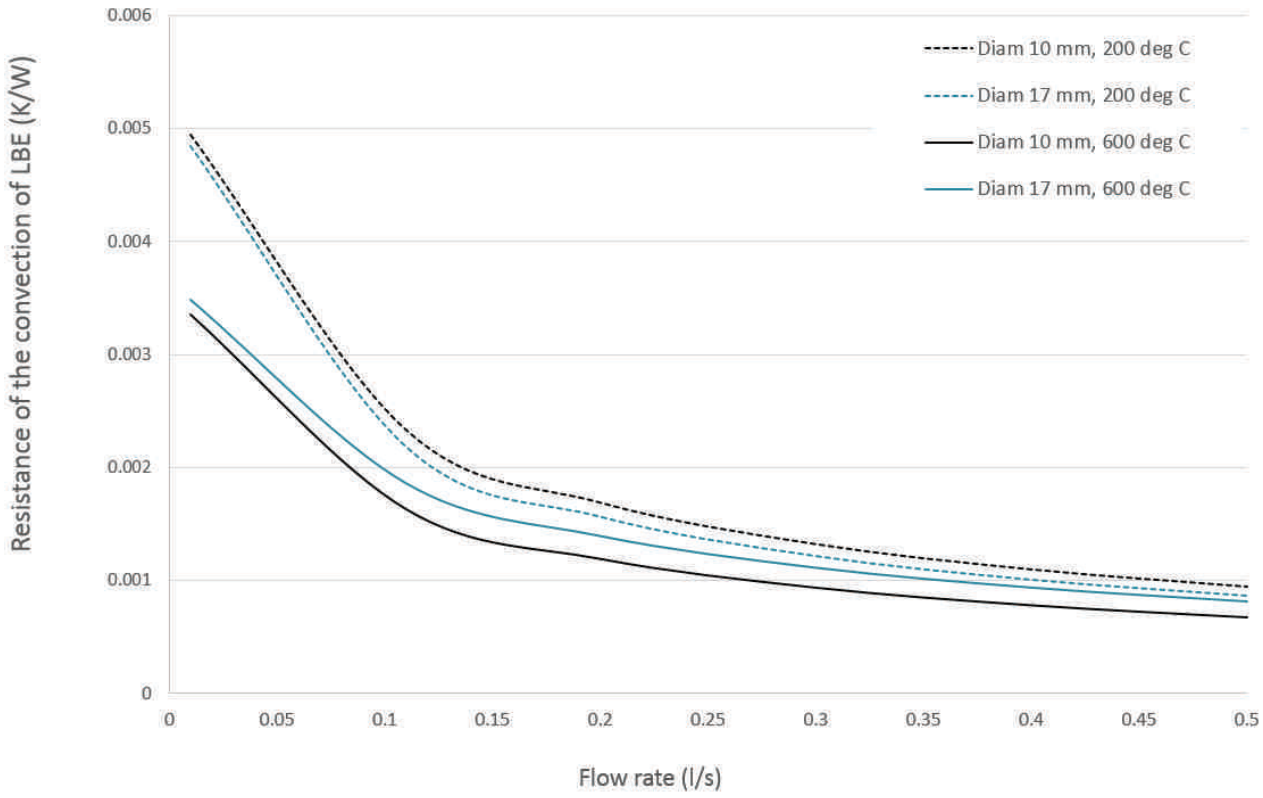

Figure 2.14: Heat resistance due to the convection in function of flow rate for LBE at 200°C and 600°C and for two diameters of pipe (10 mm and 17 mm)

As seen in Section 2.1.1, the chosen material for the piping of the loop is Stainless Steel 316L. Its properties at ambient temperature and at 600°C can be found in Table 2.2. Results from Equation 2.15 are presented in Table 2.12.

Pipe diameter *(mm)*	**10**		**17**	
Temperature *(°C)*	200	600	200	600
Resistance *(K/W)*	0.0018	0.0014	0.0011	0.0008

Table 2.12: Resistance due to the conduction through the pipe

The resistance due to the conduction through the pipe is the highest for the lowest temperature and the smallest pipe diameter. This makes sense since it means that the power extracted is higher for higher surface of exchange (bigger pipe diameter). The same happens for higher temperature.

The calculated values are in the same range than the values estimated for the convection due to the flow of LBE inside the pipe in case of a flow of about 0.5 l/s (see Figure 2.14). Generally, more power is lost by conduction than from the convection phenomenon.

Resistance of the conduction through the insulating elements

The resistance of the conduction through the insulating elements is calculated with Equation

2.15 where r_1 and r_2 become respectively for the internal and external radius of the insulating elements.

In this case, we study the impact of the thickness of the insulating element. The maximum thickness offset has been fixed at 3 mm.

Heat insulating materials have low thermal conductivity since it is usually comprised between 0.023 W/(m.K) for a good insulator and 2.9 W/(m.K) for less efficient insulators [50]. As a reference, the thermal conductivity of glass fiber usually vary from 0.05 W/(m.K) to 0.2 W/(m.K) [50]. In consequence, the analysis has been conducted with conductivity of 0.05 W/(m.K), 0.1 W/(m.K) and 0.2 W/(m.K). The results are presented in Figures 2.15. The curves adopt a logarithmic shape resulting from the numerator of Equation 2.15.

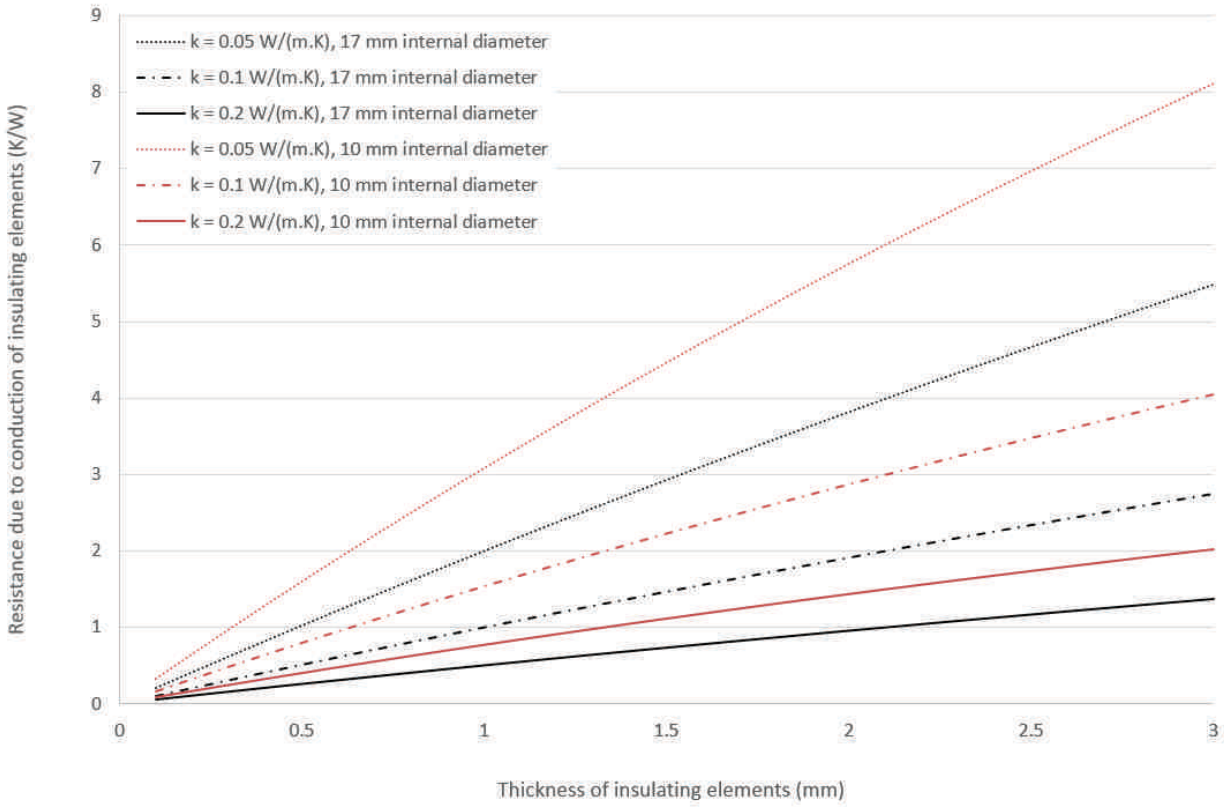

Figure 2.15: Resistance due to the conduction through the insulating elements depending on its thickness and thermal conductivity for a pipe of 10 mm and 17 mm internal diameter

Figures 2.15 shows that, as expected, the thicker the insulating element is, the larger the resistance is and thus, the less power will be lost.

It is also observed that the resistance due to the conduction through the insulating element is several order of magnitude higher than it is due to the convection of LBE inside the pipe and to the conduction through the pipe. This has therefore a major impact on the final power losses. Consequently, the insulating element has to be carefully selected.

Resistance of the radiation toward the ambient

The last resistance to consider is due to the thermal radiation of the full set toward the ambient. It is defined as follow:

$$R_{radiation} = R_{45} = \frac{1}{h_r.2.\pi.r_3.L} \tag{2.16}$$

Here, the challenge is to evaluate the radiation heat transfer coefficient h_r which is classically defined by [54]:

$$h_r = \varepsilon.\sigma.(T_s + T_{sur}).({T_s}^2 + {T_{sur}}^2) \tag{2.17}$$

with ε the emissivity, σ the Stefan Boltzmann constant ($\sigma = 5.67.10^{-8}$ W$/(m^2.K^4)$), T_s the temperature at the surface of the studied elements (here the insulating element) in K and T_{sur} the surrounding temperature or ambient temperature in K.

The combination of Equations 2.17 and 2.18 is a classical and convenient way [54] to express the non linear radiative exchange:

$$q''_{rad} = \varepsilon.\sigma.({T_s}^4 - {T_{sur}}^4) = h_r.(T_s - T_{sur}) \tag{2.18}$$

Where q''_{rad} stands for the radiative heat flux in W$/m^2$ and h_r is the film coefficient which strongly depends upon the temperature through Equation 2.17 while the temperature dependence of this coefficient for standard convective process is generally weak.

While the surrounding temperature T_{sur} is usually known, the evaluation of the surface temperature T_s is more complicated as it cannot be defined in advance. To estimate it, it is necessary to perform an energy balance at the surface [54].

$$q''_{cond} - q''_{rad} = 0 \tag{2.19}$$

with q''_{cond} the conductive heat flux in W/m^2.

By using the thermal Fourier's law and by assuming that the thickness t of the insulating element is small compared to the length of the pipe, the heat flux for the conduction part can be approximated by [54]:

$$q''_{cond} = k\frac{T_i - T_s}{t} \tag{2.20}$$

With T_i and T_s the temperatures at the two sides of the conductive part. In the studied case, T_i would be the targeted temperature varying between 200°C and 600°C and T_s the unknown and searched temperature at the surface of the insulating element.

Substituting equations 2.19, 2.18 and 2.20 yields to:

$$k\frac{T_i - T_s}{t} = h_r(T_s - T_{sur}) \tag{2.21}$$

Solving Equation 2.21 with respect to T_s gives:

$$T_s = \frac{\frac{k.T_i}{t} + h_r.T_{sur}}{\frac{k}{t} + h_r} \tag{2.22}$$

Equation 2.22 is a non linear equation with respect to T_S because h_r depends non linearly on T_S through Equation 2.17. To compute T_s, it is thus necessary to first estimate h_r thanks to Equation 2.17 with an initial guessed value of T_s (say $T_s = T_i$) and then to solve Equation 2.22 iteratively until the result converges. This can be done by using a computer software such as Matcad [24].

Furthermore, to determine h_r from Equation 2.17, it is necessary to set the emissivity. The standard value of emissivity for a classical insulation element is about 0.1, which corresponds to the emissivity of Aluminum on fiber glass. The present analysis will be conducted with three different emissivities (0.1, 0.5 and 0.9) covering the full range of possible values.

The thickness of insulating element will be varied from 1 mm to 3 mm. The results are presented in Tables 2.13 and 2.14.

	ε ->	**0.1**		**0.5**		**0.9**	
Thickness	**k *(W/(m².K))***	200 °C	600 °C	200 °C	600 °C	200 °C	600 °C
1 mm	**0.05**	1.32	4.82	6.16	17.51	10.53	26.48
	0.1	1.33	5.16	6.41	20.69	11.18	32.41
	0.2	1.34	5.36	6.56	23.37	11.59	38.05
2 mm	**0.05**	1.29	4.33	5.79	14.22	9.67	20.97
	0.1	1.32	4.82	6.16	17.51	10.53	26.48
	0.2	1.33	5.16	6.41	20.69	11.18	32.41
3 mm	**0.05**	1.27	4.00	5.51	12.42	9.09	18.14
	0.1	1.31	4.55	5.96	15.57	10.05	23.17
	0.2	1.32	4.97	6.28	18.86	10.83	28.93

Table 2.13: Radiation heat transfer coefficient h_r (Equation 2.17) in *(K/W)*

	ε ->	**0.1**		**0.5**		**0.9**	
Thickness	**k *(W/(m².K))***	200 °C	600 °C	200 °C	600 °C	200 °C	600 °C
1 mm	**0.05**	195	549	180	450	169	399
	0.1	198	572	189	501	182	458
	0.2	199	585	194	539	190	507
2 mm	**0.05**	191	514	166	390	150	335
	0.1	195	549	180	450	169	399
	0.2	198	572	189	501	183	458
3 mm	**0.05**	187	488	155	352	136	298
	0.1	193	530	173	415	158	362
	0.2	196	560	185	472	175	424

Table 2.14: Temperature T_S at the insulating element surface (Equation 2.22) in *(°C)*

In order to have a better overview of the results, four graphs are presented below, Figures 2.16 and 2.17 representing the radiation heat transfer coefficient in function of the thickness of the insulating element for different values of emissivity and of thermal conductivity of the insulating elements. Figures 2.18 and 2.19 present the final surface temperature of the insulating element in the same conditions as those of the previous Figures.

Figures 2.16, 2.17, 2.18 and 2.19 show that globally, the surface temperature will be higher for a low emissivity. The thermal conductivity of the insulating element plays as well an important role. The lower it is, the lower the radiation heat transfer coefficient and the surface temperature will be.

However, as many parameters have to be analyzed (with 36 curves presented on Figures 2.16, 2.17, 2.18 and 2.19), only 8 representatives cases have been selected since they cover the full studied range of parameters (Table 2.15).

Temperature *(°C)*	**Thermal conductivity *k (W/(m.K))***	**Emissivity value**
200	0.05	0.1
		0.9
	0.2	0.1
		0.9
600	0.05	0.1
		0.9
	0.2	0.1
		0.9

Table 2.15: Parameters of studied cases for the calculation of the resistance in the case of the radiation toward the ambient

To evaluate the value of resistance one should use Equation 2.16 where the total length L considered will be 1 m in order to allow a scaling if needed. r_3 depends on the thickness of the insulating element as $r_3 = r_2 + t$. Furthermore, the analysis has been computed for the two diameters of pipes considered as it will impact on this value of radius. The results for the 8 cases of Table 2.15 are presented in Figures 2.20 and 2.21.

From these results, it comes that for a larger thickness of insulating element, the resistance will be lower and thus, the power losses higher. This is contrary to what one should intuitively expect. Indeed, it seems more logical that for an higher thickness of insulating element, the power losses are reduced. These confusing results are explained by the fact that for a higher thickness of insulating element, the surface of radiation increases. Consequently, the losses are higher. It is also seen that the resistance will be higher for lower thermal conductivity and for lower emissivity value. This is expected as the lower the emissivity value is, the larger the heat inside the body will be kept.

Estimation of the total resistance

The total resistance for the final design of the target will have to be calculated thanks to the presented results. The total resistance and thus power losses are simply calculated with each independent terms and the power loss is calculated thanks to Equation 1.1.

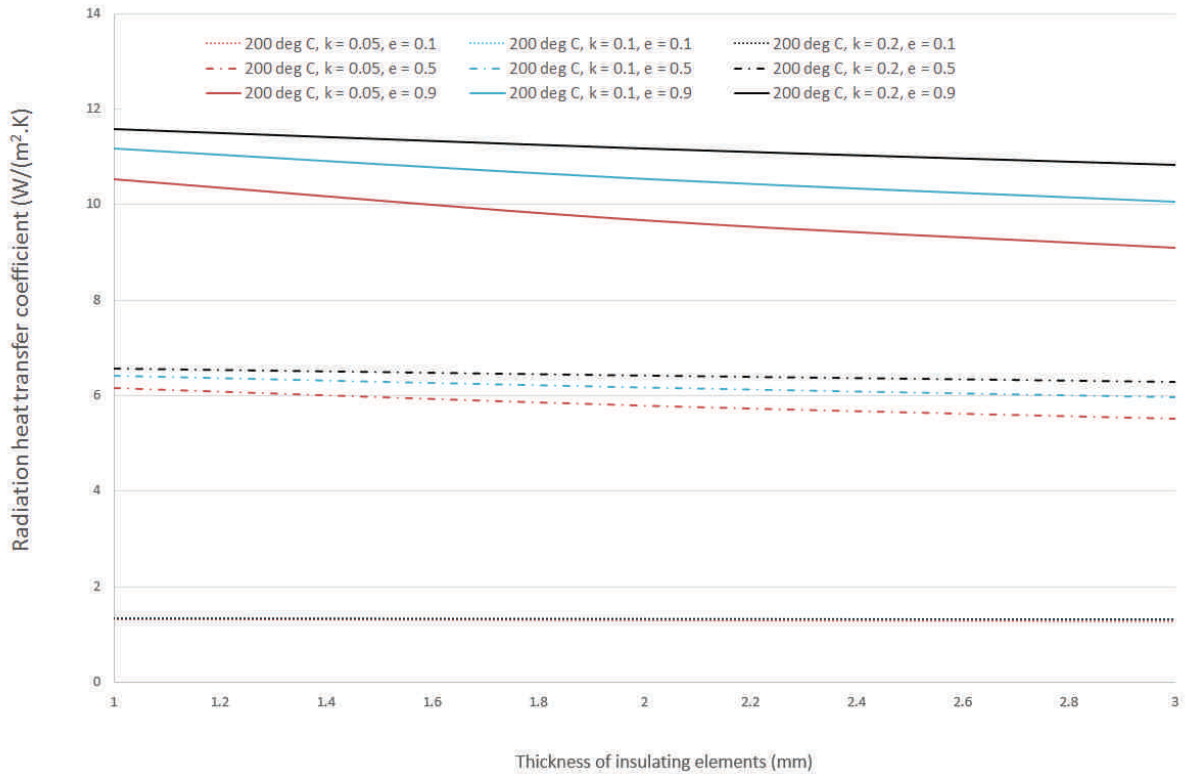

Figure 2.16: Radiation heat transfer coefficient for a temperature on the Stainless Steel pipe of 200 °C, depending on the insulating element thickness, for various given emissivities and thermal conductivities

By design and if considering a Stainless Steel 316L pipe of thickness 1 mm, only four parameters can impact on the total power losses:

- The pipe diameter,
- The flow rate of the LBE circulating inside the pipe,
- The conductivity of the insulating element chosen,
- The emissivity value of the insulating element.

In order to assess the driving parameters in terms of power losses, each of the pre-defined parameters have been considered separately. The total power losses have been calculated by varying the different parameters as follow:

- **Varying the flow rate** for a fixed thermal conductivity value and a fixed emissivity - plots for the two diameters of pipe considered (10 and 17 mm internal diameter) and for the two extreme working temperatures (200 °C and 600 °C) - Figure 2.22,
- **Varying the thermal conductivity** for a fixed flow rate value and a fixed emissivity - plots for the two diameters of pipe considered (10 and 17 mm internal diameter) and for the two extremes working temperatures (200 °C and 600 °C) - Figure 2.23,

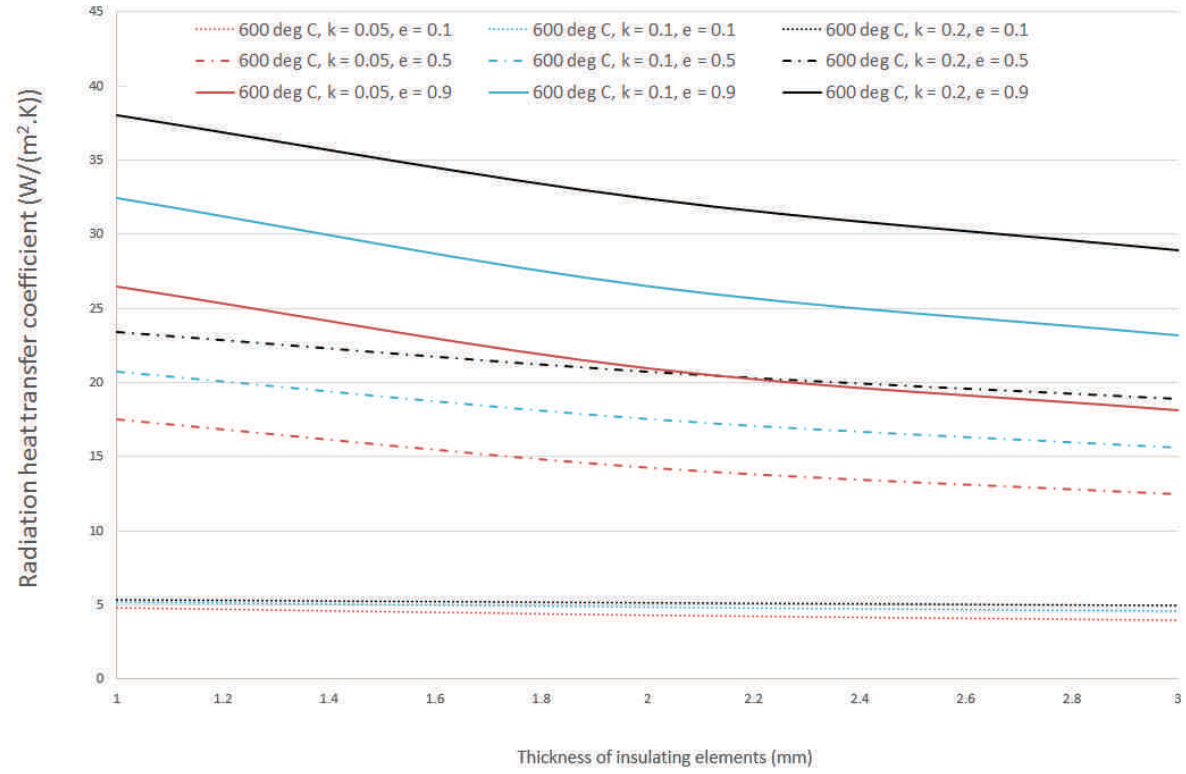

Figure 2.17: Radiation heat transfer coefficient for a temperature on the Stainless Steel pipe of 600 °C, depending on the insulating element thickness, for various emissivities and thermal conductivities

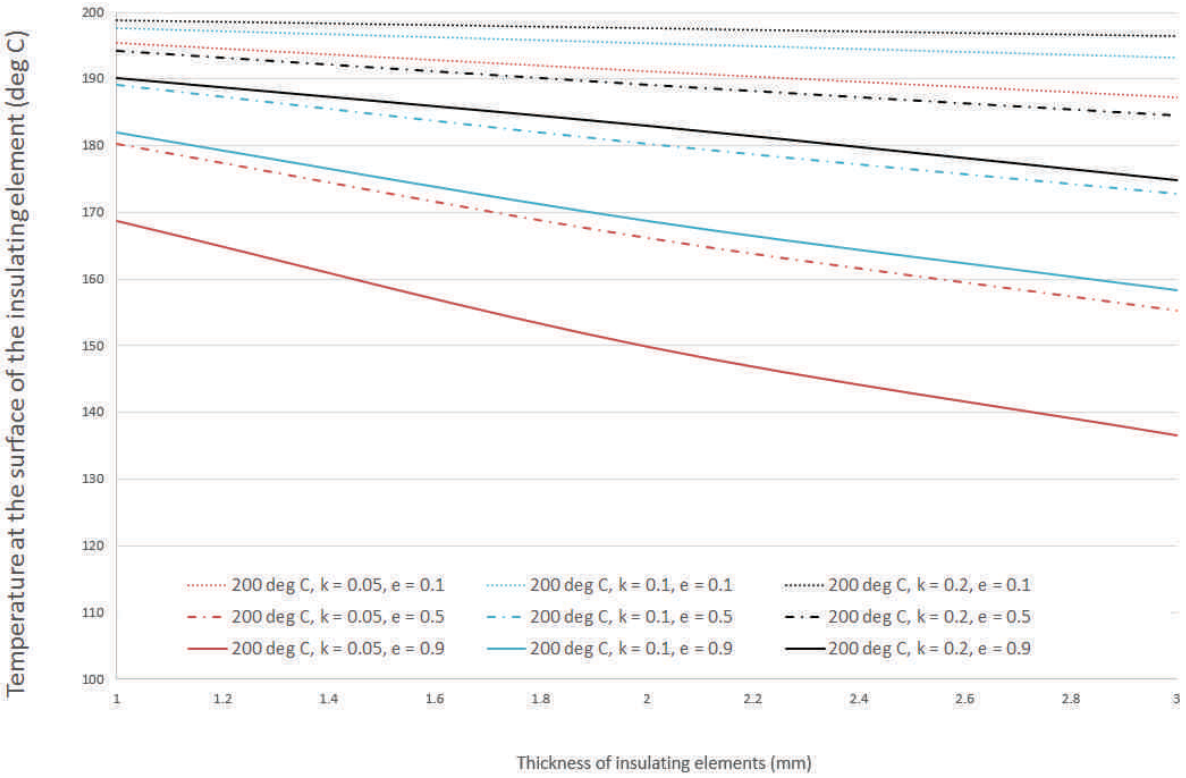

Figure 2.18: Surface temperature for a temperature on the Stainless Steel pipe of 200 °C, depending on the insulating element thickness, for various emissivities and thermal conductivities

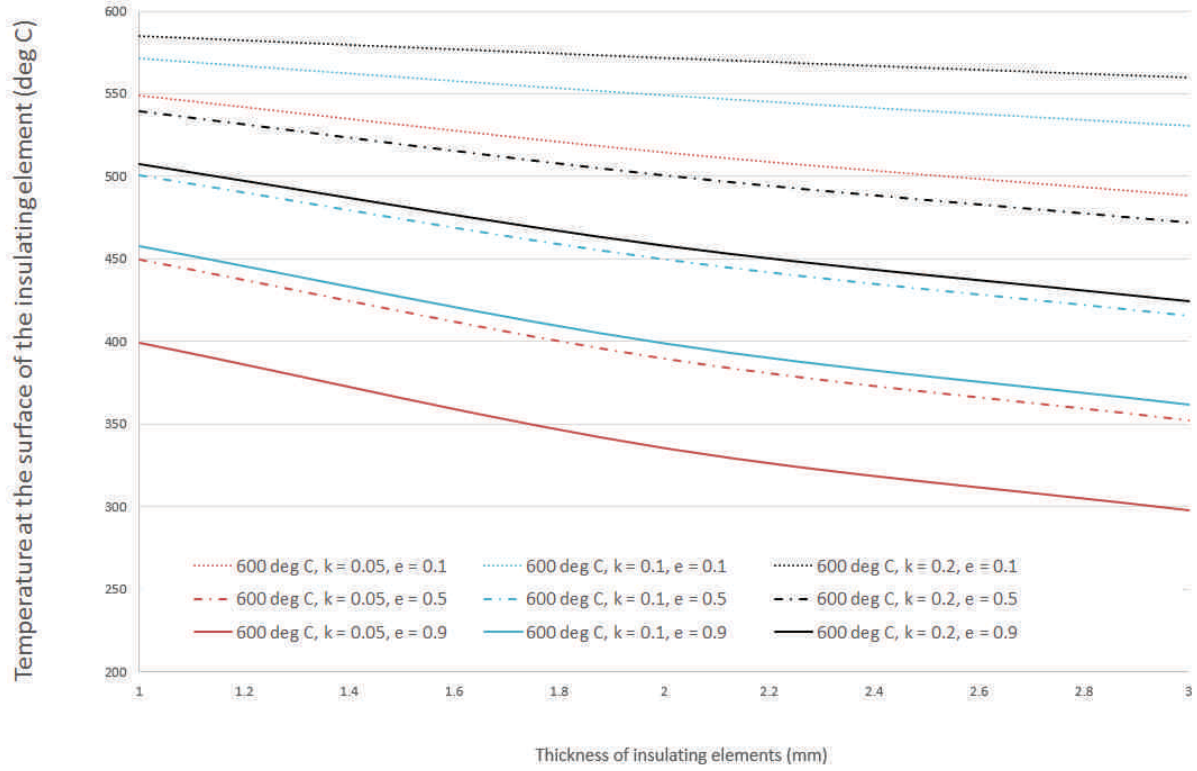

Figure 2.19: Surface temperature for a temperature on the Stainless Steel pipe of 600 °C, depending on the insulating element thickness, for various emissivities and thermal conductivities

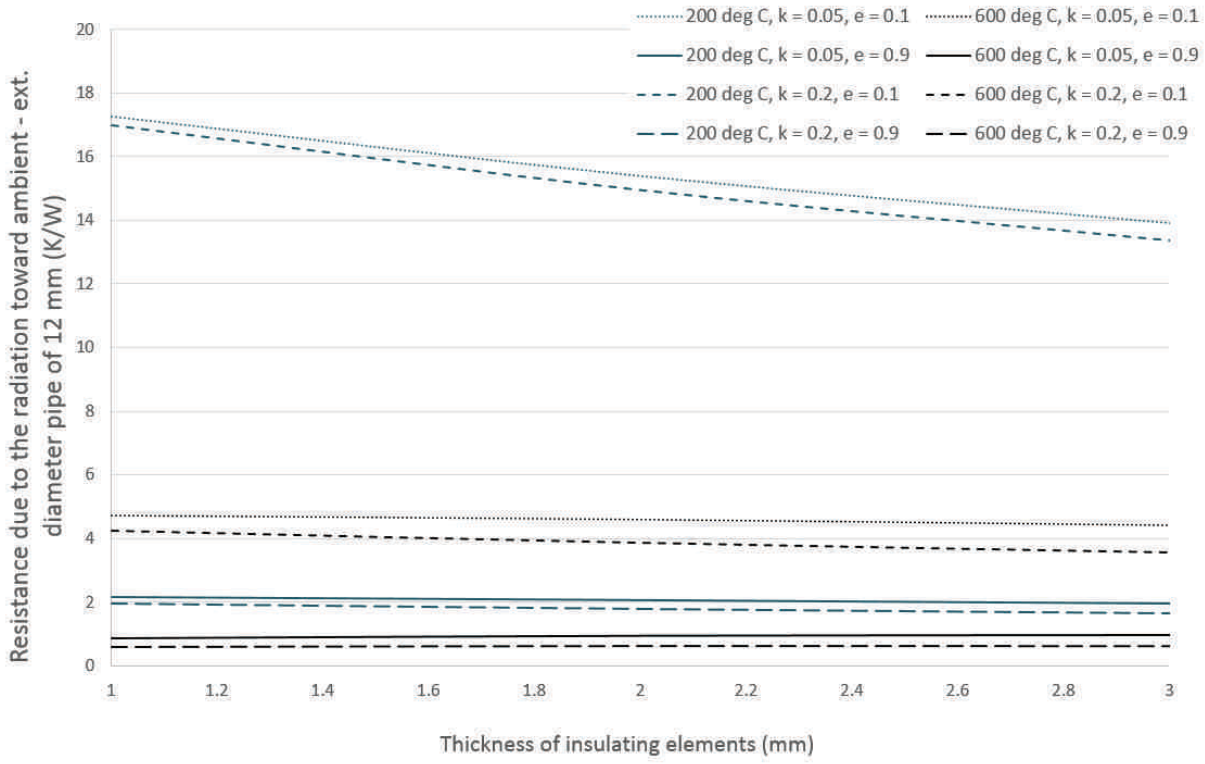

Figure 2.20: Resistance due to the radiation toward the ambient for a circulating Stainless Steel pipe of 10 mm internal diameter

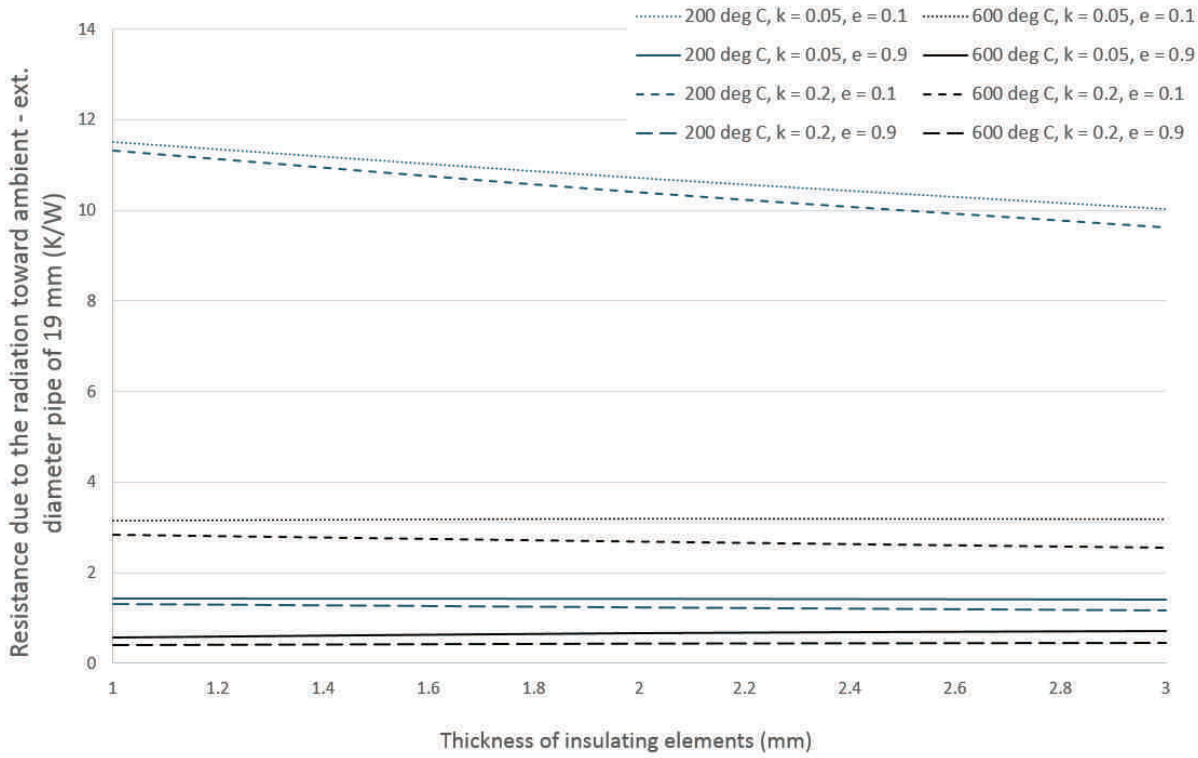

Figure 2.21: Resistance due to the radiation toward the ambient for a circulating Stainless Steel pipe of 17 mm internal diameter

- **Varying the emissivity** for a fixed flow rate value and a fixed thermal conductivity - plots for the two diameters of pipe considered (10 and 17 mm internal diameter) and for the two extremes working temperatures (200 °C and 600 °C) - Figure 2.24,

From Figure 2.22, 2.23 and 2.24, it is clear than the major driving parameter is actually the temperature. Indeed, on the three Figures, one can observe a difference of at least 80% between the power extracted at 200 °C compared to the one extracted at 600 °C. However, this parameter cannot be controlled as its variation is a requirement for the proper operation of the target. On the pipe diameter side, it seems that about 35 % less power will be extracted for an inner diameter of 10 mm compared to a 17 mm one. Furthermore, the choice of the insulating element is of major importance on the total power losses. Indeed, a gain of 50 % can be reached with a thermal conductivity of 0.2 W/(m.k) compared to a thermal conductivity of 0.05 W/(m.K) while 60 % less power will be extracted for a emissivity of 0.1 compared to an emissivity of 0.9. From Figure 2.22, it is clear that the impact of the flow rate on the total power losses is negligible. The power losses is mainly driven by the insulating elements (thermal conductivity and emissivity).

It has been shown here that the pipe diameter and the insulating element have the most important impact. These elements need to be chosen carefully in order to minimize the power losses. Also, the large range of working temperature will have an impact on the power losses: for higher temperature the losses will be significantly higher (between 80 and 90 %). This needs to be taken into account. As good practice, a good insulation will reduce this impact and have a better control on the thermal equilibrium of the loop.

This add two new Figures of Merit:

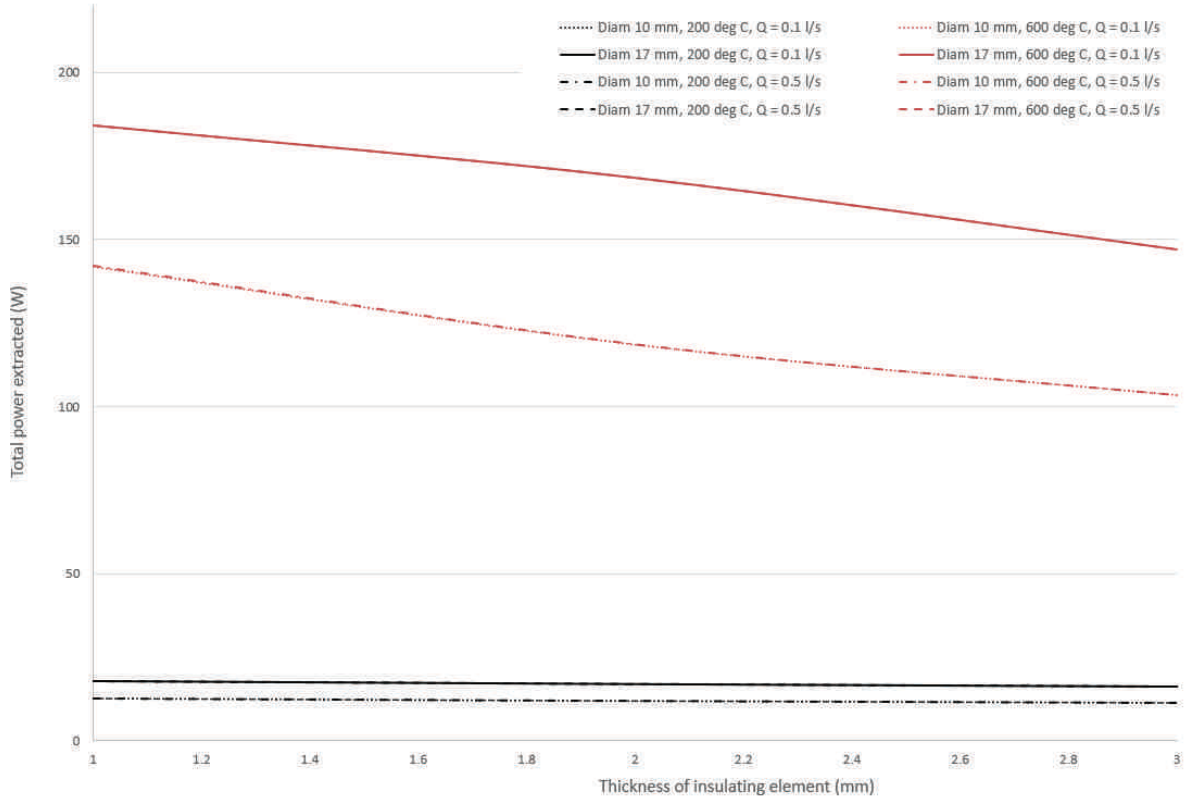

Figure 2.22: Total power losses for a fixed thermal conductivity for the insulating element of 0.2 W/(m.K) and an emissivity value of 0.1 at different flow rate for the LBE circulation

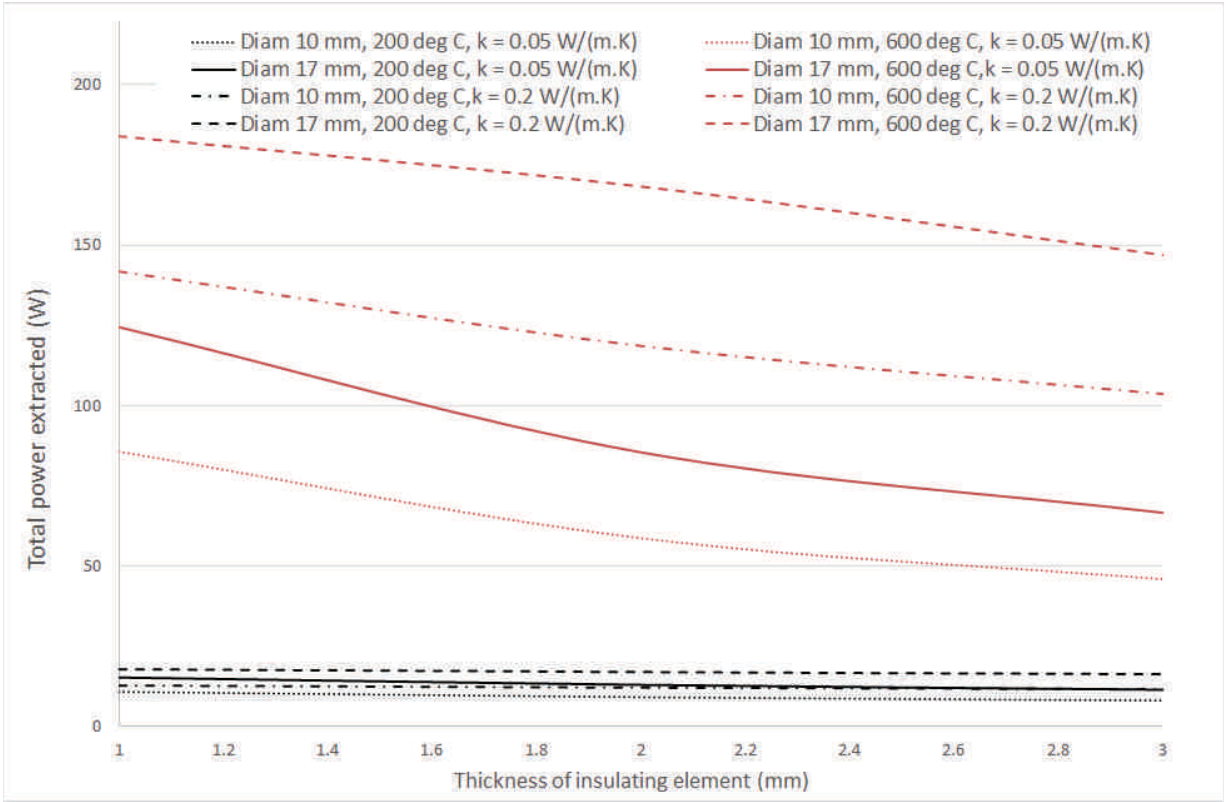

Figure 2.23: Total power losses for a fixed flow rate of 0.5 l/s for the LBE circulation and an emissivity value of 0.1 at different thermal conductivity for the insulating element

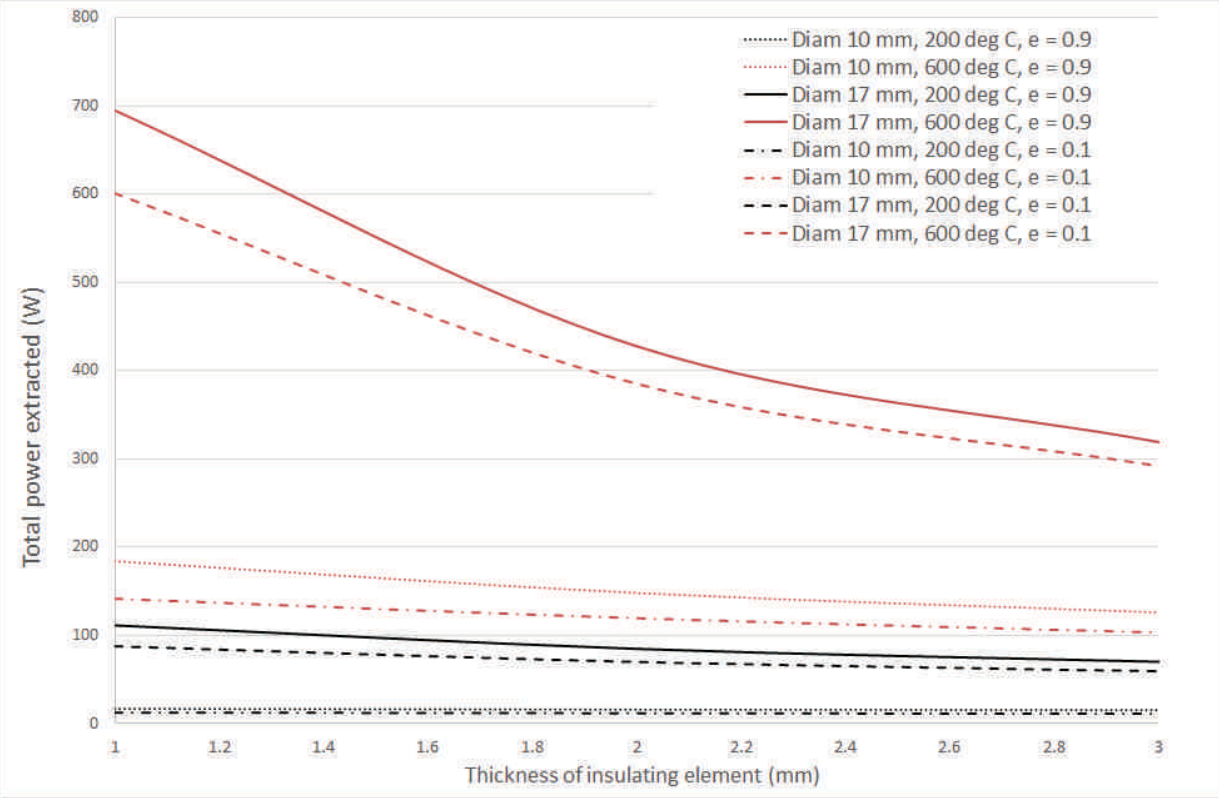

Figure 2.24: Total power losses for a fixed thermal conductivity for the insulating element of 0.2 W/(m.K) and a flow rate of 0.5 l/s at different emissivity value

- Diameter of the pipe to be chosen in function of the power losses allowed,
- Thickness and material for the insulator to be defined in function of the power losses allowed.

2.3.1.2.3 Heat Exchanger (HEX) design To design or to predict the performance of a heat exchanger, the power P *(W)* must be related to the overall heat transfer coefficient H *(W/(m².K))*, the heat transfer surface area S *(m²)* and the hot and cold fluids temperatures through the log mean difference temperature ΔT_{lm} *(K)* [54]:

$$P = H.S.\Delta T_{lm} \tag{2.23}$$

with $\Delta T_{lm} = \frac{\Delta T_2 - \Delta T_1}{ln(\frac{\Delta T_2}{\Delta T_1})}$ and $H = \frac{1}{\frac{1}{h_1}+\frac{1}{h_2}}$

where h_1 and h_2 are respectively the heat exchange coefficients of the LBE and of the water in *(W/(m².K)* and ΔT_1 the **inlet** temperature difference between the hot (LBE) and cold (water) liquid and ΔT_2 the **outlet** temperature difference between the same fluids.

Figure 2.25 shows the temperature distribution that will be reached in a parallel flow heat exchanger [54]. In the Figure, the subscripts h and c refer to the hot and the cold fluids, whereas i and o refer to the inlet and outlet conditions. Finally, C_h and C_c are the hot and cold fluid heat capacity, respectively.

A heat exchanger can be in co-axial flow or in a counter flow configuration. In our case, it has been checked numerically that both would give similar results and thus, the further analysis will be performed considering (randomly) a co-axial flow.

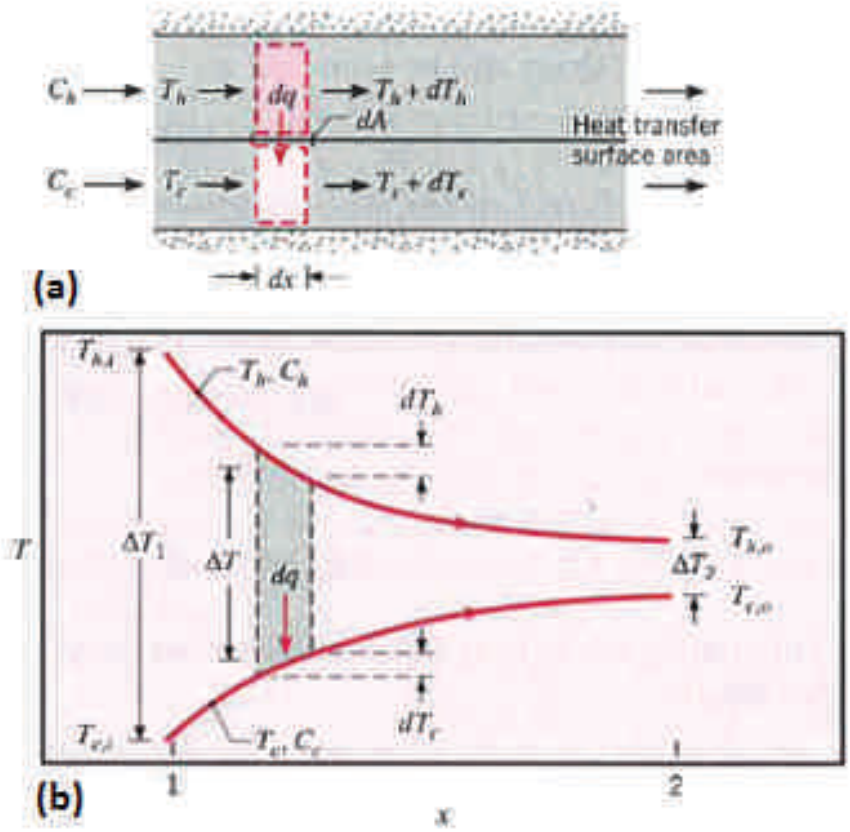

Figure 2.25: Co-axial flow HEX, temperature distribution

Considering Equation 2.23, it appears that the different parameters possibly variable and impacting the extracted power are the two fluid flow rates included in the heat exchange coefficient h_1 and h_2, the temperature of use of each of them and the total exchange surface area.
It is thus obvious that for a fixed design with a fixed flow rate for both fluids, the power extracted would be higher when the temperature would increase and this, proportionally. This is important as the working temperature of the LBE will vary from 200 °C up to 600 °C.

In order to propose a proper design of an heat exchanger for the LIEBE target, it is necessary to take into account the design constraints as well as the thermal ones. Indeed, the heat balance of the target will allow the estimation of the power to be extracted by the heat exchanger for each working temperature.

2.3.2 Target for short-lived species

2.3.2.1 Preliminary considerations

The ultimate goal of the LIEBE target is to produce short half-life species (half life in the order of hundreds milliseconds). As seen in the Section 1.3.2 (Equation 1.1), in case of an ISOL

facility as at ISOLDE, the secondary ion beam intensity i can be expressed as [40]:

$$i = \Phi.\sigma.N.\varepsilon_{target}.\varepsilon_{source}.\varepsilon_{sep}.\varepsilon_{transport} \tag{1.1}$$

The release times in static molten targets are often long compared to the radioactive decay half-life and can therefore be responsible for an important part of the losses in the case of short-lived nuclei. Minimum delay times for the diffusion process can be realized by achieving the shortest diffusion lengths and by operating at the highest possible temperatures so that release times are commensurate with the lifetime of the species of interest. This has been demonstrated during the Eurisol Design Study phase and with tests conducted at CERN-ISOLDE [12], where many analysis have been performed [20].

In the LIEBE target, the fragmentation of the lead bismuth eutectic (LBE) into a shower-type spray aims at a reduction of the diffusion lengths leading to an increase of the release efficiency of short-lived RIBs.

Consequently, the concept 1 presented in Section 2.2.2.1 is rather preferred compared to the concepts 2 and 3 as it is the one with the shorter path for the isotopes. The analysis will be done considering this concept.

The present analysis aims at the estimation of the release of specific isotopes from the LBE shower. As a most important part of the design of the LIEBE target, the dimensioning of the diffusion chamber shall be performed accounting for the predicted release efficiencies. This study focuses on the processes occurring in the irradiation and diffusion chamber, where the radioisotopes are produced, before these enter the ion source. It will give tools for the design of the target. Indeed the container and the diffusion chamber, as well as the flow parameter, must be optimized in order to get the highest possible yield.

2.3.2.2 Radioisotope release consideration

The analysis presented here has been done with T.M. Mendonca within the WP9 (Table 1.3 Section 1.5.2.3).

2.3.2.2.1 Diffusion efficiency The operating temperature of the target material is chosen according to the material melting temperature (125°C) and its vapour pressure. The LIEBE target will be operated in the temperature range between 200 and 600°C, accounting for the vapour pressure of LBE at 600°C. The diffusion out of the material is strongly dependent on the temperature as known by the Arrhenius dependence and the maximum operating temperature has been chosen as a reference in order to evaluate the highest release fractions. Mercury has been chosen as element of reference in this assessment although its diffusion coefficient in LBE is not known. In fact, only few data for diffusion coefficients of metallic elements in LBE are available in the literature (e.g. Co, Se, In, Fe and Tl [1]). Thallium has therefore been chosen due to the similar ionic radius and chemical behaviour as mercury. Figure 2.26 shows the dependence of the diffusion coefficient of thallium as a function of temperature.

For the assessment of the diffusion release transfer, two different sections have been considered: the irradiation chamber and the diffusion chamber. In the irradiation chamber it is considered

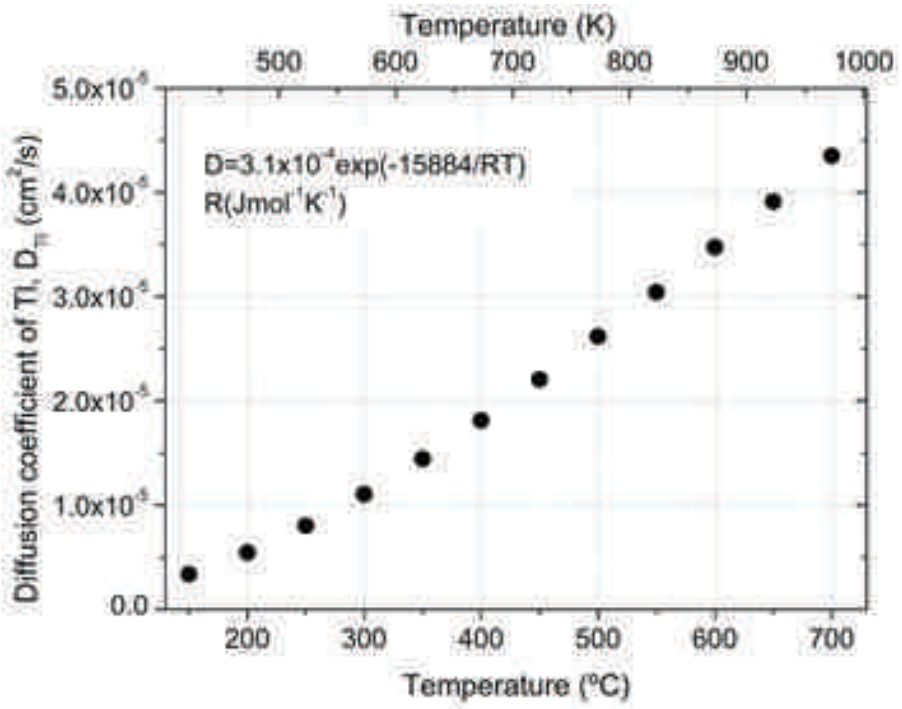

Figure 2.26: Diffusion coefficient of Thallium in LBE as a function of temperature. At 600 °C, the diffusion coefficient takes the value of $3.5.10^{-5}$ cm^2/s

that there is ideal mixing during irradiation and the isotope production N_0 at t=0 is given by N_0=C_0V_{irrad}, where C_0 is the isotope initial concentration and V_{irrad} the volume of the irradiation chamber. The flow rate (J) in the irradiation chamber is thus given by $J = \frac{V_{irrad}}{t_{irrad}}$. In the diffusion chamber, the release efficiency is classically expressed as the product of the efficiencies related to the irradiation chamber and to the diffusion chamber [55]:

$$\varepsilon(t,\lambda) = \int_{t=0}^{t_{irrad}} \frac{1}{t_{irrad}}.exp^{-\lambda.t}dt. \int_{t=0}^{t_{chamber}} P(t).exp^{-\lambda.t}dt \tag{2.24}$$

where λ is the isotope decay constant, $t_{chamber}$ the residence time in the diffusion chamber and *P(t)* the diffusion delay function.

The diffusion delay function for spherical particles is given by the following series expansion [55]:

$$P(t) = \frac{6.\mu_D}{\pi^2}.\sum_{n=1}^{\infty}.exp^{-n^2.\mu_D.t} \tag{2.25}$$

where μ_D is the diffusion parameter, which is dependent on the diffusion coefficient D and of the droplet radius r via the following expression:

$$\mu_D = \frac{\pi^2.D}{r^2} \tag{2.26}$$

The diffusion release transfer as a function of time and of the isotope decay λ is obtained by reporting Equation 2.25 in 2.24:

$$\varepsilon(t,\lambda) = \frac{1}{\lambda.t_{irrad}}.(1 - exp^{-\lambda.t_{irrad}}).\frac{6.\mu_D}{\pi^2}.\sum_{n=1}^{\infty}.\frac{1 - exp^{-n^2.\mu_D - \lambda}.t}{n^2.\mu_D + \lambda} \tag{2.27}$$

Equation 2.27 has been used to calculate the diffusion release efficiency for different isotopes as a function of the time in the diffusion chamber. Figures 2.27, 2.28 and 2.29 show the result corresponding to different isotopes diffusing out of a droplet of 100 μm radius, 200 μm and 300 μm. For the three radius, a time of 70 ms spent in the irradiation chamber has been assumed in the calculation. Indeed, this corresponds to the half of the targeted isotope ^{177}Hg half life (130 ms). It is noticed that the best efficiency is obtained with a 100 μm radius droplet.

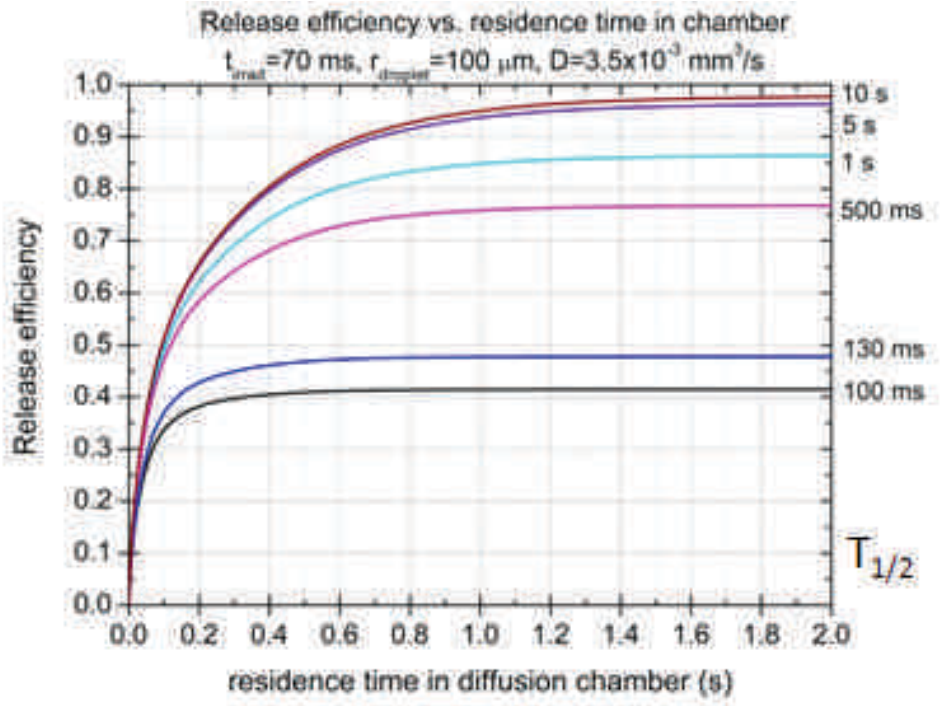

Figure 2.27: Calculated diffusion release efficiencies (Equation 2.27) for different isotopes diffusing out of a 100 μm radius droplet as a function of the residence time in the diffusion chamber

48 % of ^{177}Hg is for example released out of the droplets for 0.2 s residence time in the diffusion chamber. The fragmentation of LBE into droplets of 100 μm leads in fact to an improvement by a factor of 24 in comparison with the measured released fractions for ^{177}Hg using a static Pb target [20].

Figure 2.30 summarizes the effect of the droplets size on the calculated release efficiencies for ^{177}Hg. As mentioned before, the release efficiency is optimized for the smallest droplet size (i.e. 100 μm) and is found to be in the ratio of 44/30/23 % for droplets of 100/150/200 μm radius, respectively, for a 0.2 s residence time. For shorter residence times, a decrease in the release efficiencies is observed. The droplet size will directly depend upon the formation holes diameter as it will be seen in the Section 2.3.2.3. As a start for the analysis and considering

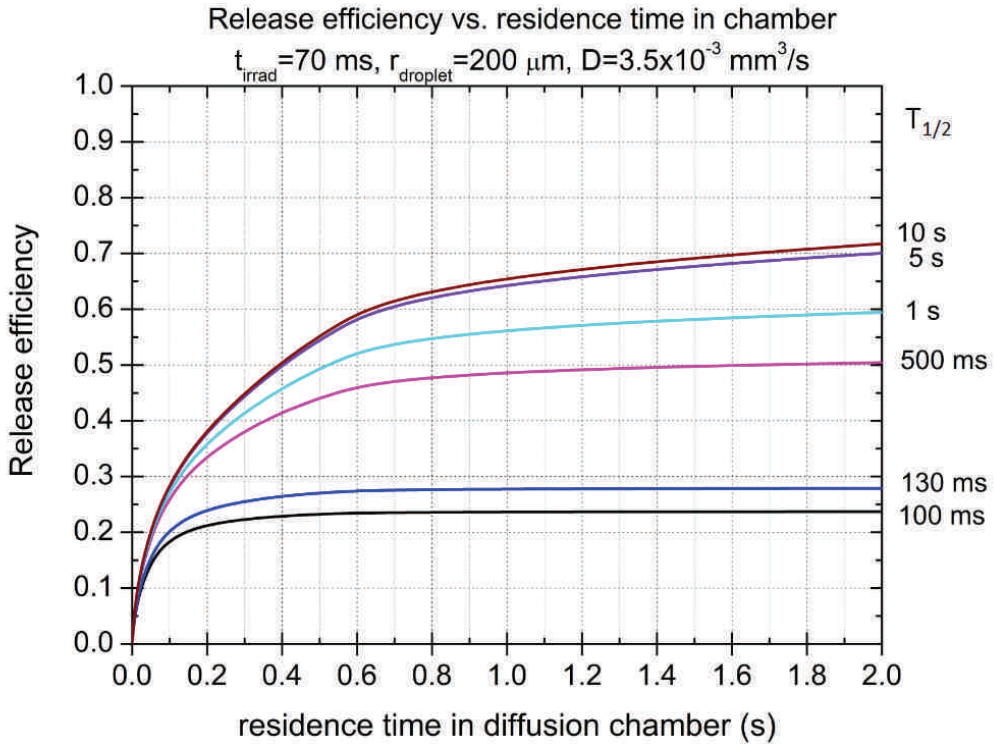

Figure 2.28: Calculated diffusion release efficiencies (Equation 2.27) for different isotopes diffusing out of a 200 μm radius droplet as a function of the residence time in the diffusion chamber

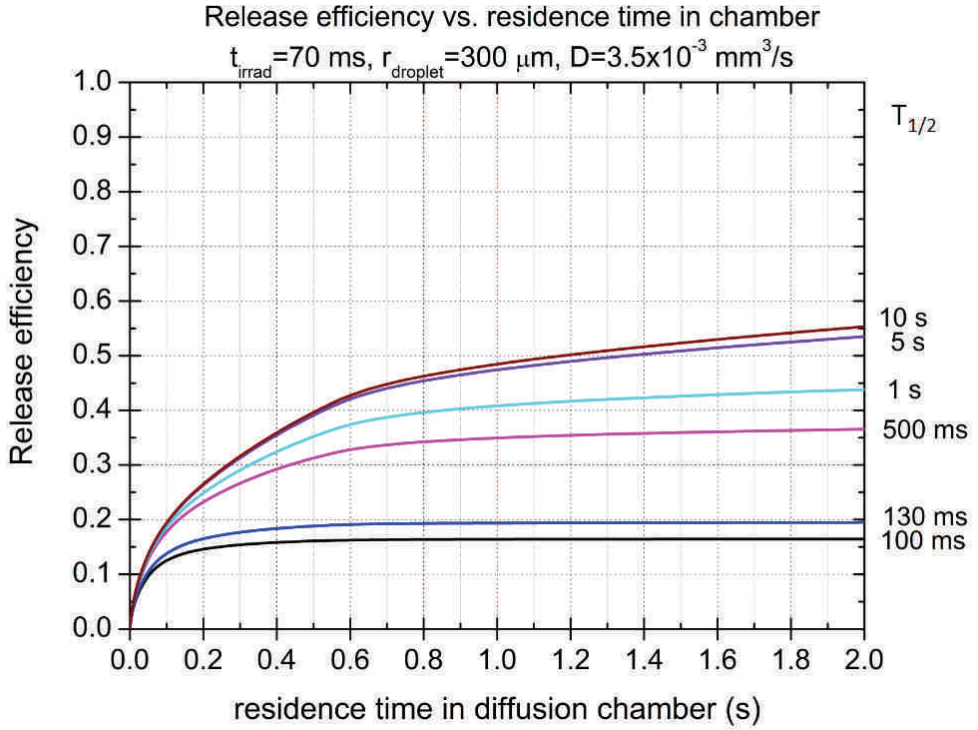

Figure 2.29: Calculated diffusion release efficiencies (Equation 2.27) for different isotopes diffusing out of a 300 μm radius droplet as a function of the residence time in the diffusion chamber

the available manufacturing tools, a minimum droplet radius of 100 μm has been considered (see Section 3.2.1.1 for more details).

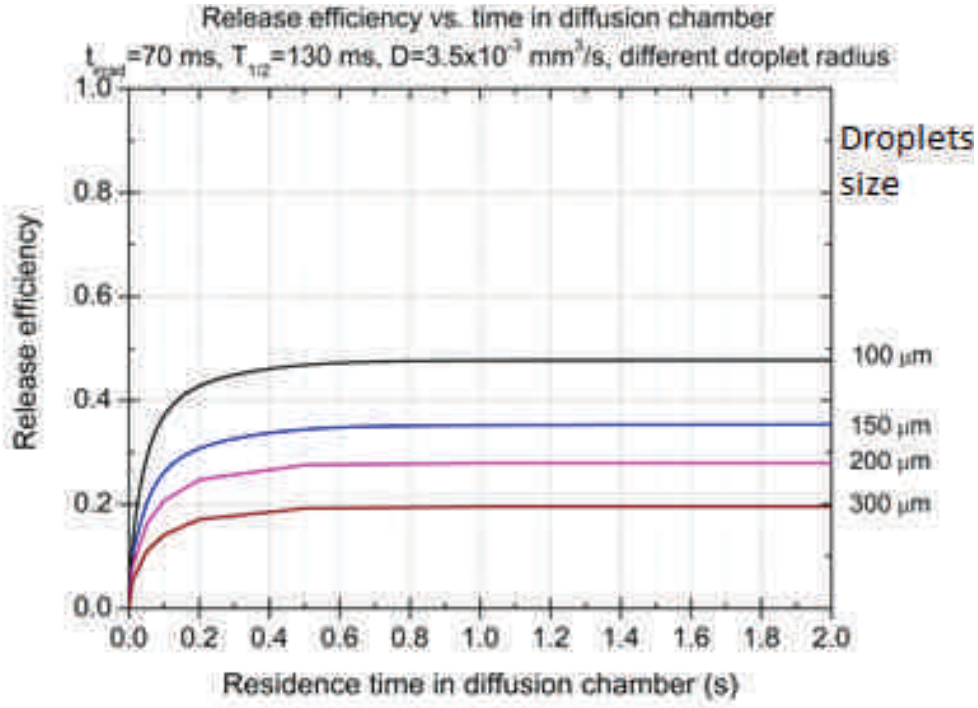

Figure 2.30: Calculated diffusion release efficiencies (Equation 2.27) for ^{177}Hg for different droplet radius as a function of the residence time in the diffusion chamber

2.3.2.2.2 Effusion efficiency After the release from the LBE droplets, the radioisotopes freely fly until they meet a wall or collide with the droplets until they are finally extracted from the ion source. Once the effusion process is started, the number *N(t)* of radioisotopes effuse to the ion source according to the following approximation [56]:

$$N(t) = N_0.exp^{-\lambda.t}.exp^{\frac{-t}{\tau_{eff}}} \tag{2.28}$$

where N_0 is the number of atoms at time *t=0*, λ is the isotope decay constant and τ_{eff} the effusion delay time in *s*. τ_{eff} is dependent on the average number of collision χ, the average flight time τ_{fl} and the average sticking time per wall collision τ_{st} via the relation [56]:

$$\tau_{eff} = \chi.(\tau_{st} + \tau_{fl}) = \frac{1}{\nu} \tag{2.29}$$

where ν represents the average time of effusion in s^{-1}.

The sticking time corresponds to the time an atom stays on a solid surface before effusing. For the effusion release assessment of the LIEBE target, it has been calculated using the Frenkel equation [57]:

$$\tau_{st} = \tau_0 . exp^{\frac{-\Delta H_{ads}}{RT}} \tag{2.30}$$

where ΔH_{ads} represents the enthalpy of adsorption, τ_0 the lattice vibration period of the containment material and R the universal gas constant. ΔH_{ads} depends on the chemical reactions between the radioisotopes and the target material and the containment surfaces. The values of ΔH_{ads} used in this assessment have been obtained via the systematics computed by Eichler [58] assuming sticking to the container walls in Stainless Steel ΔH_{Fe} and to the target material ΔH_{Pb} and are summarized in Table 2.16.

Element	**Debye temperature *(K)***	**Debye frequency *(Hz)***	τ_0 ***(s)***	ΔH_{ads} ***(kJ/mol)***
Fe	646	$7.8.10^{12}$	$1.29.10^{-13}$	-173.3
Pb	361	$1.8.10^{12}$	$5.45.10^{-13}$	-68.3

Table 2.16: Debye temperature and frequency, lattice vibration period and adsorption enthalpies values used in this assessment (for Hg)

In order to improve the effusion efficiency, we have to decrease τ_{eff} as much as possible or, in other words, to decrease τ_{st} and τ_{fl}. Figure 2.31 shows the evolution of the sticking time versus the temperature in the diffusion chamber. The sticking time has been found to be of the order of 5.10^{-12} s at 600 °C for both surfaces having a small influence in the effusion time. Furthermore, it is shown that the higher the temperature, the better the efficiency the effusion process will be. Concerning the average flight time of a particle between two sticking points, it has been defined by the mean free path d_{fl} and by the thermal velocity of the effusing element via the expression [57]:

$$\tau_{fl} = d_{fl} . \sqrt{\frac{m}{3.k_B.T}} \tag{2.31}$$

where m is the mass of the effusing element, T is the system temperature and k_B the Boltzmann constant.

The mean free path and the number of collisions were determined by using the Monte carlo Molflow code [59]. Different dimensions of the diffusion chamber (summarized in Table 2.17) have been assumed. The length considered is either 20 cm (which correspond to the length of the standard ISOLDE target), either half of it (10 cm). The width is kept at 2 cm as in standard target. The maximum height available and used for the calculation (12 cm) is defined by geometry as defined in the Section 2.1.3.

LBE was included in the model in the form of jets of 100 μm radius with 300 μm spacing (Figure 2.32).

According to Equation 2.29, to increase the efficiency of the effusion process, the mean flight time τ_{fl} or the number of collision χ should be reduced. The preliminary results show that the mean flight times are of the order of 10^{-5} s (Figure 2.33) for a number of collision assumed to be in the order of 10^6. A small decrease of τ_{fl} is also observed with the decrease of the diffusion chamber height but an increase is noticed if the length of the diffusion chamber is decreased. It is therefore difficult to obtain a definitive conclusion in terms of volume because the best

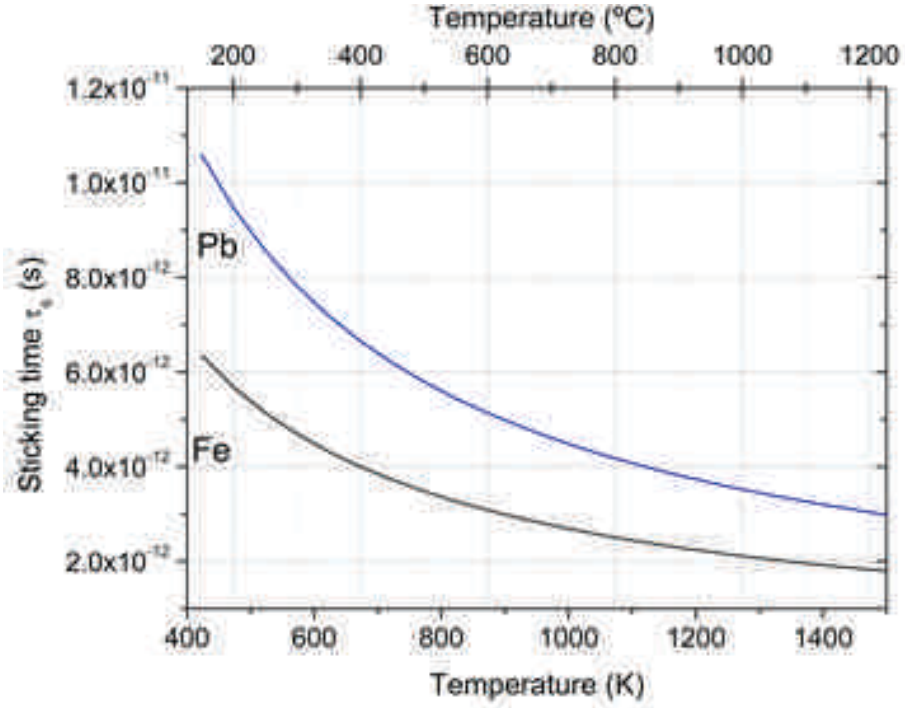

Figure 2.31: Sticking times of the radioisotopes of interest in the containment surface *Fe* and in the target material *Pb* as a function of temperature

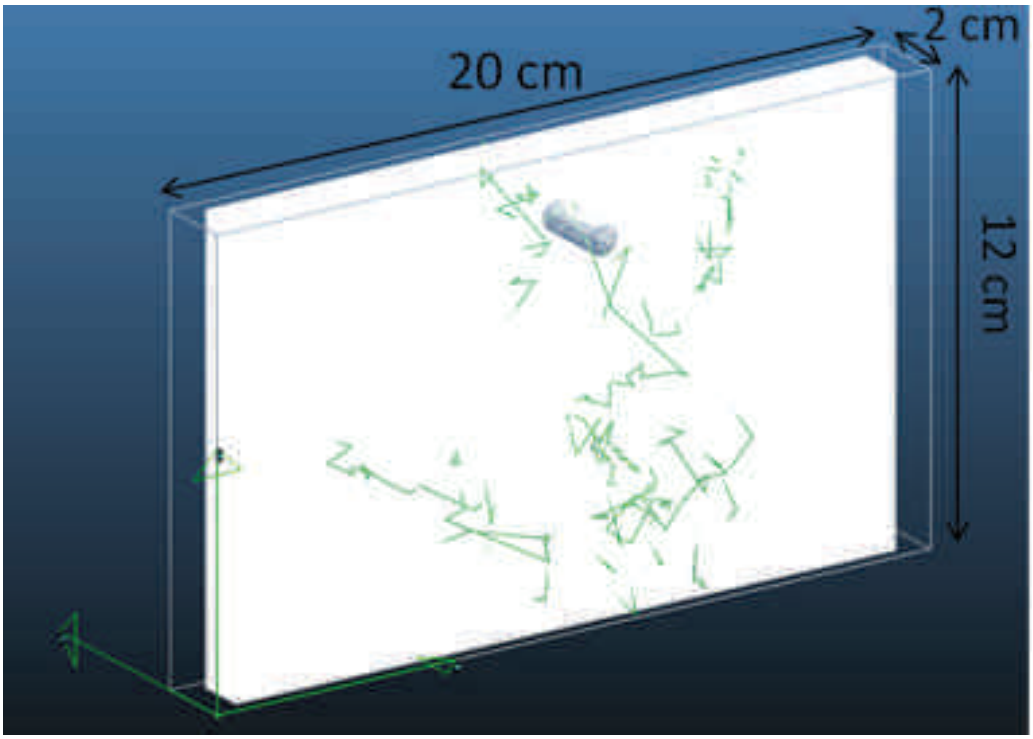

Figure 2.32: Diffusion chamber model used in the Monte Carlo calculations with 10 016 jets of 100 μm radius and 300 μm space between them

Length *(cm)*	**Height** *(cm)*	**Volume** *(cm^3)*	**Number of jets**
20	12	480	10 016
20	8	320	10 016
20	6	240	10 016
10	12	240	4 616
10	8	160	4 616
10	6	120	4 616

Table 2.17: Diffusion chamber dimensions used in the Monte Carlo calculations

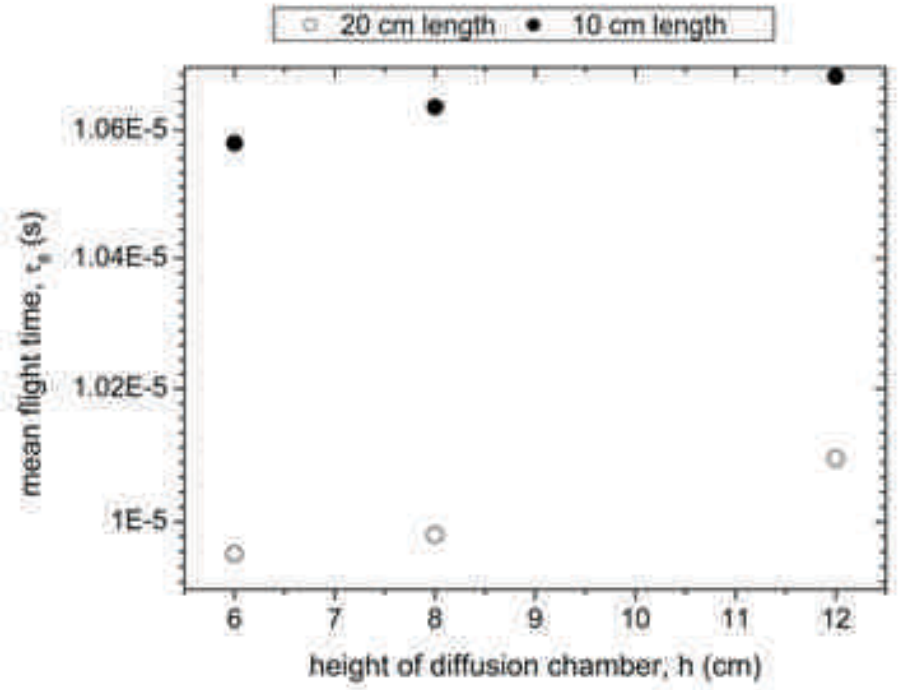

Figure 2.33: Mean flight times as a function of the height of the diffusion chamber

case corresponds to a volume equal to 240 cm^3 (third line on Table 2.17 corresponding to the point located at the left-down corner on Figure 2.33) and the worst to the same volume of 240 cm^3 (fourth line on Table 2.17 corresponding to the right-top corner on Figure 2.33). The only difference comes from the number of jets (10 016 against 4 616 as shown on the last column of Table 2.17), leading to the conclusion that the largest number of jets or droplets is more favorable, allowing possible re-interaction.

Anyway, the variation difference between the different results remains under 8 % which seems to show that the impact of the mean fligth time on the final efficiency will not be very high.

Furthermore, the probability an atom has effused between t and $t+dt$ can be expressed as [56]:

$$p_\nu(t).dt = \nu.exp^{-\nu.t}.dt \tag{2.32}$$

By integrating Equation 2.28 over time and considering Equation 2.32, the effusion efficiency is calculated for a nuclide of half life $t_{1/2}$:

$$\epsilon_{eff}(t_{1/2}) = \int_{t=0}^{\infty} \nu.exp^{-\nu.t}.exp^{-\lambda.t}dt = \frac{\nu}{\nu+\lambda} \tag{2.33}$$

2.3.2.2.3 Release efficiency The release efficiency, accounting for both diffusion and effusion processes, as a function of the radioisotope decay constant λ is given by [55],[56]:

$$\varepsilon(\lambda) = \frac{3.\tau_{eff}.(coth(W)-1)}{W^2.(\tau_{eff}+\lambda)} \tag{2.34}$$

with $W = \pi.\sqrt{\frac{\lambda}{\mu_D}}$ and *coth* represents the hyperbolic cotangent function.

Equation 2.34 accounts for the diffusion and effusion delay times determined previously through μ_D (Equation 2.26) and τ_{eff} (Equation 2.29). By using Equation 2.34, the total release efficiency for ^{177}Hg was obtained and represented on Figure 2.34 as a function of the diffusion chamber height, for different chamber lengths (l=10 and 20 cm) and different residence times (t_{diff} = 100 and 200 ms). An increase of $\varepsilon(\lambda)$ is observed for a longer diffusion chamber length but a shorter diffusion chambers height, with the highest values obtained for a chamber with 20 cm length and 8 cm height and for a residence time in the diffusion chamber of 200 ms. In this situation (corresponding to a 100 μm radius droplet), the release efficiency is of the order of 34%. **That represents a gain of 18 times in the ^{177}Hg extraction efficiency, in comparison with a static bath geometry used presently at ISOLDE [20].** The increase of $\tau_{release}$ is also favoured by longer residence times as expected from the diffusion delay times.

As a conclusion of this part, the main Figures of Merit required for the development of the LIEBE target are several:

1. Time in the irradiation chamber to be reduced as much as possible (targeted time of 70 ms), which means that the velocity of the LBE inside the container should be maximized,
2. Time of the droplets in the diffusion chamber to be maximized (targeted time of 200 ms) which means that the exit velocity of the droplets out of the grid should be minimized (more details on the chosen solution in Section3.2.1.2,
3. Droplets sizes to be minimized (targeted size of 200 μm diameter),
4. Height of the diffusion chamber to be kept around 8 cm for a total container length of about 20 cm.

The impact of points 1) and 3) on the design is addressed hereafter.

2.3.2.3 Shower and droplets formation

As seen in the previous part (Section 2.3.2.2), the droplets sizes are of major importance in the final yield efficiency of the target. Consequently, it is necessary to propose a design that will allow the formation of LBE droplets as small as possible.

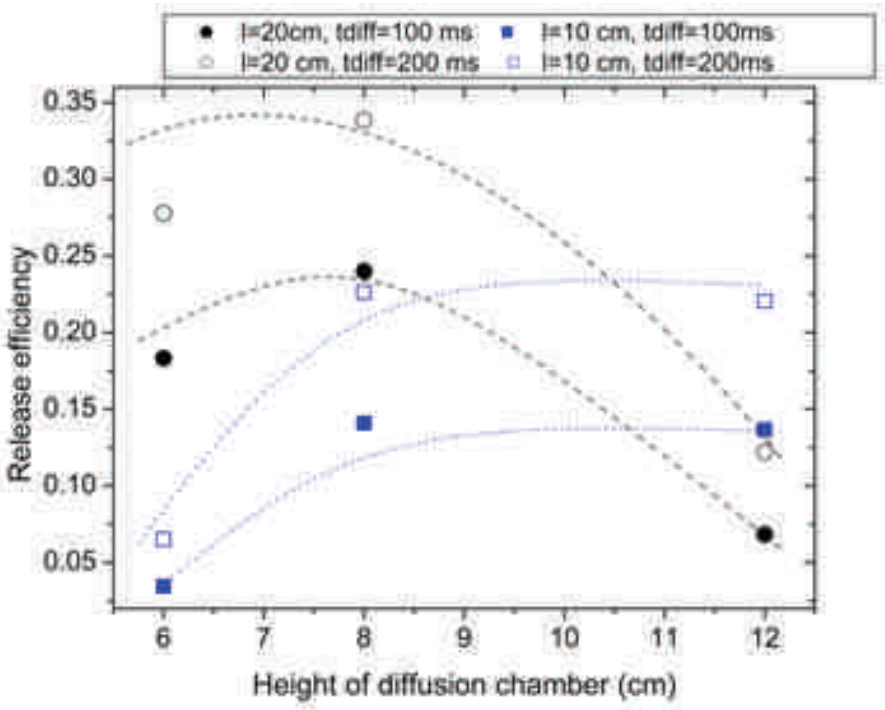

Figure 2.34: Release efficiency for ^{177}Hg as a function of the height of the diffusion chamber with 20 cm (circles) and 10 cm (squares) length and 100 ms (closed symbols) and 200 ms (open symbols) residence times. Lines are guides to the eye

In order to define the parameters to be taken into account in the design as well as the way to optimize them, it is necessary to look more in detail in the theory of breakup of liquid jets [16]. Indeed, by passing through a grid, the LBE will form either jets or droplets.

Discharging a liquid from a nozzle at sufficient large velocity leads to a continuous jet that due to capillary forces breaks into droplets. The formation of droplets by the slow emission of a liquid from a nozzle is characterized by a quasi-static balance between inertial and surface tension forces [16]. The droplet formation mechanism in this regime is called dripping. It is known that the shape of the nozzle opening can dramatically influence the size of the droplets [16]. Droplet formation in the dripping regime typically produces large droplets at low production rates.

When the liquid flow rate is progressively increased and that the liquid velocity v is sufficiently large, the kinetic energy overcomes the surface energy and a continuous liquid jet is formed. The lowest critical velocity for jet formation can be expressed in terms of the Weber number [16]:

$$We = \frac{\rho_l.r.v^2}{\gamma} > 4 \tag{2.35}$$

where ρ_l is the liquid density,r the radius of the created droplet, here considered as the radius of the droplet and γ is the surface tension of the liquid.

The regime where droplets are generated by the spontaneous breakup of the jet is called "dripping". From this regime, the Rayleigh classification as described in Figures 2.35 2.36 can be

applied.

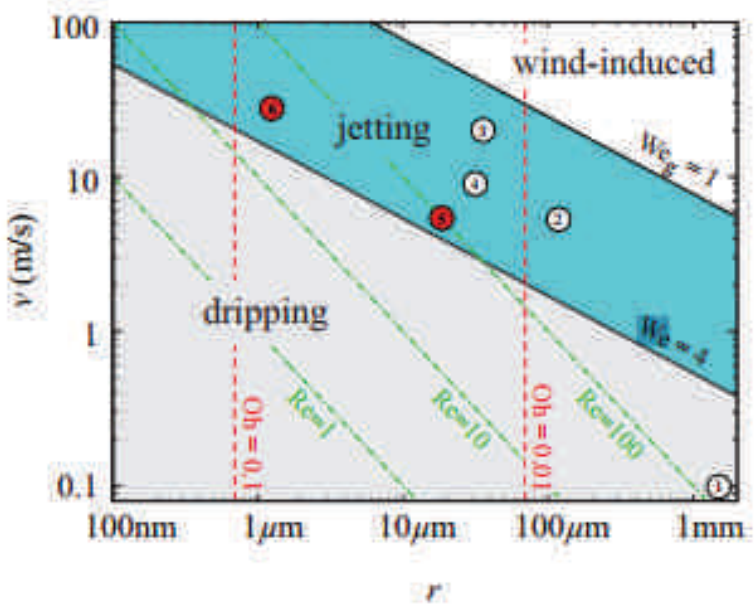

Figure 2.35: Classification of droplet formation regimes - all the lines in the Figure are indicated for pure water [16]

On Figure 2.35, r is the radius of the exit nozzle while v is the exit velocity of the jet.

Four main regimes of formation, which origin from the interplay of inertia of liquid, of surface tension and of forces of aerodynamic acting on the jet, can be identified as described on Figure 2.36:

1. The Rayleigh regime, where both dripping and jetting are described, and where the diameter of the drop d will be higher than the diameter of the nozzle d_0: $d > d_0$
2. The first wind-induced regime, where $d = d_0$
3. The second-wind induced regime, where $d < d_0$
4. The atomization regime, where $d << d_0$.

To minimize the exit velocity out of the grid and thus reach a residence time of 200 ms in the diffusion chamber, the Rayleigh regime will be preferred.

In the Rayleigh regime, two possible situations of drop formation can occur (see Figure 2.35): the dripping, where drops with constant mass periodically detach from the nozzle and the jetting, where the breakup length will linearly increase with the jet velocity till it reaches a maximum and then starts to decrease again. In this case, the produced drops are smaller.

The transition is expected when $\rho.v^2.R_i^2 \geq \gamma.R_i$, i.e. We ≥ 1, according to the definition of the Weber number We given by Equation 2.35.

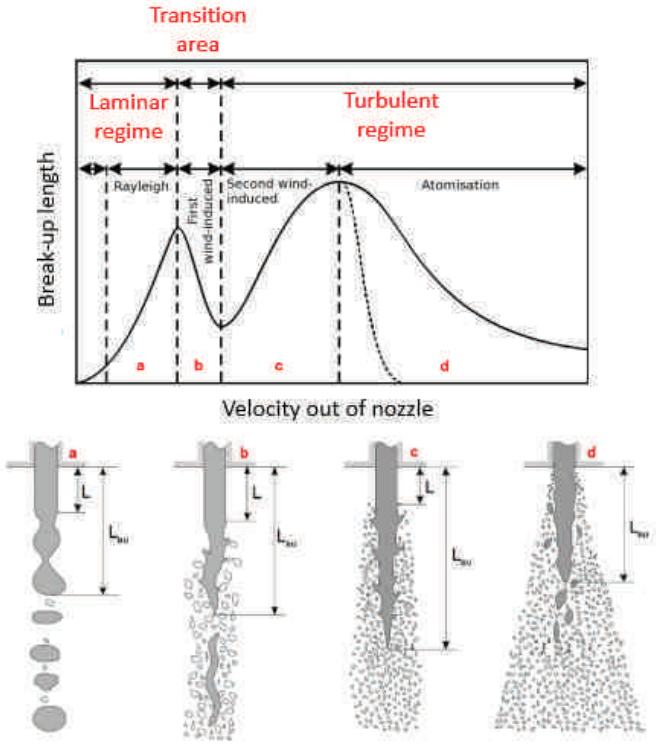

Figure 2.36: Classification of droplet formation regimes [17]

However, it is commonly said that the Weber number must be greater than 4 for the transition between the dripping and jetting transition in case of a liquid (see again Equation 2.35). But this limiting value has been evaluated for water and differs on the fluid properties. In the very specific case of LBE, experimentation should provide the proper Weber number. As a first approach, the transition velocity between the dripping and jetting regimes has been calculated from Equation 2.35 by considering a Weber number of 1 and 4.

The transition between the jetting and the first wind induced regime is the transition from a laminar to a turbulent jet due to the considered fluid velocity. The evaluation of the transition velocity between these two regimes can be estimated from Equation 2.10 considering the Reynolds number limit between a laminar and a turbulent regime of 2 300, and an exit nozzle diameter of 0.1 mm diameter. This diameter has been chosen since it is the minimum diameter achievable on a 1 mm-thick plate of Stainless Steel 316L as it will be seen in the Section 3.2.1.1. These transition velocities are presented on Table 2.18 for LBE at the two lowest and largest operating temperatures 200 ° and 600 °. The LBE properties at these two temperatures can be found in Table 2.1.

The limits velocity are presented in Table 2.18.

From Table 2.18, one can see that even though the properties of LBE vary with temperature, the impact on the transition between dripping to jetting regimes will be negligible while it will be more significant for the transition between the jetting to the first wind induced regimes.

Depending on the regime of droplets formation, the diameter of the droplets will vary. As it is a major parameter in the design and optimization of the LIEBE target, one must evaluate it

	LBE at 200 ∘C	**LBE at 600 ∘C**
$v_{dripping\,to\,jetting}(m/s), We \geq 1$	0.62	0.62
$v_{dripping\,to\,jetting}(m/s), We \geq 8$	1.76	1.75
$v_{jetting\,to\,first\,wind\,induced}\ (m/s)$	5.3	2.7

Table 2.18: Transitions velocities in the Rayleigh regime

for each of the two identified regimes.

In case of the dripping regime, the volume V_0 of the droplet created is defined by [60]:

$$V_0 = \psi.V_p \tag{2.36}$$

where V_p denotes the volume of a pendant drop on which the gravitational force resulting from the density difference between the two environments (air and droplet liquid) and the interfacial surface tension σ are balanced as:

$$V_p = \frac{\pi.D_N.\sigma}{\Delta\rho.g} \tag{2.37}$$

where D_N is the internal diameter of the nozzle and g the gravity acceleration equal to 9.81 m.s^{-1}. The Harkins-Brown correction factor, ψ, is accurately expressed, in the range $D_N(\psi/V_0)^{1/3} \leq 1.4$, by the following correlation [60]:

$$\psi = 0.6 + 0.4[1 - \frac{D_N}{1.4}(\frac{\Delta\rho.g}{\pi.D_N.\sigma})^{1/3}]^2 \tag{2.38}$$

From Equations 2.36, 2.37 and 2.38, an estimation of the droplets volume and consequently of their diameters is possible.

In case of jetting regime, Plateau and Lord Rayleigh proposed a model which is still valid nowadays [25], [16]. A small disturbance introduced by mechanical vibrations or by thermal fluctuations will grow when its wavelength exceeds the circumference of the jet. The optimum wavelength for a non-viscous liquid jet is expressed as $\lambda_{opt} = 2.\sqrt{2}.\pi.r$, with the jet radius r only. The system automatically selects this optimum wavelength and breaks up in fragments of volume:

$$V = \lambda_{opt}.\pi.r^2 \tag{2.39}$$

The calculated diameters of droplets for the two identified regimes are presented in Table 2.19. As the shower is created under vacuum, no second environment is considered for Equation 2.37.

	Dripping regime	**Jetting regime**
Ø$_{droplets}$ **(mm)**	1.3	0.4

Table 2.19: Estimated droplets diameters in case of a 100 μm holes diameter

From these results, it is obvious that it is preferable to be in the jetting regime rather than in the dripping one. However, the fluid exit velocity will have an important impact on the droplets remaining time in the diffusion chamber. Since we have underlined the importance of the remaining time in the diffusion chamber with the conclusive remarks of Section 2.3.2.2.3, (point 1), a compromise must be found. This compromise is studied in the next section.

2.3.2.3.1 Flow rate and velocity out of the grid The optimized time in the container has been set at 70 ms (refer again to point 1 at the end of the Section 2.3.2.2.3). This means than the optimized flow rate Q will be defined once the container volume $V_{container}$ is defined and known:

$$Q = \frac{V_{container}}{t} \tag{2.40}$$

Additionally, by considering the height of the diffusion chamber $h_{diff.chamber}$, the exit velocity out of the grid can be estimated with respect to the time t in the diffusion chamber:

$$h_{diff.chamber} = \frac{1}{2}.g.t^2 + v_{out}.t \tag{2.41}$$

This corresponds to a free fall of a body with an initial velocity v_{out}. As the droplets fall will be under vacuum, no buoyancy has been considered.

According to Figure 2.34, it has been established that the optimized height for the diffusion chamber would be 8 cm. Since the maximum height available is 12 cm, the time in the diffusion chamber in function of the outlet velocity is shown on Figure 2.37 for these two heights. The two Weber limits identified in the previous part for the shower regime are indicated as well by the two vertical lines.

From this Figure, it is obvious than the lower the outlet velocity, the higher the time in the diffusion chamber.

Knowing that the container must be empty in 70 ms (as a targeted time), the outlet velocity out of the grid can then be estimated from Equation 2.40 in function of the grid parameters:

$$v_{out} = \frac{V_{container}}{S_{holes}.t} \tag{2.42}$$

with S_{holes} the total surface area covered by the holes. This will obviously depend upon the number of holes in the grid and their diameter, which means it will also depend upon the spacing between each of them. This brings new Figures of merit:

- The regime of the shower that should be preferably the jetting one,
- The holes diameter should be reduced as much as possible while keeping the mechanical integrity of the grid (a targeted diameter of 0.1 mm diameter has been chosen in a first place),

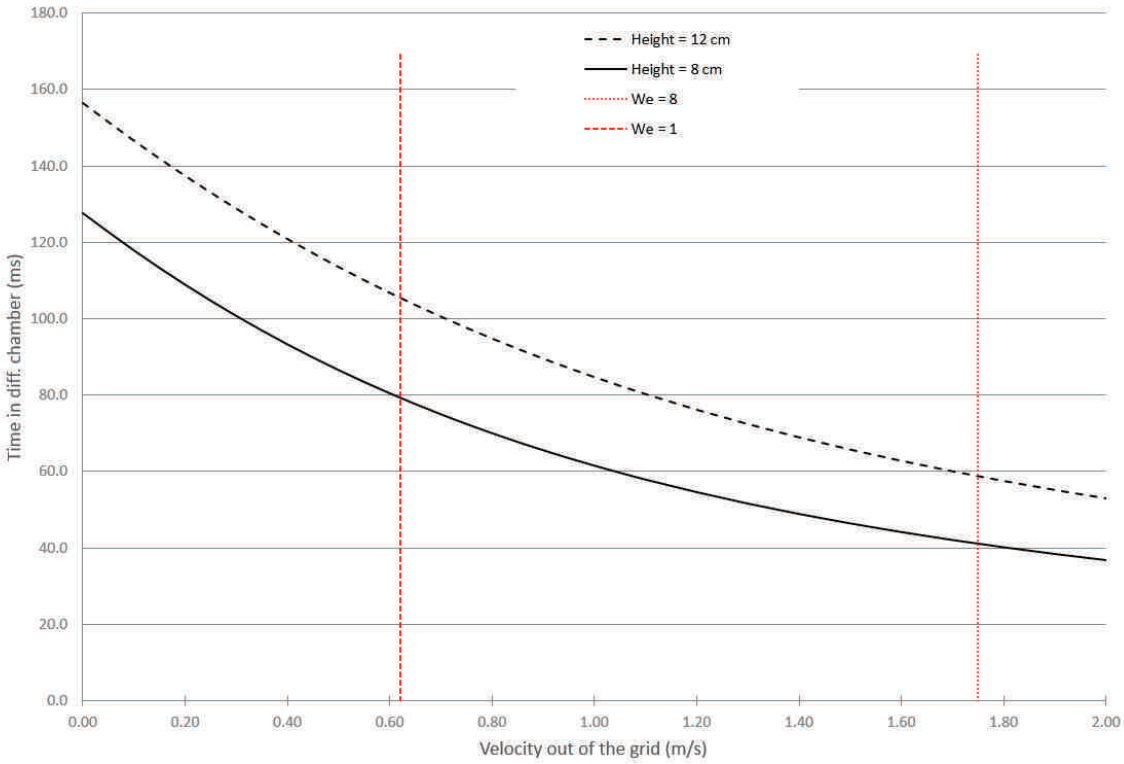

Figure 2.37: Time in diffusion chamber in function of outlet velocity

- The flow rate and the container design should be designed in agreement so that the time to empty it does not exceed the 70 ms targeted while the surface covered by the holes should be maximized in order to minimize the exit velocity out of the grid.

For a better understanding of the impact of each of the design parameters, a schematic representation is presented in Figure 2.38.

Three mains parts will impact the droplets formation:

- The container which should be emptied as fast as possible,
- The grid parameters
- The diffusion chamber dimensions, mainly its height.

Indeed, it has been shown that the jetting regime produces smaller droplets than the dripping regime. This induces a minimum velocity for the droplets at the exit of the grid. Depending on the grid parameters (mainly, the total surface covered by holes), a minimal flow rate will then be fixed. This flow rate will impact on the time to empty completely the irradiation chamber in function of its volume. Finally, the set of theses parameters should be optimized for isotope release efficiency as shown in the Section 2.3.2.2.

With a 0.1 mm holes diameter, the smallest droplets size achievable has been estimated to be 0.4 mm (cf Table 2.19). This gives a minimum inter holes spacing of 0.4 mm and thus a

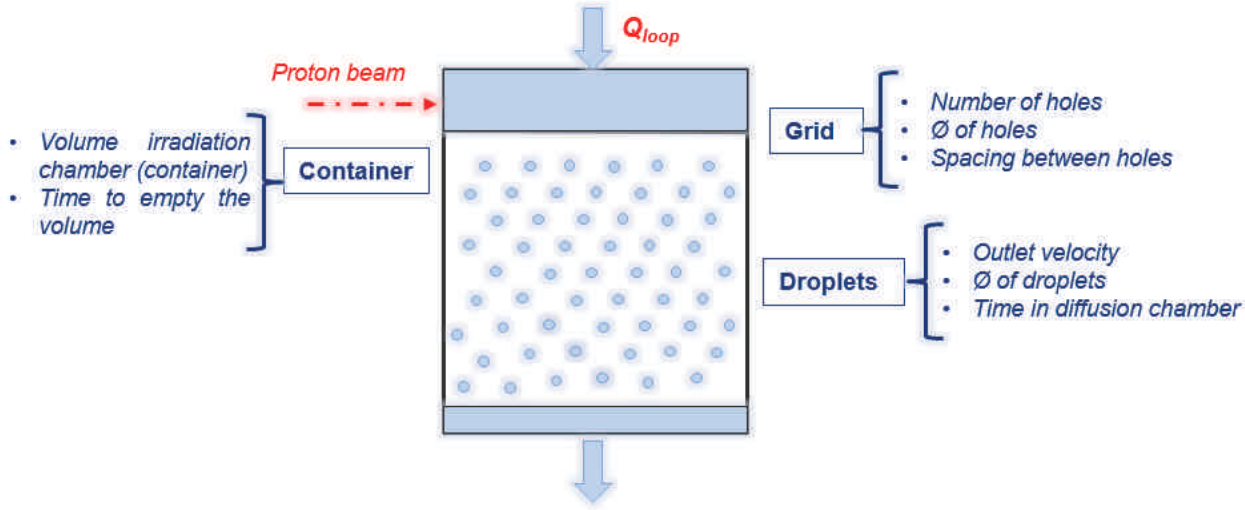

Figure 2.38: Parameters impacting onto the droplets formation - schematic layout

spacing between holes of 0.3 mm as it can be seen in Figure 2.39. This would be in an ideal case, assuming that the droplets are not merging when they are touching each other. This has been studied experimentally and results will be presented in the last chapter of this thesis.

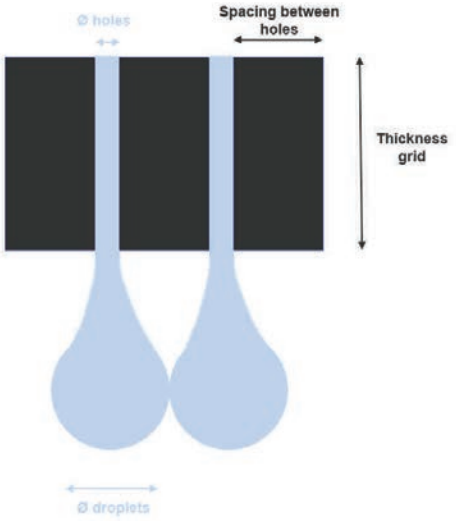

Figure 2.39: Droplets formation in the most optimized case (spacing between holes as small as possible)

Let's consider two spacing between holes to assess its impact on the target parameters. For this, a flat plate of 200 mm long (the advised length as from Section 2.3.2.2) and of width 20 mm (the width of standard targets). The grids parameters in these two cases are summarized in Table 2.20.

The ratio of number of holes between the case number 1 and 2 is 2.25 i.e. for the same volume and with a constant flow rate, the irradiation chamber could be emptied 2.25 times faster with

Case number	Spacing between holes	Number of holes
1	0.3	25 000
2	0.5	11 111

Table 2.20: Grid parameters for two spacing between holes - examples

the case 1. This also means that the flow rate would be 2.25 times faster in the case 1 to achieve the same delay to completely empty the irradiation chamber.

It is obvious that the higher the number of holes in the grid, the higher the release efficiency in the target will be. This is a key parameter of the target.

Furthermore, considering the need of a high outlet velocity for the droplets, the concept 2 presented in the section 2.2.2 is no longer valid and the concept 1 appears to be the best considering the different constraints and required parameters. As a reminder, the concept 3 had been discarded as it would not have ensured enough excess pressure at the inlet of the pump to avoid cavitation.

2.4 Conclusion on design constraints

This development of a high power target should allow a better release and consequently a higher yield of short-lives species. This brings many constraints on the design and it is difficult to accommodate all of them together.

A first hydraulic analysis (Section 2.3.1) highlighted some design possible constraints. Actually, since the planned target in a metal liquid one (Lead Bismuth Eutectic - LBE), it is mandatory to use a specific pump for liquid metal which delivers a maximum pressure of 2 bars:

- Maximum pressure losses in the loop of 2 bars which imply that it is better to avoid sharp changes in the geometry (valves, Te shape)
- The pipe diameter for the LBE circulation should be chosen consequently.

Furthermore, a detailed thermal study (Section 2.3.1.2) allowed the determination of the key design constraints to reduce the power losses. Indeed, it has been highlighted the fact that the design should tend toward a as-good-as-possible insulation solution. This induces the need of a careful choice for the following elements:

- The pipe diameter,
- The type of insulator (thickness, thermal conductivity and emissivity value),

This detailed thermal study was completed by the analysis of the effect of the target design on the production of short-lived species (Section 2.3.2.2) which is the ultimate goal of this PhD dissertation. Many points were addressed in this section as:

- The influence of the temperature on the diffusion coefficient,
- The influence of the temperature on the sticking time of the radioisotopes,
- The influence of the residence time in the diffusion chamber and the droplets radius on the release efficiency,

These new points allowed, completed by a droplet formation analysis, allowed to define the followings:

- The preferred regime is the jetting one, i.e. the exit velocity of the droplets should be at least 1.76 m/s,
- The diameter of the holes should be minimized,
- The total surface covered by the holes should be optimized in a way that it does not weakened the grid while it allows a fast emptying of the irradiation chamber.

Some optimized values for all these design parameters have been proposed and the feasibility and design proposal will fix some of them. The design will have to propose the best solution taking into account all theses constraints.

The pre-concept proposed that will address the best all of them is the pre-concept 1 (Section 2.2.2) and consequently, it is the one that will be further developed in the next chapter of this manuscript.

The third chapter will present the developed design, using the tools developed in this chapter 2. The design has been validated through numerical tools as well, as it will be seen. Finally, a shower assessment experiment has been conducted at Cern and will be presented in the last Chapter, defining precisely the minimum space between holes that allows separated droplets formation and validated the droplets dimensions.

Chapter 3

The LIEBE target: a new generation of ISOL target

3.1 General overview of the proposed LIEBE target design

The aim of the Liquid Eutectic Lead Bismuth Loop Target for Eurisol (LIEBE) is to prove the feasibility of a high power target able to produce an intense secondary beam of short-lived isotopes. The concept chosen for the design of this target has been presented in the previous chapter, and implement the different necessary elements:

- An irradiation chamber, or container, where the beam will impact,
- A diffusion chamber, in which a shower is created through a mesh or grid positioned at the exit of the irradiation chamber,
- An heat exchanger (HEX) to extract the power brought by the beam,
- A pump to make the LBE circulation,
- A recuperation tank to fill and empty the loop,
- All the elements for the monitoring and heating of the target,
- All the elements for the secondary beam extraction towards the post-accelerated line such as the temperature regulated transfer line and the ion source.

Taking into account all the constraints related to the environment as well as the main issues addressed previously, and using the tools developed in Chapter 2, a design has been proposed and further elaborated.

The proposed design is made up of two parts: a main loop in which the LBE is kept in a double envelop for safety issues and a pump/engine part with the rotating elements and engine of the pump as presented in Figure 3.1 and 3.2.

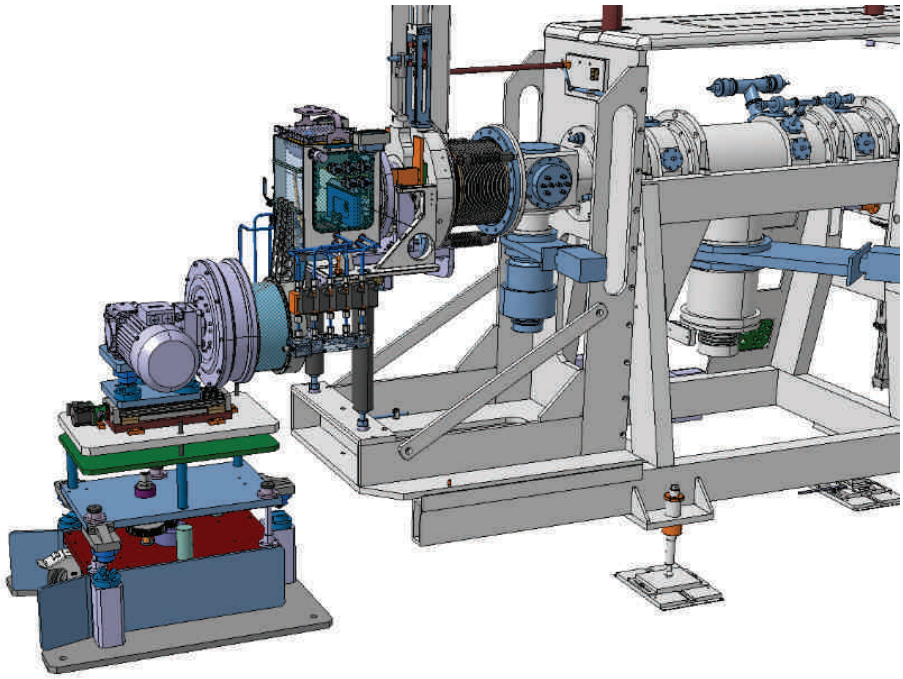

Figure 3.1: LIEBE target, unplugged position

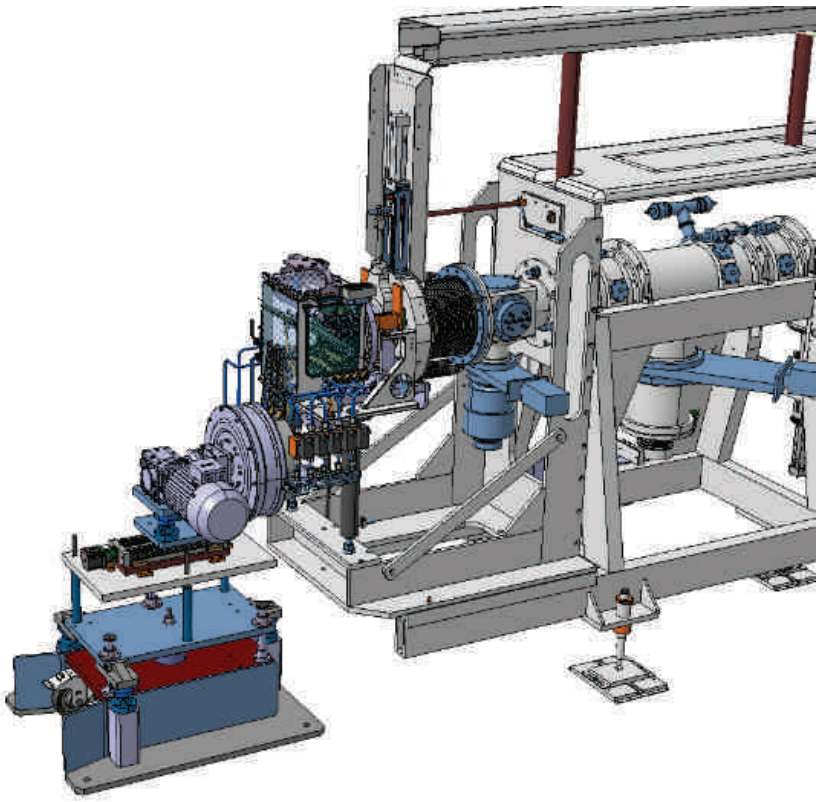

Figure 3.2: LIEBE target, plugged position

Both parts must be compatible with the ISOLDE robot as the coupling and decoupling operation of the target will be done remotely for most steps (see Appendix B).

The main loop will be brought first and coupled to the ISOLDE front end, then the pump/engine will be brought and coupled to the main loop. This strategy of two parts have been adopted in order to maintain the double envelop around the LBE while respecting the weight constraints imposed by the characteristics of the remote handling system.

All the elements in contact with LBE such as the pipes of the pump, the pipes of the loop itself, the heat exchanger, the irradiation and diffusion chambers but also the elements for filling and emptying the loop are the first barrier and must be confined inside this envelope. It means that, in case of failure of the loop or of any of its elements, the LBE will remain confined and will not pollute the ISOLDE front end.

The main loop is presented in more details in Figures 3.3 and 3.4.

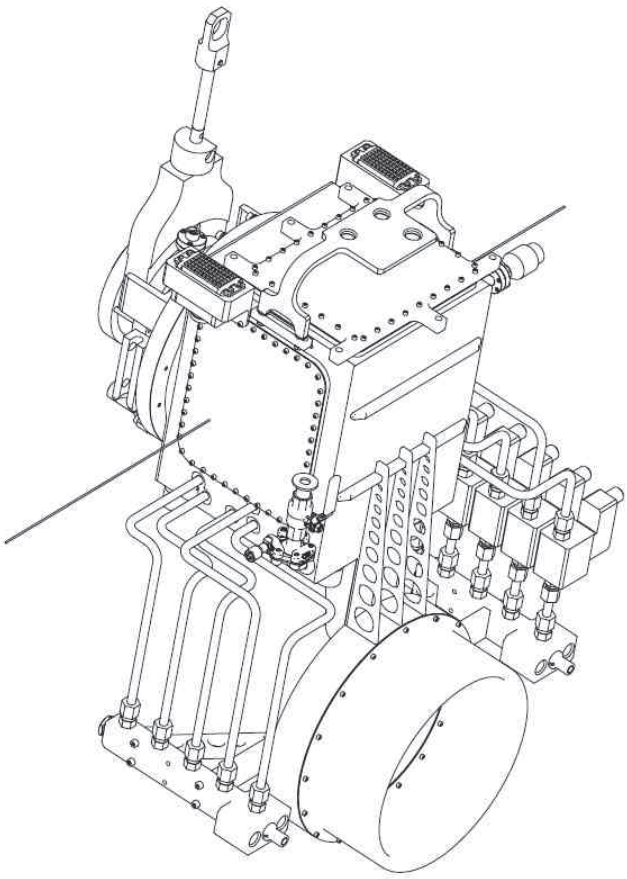

Figure 3.3: LIEBE target, main loop part - general view

The pipe internal diameter is fixed at 10 mm to provide a reduction of about 35% of weight when compared to the 17 mm internal diameter while pressure losses are still compatible with the proposed pump, as shown in Chapter 3.3.1.1.

The heating will be done with 3 heating elements wrapped around the pipes while insulating elements will cover them.

The design of the LIEBE target is based on the design of the standard ISOLDE unit. Consequently, the part that will allow the coupling with the front end as well as the ion source are

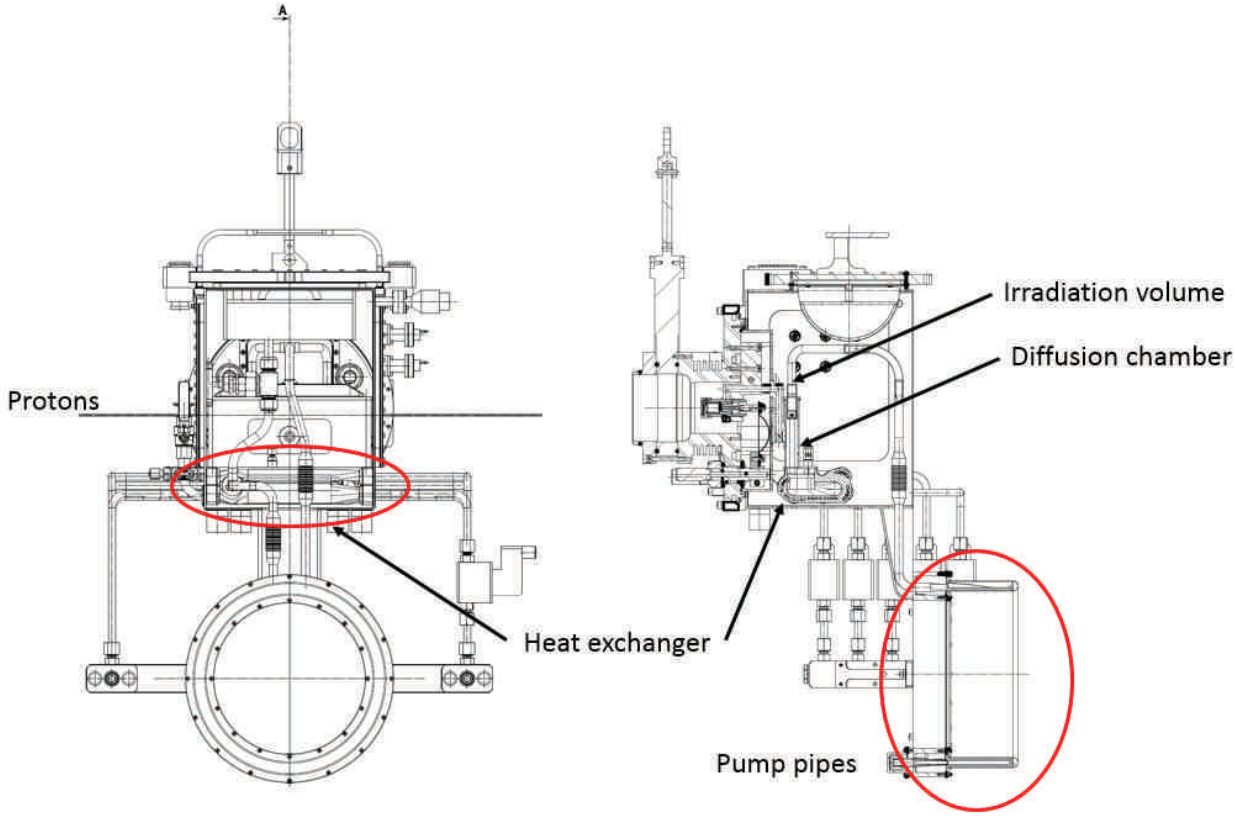

Figure 3.4: LIEBE target, main loop part - inside view

not modified.

The exit of the irradiation volume (container) is located inside the diffusion chamber to minimize the path followed by the isotopes before their extraction from the LBE. At the exit of the diffusion chamber, the Heat Exchanger (HEX) will regulate the temperature. It has been placed before the inlet of the pump to ensure the lowest possible temperature in the channels of the pump.

A filling tank is planned in order to fill the target once it is installed in the front end. No draining tank is foreseen in this design since it would require additional electro valves that would add additional complexity and pose a reliability issue. However, a manual valve to drain the loop at the lowest point of the target in the pump channel will allow emptying the target for the off-line test phase.

The target will then be vented with Argon to prevent air exposition and oxidation of the LBE. A filter is also incorporated to prevent a major clogging of the exit grid (see part 3.2.1 for more details).

The pump/engine part is made up of a trolley that will be plugged with the main loop part by sliding on a horizontal movement thanks a rail as seen in Figure 3.5. This trolley supports the magnets of the pump and the engine use to rotate them. The system allowing the coupling of this part with the main loop part is implemented as well.

The design of the pump (detailed view on Figure 3.6) has been developed by the Institute of Physics of University of Latvia (IPUL). The magnets of the pump will come around the flat

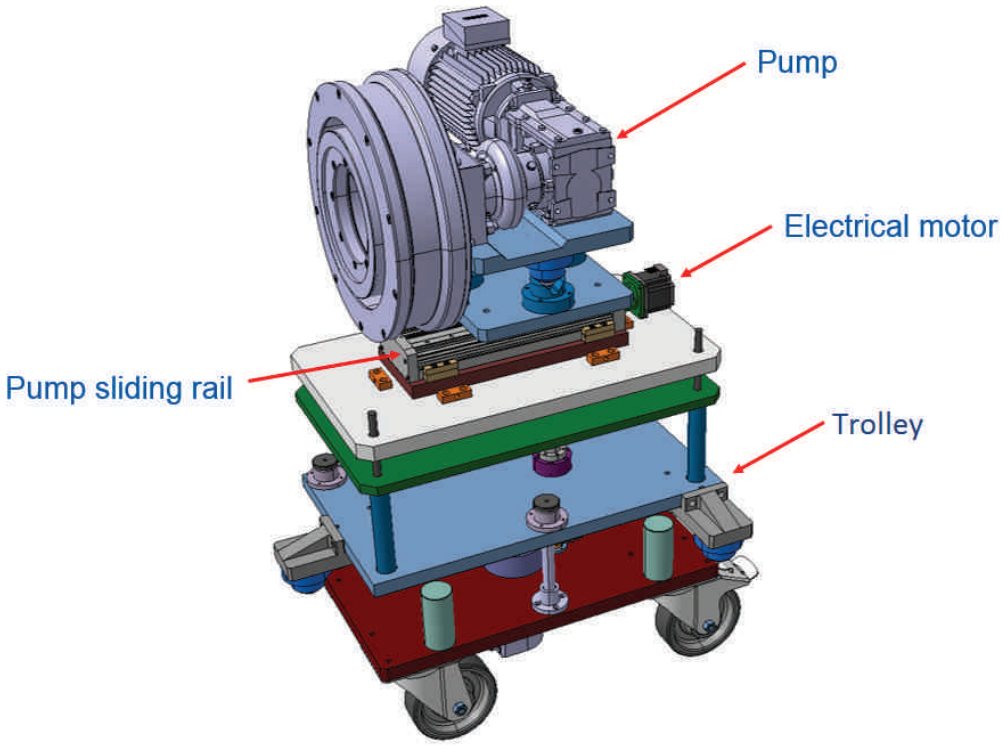

Figure 3.5: Pump/engine part of the LIEBE target

channel of the target, at the pump position, as seen in Figure 3.7. A double enclosure will come around the channel to ensure the containment with a space of 4 mm between the double enclosure and the rotating magnets and an internal gap of 2 mm between the double enclosure and the channel. Additionally, as cavitation must be avoided, a minimum height (NSPH) of 7 cm has been computed. In this design, 12 cm are provided, giving a safety margin of about 70 %.

Each of the constituting elements of the target will be presented in details in the coming sections. The choice of their design will be justified through analytical as well as numerical analysis when required.

One of the main design parameters of the loop is the flow rate which directly depends upon the diameters and total surface covered by the holes of the grid as seen in part 2.3.2.3. Consequently, the first part of this chapter will focus on the specific elements of a target in order to optimize the yield of short-lived isotopes secondary beams. In a second time, the design of the elements related to the development of a target dealing with high beam power will be next developed.

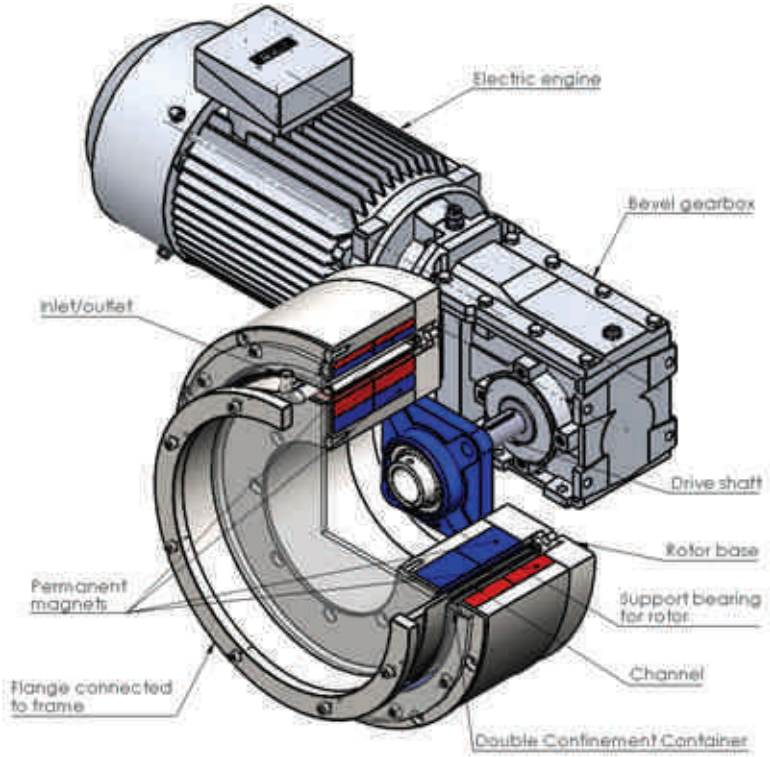

Figure 3.6: Pump of the LIEBE target

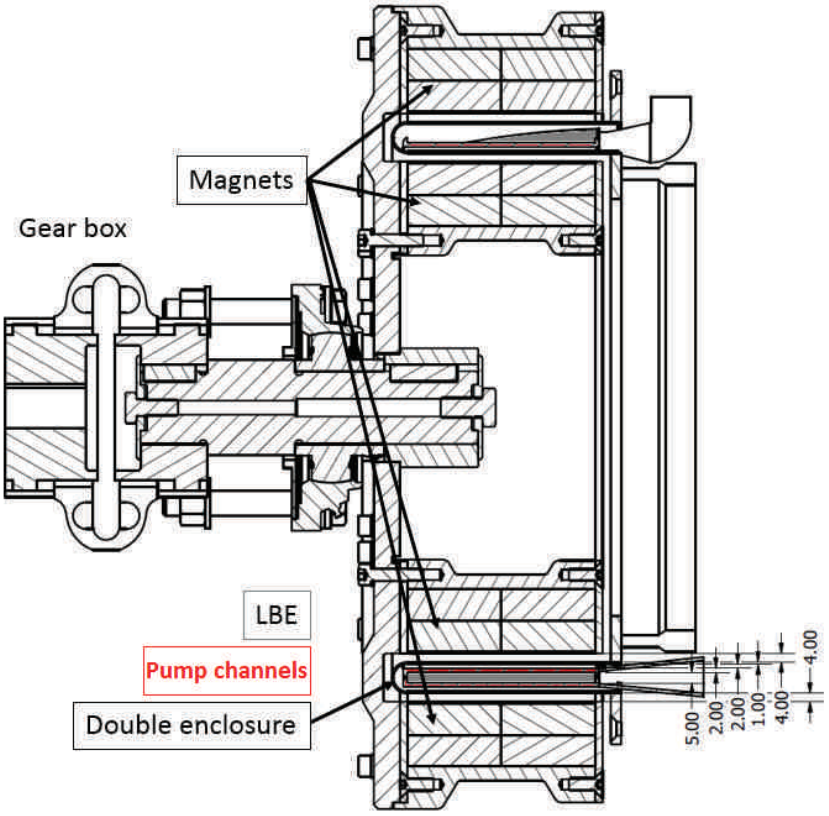

Figure 3.7: Channels pipes inside the double enclosure and magnets

3.2 Optimization of the yield of short half-life species secondary beam

3.2.1 Container and diffusion chamber of the LIEBE target and grid definition

The irradiation chamber (located inside the diffusion chamber, see Figure 3.4) has been developed in Belgium by the StudieCentrum voor Kernenergie (SCK-CEN). Some details of the design are presented on Figure 3.8.

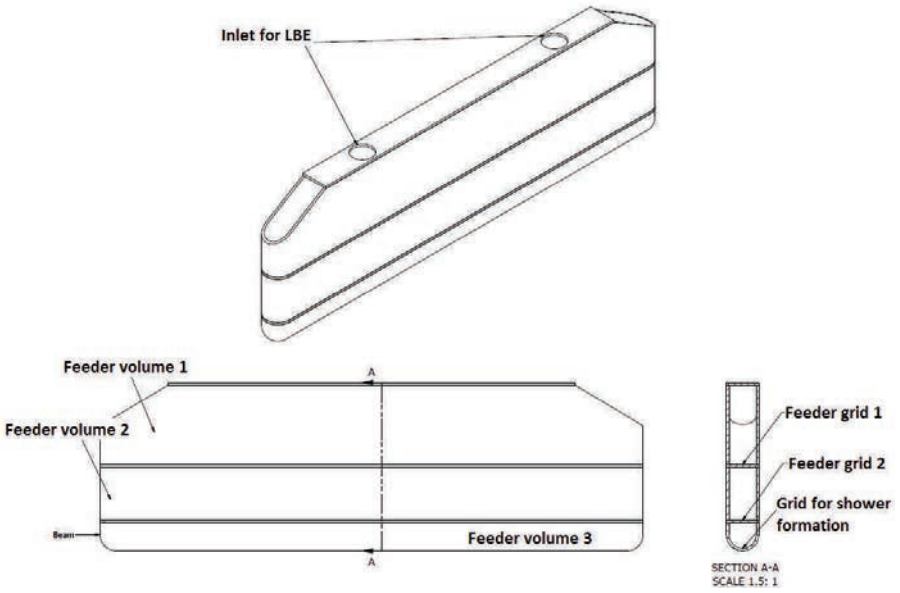

Figure 3.8: Detailed design of the irradiation chamber

The irradiation chamber is made up of three feeder volumes separated by two grids. The total internal length is 210 mm which represents 10 mm more than the standard ISOLDE target. The target width is 10 mm which is half of the standard ISOLDE targets. The beam window is here represented by a half cylinder shape in order to avoid any sharp angle that would accumulate stresses and represent a risk of failure due to shock waves from the beam impact. In the same time, the LBE flow is not disturbed by this beam window.

The two intermediate grids serve for a better distribution of the LBE flow thereby leading to a more uniform distribution of evacuation-velocity vectors at the outlet of the irradiation volume while acting as filters. This should ensure that no particles (LBE oxide for example) would come and obstruct the grid for the shower formation.

In the proposed design, the holes diameters are the same on all grids.

Two designs have been studied: a half-cylinder shape and a flat plate as shown in Figure 3.9 where only the right half-part of the shower is represented. The holes diameters are the same in both designs. In the final design, the grid is flat.

The grid shape 1 would allow a higher surface of plate inducing a higher number of holes and thus a higher surface covered by the holes. This means that a lower velocity of the droplets

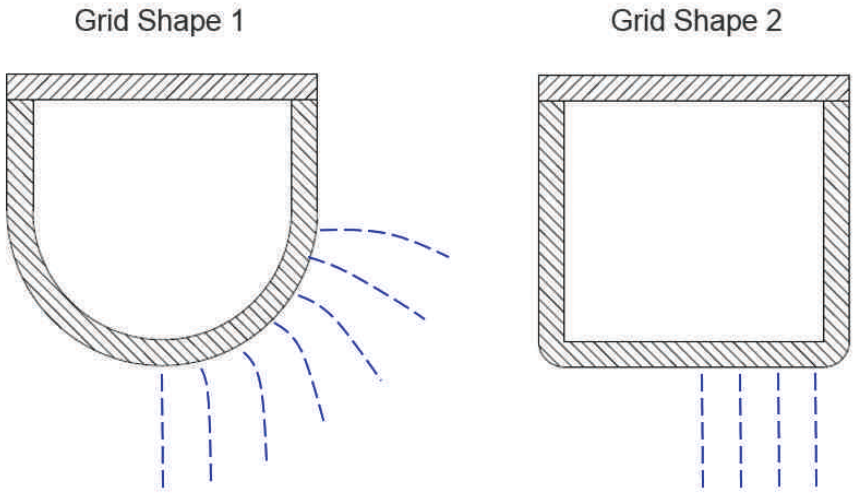

Figure 3.9: Two studied designs for at grid serving to the shower formation

would be reached for a given flow rate. Indeed, as expressed by Equation 2.42, the outlet velocity will depend upon the total surface covered by the holes as well as the flow rate inside the loop.

However, the shower created in that case will need a bigger diffusion volume as the jets will be created with variable angles. Furthermore, it has been estimated that, in order to be in the jetting regime with smaller droplets, the minimum velocity should be 0.62 m/s (part 2.3.2.3). The trajectory of the jets have been estimated for this minimal velocity of 0.62 m/s (cf Figure 3.10).

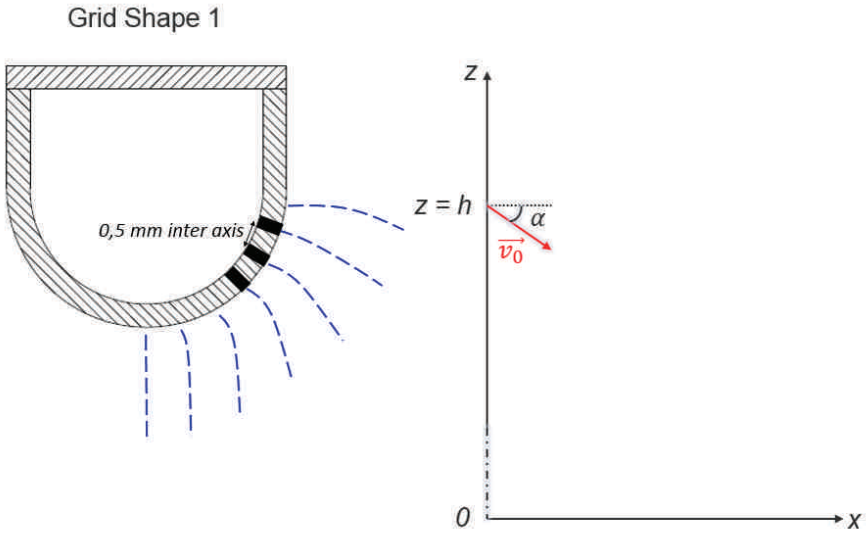

Figure 3.10: Schematic of the jets directions

Once the droplets are created, they are submitted to gravity force. By making the projection of the force onto the two axes, one can express the Equation of the trajectory *z(x)* [61]:

$$z(x) = -\frac{1}{2}g\frac{x^2}{{v_0}^2.cos^2(\alpha)} - x.tan(\alpha) + h \tag{3.1}$$

with g the gravitational constant, v_0 the initial velocity of the droplets and h the starting height of the droplets. To simplify the study, all droplets have been considered with the same starting height of 80 mm.

Taking the minimum spacing achievable between each holes (see part 4.2.2), the angle between two consecutive holes has been estimated at 4.75 °.

The result is shown on Figure 3.11.

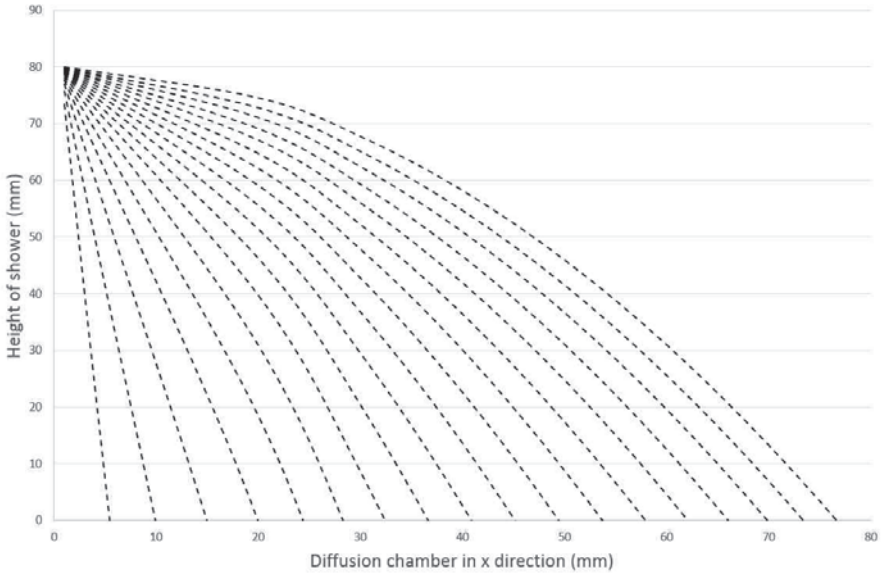

Figure 3.11: Jets trajectory for a velocity of 0.6 m/s out of the grid

A minimum distance of 76 mm (for an height of 80 mm) is required in order not to loose any droplets on the diffusion chamber walls before reaching the bottom part or a total width of 164 mm with the dimension of the irradiation chamber of 12 mm. This is not acceptable as the effusion efficiency would drastically drop for such an important volume. Indeed, as seen previously in Figure 2.33, the larger the volume of the diffusion chamber, the lower the effusion efficiency. Consequently, the design is chosen as a flat grid.

3.2.1.1 Grid parameters

Tests have been conducted in order to assess the minimum holes diameter that can be possibly manufactured on a 1 mm-thickness Stainless Steel plate (refer to Section 4.2.2). Experiments have shown that a 0.1 mm diameter can be drilled onto a 1 mm-thickness plate using laser. Furthermore, an experiment has been conducted with LBE in order to assess the minimum spacing between holes that will allow a shower formation. As it will be seen in Section 4.2.2 of the forthcoming Chapter 4, the inter axis spacing is 0.5 mm. A summary of the grid parameters can be found in Table 3.1.

From the proposed design, the irradiated volume will be equivalent to the feeder volume 3 (see Figure 3.8). As defined in part 2.3.2.2, the time required to empty this volume should tend toward 70 ms while the exit velocity should be minimized for the droplets to remain in the diffusion chamber for a targeted time of 100 ms. These optimal times directly depend upon the grid parameters.

Parameters	Units	Values
Grid material		Stainless Steel 316L
Grid thickness	mm	1
Holes diameters	mm	0.1
Inter axis spacing	mm	0.5

Table 3.1: Main parameters for the grid

In order to have a better velocity streamlines repartition, all grids of the irradiation chamber will have the same parameters. Knowing the achievable spacing for the holes and the exact geometry, it comes an immediate calculation of the surface covered by the holes. The volume of the feeder volume 3 as well as the surface covered by the holes are summarized in Table 3.2.

Parameters	Units	Values
Feeder volume 3	mm^3	20 785
Number of holes		8 314
Surface covered by the holes	mm^2	65
% covered by holes	%	3.2

Table 3.2: Parameters for release calculation

3.2.1.2 Release calculation and impact on design

It has been shown in part 2.3.2.3 that, for a 100 μm hole diameter, the created droplets will be of 0.4 mm diameter in jetting regime and 1.3 mm diameter in dripping regime. By using Equation 2.24 established in part 2.3.2.2, the diffusion released fraction can be plotted in function of the time needed to empty the irradiation chamber and in function of the residence time of the droplets inside the diffusion chamber (see Figure 3.12).

On Figure 3.12, one can see that the diffusion release efficiency is the highest for short time in irradiation chamber and long time in diffusion chamber. Furthermore, a difference of 4 is seen between the peak of diffusion release efficiency with 0.4 mm diameter droplets and with 1.3 mm droplets. As it will be seen in part 4, the jetting regime is ensured for a velocity higher than 1.76 m/s. Consequently, this is the minimum velocity required for the target design.

Equation 2.42 in part 2.3.2.3.1 shows that the time to empty the irradiation chamber and the time during which the droplets will remain in the diffusion chamber are dependent upon the surface covered by the holes and the flow rate. As well, it is shown on Figure 3.12 that the time that will have the highest impact on the release efficiency is the time inside the diffusion chamber.

Applying Equation 2.33 together with Equation 2.27, one can compute the total release efficiency taking into account the diffusion and the effusion processes (Figure 3.13).

Furthermore, it is possible to plot the time in the irradiation chamber and in the diffusion chamber depending on the outlet velocity of the droplets by using Equations 2.40 and 2.42 as shown on Figure 3.14.

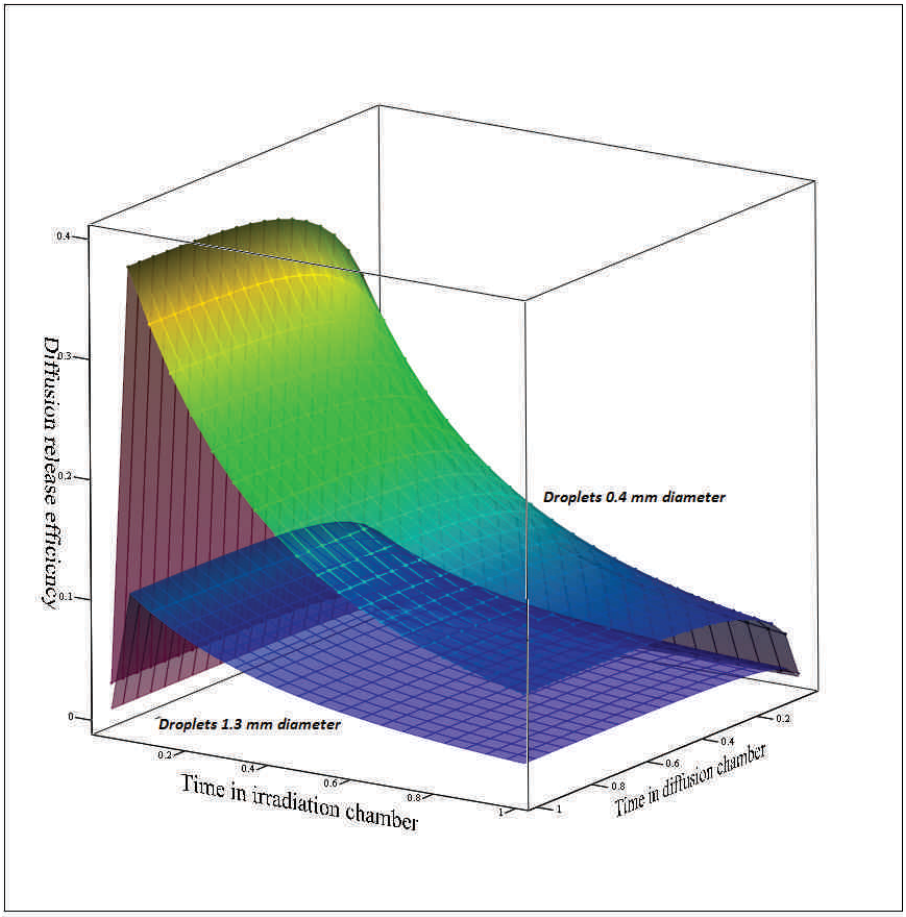

Figure 3.12: Diffusion release efficiency for 0.4 mm and 1.3 mm droplets diameters

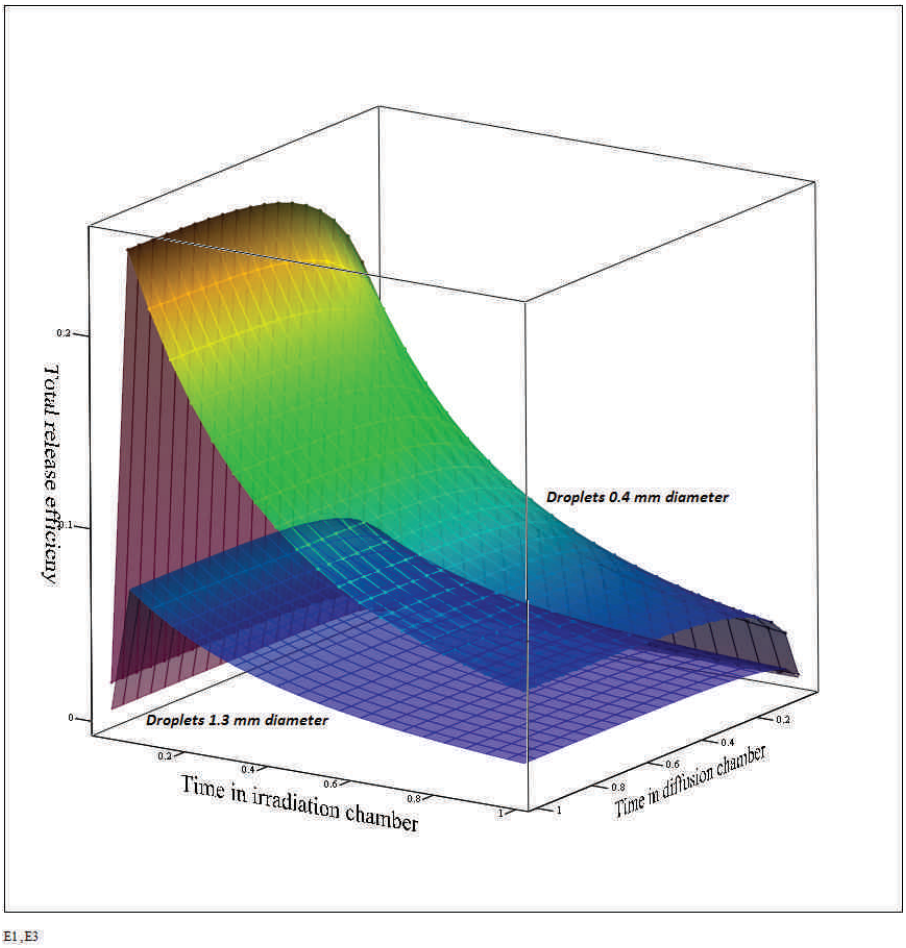

Figure 3.13: Total release efficiency for 0.4 mm and 1.3 mm droplets diameters

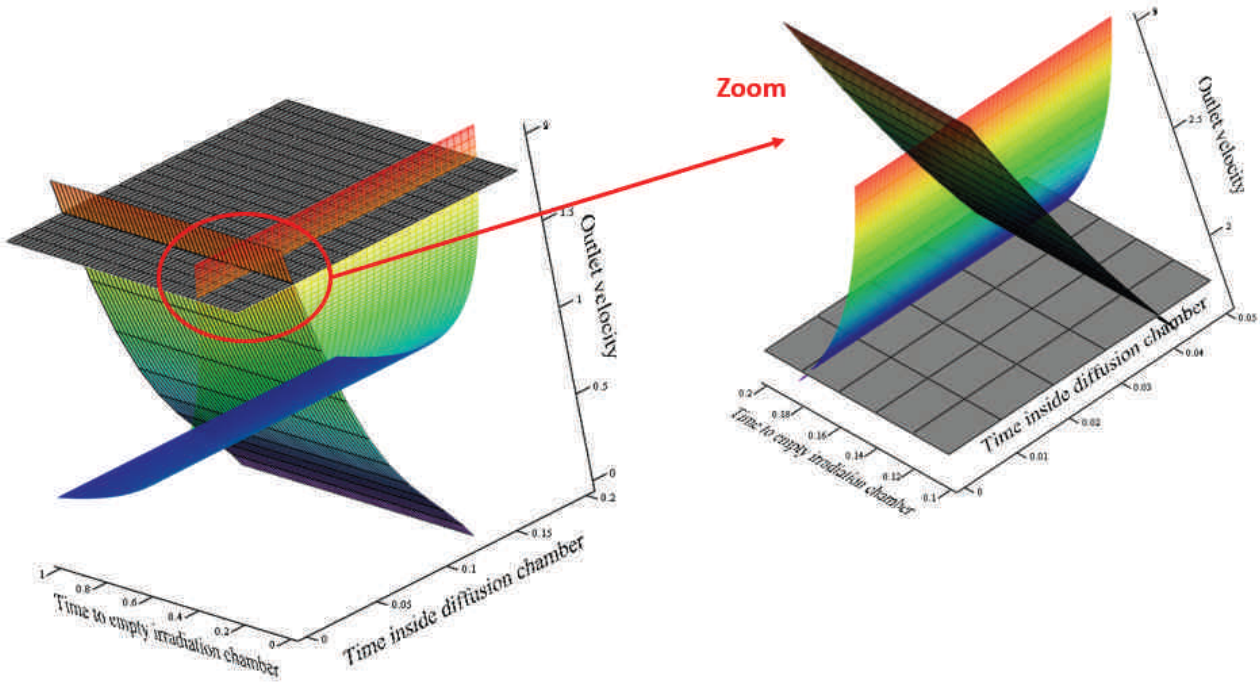

Figure 3.14: Velocity of the droplets in function of time to empty the irradiation chamber and time in the diffusion chamber

Considering the minimum required velocity of 1.76 m/s, one can zoom in Figure. To estimate properly the final release for velocity higher than 1.76 m/s, three velocities have been considered: 2 m/s, 2.5 m/s and 3 m/s. The values of time and release in all three cases are summarized in Table 3.3.

Velocity of the droplets	**Time to empty irradiation chamber**	**Residence time in the diffusion chamber**	**Total release efficiency**
2 m/s	160 ms	36 ms	8.2 %
2.5 m/s	128 ms	30 ms	8.1 %
3 m/s	107 ms	25 ms	7.8 %

Table 3.3: Total release efficiencies for different flow rate configurations

However, this estimation considers that from *t=0 sec*, 100 % of the isotopes start to diffuse. This is not correct as the beam shape is Gaussian and thus, not 100 % of the produced isotopes will be located at the grid part. It is possible to estimate the percentage of beam intensity or beam particles that will be inside the diffusion chamber for different velocities as shown in Figure 3.15.

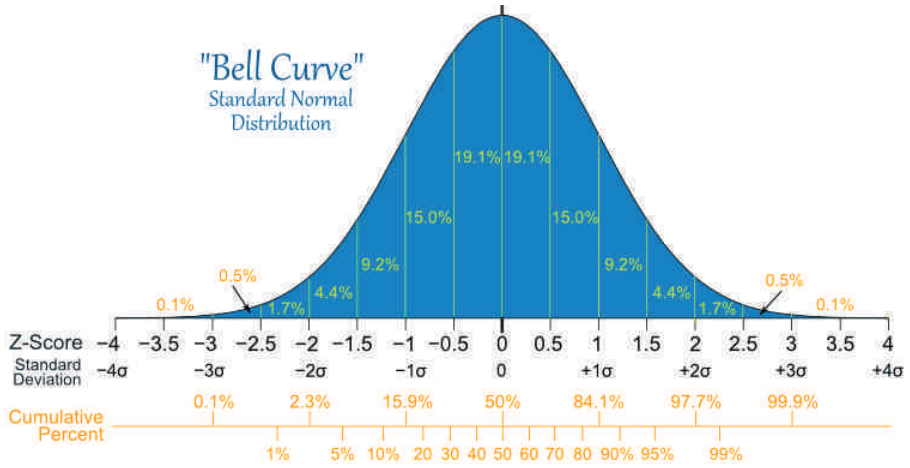

Figure 3.15: Gaussian or normal distribution - beam distribution

Considering the geometry of the feeder volume 3, where the beam impact will occur, and making a 2D projection of the beam gaussian distribution as shown in Figure 3.16, it is possible to estimate precisely the percentage of beam that will be evacuated to the diffusion chamber in function of time for a defined velocity.

The normal distribution function $\Phi(z)$ gives the probability that a standard normal variates assuming a value in the interval [0,z] [62]:

$$\Phi(z) = \frac{1}{2}[1 + erf(\frac{\frac{3.\sigma}{2} - x}{\sigma.\sqrt{2}})] \tag{3.2}$$

where *erf* is the error function.

In order to estimate the percentage of beam evacuated toward the diffusion chamber, four steps must be followed:

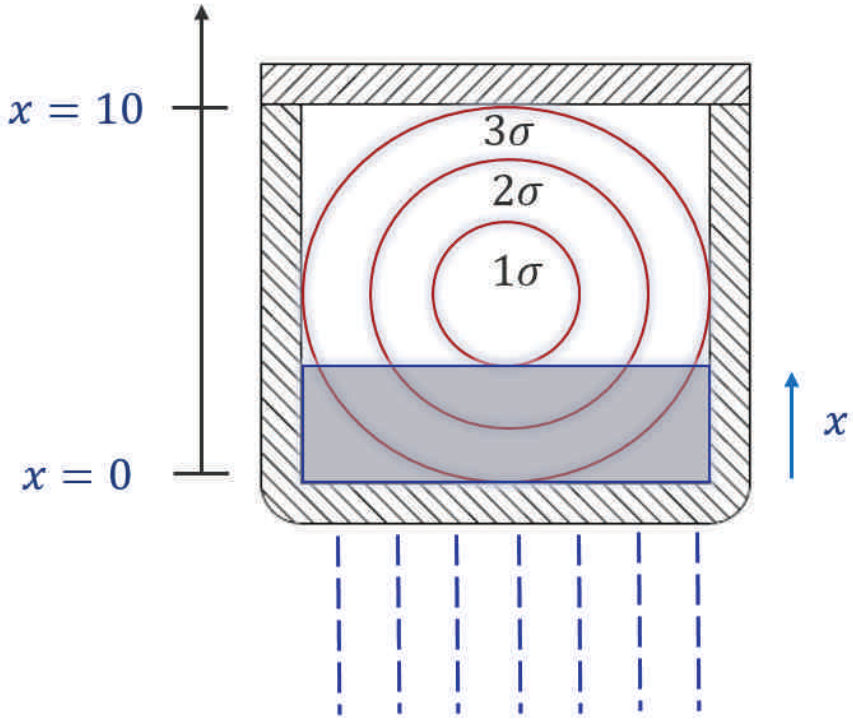

Figure 3.16: Gaussian or normal distribution applied onto the irradiation chamber - 2D view

1. Estimation of the percentage P_1 of beam included in the considered area for each x varying from 0 up to 3σ - that would give the percentage of beam in the rectangular considered (blue area in Figure 3.17):

$$P_1 = 1 - \frac{1}{2}(1 + erf(\frac{\frac{3.\sigma}{2} - x}{\sigma.\sqrt{2}})) \tag{3.3}$$

2. Estimation of the percentage P_2 of area of the "washer shape" that will be evacuated (intersection overlap of the blue and red surfaces in Figure 3.17).

   (a) Calculation of the total area S of the "washer shape" (red area) :

$$S = \pi.(\frac{(3.\sigma)^2}{4} - x^2) \tag{3.4}$$

   (b) Calculation of the segment area S_1 (intersection of the red and blue area):

$$S_1 = \frac{R^2}{2}.(\Theta - sin.\Theta) \quad \text{with} \tag{3.5}$$

$$R = \frac{3.\sigma}{2} \quad \text{and} \tag{3.6}$$

$$\Theta = cos^{-1}(\frac{h}{\frac{3.\sigma}{2}}) \quad \text{and} \tag{3.7}$$

$$h = \frac{3.\sigma}{2} - x \quad \text{for} \quad x \in [0;5] \quad \text{and} \quad h = \frac{3.\sigma}{2} + x \quad \text{for} \quad x \in [5;10] \tag{3.8}$$

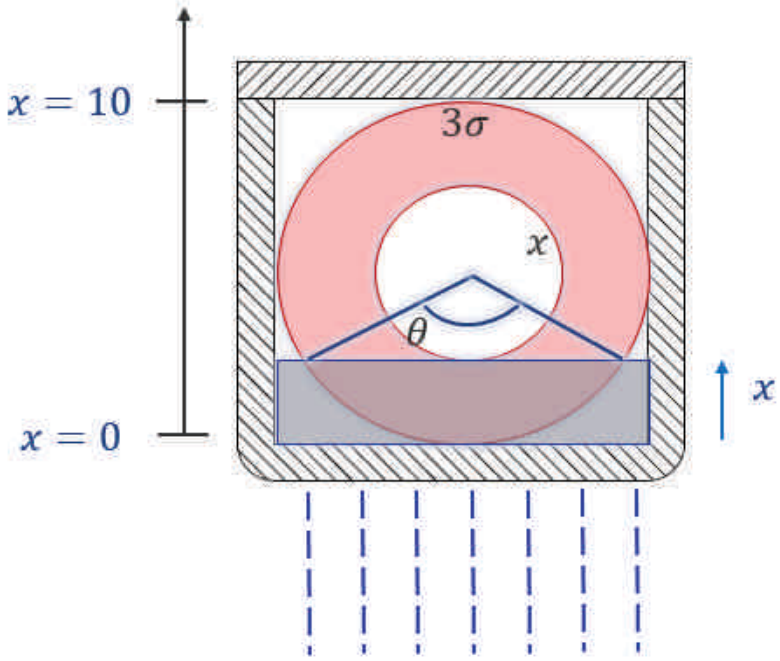

Figure 3.17: Parameters for beam percentage calculation

(c) Calculation of the percentage of area:

$$P_2 = \frac{S_1}{S} \tag{3.9}$$

3. Multiplication of these two percentages to have the total percentage of beam in the considered part,

4. Calculation of time needed to cover the distance x in function of the outlet velocity required.

Once the percentage per distance x founded, the repartition over time can be calculated in function of the time [61]:

$$\%_{isotopes} = v_{inside \quad irradiation \quad chamber} * t_{irradiation \quad chamber} \tag{3.10}$$

Applying this Gaussian contribution to the previous calculation, the total release efficiency in function of time inside the irradiation volume and diffusion chamber is computed (Figure 3.19). The Gaussian repartition is dependent upon the time to empty the irradiation chamber. Here, 160 ms has been considered as it correspond to the time to empty the irradiation chamber for a droplets velocity of 2 m/s according to Table 3.3.

It is shown that in reality, the total released fraction is the highest at the very end of the emptying of irradiation chamber which is coherent as it is at that time that 100 % of the isotopes are released. Furthermore, 100% of the isotopes have diffused once a flat shape is seen in Figure 3.18. After 600 ms, the diffusion is complete.

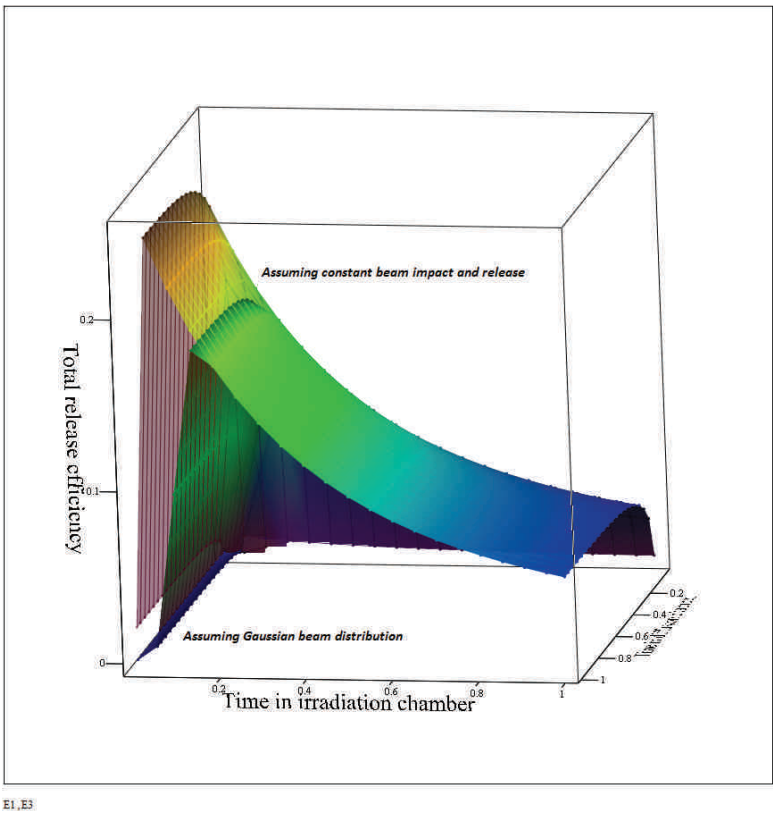

Figure 3.18: Total releasedd efficiency for 0.4 mm diameter droplets - produced isotopes with Gaussian beam and no Gaussian beam

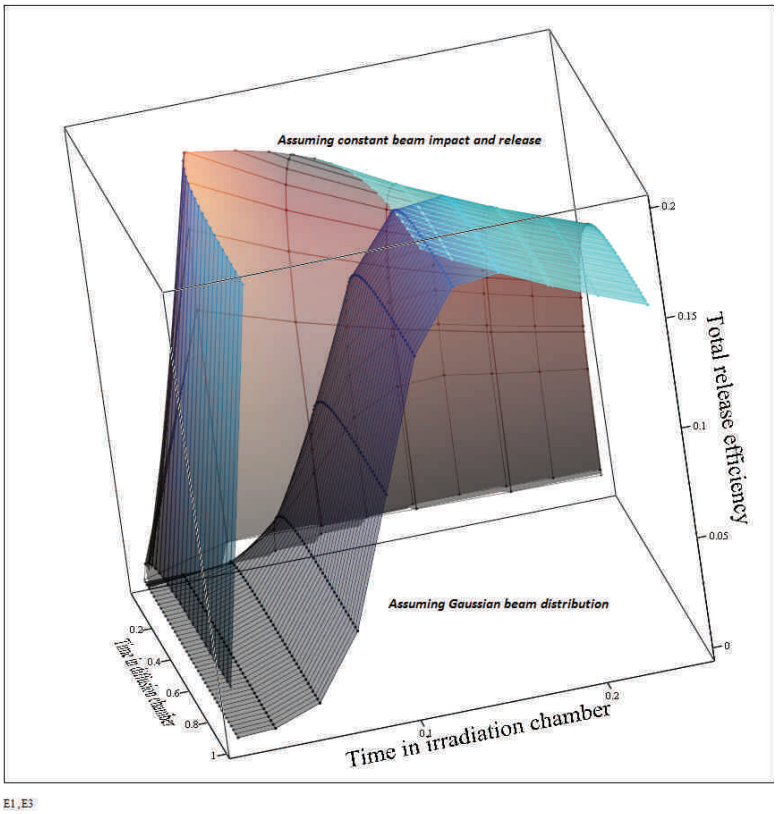

Figure 3.19: Total release efficiency for 0.4 mm diameter droplets - zoom - produced isotopes with Gaussian beam and no Gaussian beam

In the studied configuration, it is recalled that the total release efficiency is about 8.2 %. This represents an improvement of factor 5.1 compared to current results in Isolde [20]. Considering the 10 mm internal diameter of the piping of the loop and the velocity of droplets of 2 m/s, the flow rate has been estimated at 0.13 l/s.

3.2.1.3 Container and diffusion chamber of the LIEBE target - calculations

Another important point to take into account when dealing with high power pulsed beam is the shock waves created during the beam impact. It has been seen in the Section 1.4.1 that liquids targets have suffered from splashing and have been broken in the past at ISOLDE. Consequently, it is of major importance to assess the behavior of the target irradiation chamber during the beam impact in order to validate the entrance window design.

To do so, numerical analyses have been conducted with dynamic explicit software (Autodyn) by the means of meshless method as SPH (Smoothed-Particle Hydrodynamics) [63]. These analyses focus on the irradiation chamber of the target, where the beam impact occurs. The aim is to evaluate the shock waves propagating onto the LBE and see what impact they will have on the container wall while evaluating the consequences of a splash phenomenon. Since these analyses are part of another PhD thesis realized in the frame of the LIEBE project [64], very few details are provided. The presented results only aims to give the main tendency on a stress and shock waves propagation point of view.

The beam parameters considered for this analysis are the one of the staggered mode used for liquid metal targets and as presented in Table 2.11. For the Autodyn analysis, the relevant parameters are the bunch spacing, bunch width and number of particles.

A map of energy deposition have been obtained thanks to a particle physics MonteCarlo simulation package: Fluka [53]. This map of energy deposition is then applied as an heat generation load into the Autodyn model.

3.2.1.3.1 Geometry The geometry used in the numerical model is made up of two parts. The first part is the irradiation chamber with the grid made in Stainless Steel 316L, 1 mm-thickness. The second part is the LBE that fills up the chamber. Several gauges are positioned onto the beam axis to evaluate the pressure waves at different positions (the gauge 12 is located at the peak of energy deposited by the beam) as presented in Figures 3.20a and 3.20b.

In order to save CPU time, the analysis has been performed considering only the feeder volume 3, where the beam impact occurs, and the feeder grid 2 replaced by a plain plate of 1 mm thickness. It is a conservative approximation as the shock waves will propagate only into the considered volume and will not expand toward the other feeder volumes through the holes of the feeder grids. Furthermore, the holes of the exit were restricted to a minimum of 0.3 mm diameter because of the computer capabilities. The total surface covered by the holes is identical to that of the real geometry and the spacing between the holes is scaled. However, a sensitivity analysis on the holes diameter impact has been computed and if the same total surface covered by the holes is respected, the smaller the holes, the lower the stress at the grid part. Consequently, it is here assumed to be in a more conservative case.

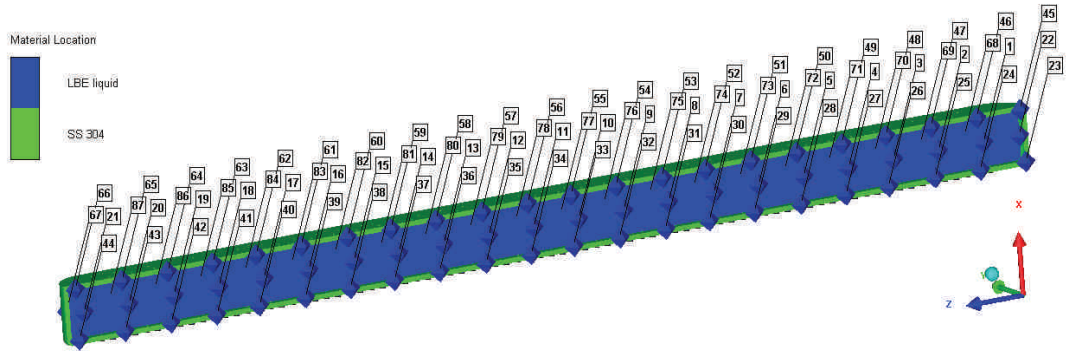

(a) Front view

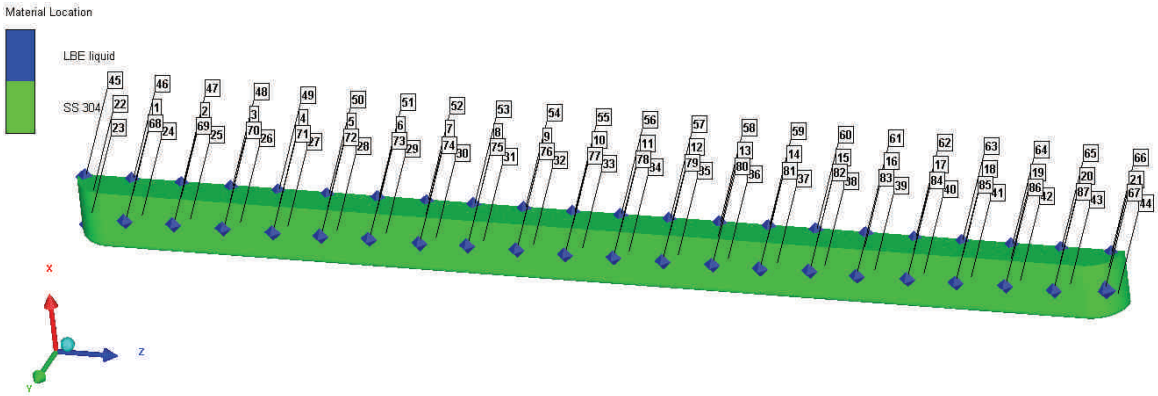

(b) Back view

Figure 3.20: half geometry of the feeder volume 3 of the irradiation chamber and gauges - Autodyn analysis

The shock waves might propagate in the loop. But this does not represent a risk for the loop integrity as in this case, the shock wave will be absorbed by the free surface at the bottom of the diffusion chamber.

3.2.1.3.2 Material definition The data used for Stainless Steel 316L have been directly taken from the Ansys Autodyn database. The Rankine-Hugoniot equation has been selected for the Equation Of State (EOS). This equation can be expressed as a linear relation between the velocity at which a shock wave travels, namely the shock wave velocity U, and the velocity at which the material moves directly after passage of the shock wave front, i.e. the mass displacement u [65]:

$$U = C_0 + S.u \tag{3.11}$$

The coefficient C_0 of Equation 3.11 can be approximated with the bulk sound velocity and S is an empirically determined material constant, which can be approximated with:

$$S = \frac{1}{2}(1 + \gamma_0) \tag{3.12}$$

In which γ_0 is the Gruneisen coefficient. At standard condition, this Gruneisen coefficient can be defined as follow:

$$\gamma_0 = \frac{\alpha_v}{C_v.K_0.\rho_0} \tag{3.13}$$

With α_v the isobaric volume expansion coefficient at constant pressure, C_v the heat capacity at constant volume, K_0 the isothermal compressibility at standard conditions and ρ_0 the density at standard condition.

The Steinberg Guinan model [66] has been selected to describe the strength model. With this model, the yield stress varies depending on strain, strain rate and temperature. The shear modulus and the yield stress are the main parameters to define. The yield stress had been set at 260 MPa for 600°C (it would be at 340 MPa at 20°C) and the shear modulus at 77 GPa.

The same EOS has been used for the LBE, while the hydrodynamic tensile limit pressure criterion has been selected for the failure model. With this failure model, the maximum principal tensile failure stress must be specified. If the negative pressure in the liquid goes over this limit, then the liquid breaks and cavitation and splashing phenomenon can occur.

This hydrodynamic tensile pressure is difficult to estimate since it highly depends upon the material purity and composition. Furthermore, under radiation, it usually drops significantly [45]. To ensure the mechanical integrity of the container in all circumstances, two values of the hydrodynamic tensile limit have been considered:

- -1.9 GPa, the referenced value for liquid lead [1],

- -150 kPa, value that has been estimated previously with a lead static bath target at CERN-ISOLDE [20].

The important difference comes from the fact that this parameter is highly dependent upon the liquid impurities. It is defined experimentally but the value can vary under different experimental conditions.

3.2.1.3.3 Numerical results Since numerical computation of shock wave phenomenon are CPU time consuming, the presented results are for a total time of less than 0.2 ms. This gives a first overview of the tendency of the LBE and the container behaviors under the beam impact, which represents the most critical part if no build up of pressure waves occur.

Hydrodynamic tensile limit of -1.9 GPa If the pressure in the LBE remains under the hydrodynamic tensile limit (set here at -1.9 GPa), the pressure waves will travel into the liquid till reaching the container wall where they will reverberate and finally vanish after several reverberations. Every new bunch will induce a new source creating a new pressure wave. This needs to be studied in detail since, depending on the container geometry, some build-up of pressure waves can occur, potentially leading to the failure of the container.

To be noted that no corrosion or pitting phenomenon has been taken into account in the study of the container integrity. Furthermore, the fatigue that can be induced by the repetition of the shock waves onto the container has not been considered neither.

The labelling of gauges inside the LBE are presented in Figure 3.21 for a better understanding of the upcoming results.

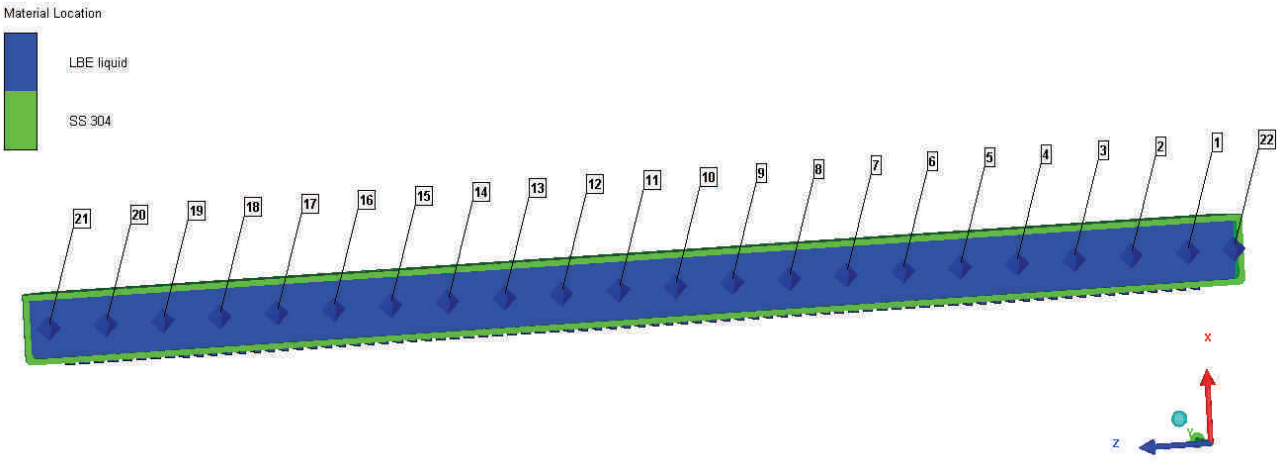

Figure 3.21: Gauges inside the LBE

In Figure 3.22, the pressure waves for all gauges are presented.

If looking more in details the values, one can see that a build-up phenomenon occurs (Figure 3.23). It is then dissipated with time.

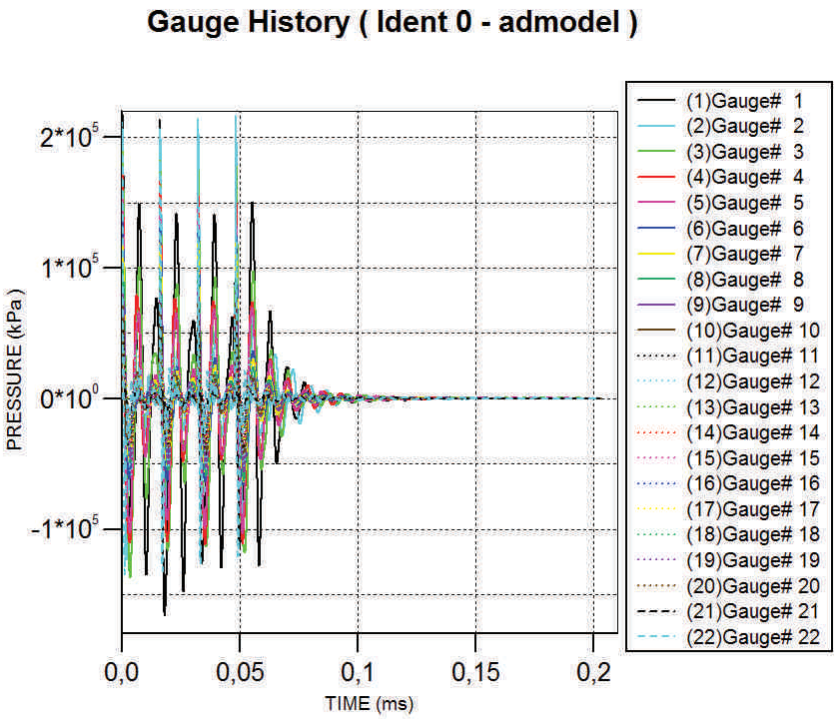

Figure 3.22: Pressure waves into the LBE at all gauges points

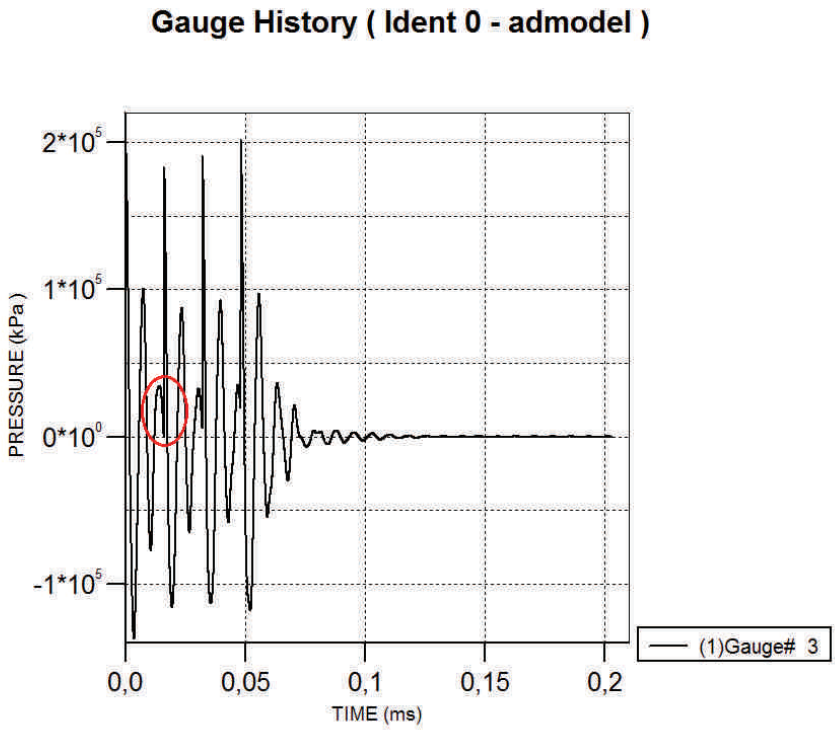

Figure 3.23: Pressure waves into the LBE at gauge point 3 - build-up of pressure wave

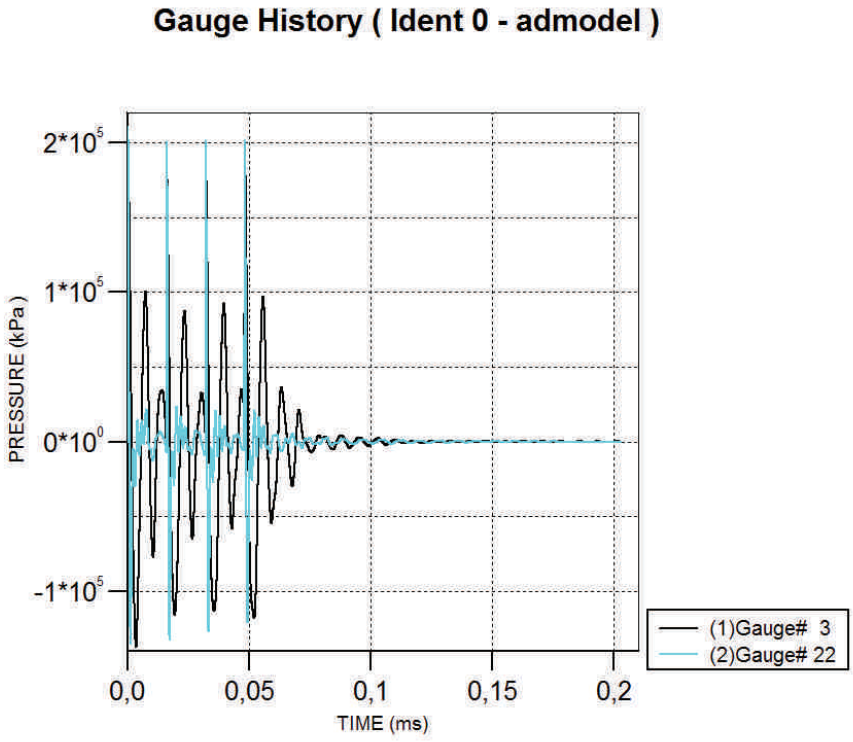

Figure 3.24: Pressure waves into the LBE at gauges points 3 and 22

At the entrance window part, where the gauge 22 is located, the pressure wave reaches the highest values as it can be seen in Figure 3.24 with a pressure wave oscillating between -140 MPa and 200 MPa.

The presented analysis does not take into account the resulting stresses into the container. This should be studied intensively in order to validate the integrity of the container.

Hydrodynamic tensile limit of -150 kPa If the pressure in the LBE goes over the hydrodynamic tensile limit, a failure will occur in the liquid and cavitation and splash phenomenon will start in the liquid.

Figure 3.25 shows the splashing phenomenon that will occur in the target container. The liquid is evacuated through the holes of the grid since it is the only free surface available. The droplets created by the splashing reach high velocity (around 7 m/s as seen in green on Figure 3.25) and thus, one could think that their remaining time in the diffusion chamber would significantly drop, decreasing the total efficiency of the target (the droplets would remain for shorter time in the diffusion chamber). However, this velocity will not be sustained over time and consequently, only the first droplets created from the splashing would reach this velocity.

During the full process of splashing, the LBE will impact the container, leading to different state of stresses, that will evolve with time. The highest state of stresses has been found at 0.041 ms with a maximum Von Mises stress of 250 MPa which remains below the yield limit of Stainless Steel 316L at 600°C of 340 MPa i.e. about 50 % of safety margin.

Furthermore, the stress field will follow the beam profile i.e. that it will first be concentrated at the highest beam profile value and will then follow the pressure waves as presented before.

Figure 3.25: Absolute velocity in LBE during splashing, 0.2 ms

This can be seen from Figures 3.26, 3.27, 3.28 and 3.29. The scale has been fixed at 90 MPa for all Figures in order to have a better visual representation and comparison for the stress fields. This value does not represent the maximum but allows a representation of the stress fields at all time presented.

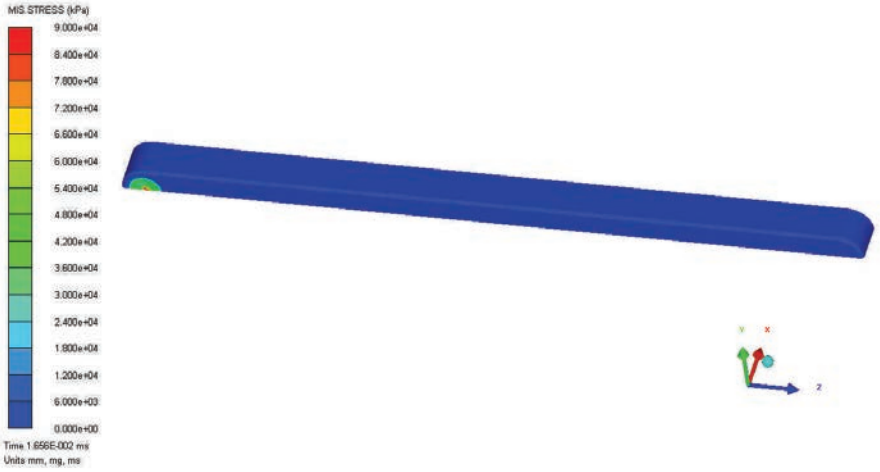

Figure 3.26: Von Mises stresses into the target container, under hydrodynamic tensile limit, 0.0017 ms

3.2.1.3.4 Discussions A sensitivity study should be performed in order to assess the impact of the holes diameter on the stresses created into the container. As well, a sensitivity analysis should be done in order to estimate the impact of the SPH elements size. Because this part is performed by SCK-CEN of the LIEBE collaboration [64], it is not further discussed here.

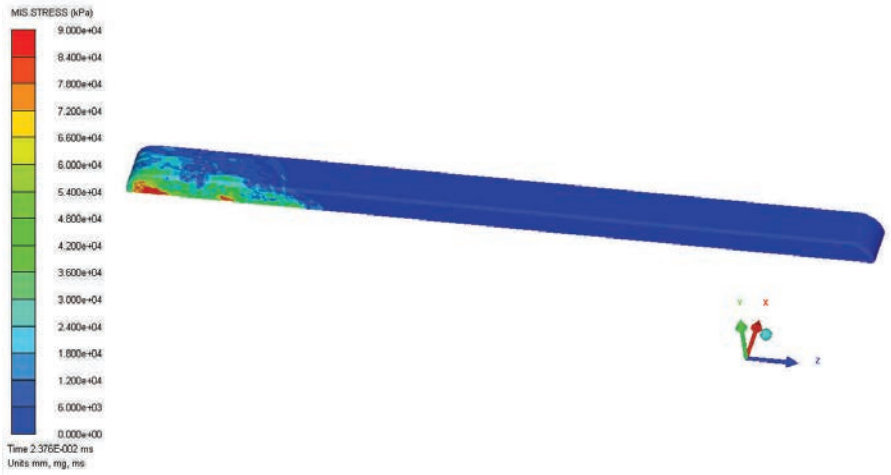

Figure 3.27: Von Mises stresses into the target container, under hydrodynamic tensile limit, 0.0024 ms

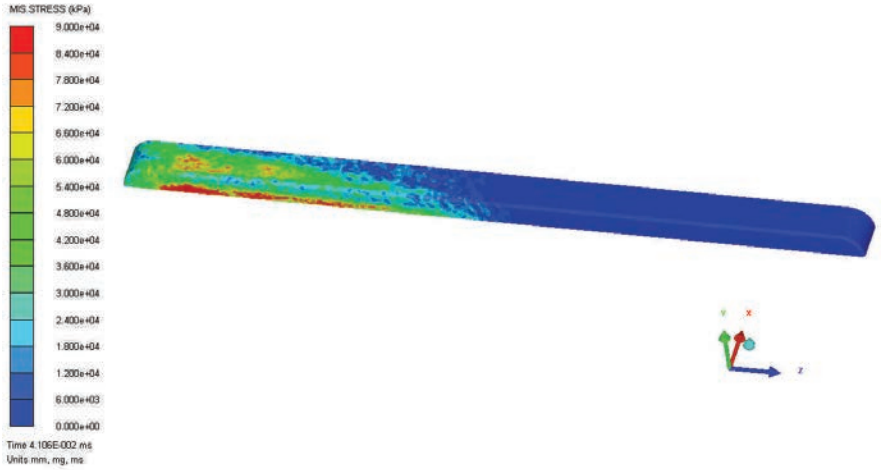

Figure 3.28: Von Mises stresses into the target container, under hydrodynamic tensile limit, 0.041 ms

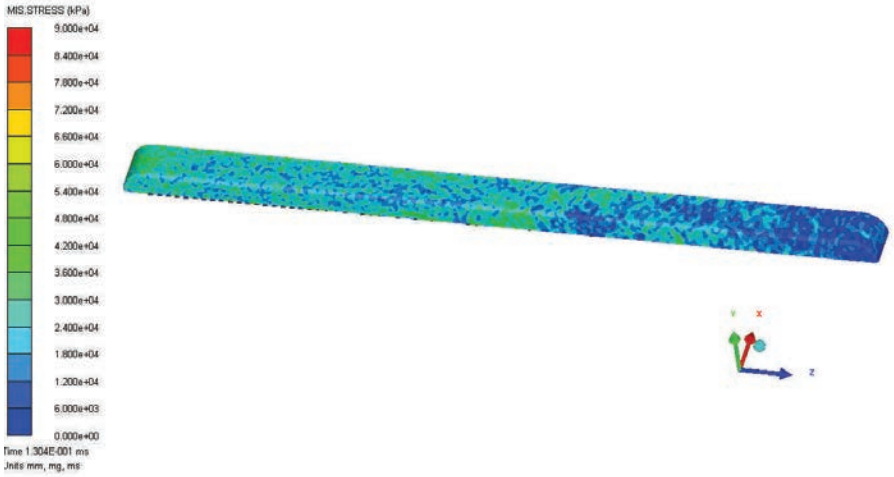

Figure 3.29: Von Mises stresses into the target container, under hydrodynamic tensile limit, 0.130 ms

3.2.2 Transfer line and ion source

The diffusion chamber is connected to the ion source via a condensation chimney and a temperature controlled transfer line as shown in Figure 3.30. These parts allow the selectivity of the ionized and extracted radioisotopes by condensing less volatile species.

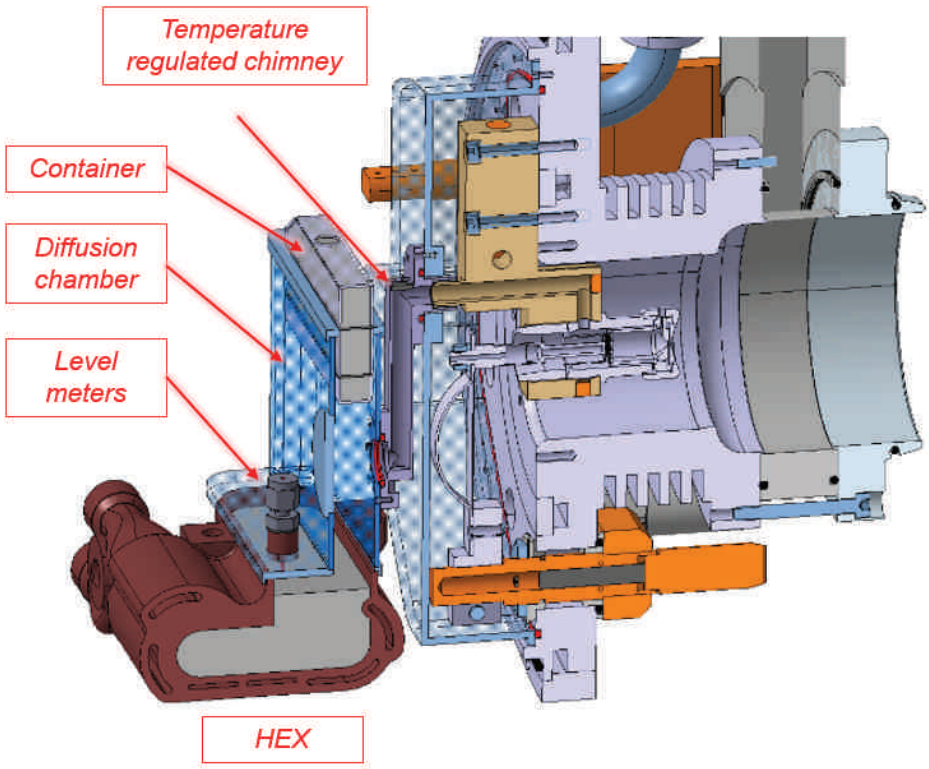

Figure 3.30: Ion source, transfer line and chimney - cross section view for the LIEBE target

The condensation chimney is equipped with an helix used to prevent blocking of the transfer line by splashing of the liquid metal while the isotopes of interest can reach the ion source (not shown on Figure 3.30). The chimney is equipped with a small oven allowing the temperature control and keep the condensed metal above its melting temperature. In addition, the inlet of the condensation chimney is tilted to allow the condensed LBE to flow back in the diffusion chamber.

The transfer line to the ion source is inside a water cooled stainless steel block (Figure 3.31), which is also equipped with an electrical resistance allowing varying the line temperature according to the radioisotopes to be studied.

The chimney and transfer line will be connected to a Versatile Arc Discharge ion source (VADIS) [8] (shown in Figure 3.32). This type of ion source has been used recently in the production of mercury beams, where gains in the yields have been observed in comparison with the previous FEBIAD (Forced Electron Beam Induced Arc Discharge) series [8]. Figure 3.33 shows in a logarithmic scale the comparison of the yields of mercury isotopes produced from static molten Pb targets with FEBIAD (MK3 type) and VADIS (VD5 type) ion sources [47].

In our study, the ion source design has not been changed compared to regular VADIS ion

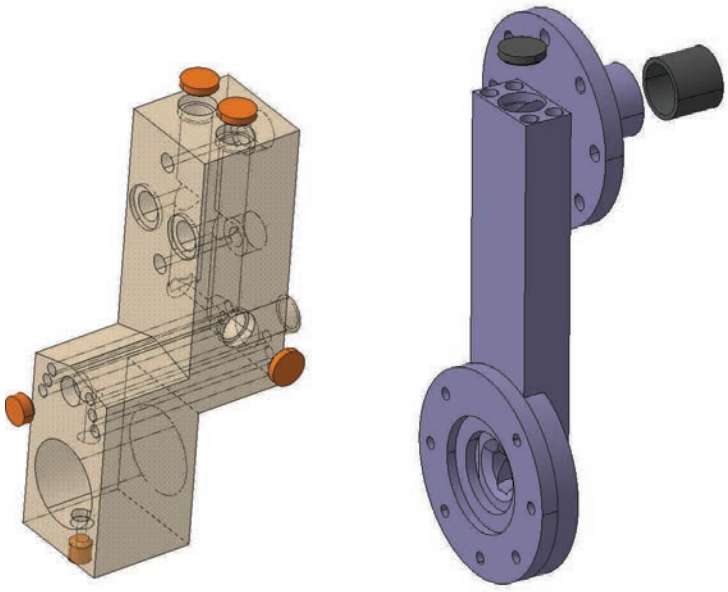

(a) Transfer line of the LIEBE target

(b) Chimney of the LIEBE target

Figure 3.31: Isotopes extraction - elements

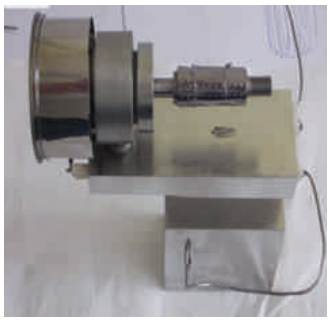

Figure 3.32: VADIS ion source

sources. However, the stainless steel bloc used for the transfer line has been slightly modified to be adapted to the LIEBE target design. Partcularly, the transfer line will be thermally regulated thanks to heaters (Tantalum wire insulated with ceramic - routinely used on several standard ISOLDE targets). Thermocouples will be also positioned all along the isotopes path (chimney and transfer line) in order to control the temperature.

3.3 Dealing with high power beam: design of related elements

3.3.1 Hydraulics parameters

Once the flow rate is defined, the hydraulics parameters of the loop can be entirely estimated. Using the equations given in the part 2.3.1.1.2, it is possible to estimate the pressure losses for a chosen diameter and consequently, to set the required parameters for the pump.

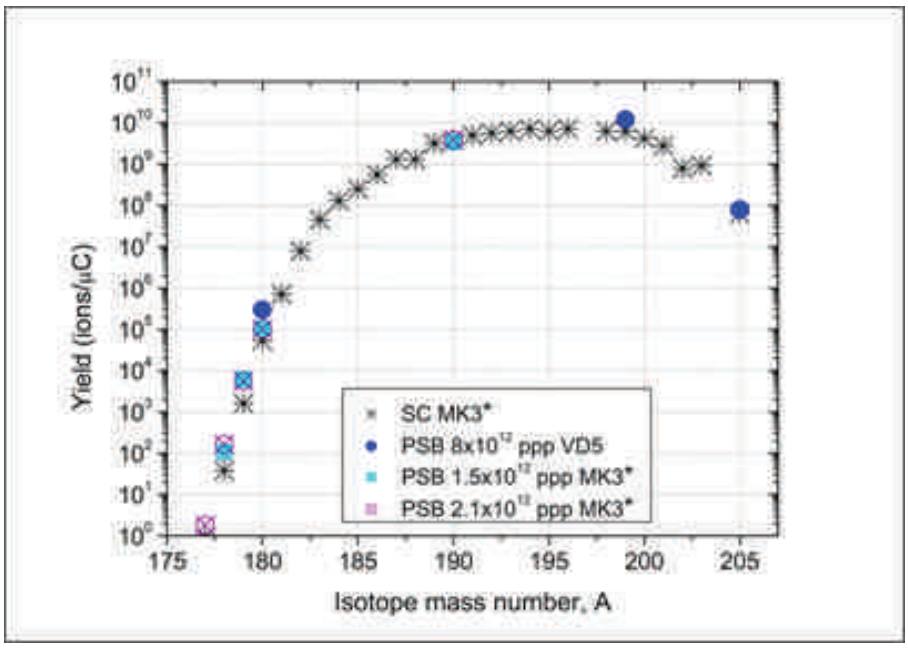

Figure 3.33: Comparison of yields of mercury isotopes produced from static molten Pb targets with FEBIAD (labbeled with MK3) and VADIS (labelled with VD5) ion sources for different proton intensities [8]

3.3.1.1 Pressure losses

As seen in the part 2.3.1.1.2, the bigger the pipe section, the lower the pressure losses for a given velocity. For a flow rate of 0.13 l/s (see Section 3.2.1.2, the corresponding velocities obtained by multiplying the flow rate by the pipe section are given for two pipes diameters in Table 3.4.

Pipe diameter	Velocity inside the pipe
Ø10 mm	1.6 m/s
Ø17 mm	0.6 m/s

Table 3.4: Velocities inside the pipe for a flow rate of 0.13 l/s

In order to make a final choice about the pipe diameter, the pressure losses in the full loop must be assessed taking into account the geometry as presented in Figure 3.34.

Results for the two considered velocities are summarized in Table 3.5. These values have been obtained by applying the method presented in part 2.3.1.1.2.

The pressure losses due to the bellows are not varying with the velocity in Table 3.5 as on the market, only one diameter of bellow was suitable to this application: a 30 mm inside diameter one, and as the flow rate inside the loop is fixed.

For both velocities, the total pressure losses are acceptable as they remain under 2 bar, the pressure required for the pump development. Even thought the margin is lower for a velocity of 1.6 m/s, the gain in total weight of the target due to the difference in volume of LBE inside the loop leads to the choice of that velocity. Consequently, the loop will be made with 10 mm internal diameters pipes.

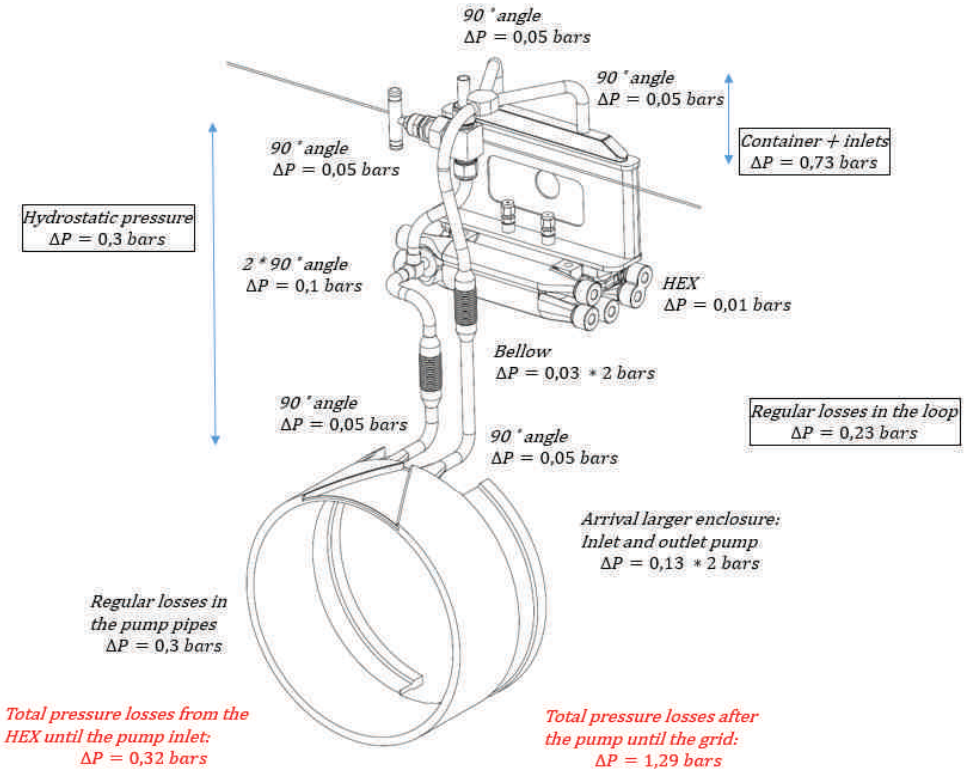

Figure 3.34: Geometry used for the assessment of the pressure losses

Type of pressure losses	**ΔP** (bar)	
	$v = 0.6\ m/s$	$v = 1.6\ m/s$
90 ° angle	0.01	0.05
Arrival in large enclosure	0.02	0.13
Pump connections	0.02	0.13
At the grid	0.03	0.2
Bellow	0.03	0.03
Regular losses in the loop (700 mm)	0.04	0.23
Regular losses in the pump pipe	0.02	0.12
Hydrostatic pressure	0.3	0.3
Total losses	0.64	1.91

Table 3.5: Summary of the pressure loss values for two different velocities

3.3.1.2 Pump design

The design of the pump has been developped and proposed by IPUL. The pump chosen is an electromagnetic (EM) induction one, namely EM induction permanent magnet pump (PMP). This pump allows the physical separation of the circulating LBE from the rotating part and meets the safety requirements concerning the double confinement around all the loop element as it can be seen in Figure 3.35.

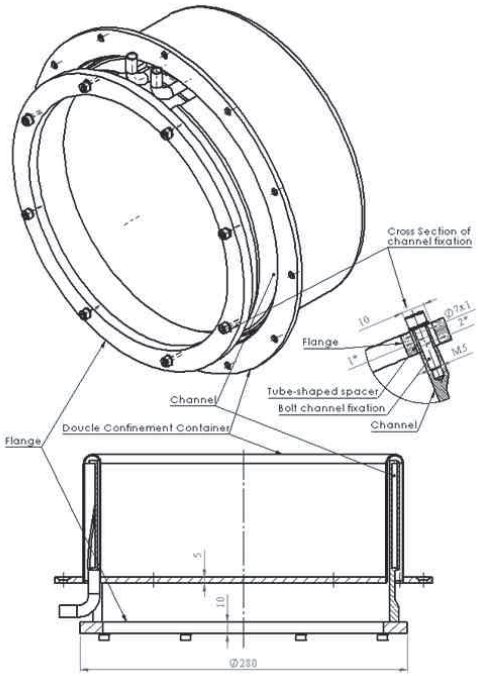

Figure 3.35: Pump channels with the double enclosure around

In order to cope with the thermal deformation of the pump channel (estimated at about 1.4 mm for a temperature of 600 °C), the fixation system of the pump is made up of several screws with spacers/washer system as it can be seen in Figure 3.35.

The pump rotor, as presented in Figure 3.36, rotates with respect to the channel, creating the rotating magnetic field needed to create the fluid movement.

The magnetic system is axially symmetric, so there is no end effects, hence no vibrations. The rotor has two active parts as magnets are located in both sides of the channels. Its permanent magnets are assembled in Hallbach array in order to increase the magnetic field in the pumps channels area. They are made of Samarium Cobalt (SmCo) as theses magnets can withstand a temperature of 300 °C. The magnetic field will decrease of about 3% every 100 °C which should not affect the pump properties.

The electric engine drives the rotor with a rotational speed going up to 800 rpm via a gearbox. In the presented configuration, the pump will have the pressure/flow rate characteristic presented in Figure 3.37.

Depending on the rotation speed chosen for the engine, the pump will have different P-Q characteristics. This allows a tuning of the loop pressure and flow rate, if needed. This will

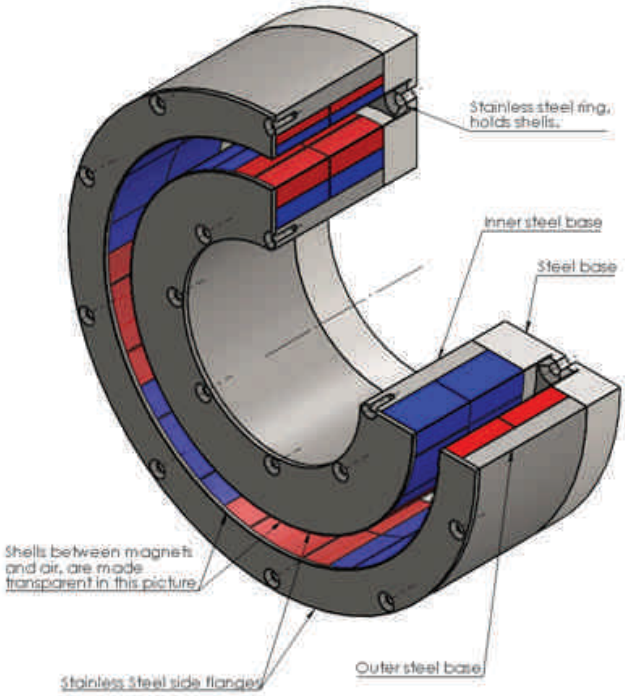

Figure 3.36: Rotor of the EM pump

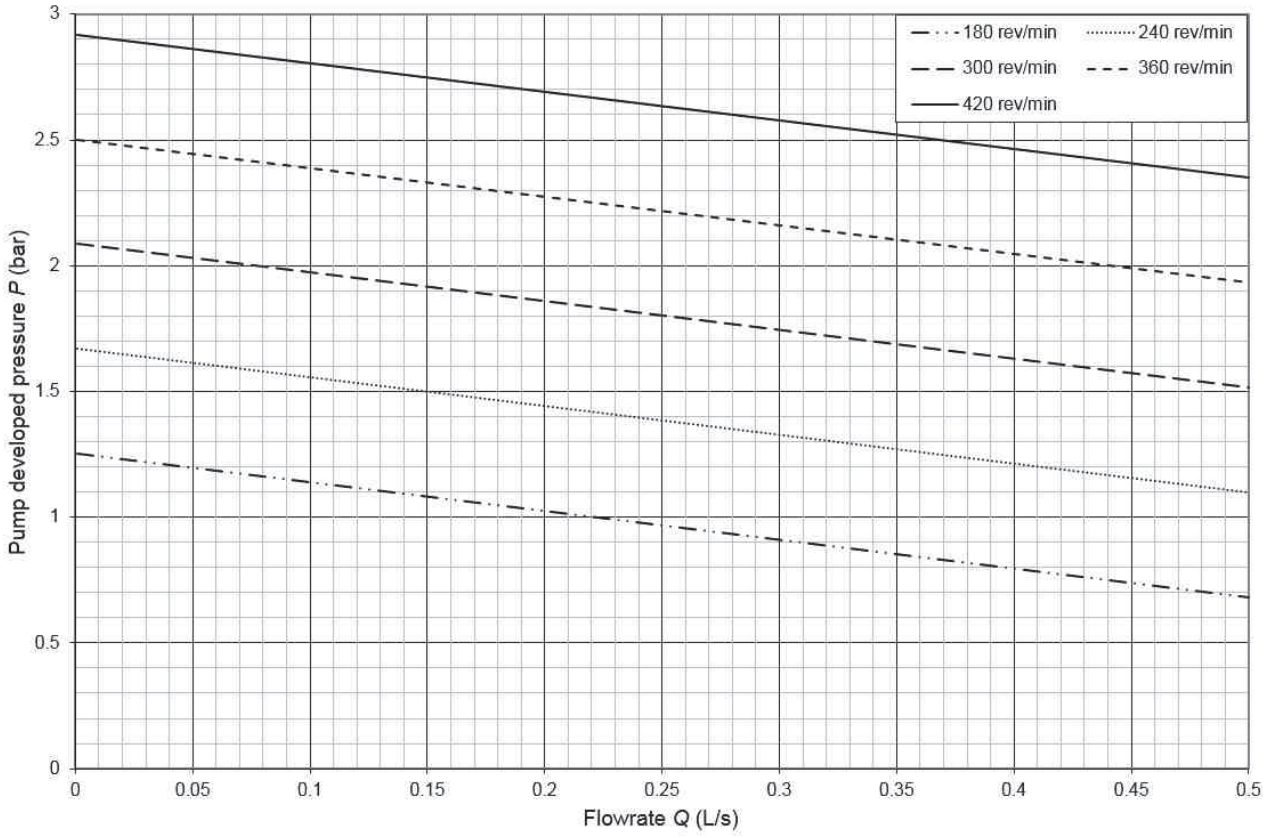

Figure 3.37: Pressure-flow rate characteristics of EM pump depending on the rotation speed of the magnetic rotor

also allow the assessment of the velocity and thus, droplet formation regime impact onto the total isotopes release efficiency.

In the proposed design, the minimum rotation speed acceptable in order not to create any cavitation points in the loop is 300 rev/min but it is advised by IPUL to operate as baseline at a minimum rotation speed of 360 rev/min. However, if the flow rate is reduced, higher rotational speed will be required to ensure the same pressure inside the loop.

Furthermore, heat will be generated by eddy current in the LBE. The summary of the total heat generated in the channel of the pump is presented in Figure 3.38. The losses due to heat radiation and due to the forced convection from the rotating elements is not taken into account here and will be assessed in 3.3.2.1.1. This is of major importance as the power transmitted by the pump to the LBE will have to be considered for the thermal balance.

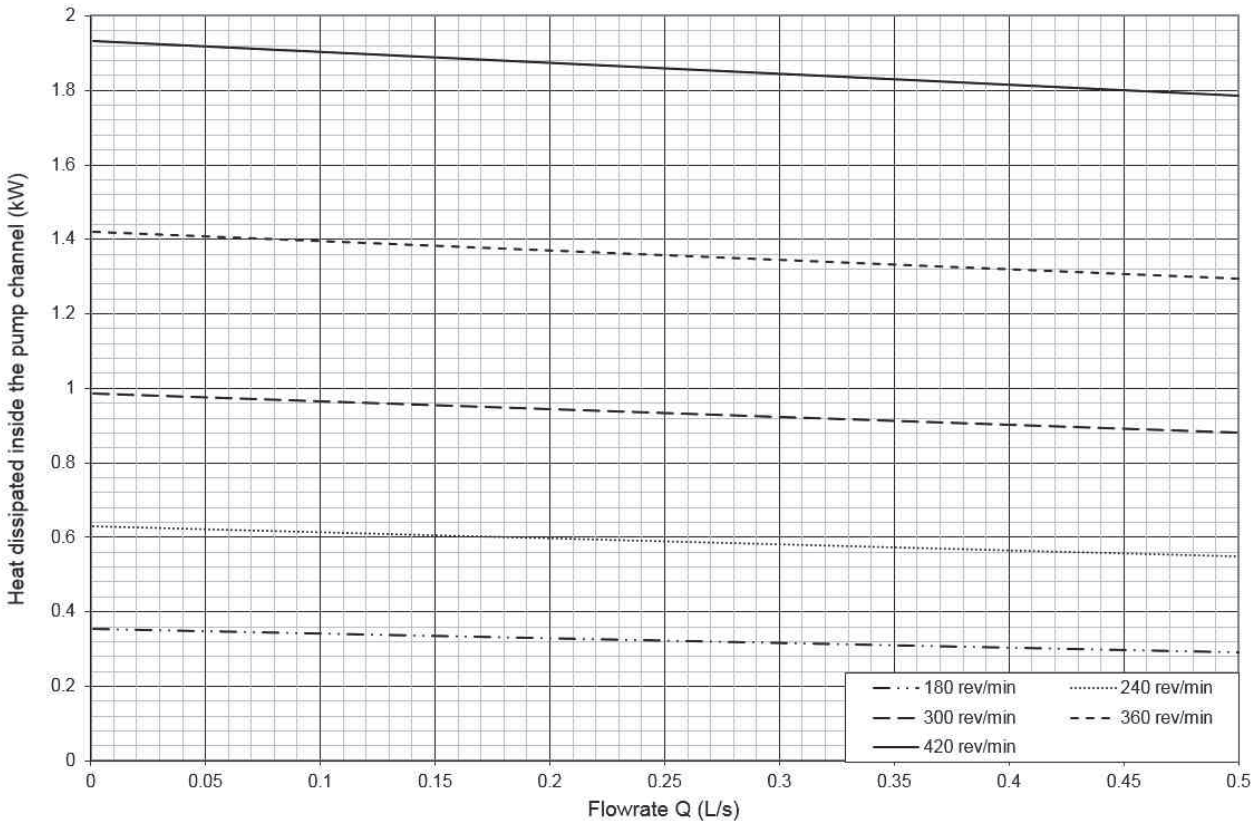

Figure 3.38: Total heat generated in the channel of the pump

From Figure 3.38, it is obvious that the higher the rotation speed of the engine, the higher will the heat transmitted to the circulating LBE be. It can go up to 1.9 kW in case of the highest rotation speed of 420 rev/min. In the advised operating condition of 360 rev/min, the heat transmitted will be of 1.4 kW. Furthermore, as the minimum rotation speed for the rotor would be 300 rev/min in order to ensure that no cavitation occurs in the loop, the minimum heat transmitted by the pump in that case would be of 900 W. This is clearly not negligible and will impact on the thermal equilibrium of the loop target. This equilibrium is studied in the next section.

3.3.2 Thermal equilibrium

As seen in the part 2.3.1.2, the balance of the heat contributions distributed along the LIEBE target is of major importance as it will allow a proper operation of the target. The heat contribution will come from the beam impact and the pump while the heat losses will occur through radiation of the loop, the forced convection and radiation at the pump part and the heat exchanger.

The contribution of the beam and the pump is known and summarized in Table 3.6. For the beam, the calculation of the deposited beam power has been done with the Fluka software [53] and for the pump, the value has been taken from Figure 3.38 assuming a required flow rate of 0.13 l/s and a pressure delivered by the pump of about 2.4 bar corresponding to a rotational speed of 360 rev/min (Figure 3.37. This allows to take a margin of 25% compared to the 1.91 bars needed.

Heat contribution	**Power**
Beam	from 0 up to 1 220 W
Pump	about 1 400 W

Table 3.6: Positive heat contributions

In order to operate the target, it is necessary to estimate the different power losses of the loop. This is also needed in order to design the heat exchanger of the LIEBE target.

3.3.2.1 Estimation of power losses

3.3.2.1.1 Losses at the pump position At the pump position, the rotation of the rotor will induce an air flow that will act as a coolant. To estimate the power losses at this part, a two-steps numerical analysis has been computed by using the CFD (Computational Fluid Dynamics) capability of the finite element software ANSYS (namely the v.15 version fo the CFX module) followed by the thermal module. In the first step, the heat transfer coefficient generated at the walls of the double enclosure by the air flow induced by the magnet rotation have been assessed. This has been done for each of the walls of the magnets and double enclosure. These parameters have then been used as boundary conditions for the 2D steady state thermal analysis conducted at various temperatures between 200 °C and 600 °C by step of 100 °C.

The 2D geometry is presented in Figure 3.39, the 3D model being the axi-symmetric extension of this model.

As the rotating velocity of the pump can vary from 300 rev/min (minimum rotation speed to ensure that no cavitation can occur in the loop) to 420 rev/min, the CFX analysis has been conducted for these two extreme velocities in order to assess the possible impact on the power losses.

Figure 3.40 presents the velocity streamlines under a speed rotation of 300 rev/min (the result will be visually equivalent in case of a rotation speed of 420 rev/min on a velocity plot point of view) while Figure 3.41 shows the same velocity but on the perpendicular plane of the magnets/pump part.

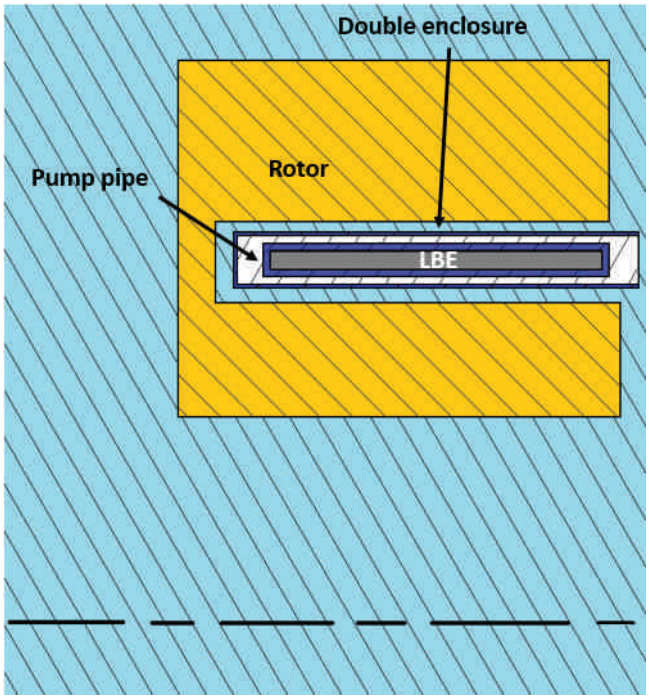

Figure 3.39: 2D geometry of the pump part for numerical analysis

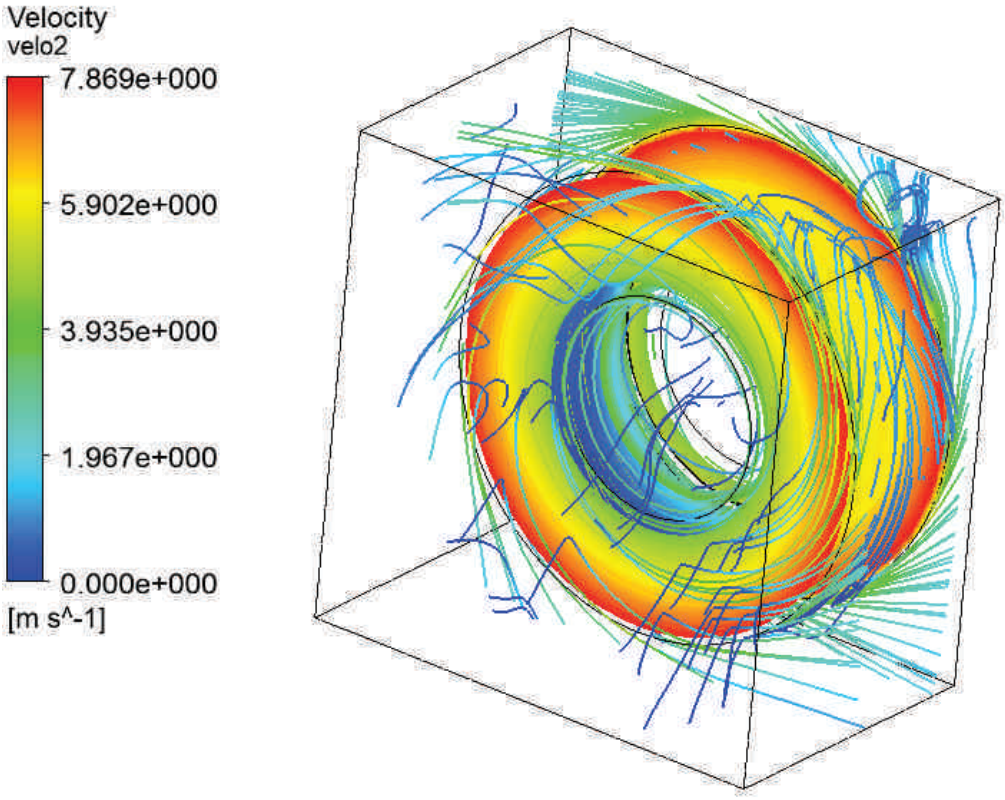

Figure 3.40: Velocity streamline for a rotation speed of 420 rev/min - pump part

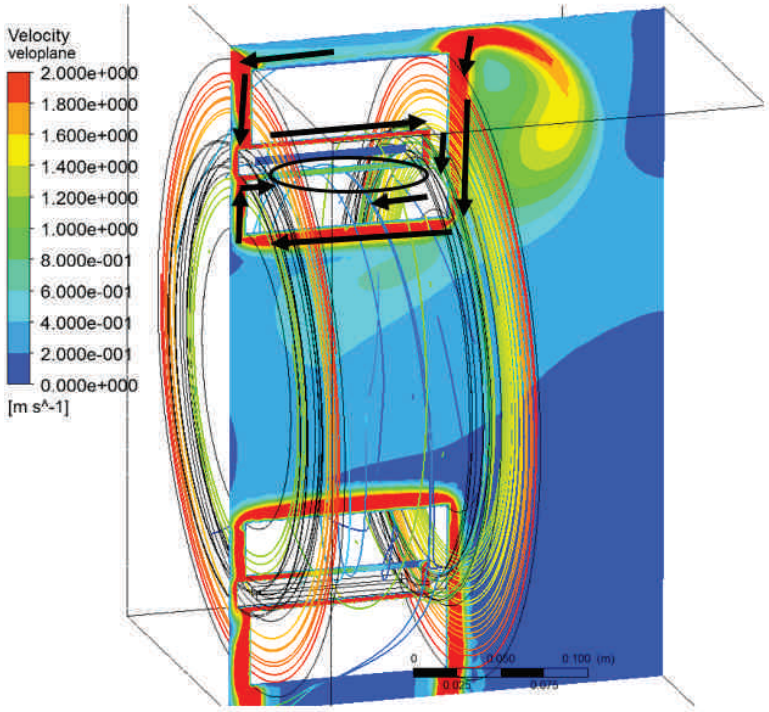

Figure 3.41: velocity field on perpendicular plane - scale fixed at 1 m/s - rotation speed of 420 rev/min

From the circular part of Figure 3.41, one can see that a low velocity area remains. This low velocity area is created from the air circulation indicated by the black arrows. Indeed, the air will enter from the small gaps separating the rotating parts and the static ones. On the biggest gap side, the air flow can occur more easily. In this case, the velocity there will be higher than in the smaller gap where the flow is not as smooth.

The corresponding field of heat transfer coefficient of the air at the rotor and double enclosure part is presented in Figure 3.42 while the results for the two studied cases are summarized in Table 3.7. For a better understanding, the symbols used in Table 3.7 are represented on Figure 3.43.

Names	**h (W/(m^2.K)) for a rotation speed of 300 rev/min**	**h (W/(m^2.K)) for a rotation speed of 420 rev/min**
$h_{rotorfront1}$	45	53
$h_{rotorfront2}$	27	38
$h_{rotorside1}$	10	13
$h_{rotorside2}$	24	32
$h_{rotorside3}$	35	47
$h_{rotorside4}$	5	8
$h_{rotorback1}$	32	45
$h_{rotorback2}$	9	12
$h_{casseroleside1}$	31	44
$h_{casseroleside2}$	4	8
$h_{casseroleback}$	9	12

Table 3.7: Heat transfer coefficients at different position of the pump elements

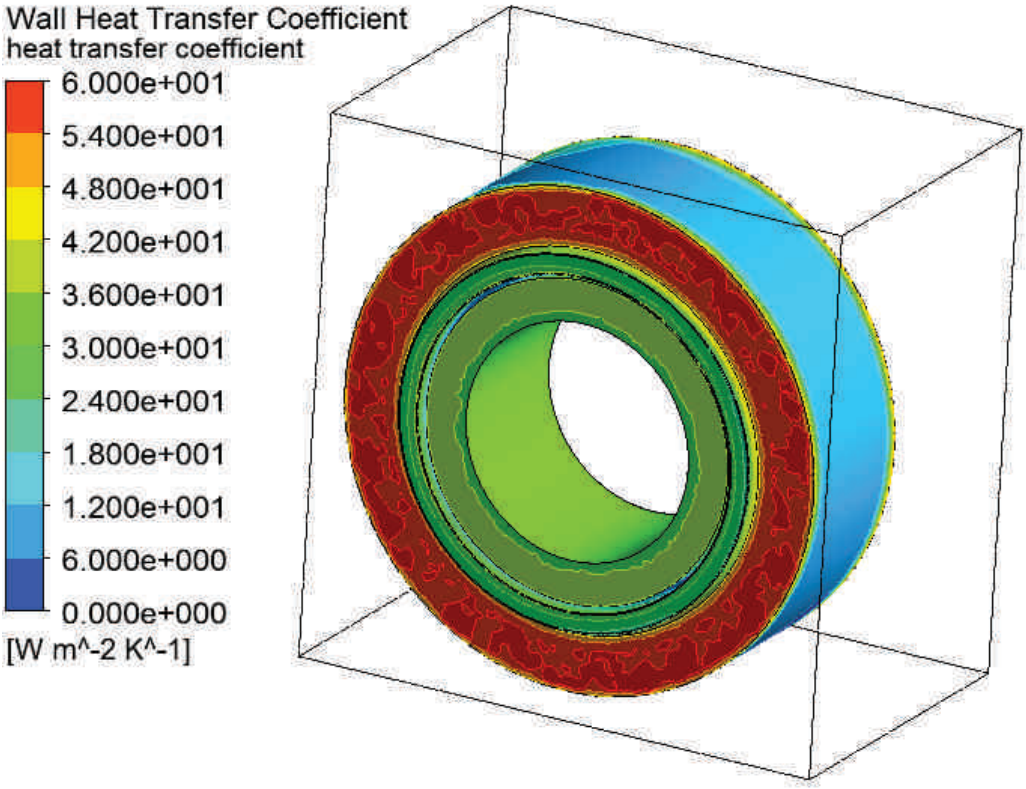

Figure 3.42: Heat transfer coefficient at the rotor part - rotation speed of 300 rev/min

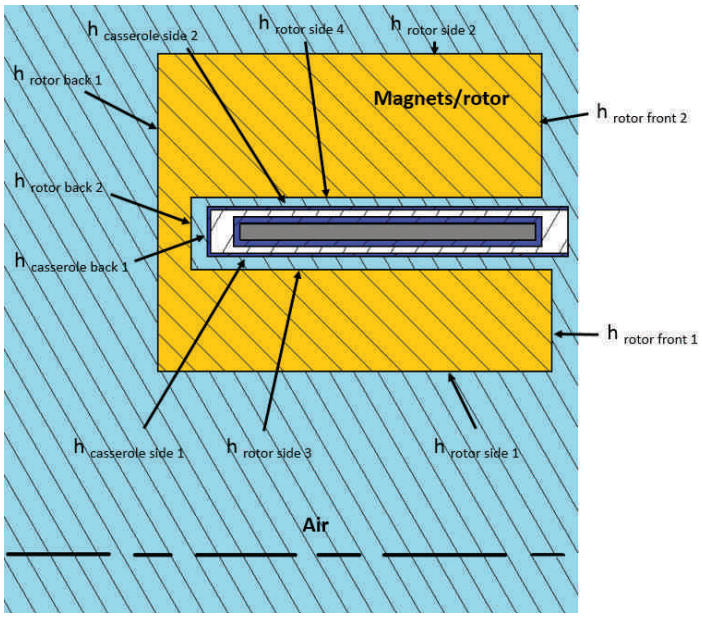

Figure 3.43: Names for the different heat transfer coefficient at the pump part

From Table 3.7, it is clear that the rotation speed of the rotor has a major impact on the heat transfer coefficient which implies that the power extracted at different rotation speed will be different as well. The higher the rotation speed is (namely 420 rev/min), the higher the heat transfer coefficient will be. An increase of the rotational speed therefore leads to an increase of the power losses.

To estimate the total power losses at the pump position (losses due to convection of air around the rotor and double enclosure and radiation of the pipes with the double enclosure and of the double enclosure with the magnets), a 2D thermal analysis has been run with Ansys v.15. Different boundary conditions have been set for the radiation and the convection and the temperature of the LBE has been varied from 200 °C and 600 °C by step of 100 °C. The same analysis have been conducted for the two extreme rotation speeds of the rotor, that is to say 300 rev/min and 420 rev/min.

Considering that the magnets holding shells, the pipes of the pump as well as the double enclosure are all in Stainless Steel 316L, the emissivity for different temperatures are reported in Table 3.8 [50].

Temperature (° C)	**Emissivity value**
200	0.56
300	0.57
400	0.58
500	0.59
600	0.60

Table 3.8: Emissivity values of Stainless Steel 316L at various temperatures

The different values of power extracted for the different temperatures are summarized in Table 3.9.

Temperature (° C)	**200**	**300**	**400**	**500**	**600**
Power losses (W) for 300 rev/min	134	303	571	977	1 524
Power losses (W) for 420 rev/min	153	345	671	1 140	1 786

Table 3.9: Power losses at the pump area for different temperatures

As expected, the higher the temperature is, the higher the power losses. Furthermore, it is seen that the power losses are higher for a higher rotation speed of the magnets which as expected as well as the convection will extract more power according to Table 3.7.

3.3.2.1.2 Losses by radiation The second type of power losses will occur through the heat radiation toward the ambient. The estimation of these losses have been done following the model presented in Section 2.3.1.2.2. The model using an equivalent electrical circuit is recalled.

$$P_{losses} = \frac{T_1 - T_{amb}}{R_{tot}} \quad \text{and} \quad R_{tot} = R_{12} + R_{23} + R_{34} + R_{45} \tag{2.8}$$

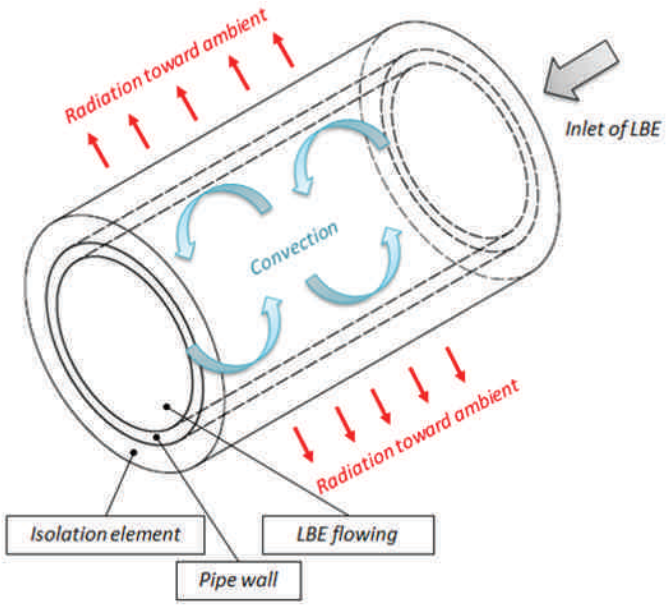

(a) Geometry considered for the power losses

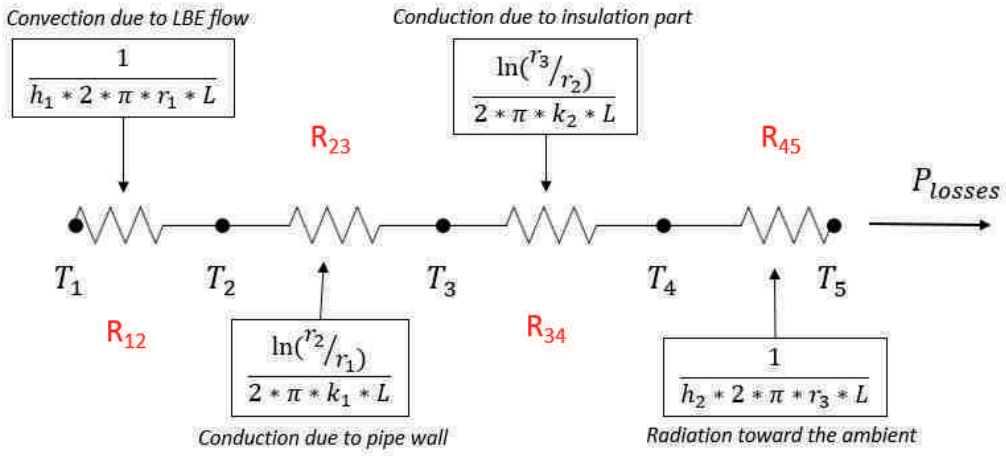

(b) Equivalent thermal circuit

Figure 3.44: Radiation toward the environment: models

Considering the inner and outer diameter of 10 mm and 12 mm, the different resistances can be calculated analytically using the formulas contained in the boxes in Figure 3.44. The flow rate considered is the operational flow rate of 0.13 l/s. However, as seen in the part 2.3.1.2.2, the impact of the flow rate on the total power losses is very low and thus, the calculated power losses are applicable for other flow rates. A fiber glass insulation with an emissivity of 0.8 and a thermal conductivity of 0.08 $W/(m^2.K)$ is chosen. Its thickness is 3 mm. The results for each temperature are presented in Table 3.10.

The maximum temperature reached on the surface of the insulating elements is of 352 °C. Furthermore, as expected, the power extracted is higher at a higher temperature of LBE. This means that the power equilibrium at each temperature is not identical.

T_{LBE} (°C)	R_{12}	R_{23}	R_{34}	R_{45}	$T_{surface}$ insulators (°C)	P extracted (W)
200	0.0017	0.0018	5.07	8.8	155	13
300	0.0016	0.0017	5.07	11.5	215	17
400	0.0016	0.0016	5.07	14.3	267	20
500	0.0015	0.0015	5.07	17.1	313	22
600	0.0015	0.0014	5.07	19.9	352	23

Table 3.10: Resistances estimations and power lost for each LBE working temperature

3.3.2.2 Thermal balance

By making a thermal balance of the power contribution and power losses in the full target loop, it is possible to estimate the required power to be extracted by the Heat Exchanger (HEX). This can be achieved by using the data contained in Tables 3.6, 3.9 and 3.10. The results are presented in Table 3.11.

Power (W)		**200**		**300**		**400**		**500**		**600**	
		min	max	min	max	min	max	min	max	min	max
+	beam	0	1 220	0	1 220	0	1 220	0	1 220	0	1 220
	pump	900	1 400	900	1 400	900	1 400	900	1 400	900	1 400
-	radiation	13		17		20		22		23	
	pump	134	153	303	345	571	671	977	1 140	1 524	1 786
	HEX	753	2 454	580	2 258	309	1 929	-	1 458	-	807

Table 3.11: Power equilibrium for the full loop target

It is clear that the power required from the HEX for a given temperature of LBE varies. This power can vary over time since it will be varied by the person in charge of operating the target, the HEX must be able to extract the highest power required. However, this would lead to situation where the HEX will extract too much power. Consequently, additional power should be brought by an external source to compensate for this effect. The easiest way to do this is to add this missing power thanks to the heating elements already installed on the loop. This additional power should be able to compensate the power extracted at 500 °C and 600 °C. The corresponding values are of 99 W at 500 °C and 647 W at 600 °C.

The chosen heating elements consist in heating cables that will be wrapped around every part of the LBE loop. In addition, a layer of insulation will be installed in order to decrease the power losses by radiation.

Different requests have been made to different companies specialized in heating elements and, considering the dimensions of the loop, the maximum power that can be applied on the loop has been evaluated at 2.9 kW. This power should be used both to change the temperature of the loop and to balance the power extracted by the HEX if needed.

In order to keep some power to tune the temperature of LBE during the operation, a power of only 1.8 kW has been selected for the HEX dimensioning. That gives for each temperature a range of power possibly extracted, the minimum being the minimum power to be extracted as from Table 3.11 while the maximum corresponding to this minimum value plus the tuning power of 1.8 kW. These values are summarized in Table 3.12.

T (°C)	**200**		**300**		**400**		**500**		**600**	
-	min	max	min	max	min	max	min	max	min	max
Power (W)	753	2 553	580	2 380	309	2 109	0	1 800	0	1 800

Table 3.12: Power to be extracted by HEX

In all cases, the power delivered by the heating element will be enough to compensate the power losses. The design of the HEX is described in the next section and has been performed in order to be as close as possible from the aimed extracted power at all temperatures of use of LBE.

3.3.2.3 Heat Exchanger design

The available Isolde cooling circuit has the following parameters (Table 3.13).

Parameters	**Units**	**Value**
T_{inlet} water	$^\circ\ C$	27
Flow $rate_{max}$	l/s	0.22
Pressure of water	bar	10

Table 3.13: Main parameters of the Isolde cooling circuit

To extract a power decreasing when the temperature increases, and considering the conclusion reached with Equation 2.23, two options are possible:

- **Varying the flow rate** In this case, the water would circulate always in the same pipe while the flow rate should be decreased when the temperature increase to extract less power. The risk of this solution is that the temperature of the water would reach a too high value, with possible fast vaporization and thus, increase of pressure that could lead to the failure of the HEX.
- **Varying the surface of exchange** In this case, the water would be directed in different pipes depending on the temperature. This solution allows a change of surface of exchange by timing the shape and distance of the pipe. It is the solution retained.

3.3.2.3.1 Detailed design of the HEX The design for the heat exchanger (HEX) is presented on Figure 3.45. It is positioned at the bottom of the diffusion chamber. Following the conclusion established thanks to the thermal balance, 5 different LBE temperatures have been defined: 200 °C, 300 °C, 400 °C, 500 °C and 600 °C.

For each of these temperatures, different water channels with different references temperatures will be selected as shown in Figure 3.46. The selection of the different channels will be operated with the elctro-valves shown on Figure 3.47. The flow rate will be constant at 0.22 l/s, the maximum flow available (Table 3.13).

In the proposed design, the LBE is forced to flow from one side to the other. The difference of power extracted is due to the position of the water channel and the conductivity of the material used for the HEX (Stainless Steel 316). Its complex shape can be manufactured by additive manufacturing or 3D printing.

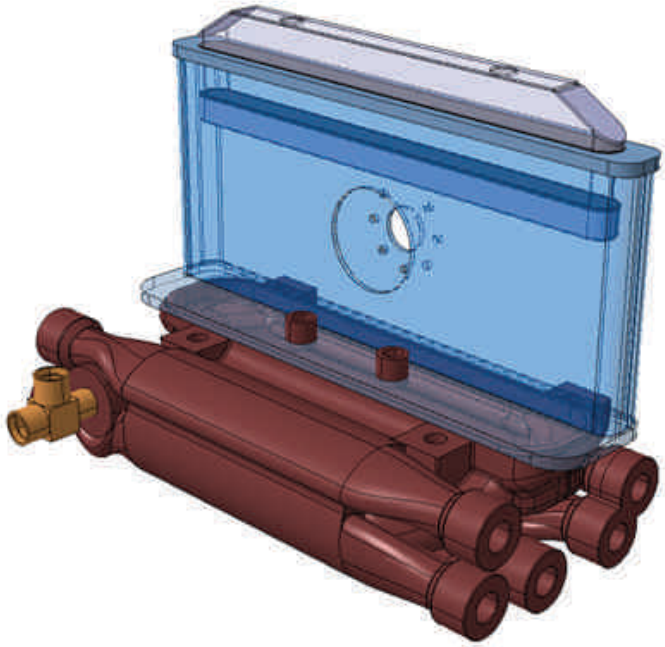

Figure 3.45: Design of the LIEBE heat exchanger

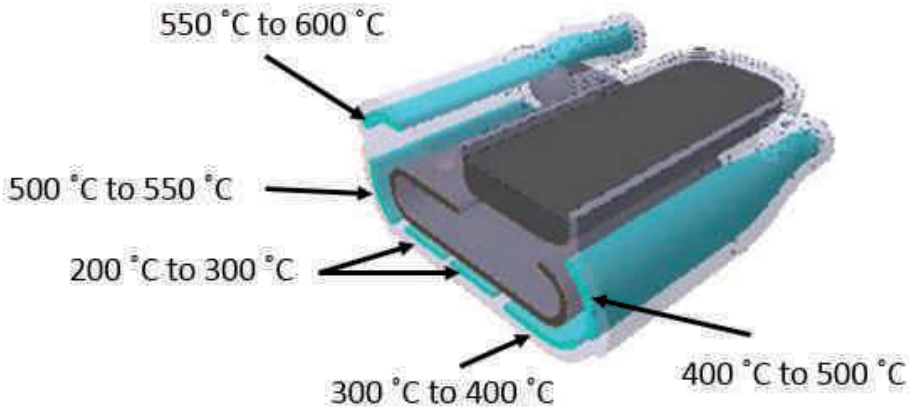

Figure 3.46: Design of the LIEBE heat exchanger - cut view with the water channels

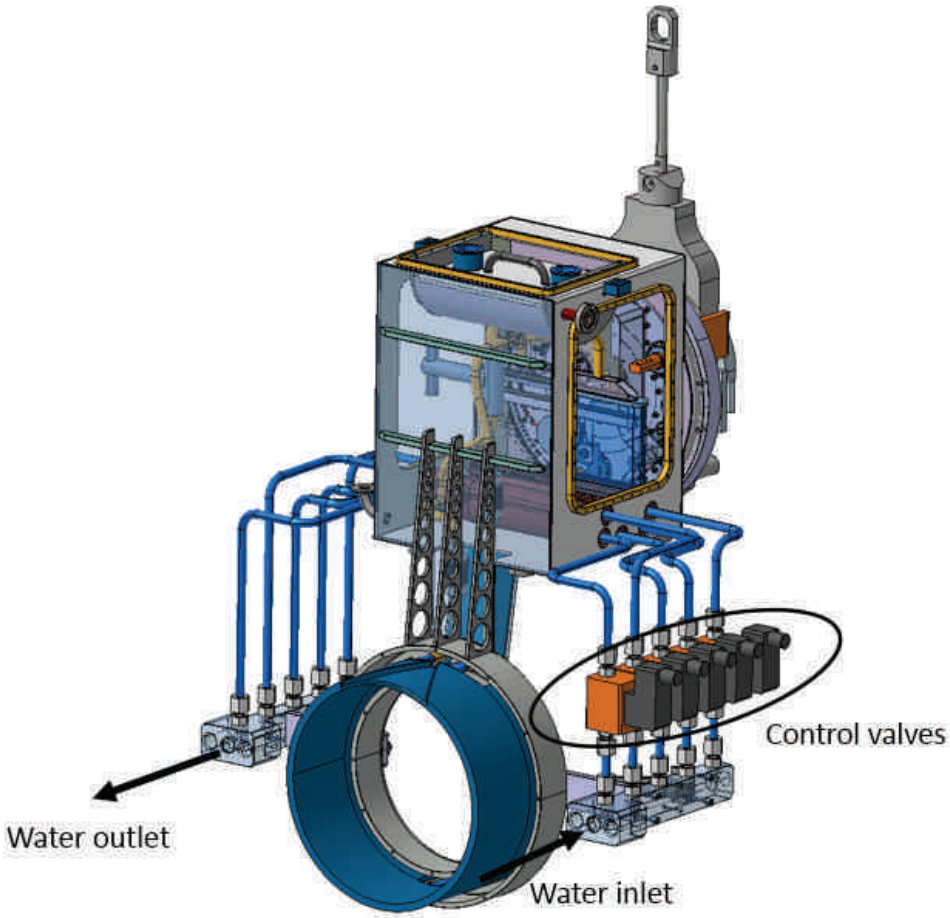

Figure 3.47: General view of the target - position of the electro-valves for HEX control

3.3.2.3.2 Numerical analysis Designing the HEX that would allow the proper evacuation of heat while keeping the water temperature under an acceptable limit is a complex subject. To adress this issue, computational fluid dynamics analyses have been conducted by using the CFX module of ANSYS software. As the water pressure is of 10 bar, the maximum temperature allowed in the water would be of 177 °C as from the Duperray equation [67].

$$P = (\frac{T}{100})^4 \tag{3.14}$$

In the Duperray equation, the water pressure P is expressed in *bar* and the temperature T in *degree Celsius*. However, for safety reason, a margin of 30% on the temperature has been taken, which brings the maximum allowed temperature to 120 °C.

The CFX analyses [68] have been conducted for every LBE working temperature defined in Table 3.11 and the power extracted as well as the water maximum temperature have been estimated.

The analyses have been done considering the material properties of LBE variable with temperature as defined in Table 2.1.

Figures 3.48 and 3.49 show the water temperature distribution at the lowest and highest temperatures given in Table 3.11 (200 °C and 600 °C respectively). It is observed that the temperature distribution, as well as the minimum and maximum levels, are quite similar.

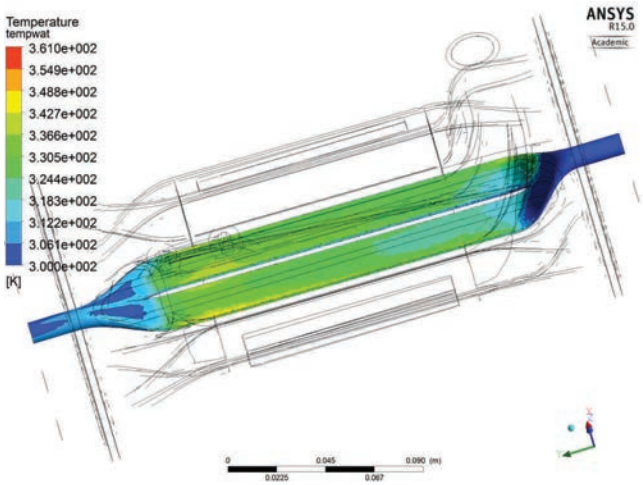

Figure 3.48: Water temperature distribution in the channel for LBE temperature at 200 °C

The LBE velocity streamlines are presented in Figure 3.50. In order to obtain a large surface area of exchange between the LBE and the cooling fluid with a low flow rate of LBE, the velocity of the LBE is increased through the obtrusion of the LBE flow.

The LBE flow is well guided on the bottom side as it can be seen in Figure 3.51.

The pressure losses inside the water channels are negligible for all the channels. On the LBE side, they are of around 0.008 bars according to the CFD calculation as shown on Figure 3.52.

This means that a minimum height of LBE is required before the inlet of the HEX to ensure that no cavitation occurs. This minimum height required is estimated from [67]:

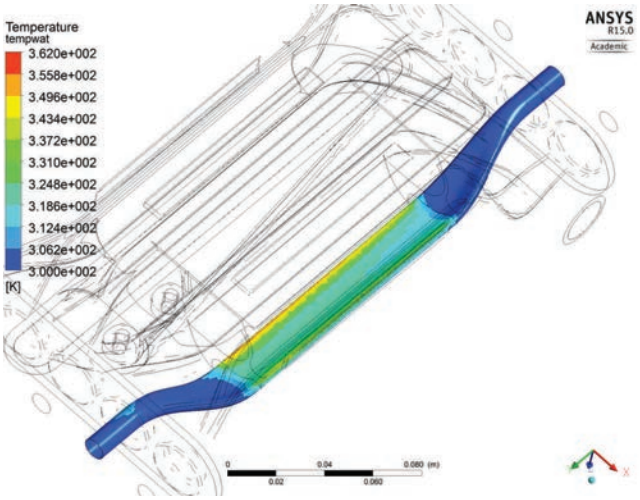

Figure 3.49: Water temperature distribution in the channel for LBE temperature at 600 °C

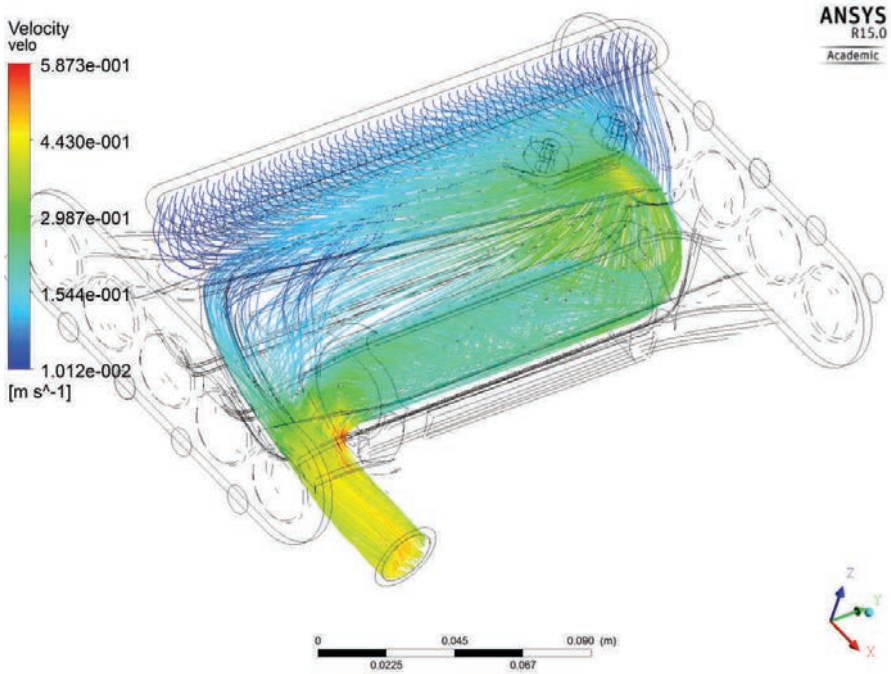

Figure 3.50: Velocity streamlines of LBE inside the HEX - up view

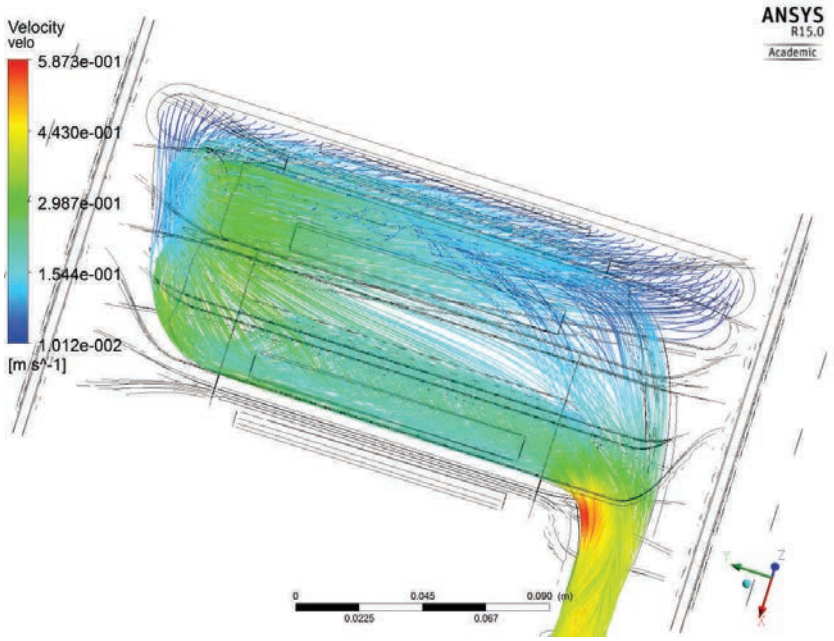

Figure 3.51: Velocity streamlines of LBE inside the HEX - down view

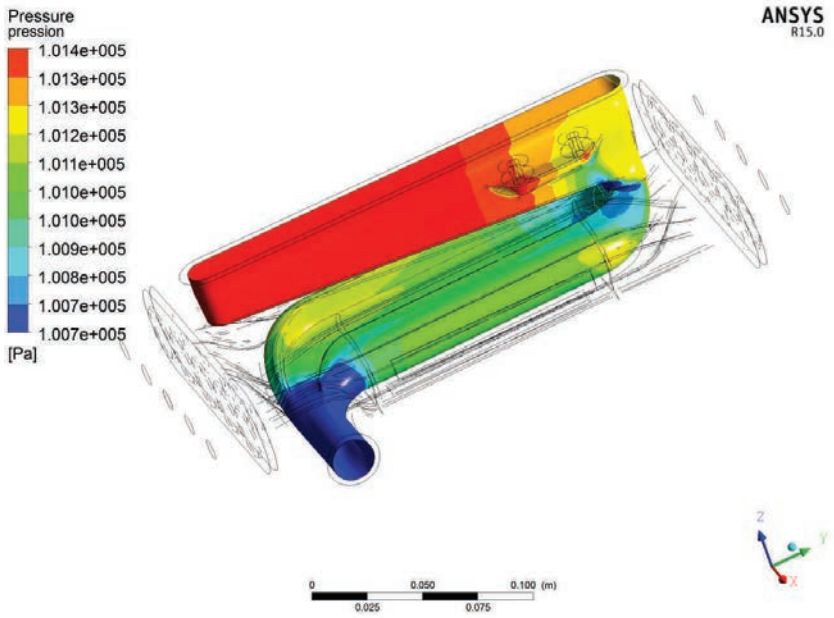

Figure 3.52: Pressure in LBE - numerical analysis

$$\Delta P = \rho.g.\Delta h \tag{3.15}$$

With ΔP the pressure difference, ρ the fluid density, g the constant acceleration and Δh the height of fluid above the point of measurement. In our case, the application of Equation 3.15 gives: Δh = 8 mm.

For every working temperature of the LBE, the maximum temperature in water and the power extracted are summarized in Table 3.14. The minimum and maximum power to be extracted for each temperature is also recalled.

T_{LBE}	T_{max} **in the water (°C)**	**P extracted (W)**	**Max P to be extracted (W)**	**P to be extracted (W)**
200 °C	88	2 521	2 553	2 454
300 °C	92	2 318	2 380	2 258
400 °C	83	2 054	2 109	1 929
500 °C	91	1 576	1 800	1 458
600 °C	89	1 379	1 800	807

Table 3.14: Maximum water temperature and power extracted by the HEX for each LBE working temperature

In all cases, the extracted power is sufficient while remaining under the maximum power to be extracted as defined in Table 3.12. However, the target will fluctuate on a full range of temperature between 200 °C and 600 °C which means that it has to accommodate all these temperatures.

In order to validate the design of the HEX, the power extracted per water channel has been evaluated on the full range of temperature as presented in Figure 3.53.

It is noted that several channels can be used for a specified temperature. For example, for the use of the target at a LBE temperature of 250 °C for which a power of about 666 W should be extracted with a beam off and about 2 466 W for a beam at maximum power, several options are possible in function of the beam power. All channels can be used, except for the one planned for 600 °C.

3.3.2.3.3 Operating procedure An operation procedure has been defined to prevent any cooling or overheating:

- Stop the beam,
- Change the channel used (example: from the 200 °C channel to the 300 °C channel),
- At that point, the HEX will extract less power and consequently, the temperature of LBE will increase until it finds its equilibrium. Meanwhile, the heating elements will compensate when needed to reach the desired temperature of LBE,

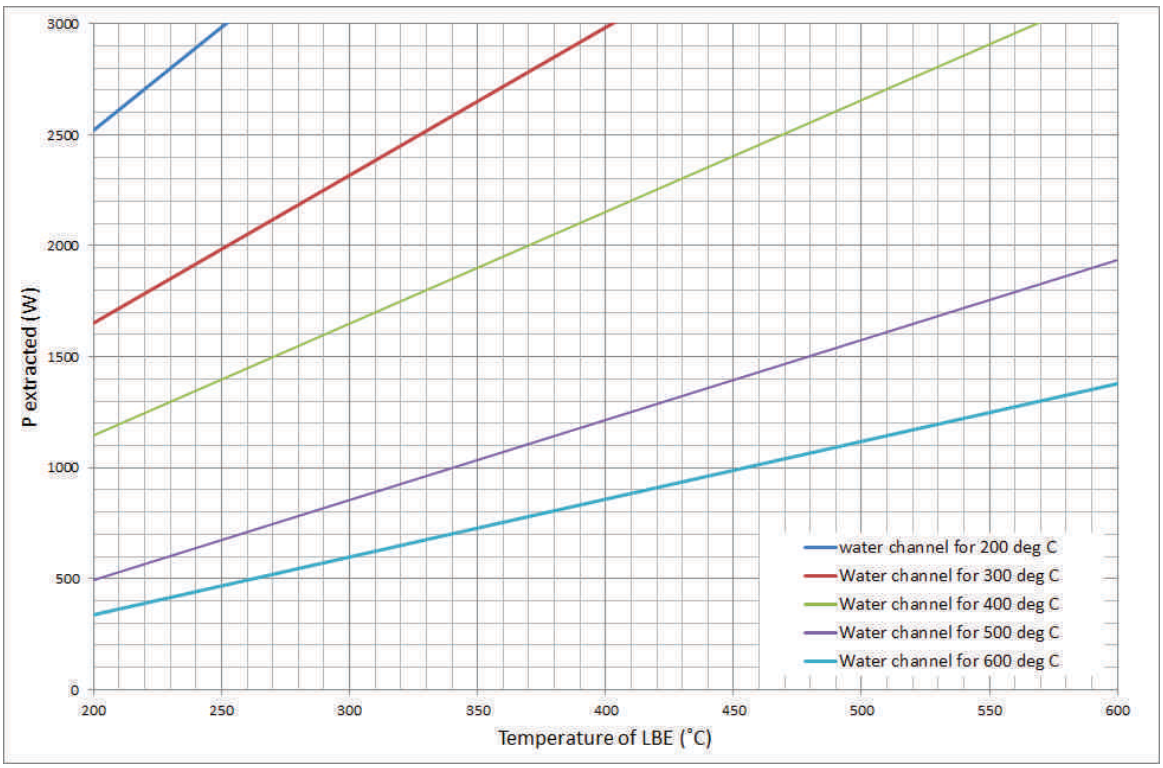

Figure 3.53: Power extracted in function of the LBE temperature and per water channels

- Once the requested temperature is reached and stable, the beam can be sent back on the target (and thus, the heaters will deliver less power as the beam power will not be compensated anymore).

In order to assess the behavior of the extracted power when changing channels, a transient analysis has been conducted with CFX. The results are presented on Figure 3.54 where the power extracted by the HEX is compared to the log mean difference temperature defined in Equation 2.23 when switching from the 200 °C channel to the 300 °C one.

At *t=0 s*, the change of channel is operated. The power extracted drops since the channel used has been changed while the LBE temperature is still at 200 °C. Then, the power extracted will increase at the same speed than the LBE temperature increase. This can be seen through the curve representing the log mean difference temperature ΔT_{lm} which represents the temperature change in both the water and the LBE. Beyond $t = 60\ s$, the extracted power is stabilized. As well, both temperatures of the water and LBE are stabilized after that time. The change in power extracted and temperature is quite smooth.

As it is a complex design, a prototyping and testing has to be done before validation of the design. It is currently on-going. This testing phase plan:

- Prototyping of the HEX block using additive manufacturing (3D printing) and validation of the part,
- Testing of the HEX block with LBE from 200 °C up to 600 °C.

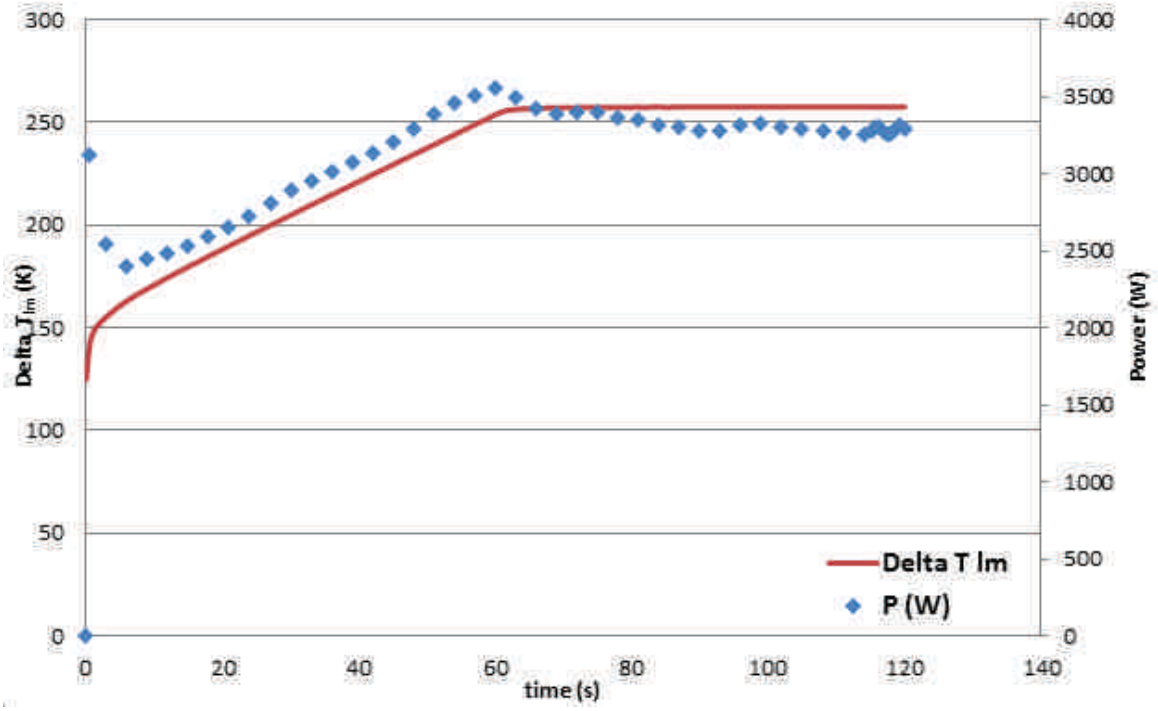

Figure 3.54: Power extracted by the HEX in function of time in comparison with the log mean difference temperature

3.4 Operating a complex unit at ISOLDE: design adaptation

3.4.1 Double enclosure

For safety reasons, a double enclosure surrounds all the LBE loop. This ensures that no LBE can pollute the ISOLDE front end in case of leak or break up of the LBE loop, considered as the first enclosure. As it is a safety measure, it is mandatory to ensure that it will resist in the worst thermo-mechanical situation. To test this resistance, several numerical analyses have been conducted for different severe loading cases:

- Double enclosure at 600 °C, vacuum inside: this case should not occur as the double enclosure is irradiating toward the ambient and as the LBE loop is insulated thus the temperature of the double enclosure will remain lower than 600 °C. However, the material properties of the Stainless Steel will be decreased with temperature. The lowest yield strength will be reached for the highest temperature considered.

- Double enclosure at 600 °C, all LBE at the bottom of the double enclosure in case of a full rupture of the LBE loop: in this situation, the full weight of LBE will be located at the bottom of the double enclosure,

- LBE loop at 600 °C (no insulation considered) and irradiation toward the double enclosure with and without the magnets turning: in this case, the double enclosure will be submitted

to differences in term of temperature field leading to different thermal stresses. This is close to the real situation.

In all cases, the double enclosure should remain under the yield limit of the LBE at 600 °C (worst case scenario). Furthermore, the induced deformation should be low enough to have no impact on the pump coupling of the magnets around the pump pipes.

For all the analysis, the material properties used are given in Table 2.2. It is reminded from this Table that the yield strength of Stainless Steel 316L at 600 °C is 175 MPa.

3.4.1.1 Double enclosure at 600 °C, vacuum inside

This first analysis considers the full vessel at 600 °C and under vacuum. Consequently, 1 bar of pressure is applied on the walls of the Stainless Steel double enclosure. The resulting stress field is presented in Figure 3.55a) while the total deformation obtained is presented on Figure 3.55b). A scaling factor of 10 is applied on the geometry in order to better see the deformations.

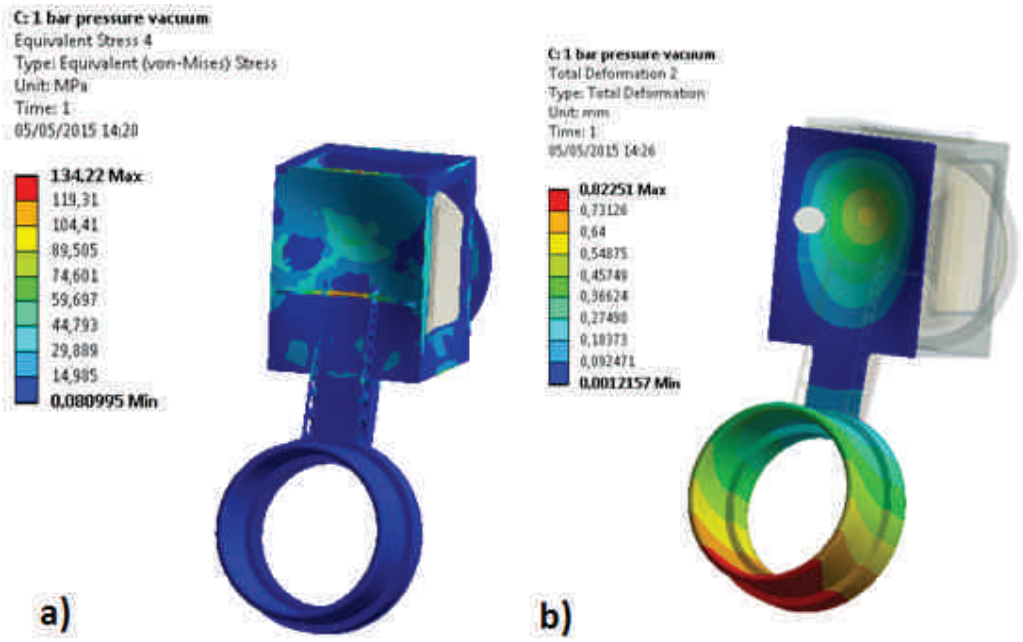

Figure 3.55: Von Mises stress repartition for the vessel at 600 °C and under vacuum

As seen in Figure 3.55, the maximum Von Mises stress reaches 134 MPa which remain under the yield limit with a safety factor of 1.3. The corresponding deformation remains under 1 mm in all directions which is acceptable according to Figure 3.7 where the gaps are shown to be of 4 mm between the double enclosure and the internal magnet and 5 mm between the double enclosure and the external magnet. Consequently, in this loading condition the vessel is considered as safe.

3.4.1.2 Double enclosure at 600 °C, LBE at the bottom of the double enclosure

In case the pipes would break, the full LBE could go at the lowest point i.e. in the circular lower part of the double enclosure, at the pump part, as seen in Figure 3.56.

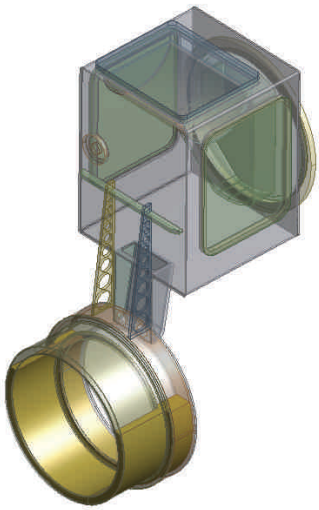

Figure 3.56: LBE representation in case of full break-up of the pipes.

The corresponding Von Mises stresses and total deformation are presented in Figure 3.57.

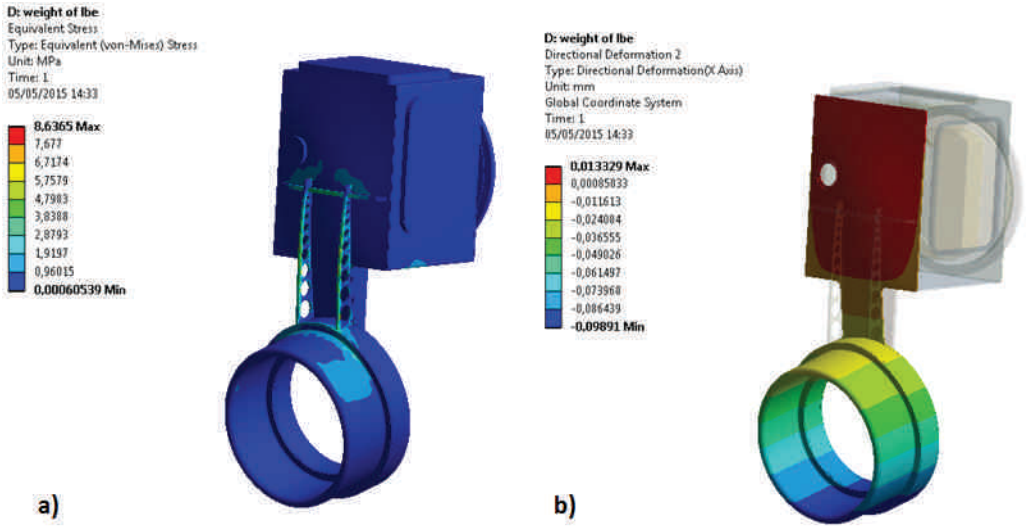

Figure 3.57: Von Mises stress repartition for the vessel at 600 °C with full LBE leak (no vacuum).

Here, no vacuum inside is considered as this is the worst loading case at the bottom part of the double enclosure. Indeed, under vacuum, the part around the pump pipes tends to go to the front as seen in Figure 3.55,b) while it will tend to bend toward the back under the LBE weight.

In terms of stress and deformation, the results are lower than in the previous considered case since this studied case does not consider the vacuum but only the weight of LBE. If taking into

account the two loading cases, the stresses and deformations will remain lower than the first case as the deformations occur in different direction so they compensate each other.

3.4.1.3 LBE loop at 600 °C, no magnets rotation

When the target will be operated, a thermal equilibrium will be reached. This final temperature field can induce high stresses and deformation as the temperature will not be homogeneous on the full part.

An analysis has been conducted in order to assess the thermal equilibrium of the double vessel by considering the LBE loop inside at a forced temperature of 600 °C and a cooling by inter radiation of the loop with the vessel walls. Furthermore, a radiation toward the ambient has been considered for the outside walls.

This gives the thermal equilibrium and corresponding Von Mises stress field presented in Figure 3.58.

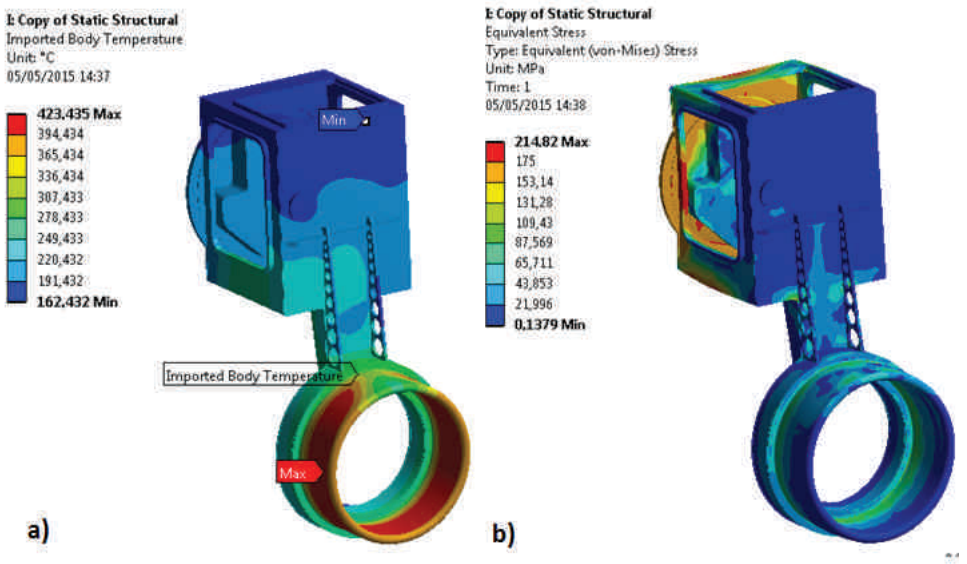

Figure 3.58: Thermal equilibrium for loop at 600 °C and corresponding Von Mises stress field, without the rotation of the magnets.

In that analysis, the cooling due to the forced convection from the pump magnet rotation is not considered (but it will be in the following part).

The corresponding stresses remain in the elastic domain (the parts over the yield limit are here due to the fixed support at the back of the target which is not representative of the real support situation) but very high deformations occur as it can be seen in Figure 3.59.

From this Figure, it is obvious than the induced deformation are not negligible, specifically considering the small gaps of 4 mm between the double enclosure and the internal magnet and 5 mm between the double enclosure and the external magnet as shown on Figure 3.7. For the conducted analysis, no results on the x direction are presented as no dimensional restriction exist on that axis. On the y and z directions, they are remaining under an acceptable limit

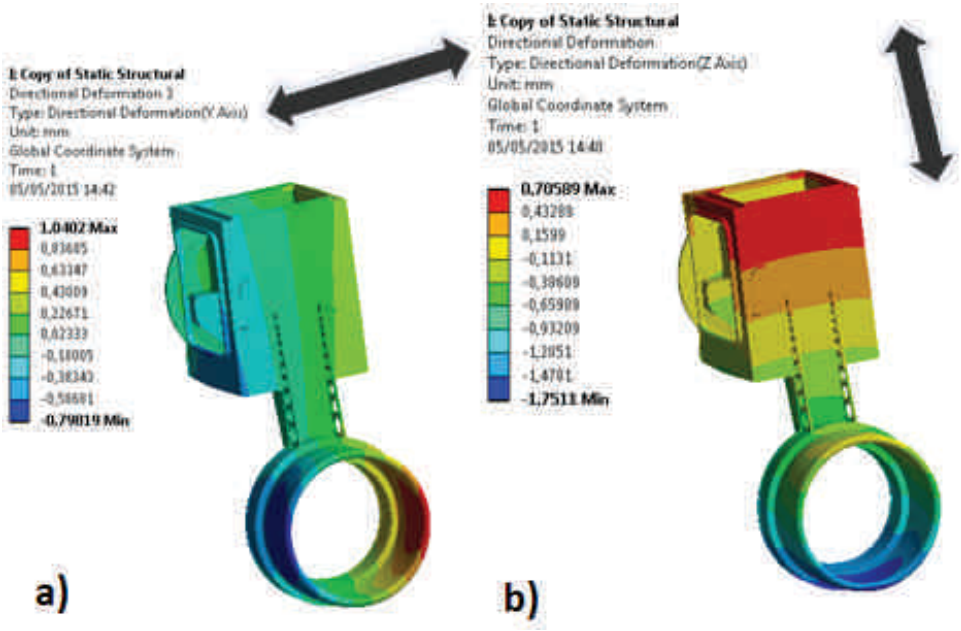

Figure 3.59: Directional deformations for the thermal field presented in the Figure 3.58a)

as the smallest safety factor is here 2.3 (worst case: deformation of 1.75 mm for the internal diameter).

3.4.1.4 LBE loop at 600 °C, magnets rotation

The same analysis has been conducted but considering the rotation of the magnets around the vessel at the pump part. The worst case scenario has been considered i.e. a rotation speed of 420 rev/min. In this configuration, a corresponding convection coefficient estimated analytically as shown in Section 3.3.1.2 is applied onto the walls of the double enclosure. A new thermal field is estimated as seen in Figure 3.60.

Once again, the stresses are acceptable as they are remaining in the elastic domain but the deformations are quite significant as seen in Figure 3.61. However, the induced deformations are lower than without magnets rotation because the thermal field is more homegeneous (see Figure 3.61 vs. Figure 3.58a)) leading to less deformation of the double enclosure.

3.4.1.5 Conclusion on double enclosure integrity

The integrity of the double enclosure is mandatory as it is a safety measure taken in order to ensure that no activated LBE could pollute the front end area. Furthermore, as magnets are rotating around the double enclosure, they should not touch this part at any time of the operation in order not to break the part or transmit any effort to the front end. Its thermo-mechanical behavior has been assessed numerically under several loading conditions. It is shown that for all considered case, the design is safe. In order to achieve these results, reinforcement have been added in the front wall of the double enclosure to minimize the bending of the bottom part compared to the upper fixed one. As well, the gaps between the magnets and the double

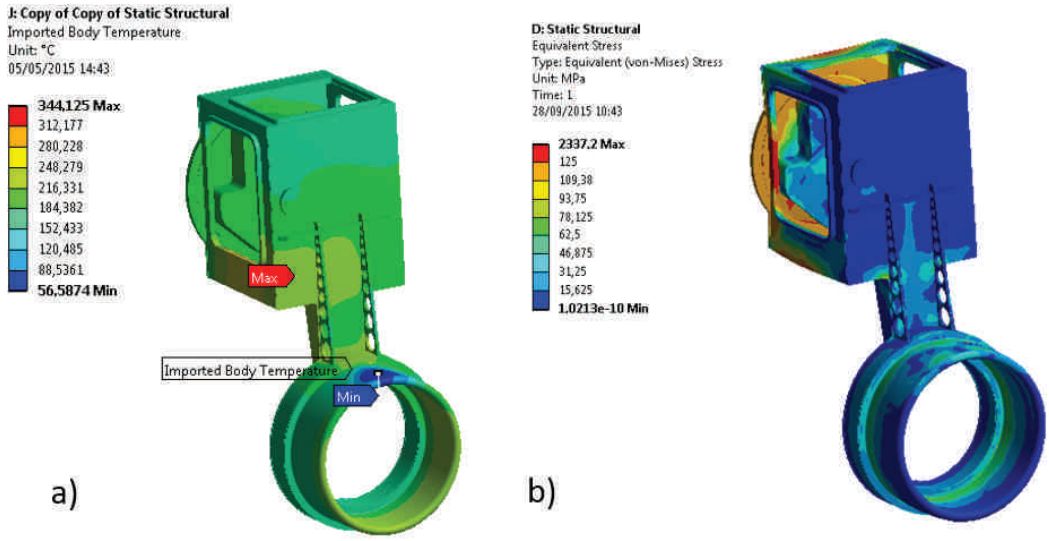

Figure 3.60: Thermal equilibrium for loop at 600 °C and corresponding Von Mises stress field, with the rotation of the magnets at 420 rev/min

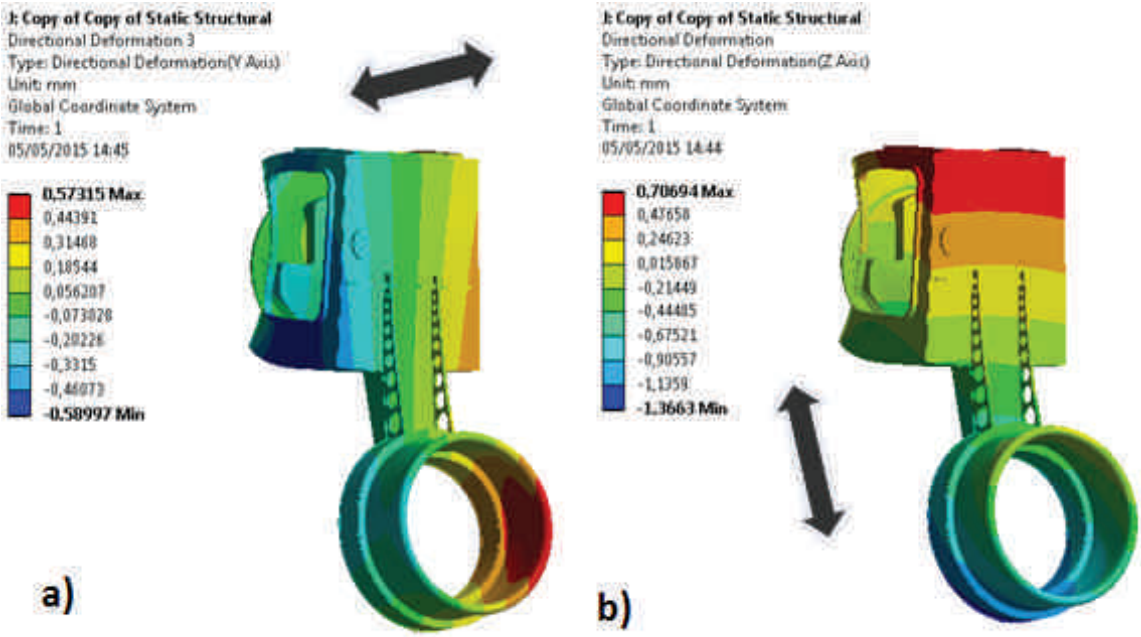

Figure 3.61: Directional deformations for the thermal field presented in Figure 3.60

enclosure have been increased by 1 mm, as compared to the initial design proposed, in order to increase the safety factor.

3.4.2 Monitoring and control of the LIEBE target

So far on standard ISOLDE targets, the monitoring of the target is made thanks to calibration tables made on the off-line front end. This is important as the temperatures are not recorded once the target is installed. When targets operate with thermocouples, these elements sometimes fail. Consequently, in the case of the LIEBE target, the thermocouples will be doubled at each point.

This gives a high total number of thermocouples (37). In order to connect them reliably, it has been decided to make first the mechanical connection of the target to the front end and then the connection of the monitoring elements.

In this case, the target base will only be coupled with the standard feedthroughs as seen in Figure 3.62.

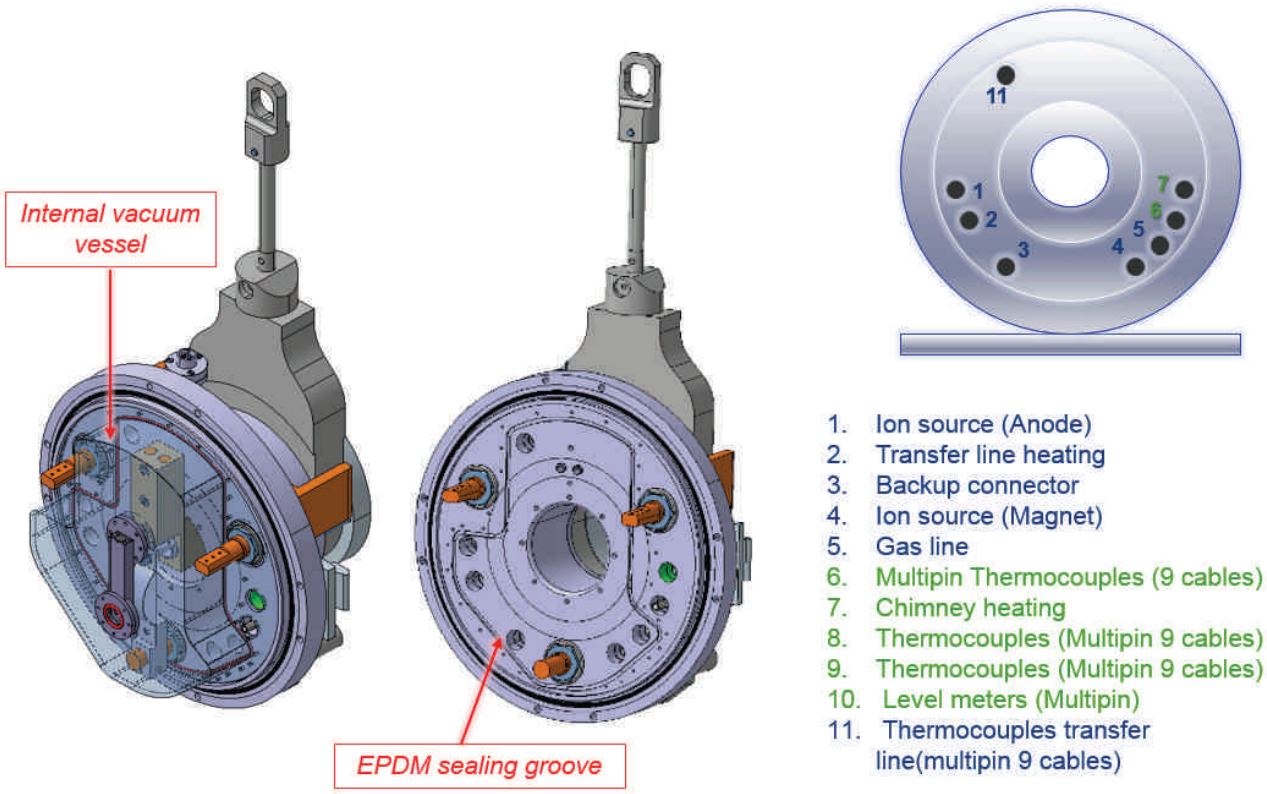

Figure 3.62: Monitoring elements and target base

The elements indicated in blue are in vacuum while the ones indicated in green are in the low pressure gas environment.

A groove of 3 mm is machined on the target base in order to position a EPDM (Ethylene Propylene Diene Monomer) joint inside to establish the vacuum tightness in between the internal vacuum vessel and the low pressure gas. This is needed as the full ion source/transfer line/chimney/LBE circulation must be under vacuum.

However, additional monitoring elements are required. Consequently, several multipin connectors have been added as seen in Figure 3.63. The cables will then go from the different multipins to the connector panel. This connector panel will be connected once the target will be coupled to the front end.

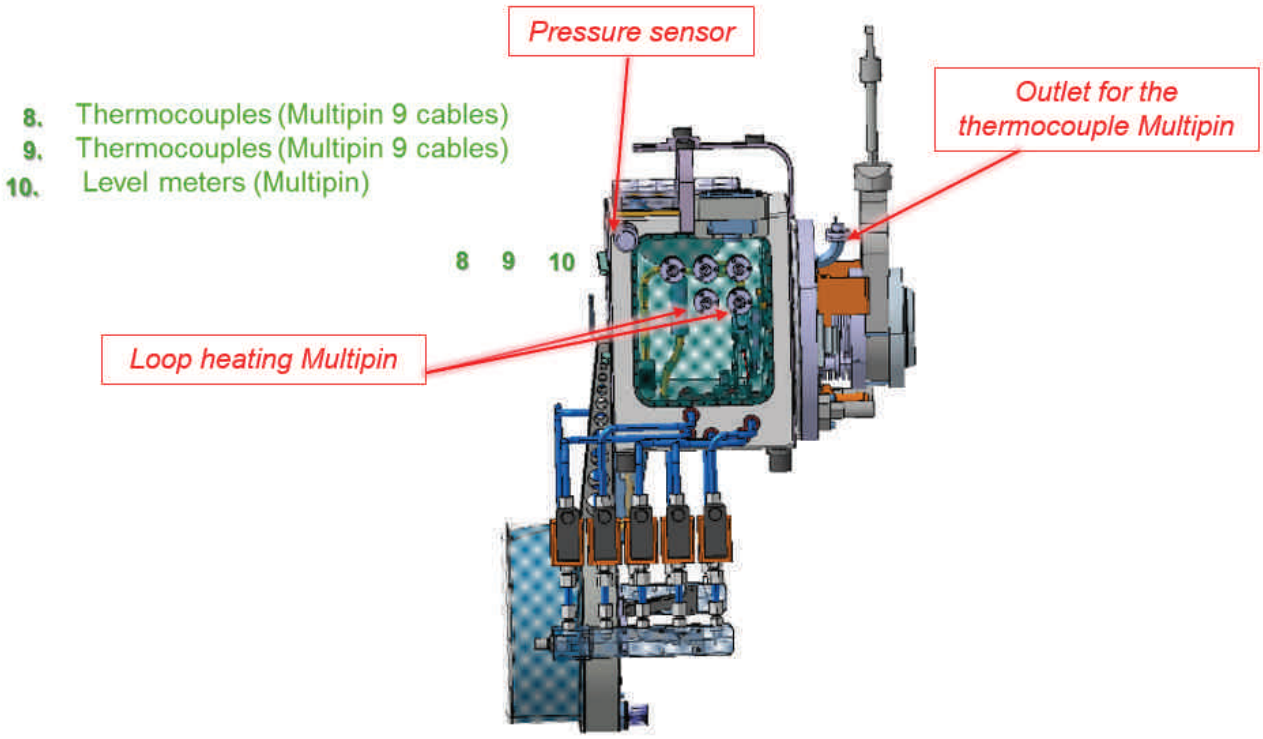

Figure 3.63: Monitoring elements and feed-through

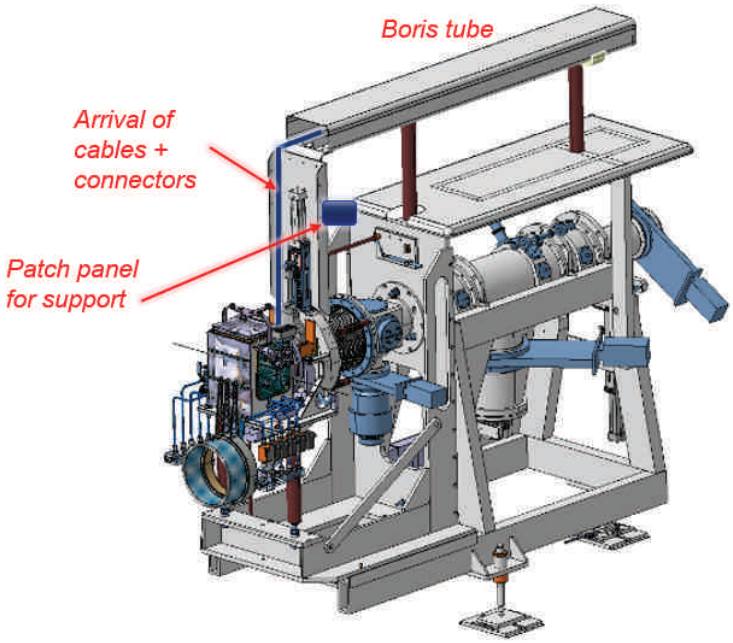

Figure 3.64: Expected cabling for the connector panel

On Figure 3.64, the cables should arrive through a tube (called "Boris tube") that allows the transport of cables from the high tension room where the power supplies are. All the way from the high tension room to the target is put at high voltage (between 30 kV and 60 kV). After disconnecting the patch panel, the part from the front end will be placed with the robot onto an additional patch panel placed on the front end.

3.4.3 Coupling of the LIEBE target - design of the trolley part

As seen in Section 3.1, the target is made of two separated parts: the main loop where the LBE is circulating and the trolley/pump where the pump and its engine are brought on a trolley. The main reason for this is to separate the weight of the main loop target and of the pump. Indeed, the main loop target is brought thanks to the ISOLDE robot which has a weight limitation of 65 kg.

This section will focus on the design of the trolley part. This trolley has several goals:

- Bringing the heavy (about 100 kg) magnets/engine set,
- Maintaining the parts (magnets/engine) in a fixed and precise position compared to the target in order to allow the coupling with the main loop part of the target,
- Translating the magnets,
- Allowing the coupling of the water connectors for the HEX.

The general design of the trolley is presented in Figure 3.65.

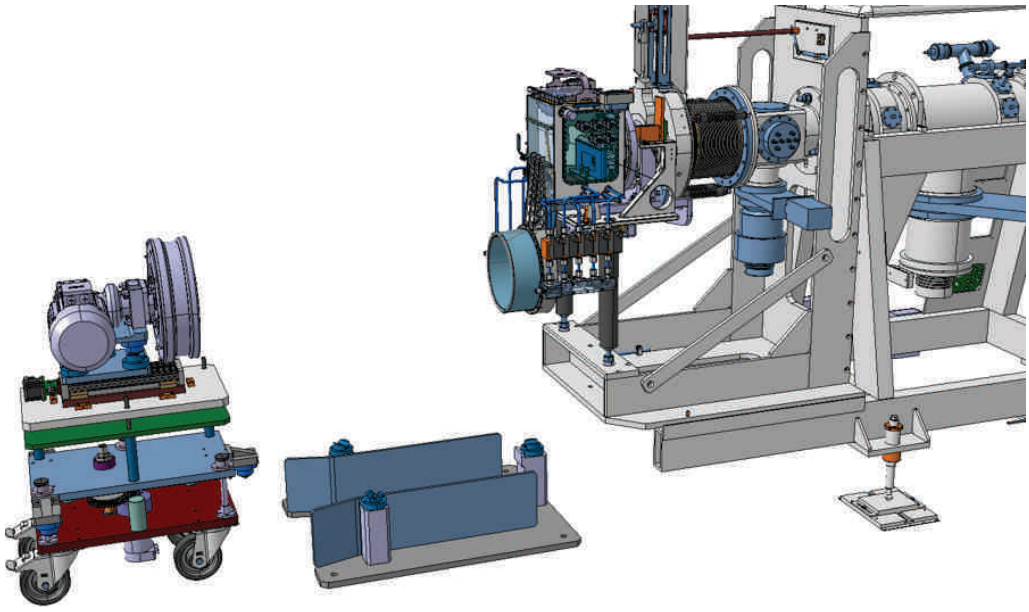

Figure 3.65: Trolley for the connection of the pump and the main loop part

A separated plate is positioned on the floor in front of the front end in order to have a reference point for the positioning of the trolley. On the trolley can be found the pump with the magnets

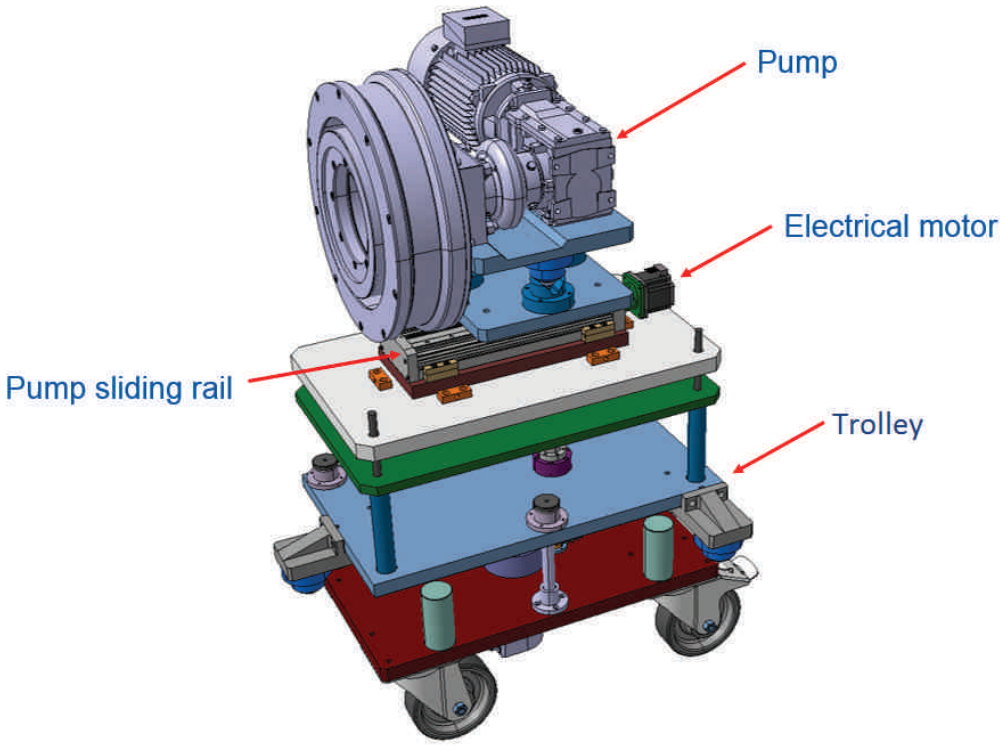

Figure 3.66: Trolley details

and the engine and an electrical motor for the translation of the magnets/engine part on the sliding rail. The precision of the system is under 0.1 mm (see Figure 3.66).

The positioning of the trolley vs the main loop of the target is made separately thanks to the plate positioned in front of the front end and on which the trolley will lay on. The plate will be installed at the position needed thanks to reference points installed on the main target itself. The use of a separated plate allows to ensure that no effort from the coupling will be transmitted to the front end. This is important not to damage the front end.

The trolley is brought and positioned thanks to the reference plate. Then, thanks to a motor with gearbox (see Figure 3.67), the support points and full upper part of the trolley are going down onto the positioning points (see Figure 3.68). Finally, the wheels are going up in order for the trolley to only rest on the positioning plate and to be completely disconnected from the floor.

The control of the different motors and actuators will be done through a control panel similar to the target one and that will be positioned onto the trolley.

The complete procedure of operation of the LIEBE target at ISOLDE is described in Appendix B.

3.5 Conclusion on the proposed LIEBE target design

A high power liquid loop target has been developed in the frame on the LIEBE project. This target answers the problematic related to high power target while improving the release of short

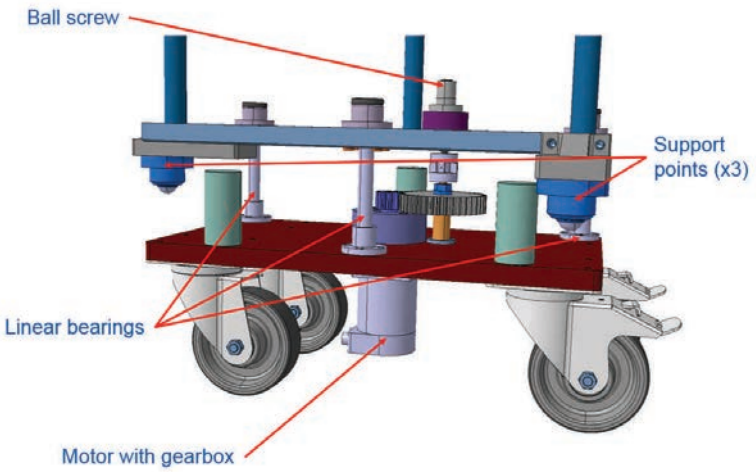

Figure 3.67: Trolley for the connection of the pump and the main loop part

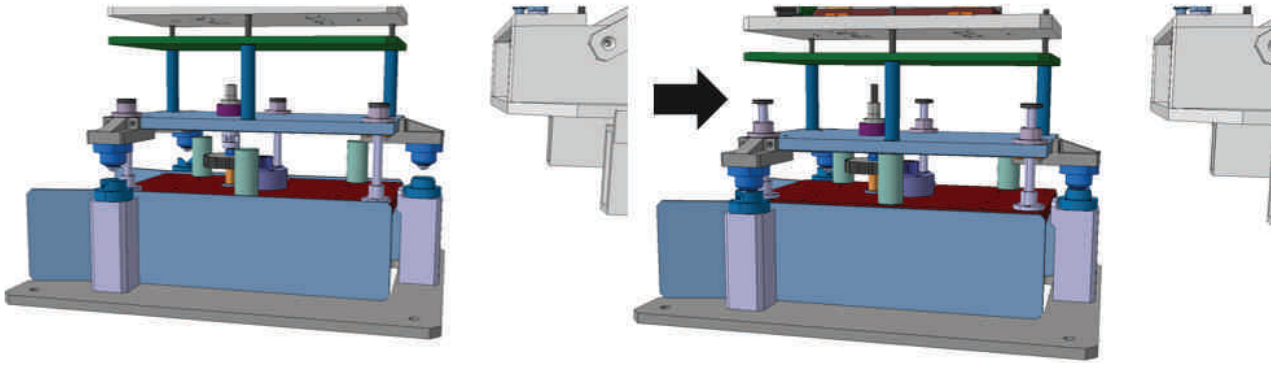

Figure 3.68: Trolley for the connection of the pump and the main loop part

lived species. Furthermore, all the required elements specified during the Eurisol design study phase (Figure 1.27) have been integrated in a target unit answering the requirements of the Isolde environment. Amongst them, the dimensions constraints which required the target to fit in a general box of about 300*300*800 mm (L*l*H).

More specifically, the developed target makes use of an electromagnetic pump, ensuring a double enclosure around all LBE circulating elements. Additional elements of control have been implemented as the number of thermocouples has been multiplied by 10 compared to a standard ISOLDE unit.

The pulsed proton beam impacting into the target will have several consequences: shock waves propagating in the LBE and transmitted to the target irradiation chamber as well as power in the order of few kW in average for about 1 GW during the peak beam impact deposited onto the liquid. The stresses induced by the shock waves have been analyzed and validate the proposed design. Furthermore, complementary analyses have been done by the StudieCentrum voor Kernenergie (SCK-CEN) in Belgium. The heat brought by the beam impact has been assessed and taken into account in the thermal equilibrium of the loop target.

The control of the loop temperature is performed by the use of 26 wires heating elements but also thanks to the developed heat exchanger. This heat exchanger, that will be produced by additive manufacturing, is LBE temperature dependent as different water channel are planned and that the choice of use of one or the other channel will be done by the operator in function of the target temperature. The design allows a certain flexibility as several channels can be used for a same temperature. This heat exchanger will extract a certain amount of power and the thermal regulation is done thanks to the heating elements.

The developed target aims to optimize the release efficiency of short life species. In case of the isotope of interest ^{177}Hg, it has been shown an expected improvement of 8.2% compared to the yields measured at ISOLDE with a pulsed proton beam onto a Lead target. The yields measured in the past with a Lead target are hardly reproducible from one unit to the other one. The developed LIEBE target is expected to operate on a stable way even for short lived species.

Finally, the proposed design has been validated thanks to thermo-mechanical analysis, ensuring its mechanical integrity under several thermal loading conditions. A procedure of use of the target is proposed for a better understanding of its operation at ISOLDE.

Chapter 4

Formation of droplets with Lead Bismuth Eutectic (LBE)

Introduction

In Chapters 2 and 3 (part 2.3.2.2 and 3.2.1.2), it has been shown that a small size droplet will increase the diffusion driven release efficiency of the created isotopes. The smaller the droplets, the faster the diffusion out of the droplets and thus, the higher the total release efficiency. This is of major importance for the LIEBE target since one of its main goal is also to improve the release efficiency of short lived species.

Consequently, a shower is created within a diffusion chamber by pushing the liquid LBE through a grid. The geometric parameters of this grid are of major importance and it has been demonstrated in Section 2.3.2.2 that the constituting holes characteristic diameter must be minimized while, at the same time, the holes surface fraction should be maximized.

This chapter presents the series of tests that has been conducted at CERN in order to assess both the feasibility of sub-mm diameter holes and of the creation of a proper shower of LBE droplets.

First we present the test bench used for the experiments and its different components, in particular the grid used.

Second, the equations used are detailed and correlated to the theoretical expectation. The proposed correlation is then used to analyse the experimental results.

Finally, a discussion about the results and possible improvements is proposed.

4.1 General considerations

From the theory introduced in Section 2.3.2.3, the regime of droplet formations will influence their sizes. For a 100 μm grid hole diameter, the droplet will be of 1.3 mm diameter in case of dripping regime or of 0.4 mm diameter in case of jetting (see Section 2.3.2.3), clearly favouring the jetting regime to meet our goals. From a geometrical consideration, it also implies that the

minimum inter axis distance between successive holes is of 0.4 mm to prevent the merging of two neighbouring droplets.

In such configuration, the formed droplets would be in contact but should not merge by coalescence. An experiment has been conducted to verify this prediction in real conditions with the purpose of determining the following characteristics:

- What is the minimum distance in between holes in order to create separated droplets,
- Which droplets diameter is generated for various regimes thus flow velocity,
- What is the critical Weber number above which the dripping regime evolves toward the jetting regime for LBE at 200 °C.

4.2 Test bench presentation

4.2.1 General overview

The principle of the test is shown on Figure 4.1. A certain volume V of LBE is forced by gravity through a grid (5) clamped between two joints and pictures of the shower are taken. 5 different grids have been tested, each of them with a different inter axis distance between two successive holes of 100 μm in diameter to determine its minimum acceptable. The shower is formed after the grid. The volume V is controlled by two valves (upper valve (2) and middle valve (4)).

The upper tank is dimensioned to make 5 consecutive tests before a new filling is required. The shower develops inside a bottom tank (6) equipped with two glass windows in order to take pictures of the droplets thanks to a camera (aperture time: 1/60 sec) and a flash of white light positioned at 90 degrees.

The whole system is kept under a 10^{-3} mbar vacuum thanks to a vacuum pump, pumping constantly, while the pressure is monitored through a pressure sensor, as shown in Figures 4.2 and 4.3.

A camera is installed in front of the shower while a flash light is positioned at 90 degrees and is triggered with a flash for each picture. It should be noted that 5 pictures were taken per second, every 200 ms. This limit was defined due to the flash capability.

The full system is kept at 200 °C thanks to heating wires. The temperature is monitored thanks to thermocouples positioned in three different zones of the test bench: the upper tank, the column and the bottom tank. Feedback control is used on the power supply of each heating element to maintain the desired temperature (see Figure 4.4).

The temperature of the bottom tank in which the shower develops is monitored thanks to a multimeter (see Figure 4.5).

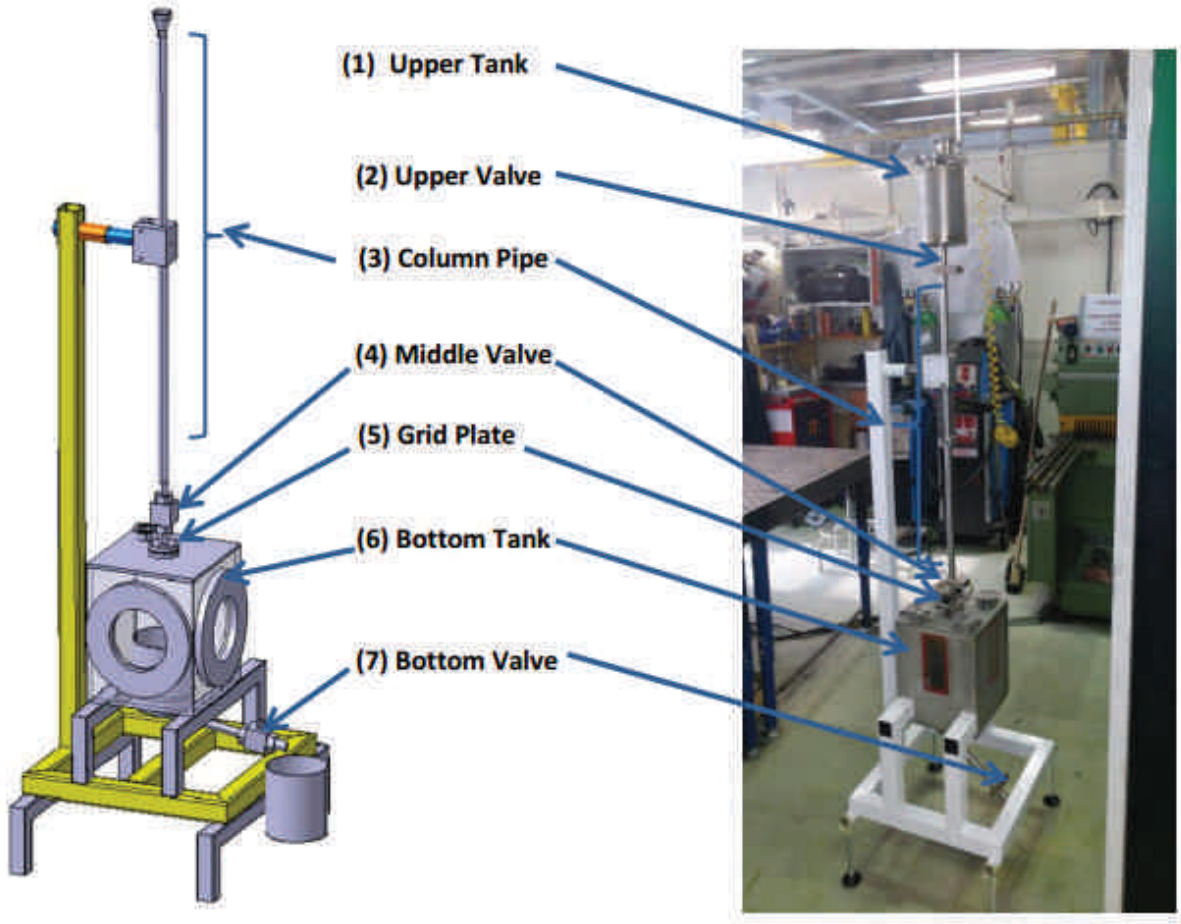

Figure 4.1: Test bench used for the assessment of the LBE shower before the use of heating elements and insulators

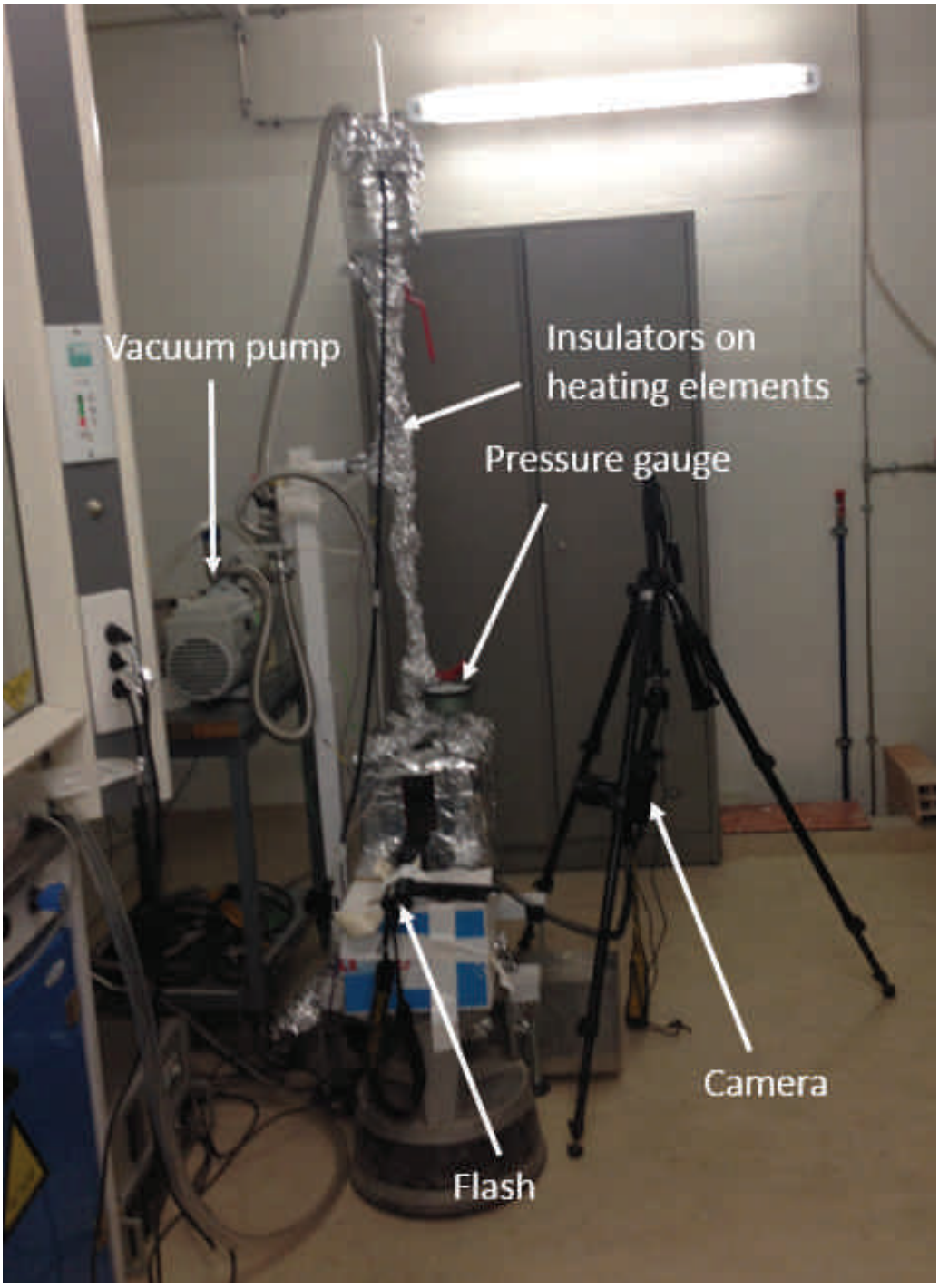

Figure 4.2: Test bench in the laboratory

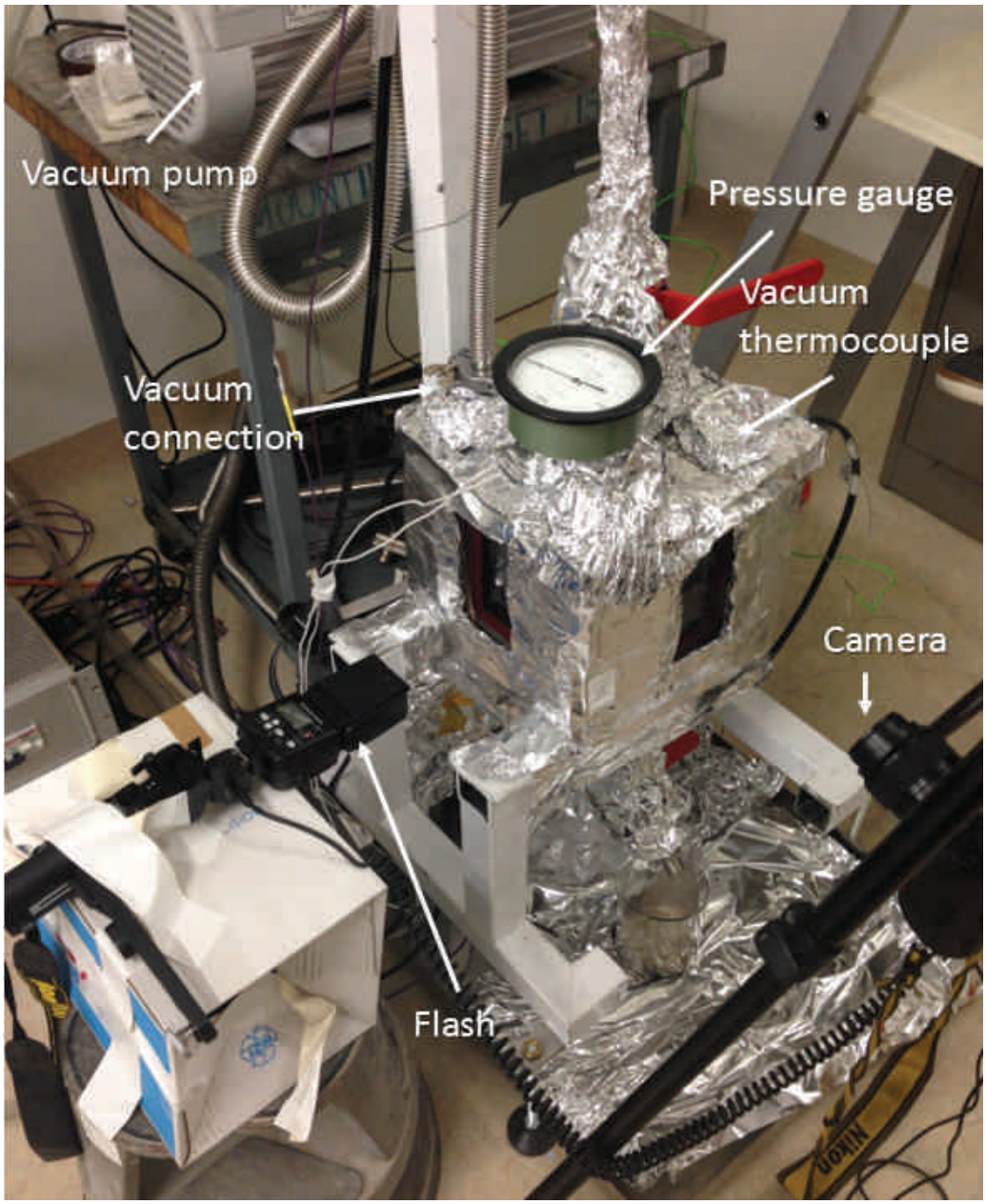

Figure 4.3: Detail of the test bench

Figure 4.4: Regulation system for the temperature regulation of the test bench

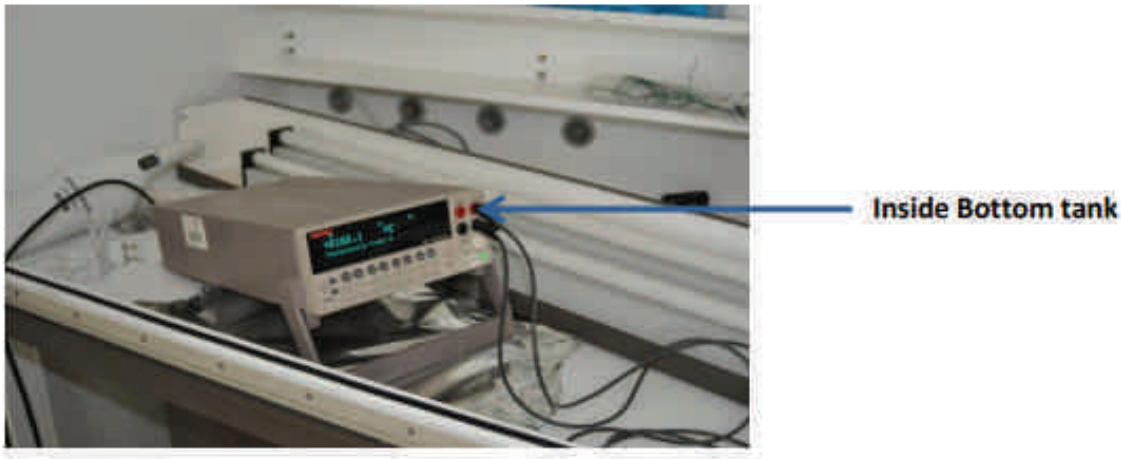

Figure 4.5: Thermocouple reading inside the vacuum - bottom tank

4.2.2 Grids

Five different grids have been used for the assessment of the shower formation. Their general representation is shown in Figure 4.6 while its characteristics are summarized in Table 4.1.

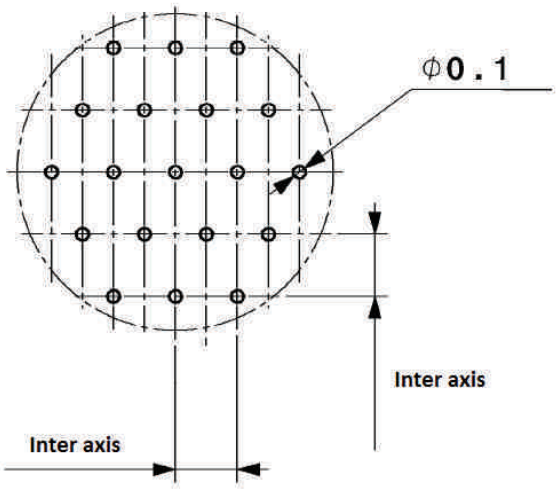

Figure 4.6: General representation of the holes for the grids

Grid reference	Holes inter axis *(mm)*	Distance between holes *(mm)*	Number of holes
1	0.4	0.3	2 116
2	0.5	0.4	1 444
3	0.6	0.5	961
4	0.8	0.7	576
5	1	0.9	400

Table 4.1: Main characteristics of the tested grids

The grids have been produced by laser drilling after having tested of other manufacturing techniques such as mechanical drilling and 3D printing. Once the holes were made, the grid has been cleaned thanks to an ultrasound bath and demineralised water. The geometrical precision of the grid and the morphology of the holes were assessed by optical measurements. The measured diameters and inter axis distances are presented in Figures 4.7 and 4.8.

The data shows that the average diameter is of 120 μm $^{+50\mu m}_{-40\mu m}$ while the distance between holes had a tolerance of $^{+80\mu m}_{-30\mu m}$ with a few holes very close from each other (around 100 μm) [69]. The difference in the spacing between holes was due to the fact that the holes were slightly bigger than requested.

It has been also noticed that the holes do not exhibit a constant diameter across the plate thickness. Indeed, and this is characteristic of the laser drilling process, the diameter is about 50 % larger at the entrance compared to the exit as shown on Figure 4.9. For this reason, the grid must be positioned with the exit of the laser drilled holes at the exit side of the grid when installed for the creation of the shower.

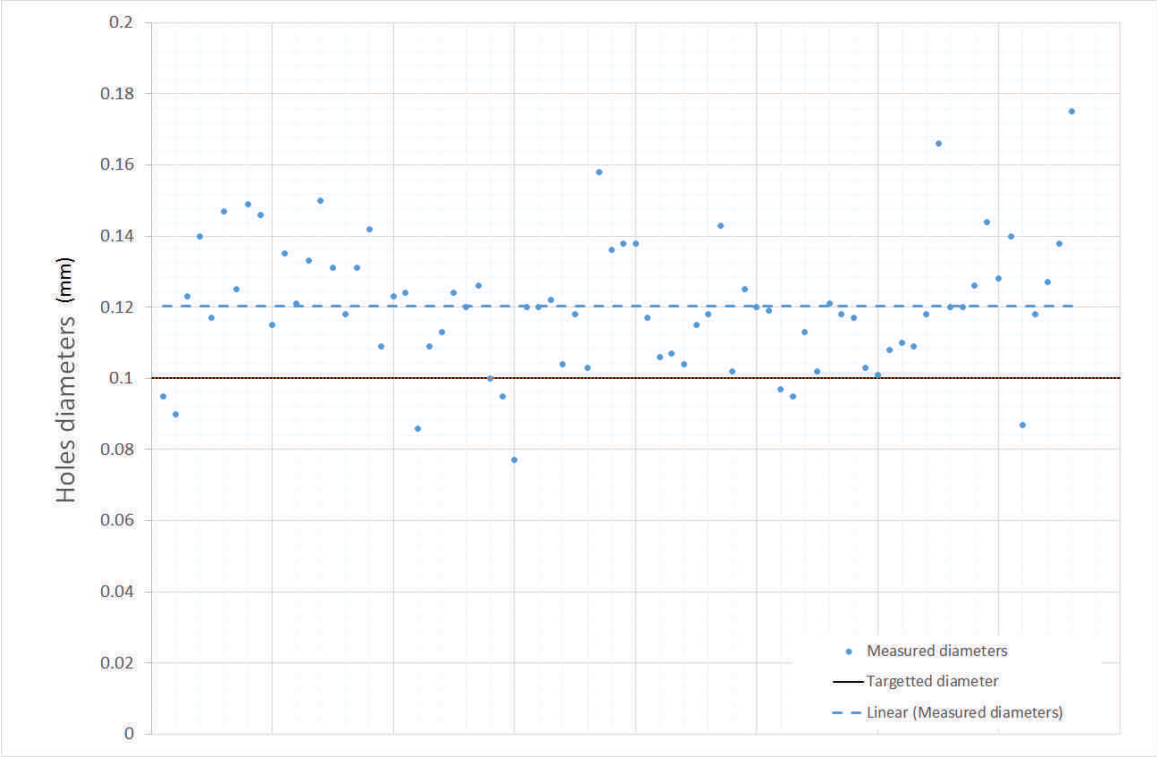

Figure 4.7: Measured diameters for laser drilled plate

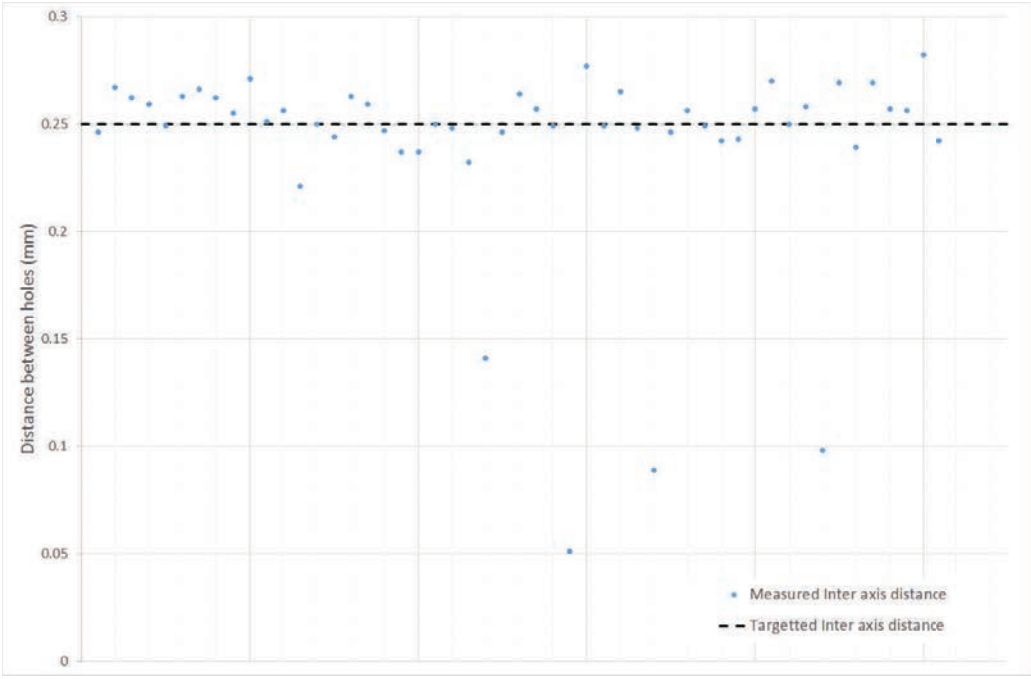

Figure 4.8: Measured inter axis diameter for a laser drilled plate (75 points measured)

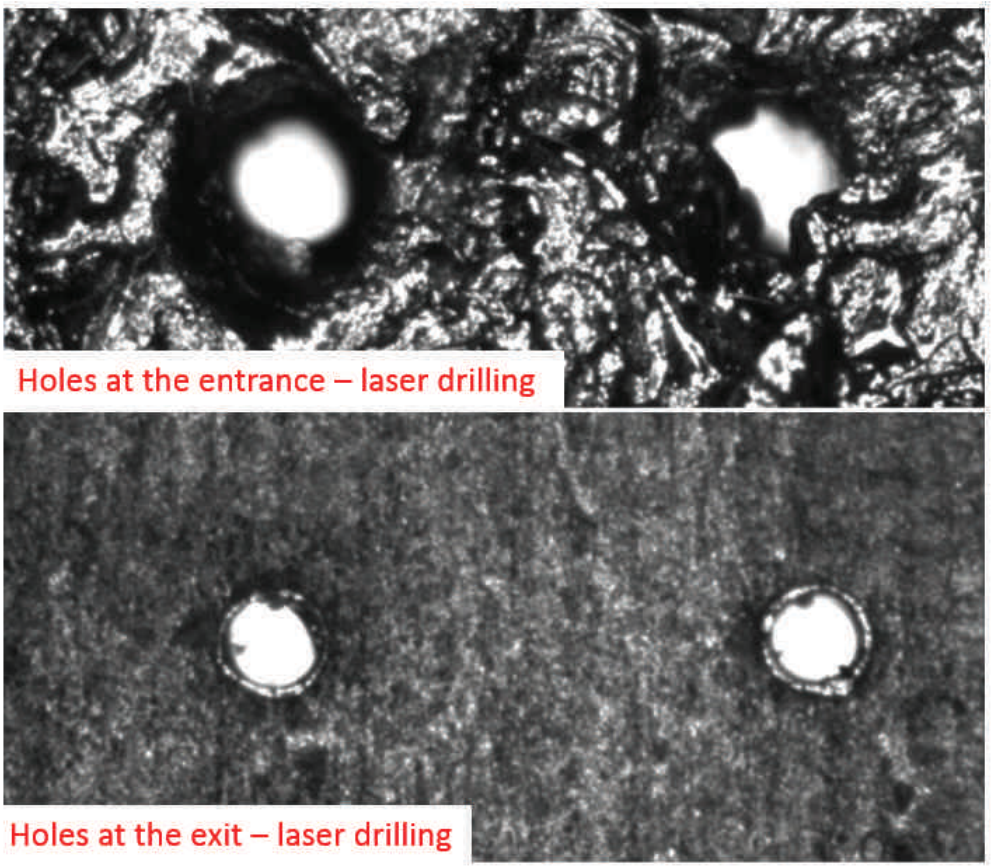

Figure 4.9: Visualisation of the laser drilled holes at the entrance and at the exit of the plate

4.3 Shower formation and regimes

4.3.1 Theory

The purpose of the conducted tests is to link the droplet velocity and its size for each of the pictures i.e. at different given time. To do so, it is necessary to first estimate at each time of the draining what the outlet velocity *v(t)* of the droplets would be. To a given time t_g corresponds a velocity $v(t_g)$ that can then be related to a regime of droplet formation. To this same time t_g corresponds a picture on which the droplets dimensions can be estimated. The combination of both informations allows the validation of droplets dimensions in function of the velocity and allows also the estimation of the limit Weber number between the dripping and the jetting regime.

There is different possible ways to estimate the outlet velocity of the droplets:

- Using a fast camera and follow one droplet on a series of pictures,
- Estimating analytically the velocity, from estimation of some parameters,
- Using laser-induced fluorescence [70],

The use of a fast camera has been chosen for the tests conducted during the EURISOL design study phase. This was feasible as the test was conducted with special grids in which only 3 holes were available for measurements in the middle of the grid. This induced nicely separated jets and droplets, making possible the use of a fast camera. In our case, the density of the shower is too high for the use of a fast camera.

Scientific instruments such as laser or speedometer require to acquire specific knowledge for a proper use. Consequently, in the present test, the estimation of the velocity has been done by analytical correlation.

To correlate the velocity of the exiting droplets with time, one can define the height of the column H versus time t by using the continuity equation and the Bernouilli's principle. Indeed, let's consider a simple representation of the test column and of the grid as shown in Figure 4.10a. Here, for a simplification purpose, the grid is represented by only one hole.

The analytical estimation of the velocity *v(t)* will be done in several steps:

- Analytical estimation of H(t)
- Analytical estimation of the minimum force (and thus, height) to counter balance the surface tension of the fluid and thus, allow the flow of liquid through the holes,
- Analytical estimation of v(t) based on H(t).

Applying Bernouilli's principle [26] and considering two points 1 and 2 located on a streamline, it comes:

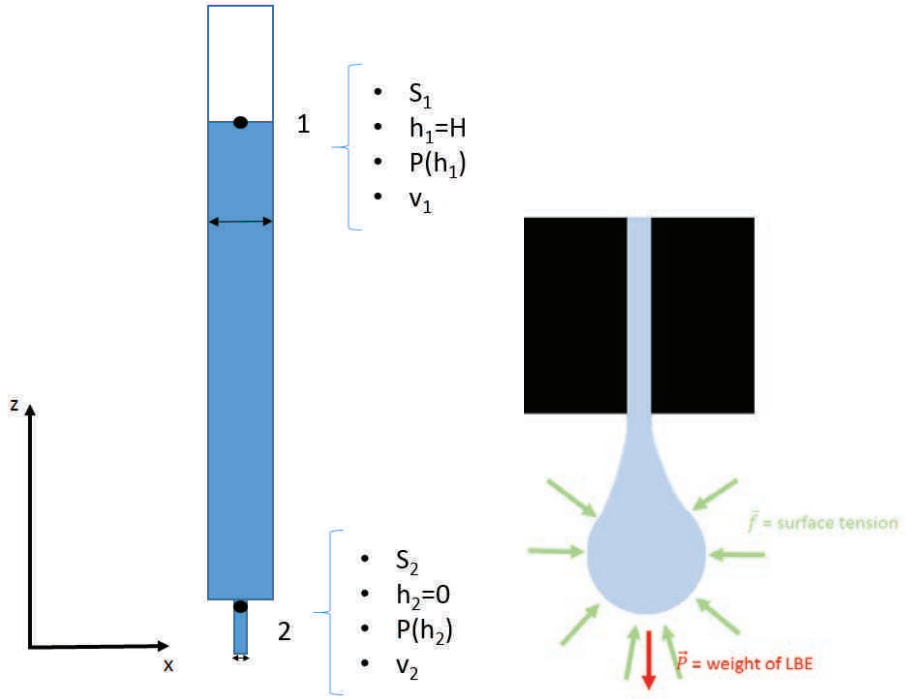

(a) Simplified representation of the test bench

(b) Forces on droplet at equilibrium

Figure 4.10: Simplified model and forces on droplets

$$\frac{1}{2}.\rho.{v_1}^2 + \rho.g.h_1 + P_1 = \frac{1}{2}.\rho.{v_2}^2 + \rho.g.h_2 + P_2 \tag{4.1}$$

with v is the fluid flow velocity at a point on a streamline in m/s, g is the gravity constant (9.81 m/s^2), h is the elevation of the point above a reference plane in m, P is the pressure at the chosen point in Pa and ρ is the fluid specific mass in kg/m^3.

As the full column is under primary vacuum, P_1 and P_2 can be both considered to be equal to 0. Furthermore, let's fix $h_1 = H$ and $h_2 = 0$. Finally, the velocity of all particles located at the free surface is equal to 0 as they are locally at rest. Here, it is not the fluid that is considered and thus not the continuity equation that is applied, but a particle movement considered locally motionless compared to the fluid itself. So it comes:

$$v_2 = \sqrt{2.g.H} \tag{4.2}$$

This condition is fulfilled as long as the pressure due to the LBE weight is higher than the surface tension. Indeed, for the liquid to be forced through the holes of the grid, a minimum height is required.

In order to vary the external surface of liquid of a dS quantity, an energy dE proportional to a quantity γ called surface tension in N/m [71]:

$$dE = \gamma.dS \tag{4.3}$$

Physically, the energy required to deform this external surface finds its origin in the cohesive forces among the liquid molecules. The deformation energy dE is then the result of a force called the surface tension force f, along a path perpendicular to the periphery of the surface dr [71]. It comes hence:

$$dE = f.dr = \gamma.dS \tag{4.4}$$

Here, the surface of LBE at the exit of the hole is in equilibrium if the different forces balance each other (see Figure 4.10b). This concerns mostly the surface tension and the weight of the LBE column (the simplified model does not consider any possible chemical reaction in between the liquid and the grid which could form species that could modify the surface tension or any physical adhesion of the liquid on the grid):

$$F = f - \rho.g.H.S_2 \tag{4.5}$$

Here again, the effect of the atmospheric pressure is neglected versus other effects as the full column in under primary vacuum. The resultant F is negative (and thus, the movement of the fluid toward the bottom) if the surface tension is not balancing the force due to the weight:

$$F < 0 \quad \text{for} \quad f < \rho.g.H.S_2 \tag{4.6}$$

Furthermore, according to Equation 4.4, it comes:

$$f = \gamma.\frac{dS_2}{dr} \tag{4.7}$$

For a circular surface of radius r, a radial increase in the surface $dS_2 = d(\pi.r^2 = 2.\pi.r.dr)$ corresponds to an increase in the surface tension force:

$$f = 2.\pi.\gamma.r \tag{4.8}$$

This induces that a minimum height H is required to allow the liquid flowing through the grid:

$$H > \frac{2.\gamma}{\rho.g.r} \tag{4.9}$$

Using the surface tension data in Table 2.1, and considering a 100 μm hole diameter, it comes that the minimum height required for the liquid to flow through the grid is about 16 cm.

The distance between the two valves (upper and middle valves) on the test bench has been set at 96 cm, to have at least the 80 cm available (*i.e.,* 96-16 = 80) for the shower formation.

To correlate the height of LBE with the time, one should consider the continuity equation. It comes that the mass of LBE flowing through the section S_2 (cf Figure 4.10a) at a velocity v_2 is the same than the mass moving in H through the section S_1 at a velocity v_1:

$$v_1.S_1 = v_2.S_2 \tag{4.10}$$

Since the velocity v_1 is equivalent to the variation of the height H of the column per unit of time t, it comes:

$$v_1 = dH/dt \tag{4.11}$$

Considering Equations 4.2, 4.10 and 4.11, and rearranging them, it comes:

$$\frac{dH}{dt} = -\frac{S_2}{S_1}.\sqrt{2.g.H} \tag{4.12}$$

By integrating Equation 4.12 and considering that at the final time t_{max} the height H is equal to H_0, it comes:

$$t_{max} = \frac{S_1}{S_2.g}.\sqrt{2.H_0.g} \tag{4.13}$$

As well, the height H can be expressed in function of time:

$$H(t) = H_0.(1 - \frac{S_2}{S_1}.\sqrt{\frac{g}{2.H_0}}.t)^2 \tag{4.14}$$

With H_0 the initial height of LBE in m. The expression of the height of liquid in the column versus time is thus a quadratic function decreasing in magnitude versus time. This expression is valid as long as:

$$t \in [0; t_{max}] \tag{4.15}$$

The height of the test bench and the column diameter are reported in Table 4.2.

Parameters	**Unit**	**Value**
ϕ column	mm	29.7
H_0	mm	800

Table 4.2: Dimensions used for the calculation - test bench

4.3.2 Velocity versus time

4.3.2.1 Validation tests

For each grid, 4 to 6 different showers have been performed consecutively. The column was filled back following the precedent test to be able to create the next shower. The time for each

shower represents the duration defined by the first droplets formation and the time when only a few droplets were generated and thus, the equilibrium was reached.

The experimental measured times are shown in Table 4.3 together with the theoretical one calculated with Equation 4.13 .

		Grid 1 (0.4 mm inter-axis)	**Grid 2 (0.5 mm inter-axis)**	**Grid 3 (0.6 mm inter-axis)**	**Grid 4 (0.8 mm inter-axis)**	**Grid 5 (1 mm inter-axis)**
Time (s)	$t_{theoretical}$	16.8	24.7	37.1	61.8	89.1
	Shower 1	46	121	50	180	274
	Shower 2	60	135	123	165	298
	Shower 3	66	134	117	125	383
	Shower 4	78	140	115	180	388
	Shower 5	77	138	149	181	
	Shower 6	82	150	148	229	

Table 4.3: Time for each shower

To be noted that the tests have been conducted in the following order: grid 5, grid 4, grid 3, grid 1 and grid 2.

A clear difference between the theoretical expectation and the data are reported: the measured time are systematically several times higher than the theoretical ones. Furthermore, the duration is not constant over the consecutive showers for a same grid: it systematically increases. The timing for the grid 2 is higher than the grid 3 which is absolutely counter intuitive. An additional effect, not considered in the modelling, must be at the origin of this observation.

It is suspected that the oxidation of LBE plays a significant role here. During the test, it has been clearly identified that the LBE was reacting with oxygen and created an oxide layer at the free surface of LBE after only a few minutes (cf Figure 4.11).

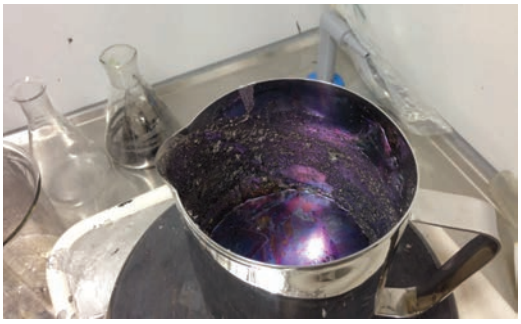

Figure 4.11: Beginning of oxidation process

After about 1 hour, the layer developed further until it formed a solid crust on top of the liquid LBE (Figure 4.12).

This was not anticipated and thus, no specific care has been taken when conducting the tests to avoid interaction in between LBE and oxygen. The test bench, even though the tests were conducted under primary vacuum, was put under oxygen at several occasions during the filling of the upper tank.

Figure 4.12: Crust of LBE oxide

Oxide was also seen inside this tank (Figure 4.13) and it is clear than from the very first shower, LBE oxide was present inside the column. As a consequence, solid oxide can partially or fully penetrate in the holes of the grid, leading to a decrease of the holes diameter, inducing in the worst cases clogging.

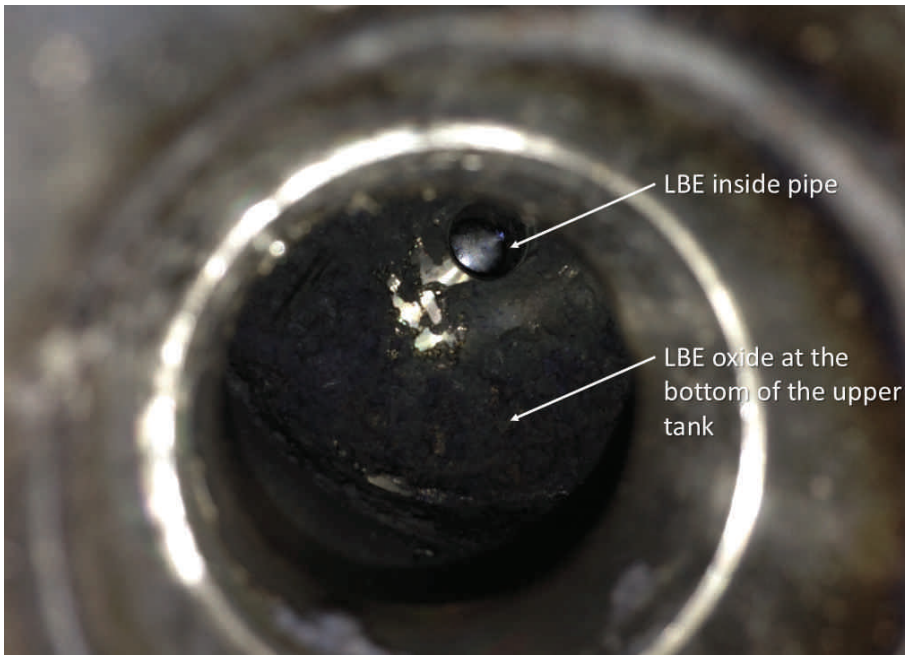

Figure 4.13: LBE oxide inside the filling upper tank

This implies that Equation 4.14 must be modified in order to take into account the induced clogging. Indeed, the surface of the holes will decrease as some of the holes will be blocked by the oxides as shown on Figure 4.14.

Let's reconsider Equation 4.14 in order to take into account this reduction of holes surface due to the oxide blocking part of the holes over the duration of the shower. Here, the surface of the holes is represented by S_2. In reality, S_2 varies over time. Consequently, we have taken S_2 versus time to a first approximation that is a decreasing linear function:

$$S_2(t) = -a + bt \tag{4.16}$$

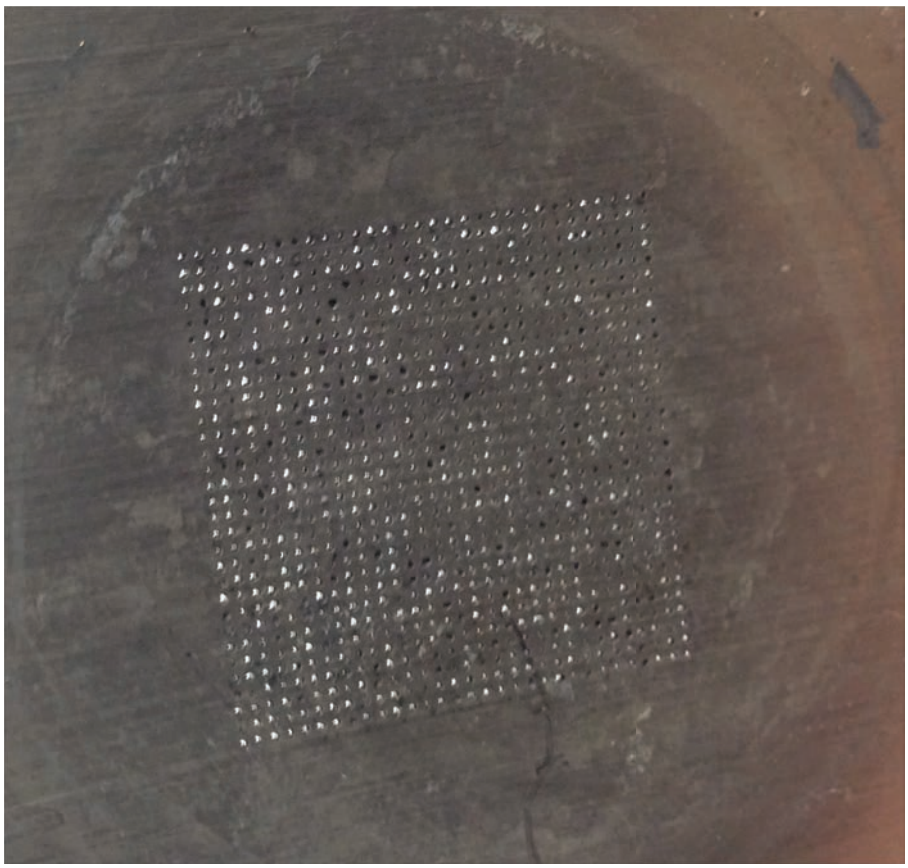

Figure 4.14: Grid after test - about 40 % of holes blocked by oxide

Physically, a represents the holes surface area at $t=0$ of the shower which means at start while $(-a+bt_{max})$ represents the surface at the end of the shower.

No evidence exists to assume what a more realistic function would be. Consequently, the height of liquid in the column over time can be expressed as follows:

$$H(t) = H_0.(1 - \frac{(-a+bt)}{S_1}.\sqrt{\frac{g}{2.H_0}}.t)^2 \tag{4.17}$$

Equation 4.17 can be used to express a in function of b and t using Matlab:

$$a = \frac{-S_1 + b.\sqrt{\frac{0.5.g}{H_0}}.t_{max}}{\sqrt{\frac{0.5.g}{H_0}}.t_{max}^2} \tag{4.18}$$

Here again, the function $H(t)$ should be a quadratic function valid only in the $[0; t_{max}]$ range. However, the expression of $H(t)$ according to Equation 4.17 is a polynomial function of 4^{th} order. This means that the $(a;b)$ parameters pairs will take accepted figures to allow the polynomial function of 4^{th} order to become degenerated to a polynomial function of 2^{nd} order, as shown in Figure 4.15.

The $(a;b)$ parameters pair has been evaluated by iteration for each shower until the function $H(t)$ had one absolute minimum over the $]-\infty;+\infty[$ range.

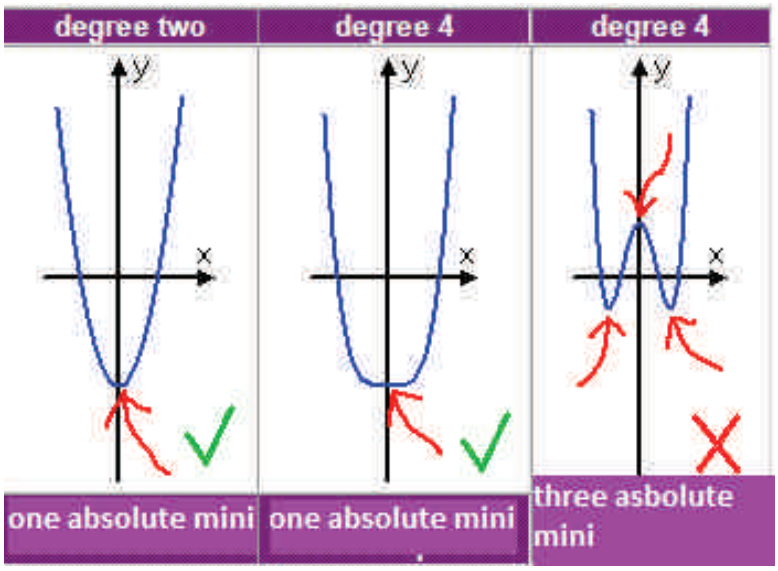

Figure 4.15: Plots of polynomial functions

The function of *v(t)* has then be obtained by considering Equations 4.2 and 4.17. By replacing the constant H in Equation 4.2 by its time dependent function *H(t)*, from Equation 4.17, *v(t)* takes the form:

$$v(t) = \sqrt{2.g.H_0.(1 - \frac{(-a+bt)}{S_1}.\sqrt{\frac{g}{2.H_0}}.t)^2} \tag{4.19}$$

The function *v(t)* is a quadratic function as *H(t)*. It is valid in the same range $[0; t_{max}]$.

4.3.2.2 Visual observations

First of all, the visual observations allowed classifying the shower into two distinctive categories as presented in Figure 4.16:

- Category 1: droplets initially separated at the exit of the holes, which remain separated during their flight (Figure 4.16a),
- Category 2: droplets initially separated, that form larger droplets by coalescence (Figure 4.16b).

The Category 2 droplets are obviously much larger than predicted and thus, this is not a suitable configuration for the present work. The shower of the LIEBE target should hence belong to Category 1. All created showers show a proper separation of the droplets except in the case of the grid with inter axis of 0.4 mm (shown in Figure 4.16b). This may be due to the error on the holes diameters that might make the droplets being slightly bigger than the ones expected. It could also come from a problem of parallelism of the holes, making coalescence of droplets to occur. A variation of LBE properties (surface tension, temperature of test, thermal

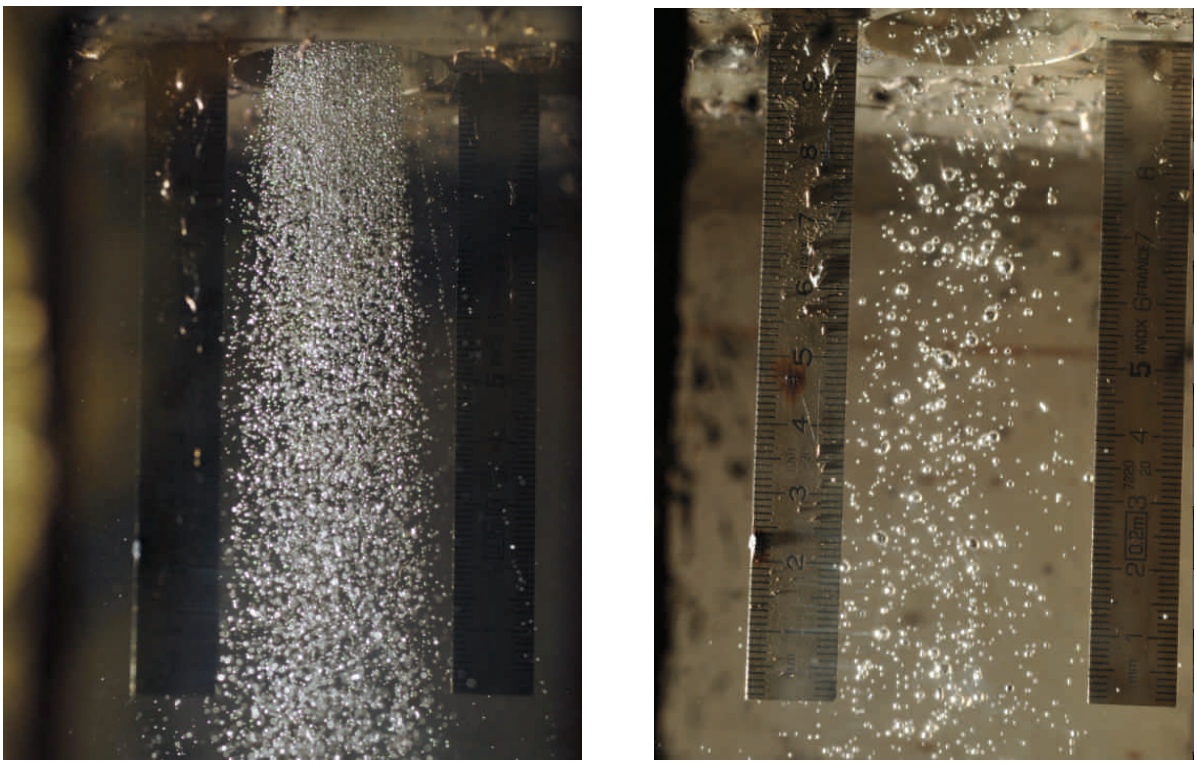

(a) Separated droplets formation (b) Re-merging of the droplets

Figure 4.16: LIEBE target

conductivity) can also be envisaged. However, this is unlikely as the change in properties to reach the mentioned droplets diameter would be of one order of magnitude.

For each studied grid, a randomly selected picture of the showers at start (among around 200 capture pictures per shower), is presented in Figures 4.17 and 4.18.

The density of droplets in the shower formed with the 0.5 mm inter axis spacing grid is visually lower than the one formed with the 0.6 mm inter axis spacing grid. This can be simply explained since the 0.5 mm inter axis grid is the last grid that has been tested and consequently more oxides were formed (and collected at the end inside the test bench). Accordingly, the average distance in between droplets is larger in showers depicted in Figure 4.17a than in Figure 4.17b. For the showers created with the grids 4 and 5, the density of droplets is coherent with what is expected.

4.3.2.3 Mathematical extrapolations and droplets dimensions

When solving Equation 4.19, one can plot the evolution of the velocity versus time, as shown in Figure 4.19 for the grid 2. The same plots have been done for the others grids and can be found in Appendix C.

The shape of the curves is given by the polynomial function estimated analytically. 5 different curves are here represented, corresponding to 5 over the 6 different showers done with the grid 2. As 2 of the showers (shower 2 and shower 3) had very similar times, only one curve has been

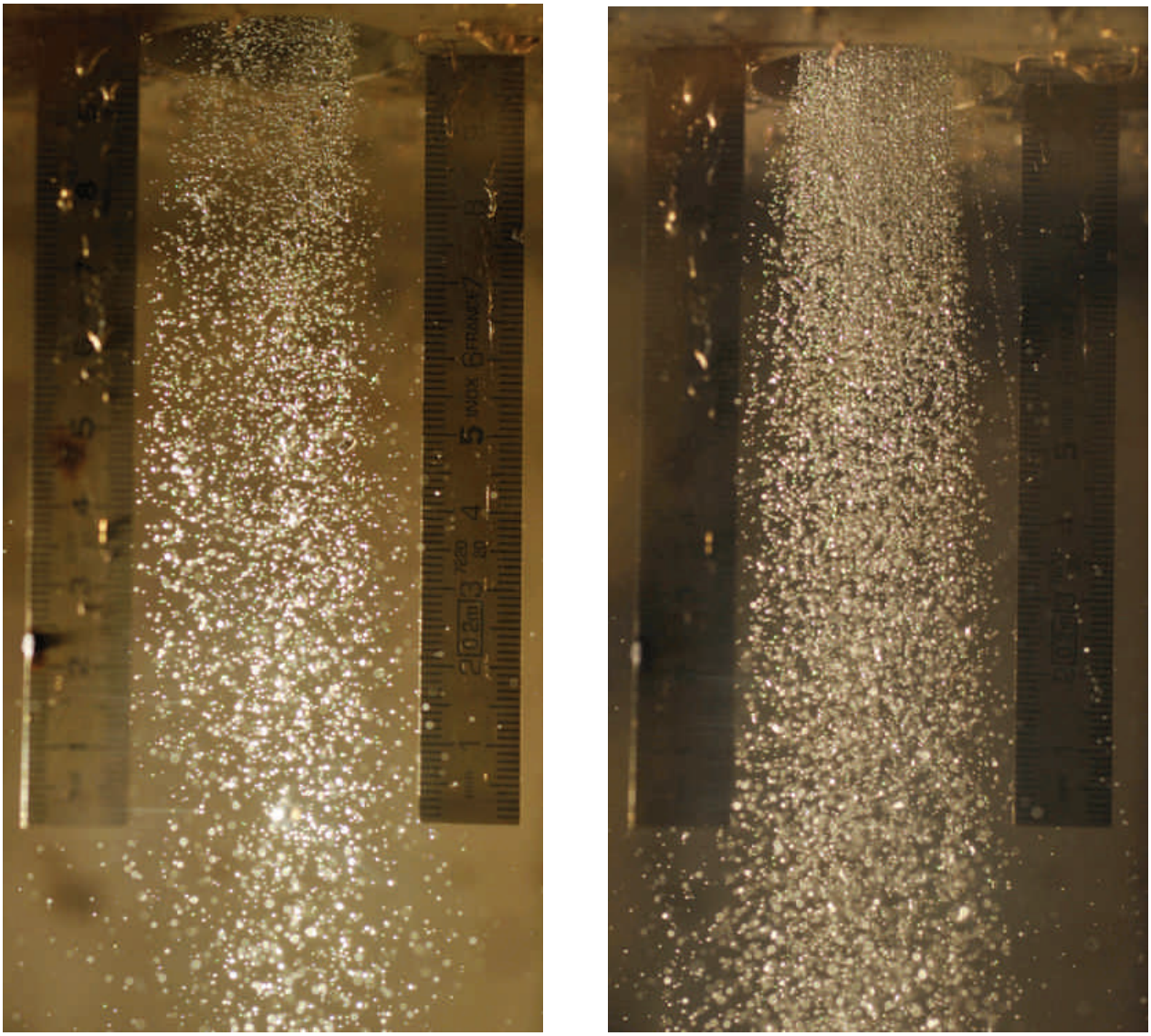

(a) 0.5 mm inter axis spacing - shower at start (b) 0.6 mm inter axis spacing - shower at start

Figure 4.17: Shower at start for 0.5 mm and 0.6 mm inter axis spacing

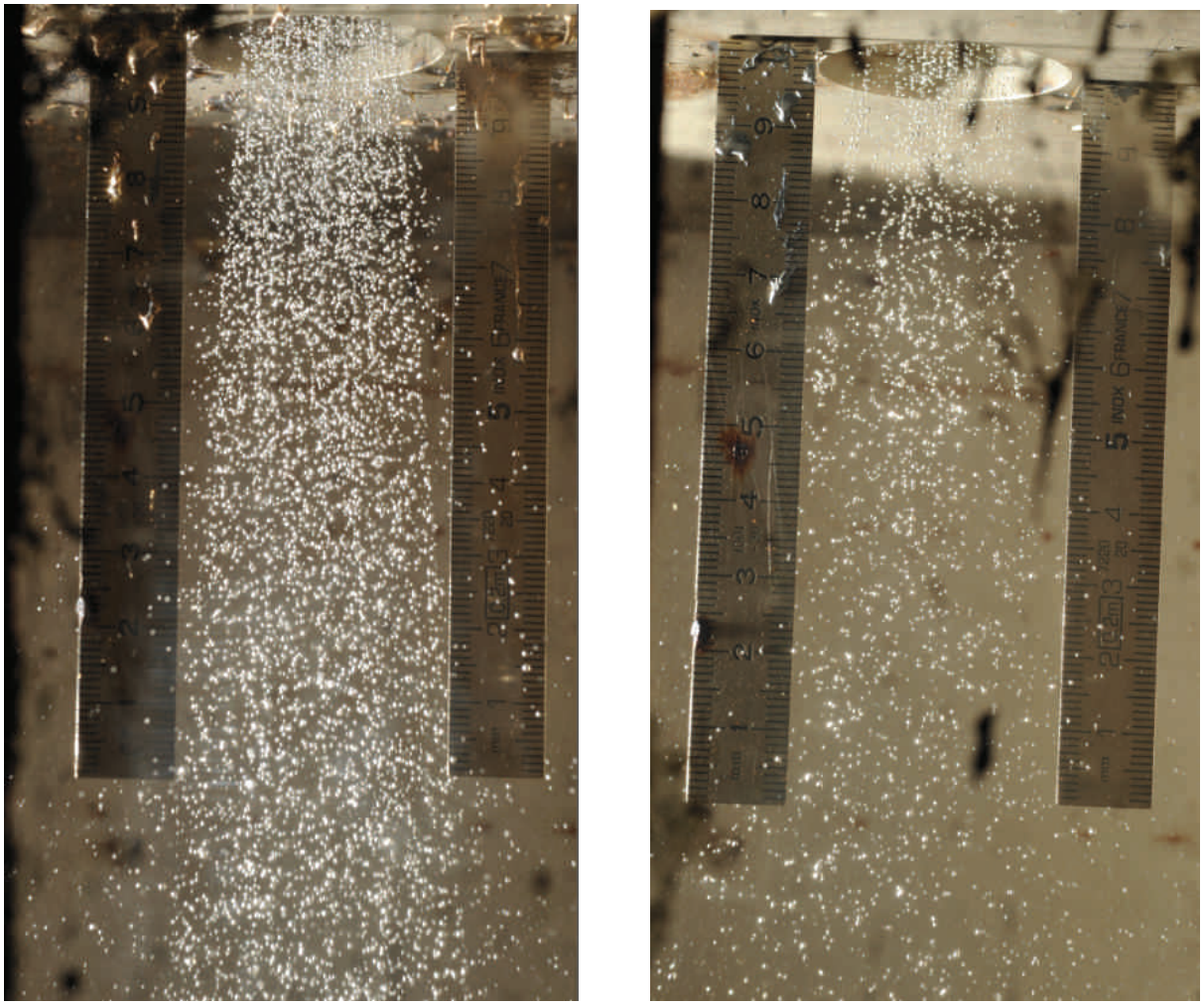

(a) 0.8 mm inter axis spacing - shower at start (b) 1 mm inter axis spacing - shower at start

Figure 4.18: Shower at start for 0.8 mm and 1 mm inter axis spacing

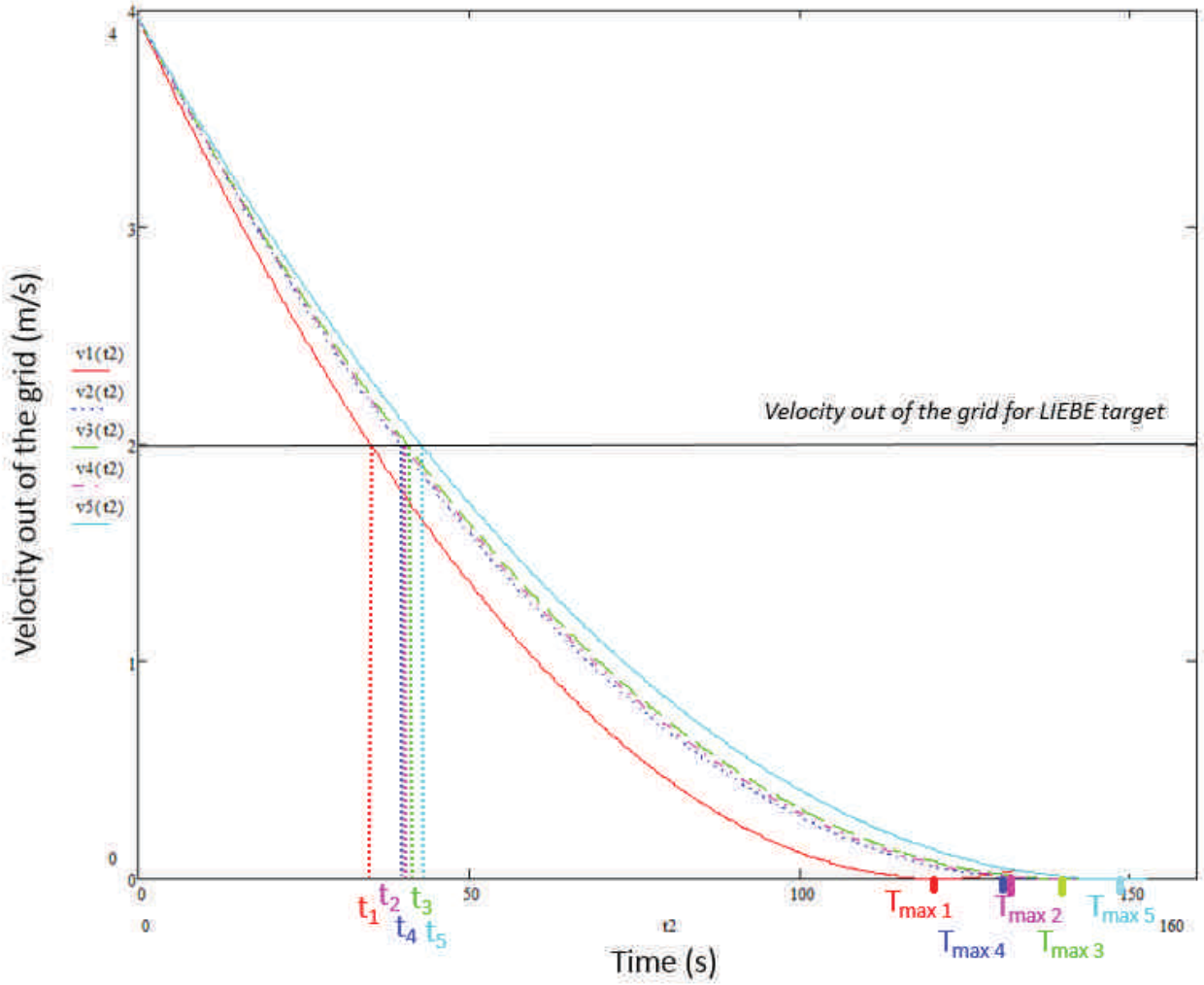

Figure 4.19: v=f(t) - for each shower - 0.5 mm inter axis spacing

represented for the both. The difference in final time comes from the difference of clogging for each of the showers.

Table 4.4 expresses the surfaces of holes at the start and end of each showers and per grids.

Grid	*Shower number*	*Initial surface (%)*	*Final surface (%)*
Grid 0.5 mm	1	40.9	20.5
	2	36.3	18.3
	3	36.3	17.7
	4	35.8	17.9
	5	33.6	16.5
Grid 0.6 mm	1	74.1	66.25
	2	64.5	32.25
	3	63.3	31.7
	4	57.6	30.1
	5	49.8	24.9
Grid 0.8 mm	1	79.0	49.5
	2	75.0	37.5
	3	68.5	34.4
	4	68.4	34.2
	5	54.4	27.0
Grid 1 mm	1	65.6	32.5
	2	59.8	29.9
	3	46.5	23.3
	4	44.9	23.0

Table 4.4: Initial and final surface of holes during the conducted experiment

The data in Table can indeed be interpreted as if oxide is transported by the flowing LBE. For higher pressure, more oxides are pushed trough the holes of the grid which explain why the final surface in one shower is not the starting surface of the following one. A significant amount of oxide is present and highly influence the final surface of the grid. This is seen on the pictures taken at the end of the showers (cf Figure 4.28b in Appendix C for example).

The final times t_{max} of Figure 4.19 are obtained experimentally and allow the estimation of the parameters a and b of the linear extrapolation for the holes surface area. The velocity out of the grid in case of the LIEBE target has been estimated at 2 m/s. For each of the corresponding times t_1, t_2, t_3, t_4 and t_5, the taken picture has been studied. In all cases, the droplets diameters are of the order of 0.4 mm diameter, characteristics of the jetting regime.

A representation of the droplets size for the different showers can be found on the Figures 4.20, 4.21, 4.22 and 4.23. On these Figures, an error bar of 10 % (considering the uncertainties related to the measuring tools and scaling) is considered for each of the values while the two different regimes are presented:

- **The Jetting one** in yellow,
- **The Dripping one** in orange.

The expected diameter for the jetting and dripping regime are represented by vertical dotted lines.

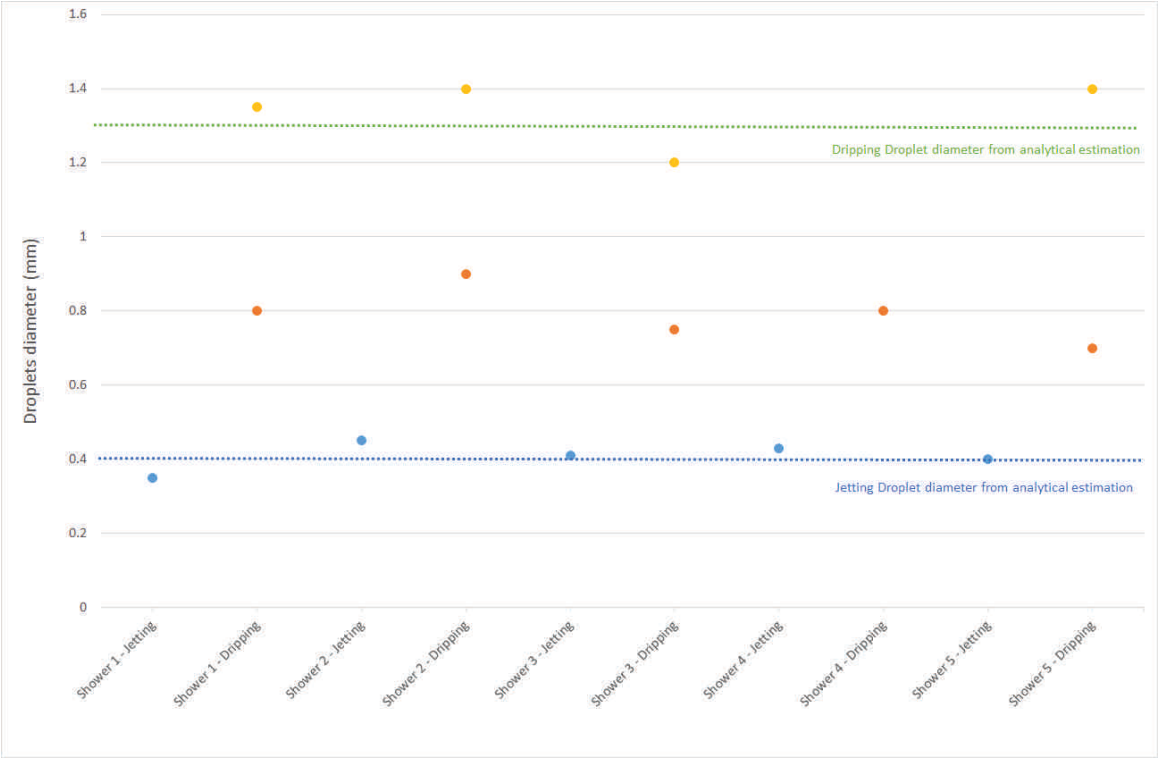

Figure 4.20: Droplets diameters for each of the shower - 0.5 mm inter axis spacing

Figure 4.21: Droplets diameters for each of the shower - 0.6 mm inter axis spacing

One can observe at first that, for the jetting regime, the measured diameters are in good

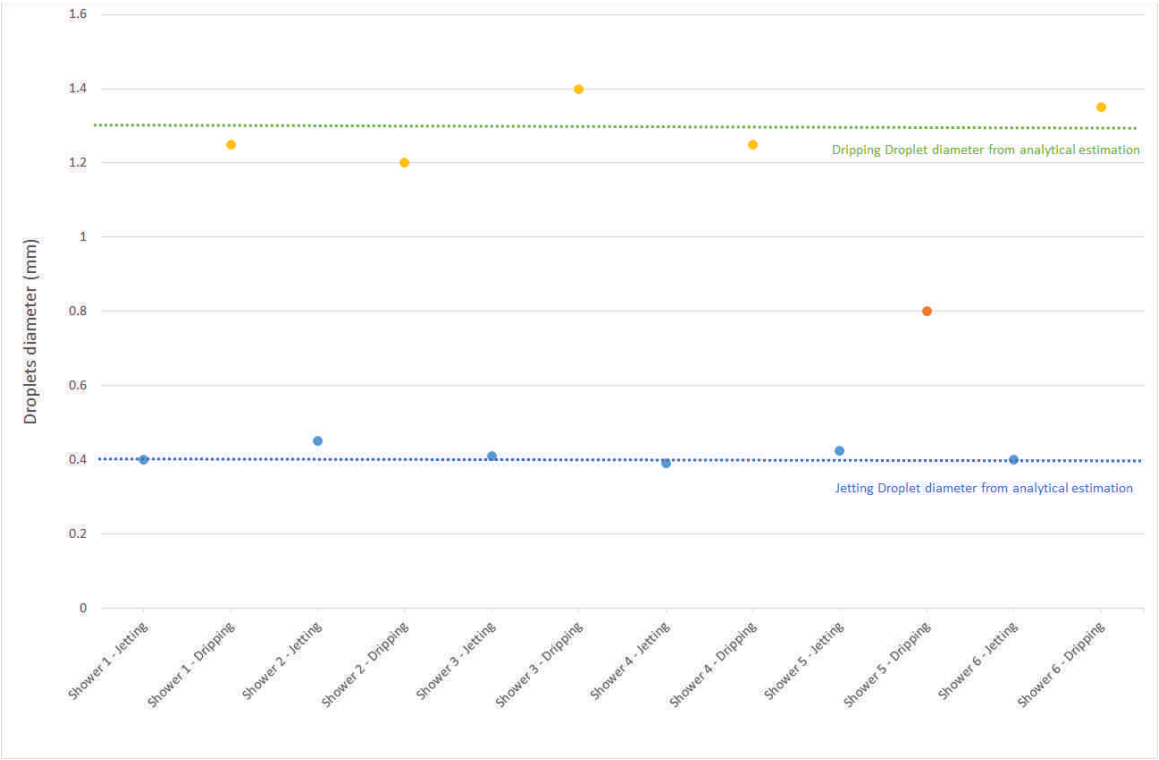

Figure 4.22: Droplets diameters for each of the shower - 0.8 mm inter axis spacing

Figure 4.23: Droplets diameters for each of the shower - 1 mm inter axis spacing

agreement with the theory. In case of the dripping regime, two different orange colors have been used since two different characteristic dimensions of droplets (< 1 mm and > 1 mm) for the same shower have been observed, as it can be seen in Figure 4.24.

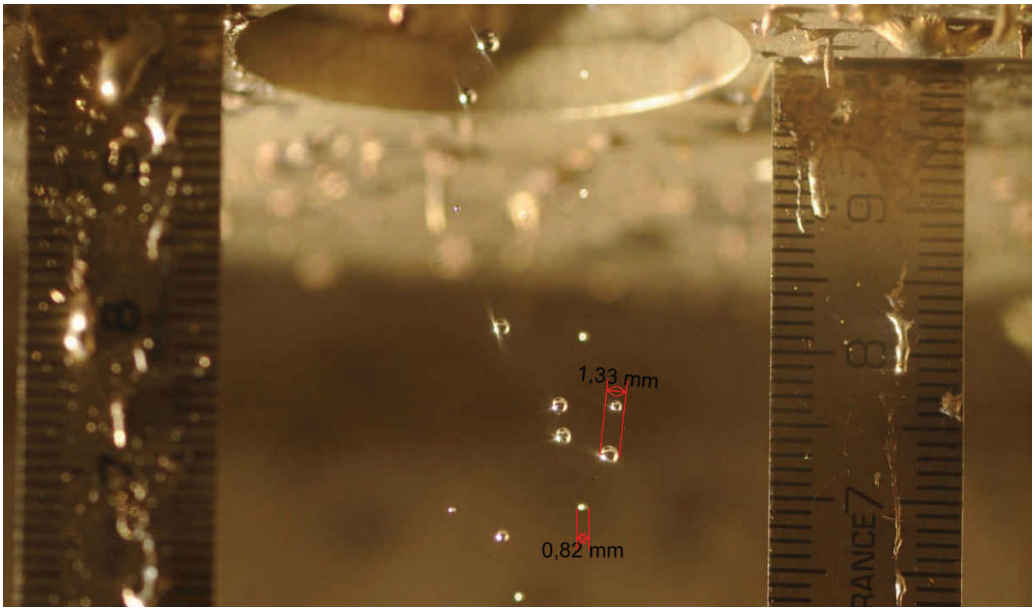

Figure 4.24: Visualization of two characteristic dimensions of droplets in dripping regime

Three different cases can be identified:

- Only droplets of 0.75 mm diameter are detected, which is not expected from the initial calculations,
- 0.75 mm diameter droplets together with the expected 1.3 mm diameter droplets are observed,
- Only droplets of the expected 1.3 mm diameter are observed.

The theory states that droplets in the Dripping regime should be in the order of 1.3 mm diameter. Other diameters, significantly lower, can be however identified. These diameters are not randomly distributed. This means that they are due to an additional reproducible phenomenon. From Equation 2.36, one can identify only three main parameters that could influence the droplets diameter in the proposed dripping regime:

- the diameter of the hole,
- the surface tension of the liquid,
- the density of the liquid.

Nevertheless, this model is a simplified one and does not take into account other liquid characteristics, such as its viscosity for example.

Three explanations for the formation of 0.75 mm diameter droplets are possible:

- A mixed droplet formation regime exists in between the dripping and the jetting one (that is to say both regimes exist in a narrow range of transition) and is observed here,
- A characteristic of the LBE is varying over time and makes the surface tension of the fluid or its density varying so much that it impacts the droplets formation.
- A secondary fragmentation occurs. This usually happens in the transition breakup regime. In this case, a mother drop fragments into a larger drop and several smaller drops (Figure 4.25).

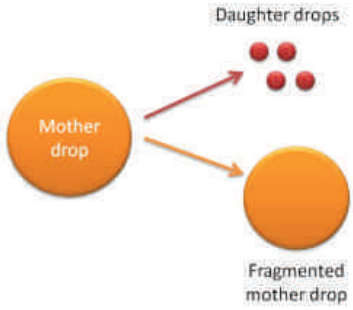

Figure 4.25: Visual representation of fragmentation process [18]

To really understand what parameter is impacting on the droplets formation in the dripping regime, further investigation would be necessary. This has not been pursued here since the suitable jetting regime has been properly detected.

4.3.2.4 Experimental determination of the Weber number

In Section 2.3.2.3, some uncertainty about the critical/limit Weber dimensionless number has been hypothesized in case of a LBE shower. Indeed, this critical Weber number corresponds to the limit between the dripping regime in which the droplets are of 1.3 mm in diameter and the jetting regime where the droplets are of 0.4 mm in diameter. Practically speaking, in order to ensure the shower is in the Jetting regime, an outlet velocity of 2 m/s was decided (cf Section 3.2.1.2). Further analysis has been conducted and is presented hereunder.

The plots of the velocity versus time *v(t)* are presented in Figures 4.26a, 4.26b, 4.27a and 4.27b.

For each shower created experimentally, the transition time at which the droplets of 0.4 mm diameter turn into bigger droplets has been found from the pictures. This point has been reported on each of the analytical graphs (Figures 4.26a to 4.27b). For a velocity higher than this point (and thus a time smaller), all droplets were in the order of 0.4 mm diameter as presented in Figure 4.28a, 4.29a, 4.30a and 4.31a. Some large droplets (diameter higher than 1.4 mm) are identified as well on three grids over four. These larges droplets are seen at all time and thus, it is likely that they are due to the grid itself. This is considered as being the jetting regime. No clear rupture is seen between this regime and the following one is seen. Droplets of the order of 0.4 mm diameter are seen at the start of the dripping regime.

For lower velocity (and thus, higher time), three droplets dimensions are seen (cf Figures 4.28b, 4.29b, 4.30b and 4.31b):

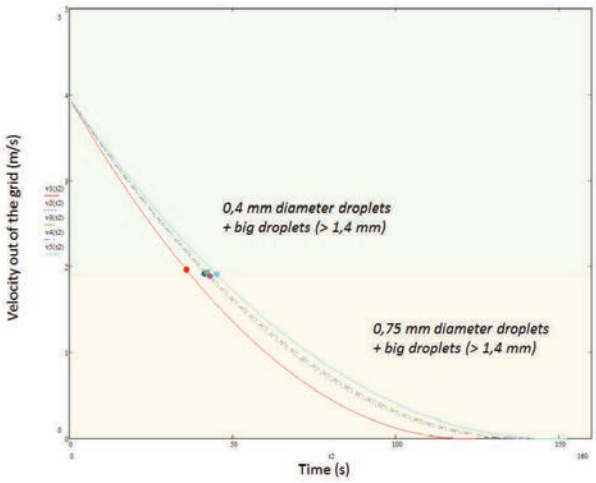

(a) v=f(t) - for each shower - 0.5 mm inter axis spacing grid

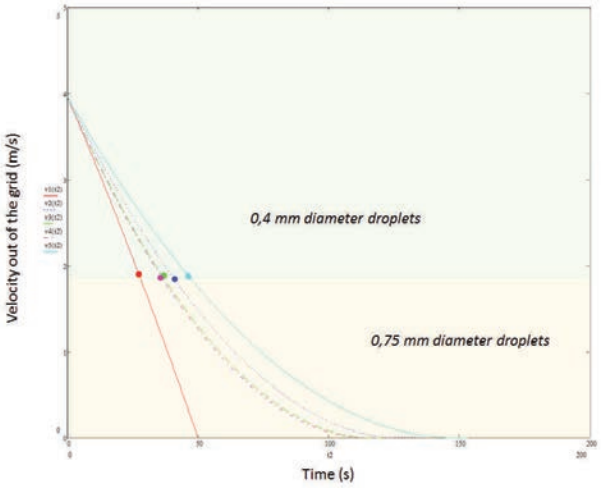

(b) v=f(t) - for each shower - 0.6 mm inter axis spacing grid

Figure 4.26: 0.5 mm and 0.6 mm inter axis spacing grids

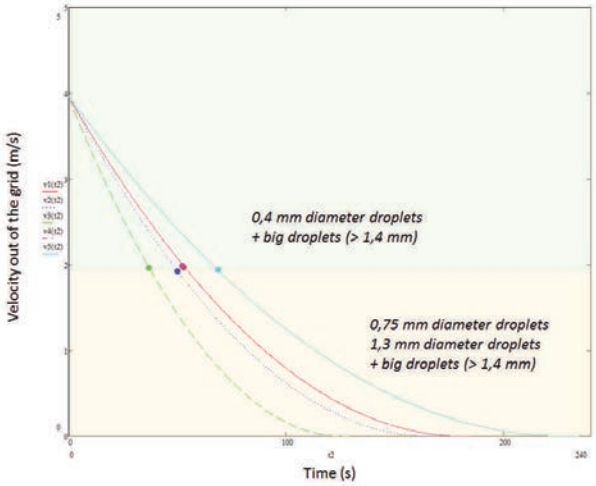

(a) v=f(t) - for each shower - 0.8 mm inter axis spacing grid

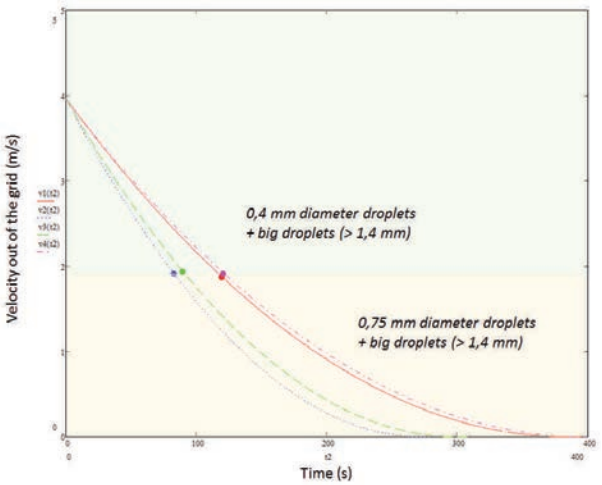

(b) v=f(t) - for each shower - 1 mm inter axis spacing grid

Figure 4.27: 0.8 mm and 1 mm inter axis spacing grids

- Droplets exhibiting a characteristic dimensions in the order of 0.75 mm in diameter,
- Droplets exhibiting a characteristic dimensions in the order of 1.4 mm in diameter,
- Droplets exhibiting a characteristic dimensions bigger than 1.4 mm in diameter.

From the graphs presented, the limit between the dripping regime and the jetting regime is obtained for a outlet velocity of the droplets of 1.8 ± 0.2 m/s. This would corresponds to a Weber number of 8.4. This allows the estimation of the proper Weber limit number to be of 8 to correlate with the bibliography.

The droplets diameters determined experimentally are in good agreement with those predicted by theory (presented in Section 2.3.2.3). Indeed, as expressed in Table 2.19, the expected droplets diameter in the Dripping regime is 1.3 mm, while the one expected in the Jetting regime is about 0.4 mm. The intermediate value of 0.75 mm diameter has been discussed previously and very likely corresponds to a transition regime in between the dripping and the jetting regimes.

Furthermore, the very large droplets (i.e., exhibiting a diameter larger than 1.4 mm) formed at the grid result from a coalescence of the droplets after their formation due on one hand to the direction of the holes not perfectly perpendicular to the grid reference surface and on the other hand to variations in the distances in between successive holes, some of them being too closed to each other (Figure 4.28).

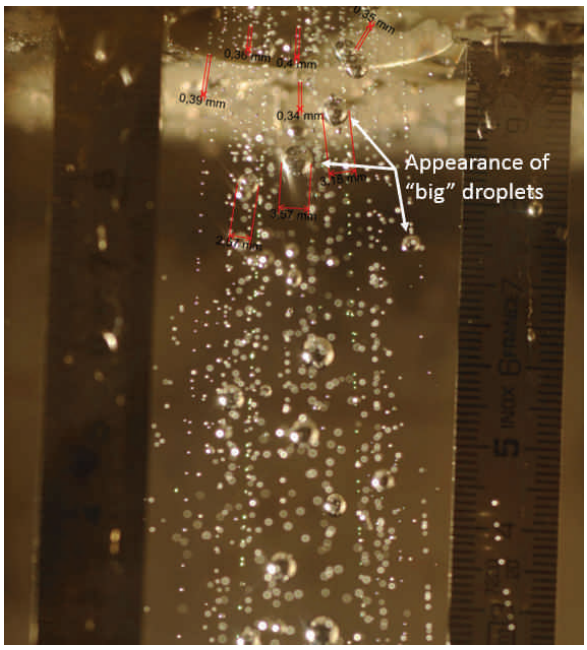

(a) 0.5 mm inter axis spacing - Weber number = 8

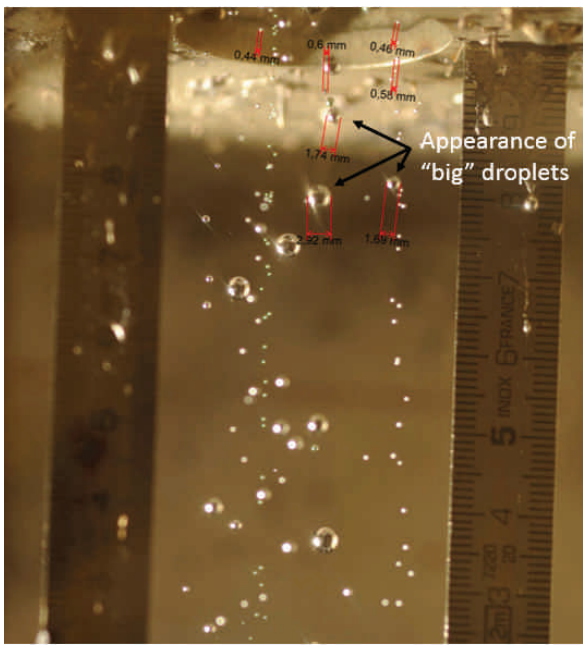

(b) 0.5 mm inter axis spacing - Weber number = 1

Figure 4.28: Comparison between picture for timing corresponding to a Weber number of 1 and 8 - 0.5 mm inter axis spacing grid

In Figure 4.28, the density of droplets in the shower is not as high as expected but this is explained by the high quantity of oxide found afterwards in the test bench for this grid. A cleaning of the column has been attempted but without a significant change.

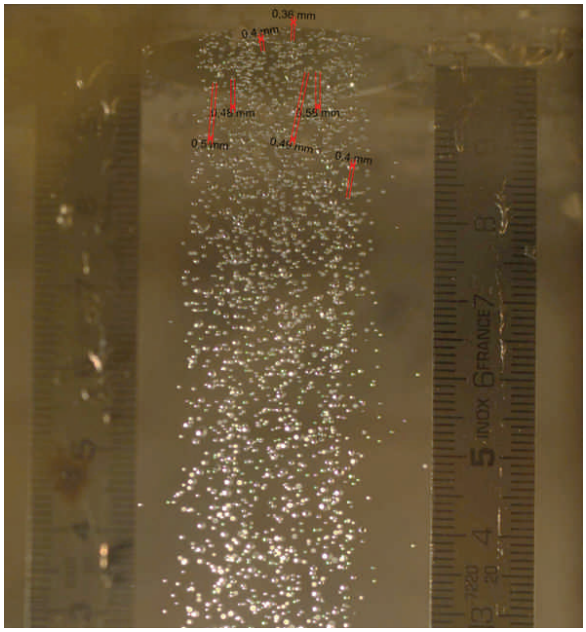

(a) 0.6 mm inter axis spacing - Weber number = 8

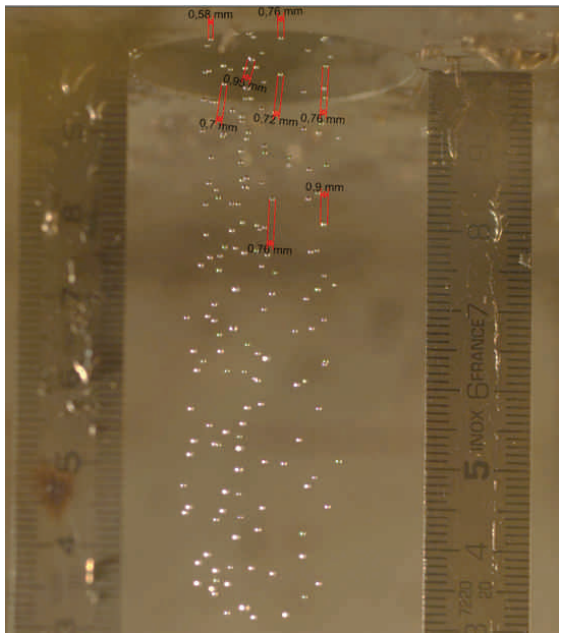

(b) 0.6 mm inter axis spacing - Weber number = 1

Figure 4.29: Comparison between picture for timing corresponding to a Weber number of 1 and 8 - 0.6 mm inter axis spacing grid

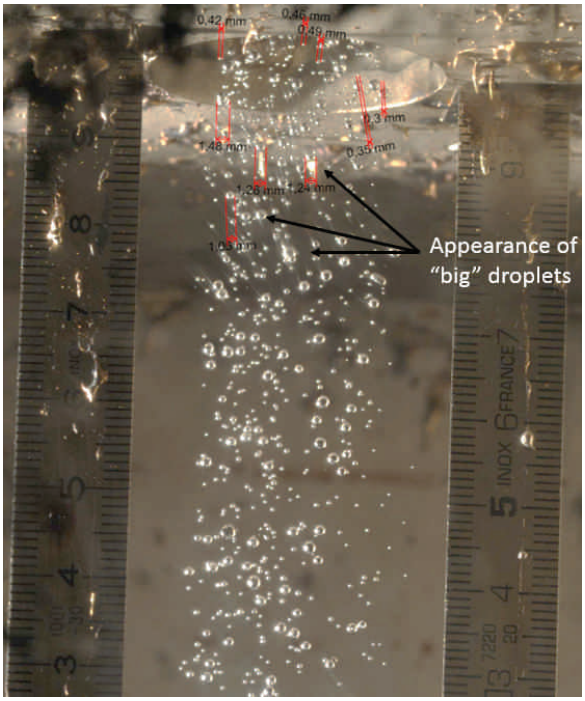

(a) 0.8 mm inter axis spacing - Weber number = 8

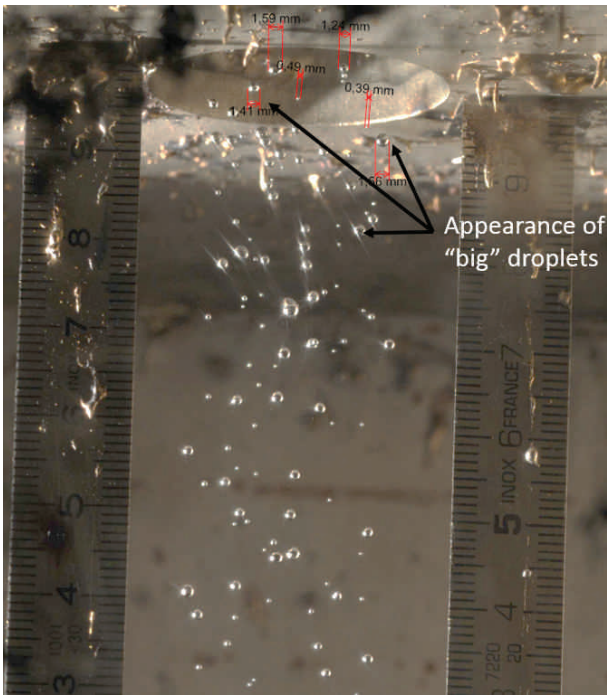

(b) 0.8 mm inter axis spacing - Weber number = 1

Figure 4.30: Comparison between picture for timing corresponding to a Weber number of 1 and 8 - 0.8 mm inter axis spacing grid

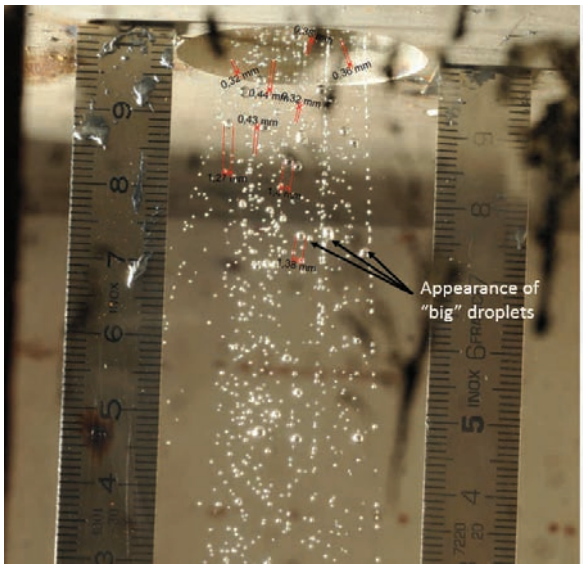

(a) 1 mm inter axis spacing - Weber number = 8

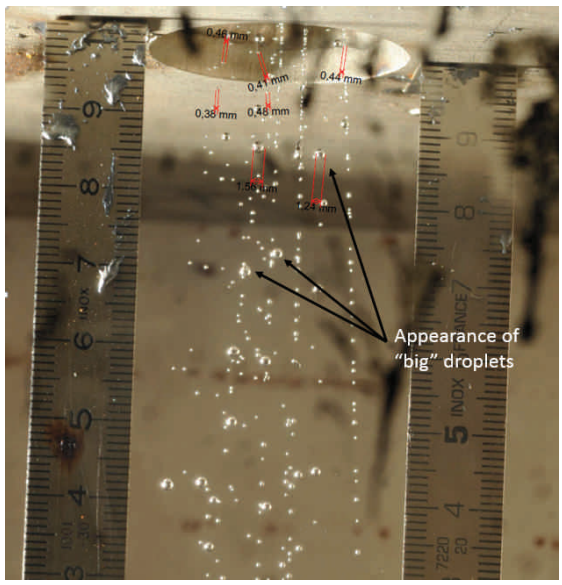

(b) 1 mm inter axis spacing - Weber number = 1

Figure 4.31: Comparison between picture for timing corresponding to a Weber number of 1 and 8 - 1 mm inter axis spacing grid

Figure 4.29 displays a view of a shower having a higher droplets density. This is coherent as the grid has been tested at the start of the experiment and thus, less oxides were formed inside the column or at the bottom of the upper filling tank. Droplets having diameters in the order of 0.45 mm, characteristic dimensions, can be identified in case of a high flow velocity ($v \approx 1.76$ m/s - We = 8) while slightly bigger droplets are identified for a slower flow ($v \approx 0.62$ m/s - We = 1). Indeed, droplets of about 0.7 mm average diameter are detected. This is also coherent with the dripping regime identified in the previous section. This is a clear indication that the dripping regime is already fully established.

In Figure 4.30a, the regime could correspond to the jetting regime with possible presence of dripping droplets of 1.3 mm diameter droplets. In the same manner, Figure 4.30b displays a shower where the dripping regime is predominant while some droplets characteristic of the jetting regime are still identified.

Finally, Figure 4.31 shows similar results as those of Figure 4.30: the jetting regime is predominantly established with the presence of droplets characteristic of the dripping regime for Figure 4.31a, and vice-versa for Figure 4.31b.

All theses results tend to indicate that for a dimensionless Weber number equal or higher than 8, the jetting regime is fully established and no dripping regime occurs. For a Weber number just above 1, it is difficult to be conclusive regarding the nature of the regime that can be classified as intermediate (both regimes, the dripping and the jetting ones, develop). However, in the considered application, it is mandatory to operate the system with a Weber number higher than 8 in order to ensure the formation of the smallest possible droplets. The condition is fulfilled with an outlet velocity of 2 m/s.

4.4 Discussion

In this Chapter, results about shower formation with liquid LBE have been presented. In the frame of the LIEBE project, the main goal was to determine which characteristics would the generated droplets have in the most optimized case (thus, the smallest diameter) and to validate at the same time the theory introduced in Section 2.3.2.3. The results are based on the use of a grid with holes diameters of 100 μm. This is the lowest possible diameter achieve at the time of the tests. This is based on laser drilling on a 1 mm thick plate made of 316L Stainless Steel (the plate composition is deduced from the target requirement and cannot be changed).

Results show that a minimum droplet diameter of 0.4 mm can be obtained reproducibly. This is in good agreement with the proposed theory for a jetting regime and corresponds to the diameter considered for the total release efficiency presented in Section 3.2.1.2.

For some of the operating conditions, a dripping regime has been identified as well. This regime is more complex as the diameter of the droplets varies from 0.8 mm to 1.3 mm, where 1.3 mm diameter are the one expected according to the theory. The reason for the smaller formation of the droplets is not yet clear. In order to better understand the involved phenomenon and to be fully conclusive,additional experiments should be conducted.

Furthermore, an attempt to identify the Weber number for which the transition between the jetting and the dripping regime occurs, has been made. The results indicate a transition occurring at quite a high velocity (i.e., 1.8 m/s) and consequently, for a We of about 8. However, since the determination of velocity versus time is based on the assumption of a linear decrease of the holes surfaces with time, it is difficult to be fully conclusive.

A possible improvement of this experiment would implement the control of the level of the LBE versus time in the upper tank. Also, the very high and fast oxidation occurring when LBE in liquid phase is in contact with oxygen must be prevented. Indeed, this chemical reaction makes much more complicated the results analysis as it disturbs the flow.

Conclusion

The study of intense radioactive ion beams (RIBs) requires the development of a new type of targets able to cope with the increase in beam power (i.e. several hundreds kW of beam power compared to a few kW, average value nowadays) delivered by facilities, at CERN-ISOLDE in particular. This induces new constraints and challenges to be faced by the proposed target design. Amongst them can be cited the main ones: 1) shock waves propagating onto the target material during pulsed beam impact, 2) major beam power deposition and subsequent heat to be extracted, 3) radiation damages. To address these challenges, not only the design configurations have to evolve but also new types of materials have to be envisaged. Consequently, circulating liquid metal are considered as they can fulfil most of the requirements. This, in turn, induces new challenges but also, new possibilities as the diffusion release process is different in case of liquid or solid. It has been simulated that atomizing a liquid stream into droplets allows a major increase in isotope release efficiency. This is particularly interesting for short-lived species, that are hardly extracted with standard solid or liquid units. As an example, static liquid lead target developed and operated at CERN-ISOLDE displayed a released fraction of ^{177}Hg (130 ms half life) of about 1.6 % [20]. Using a fragmented liquid stream of Lead Bismuth Eutectic (LBE) (droplets of 0.2 mm, average diameter), a release fraction of 16 % is expected, that is to say a gain of one order of magnitude.

The proposed design developed during this PhD addresses the different requirements and constraints applied to a high power target. At first, numerical simulations have been used to assess shock waves induced by the beam impact and propose a validated design. It showed that, in order to avoid build-up of shock waves, the dimensions of the irradiation chamber (where the primary proton beam impinges) has to be chosen carefully.

At second, a thermal balance has been computed, taking into account the different heat sources and heat losses. This was based on an analytical model and on numerical simulations, and led to the design of an innovative water-cooled heat exchanger. The proposed Heat Exchanger (HEX) can hence extract up to 2.5 kW while being adaptable to different LBE temperatures. Indeed, the target can be operated from 200°C up to 600°C. The designed device has been manufactured by additive manufacturing (3D printing) and is currently under test for validation.

As already mentioned, an increase in the released fraction of short-lived species is possible when the liquid metal is in the form of droplets. The smaller the droplets average diameter, the higher the release fraction of short-lived species. This induces limits in the velocity of the droplets to reach the jetting flow regime in order to achieve as small as possible droplets diameters. Experimental tests have shown that the smallest achievable diameter hole with the existing manufacturing techniques onto a 1 mm-thick Stainless Steel plate was 100 μm. This sets a minimum velocity of the droplets out of the grid of 1.76 m/s to remain in the jetting regime. The resulting droplets diameter in this regime has been measured at 400 μm, thus demonstrating

the feasibility of a LBE shower under such conditions. The expected improvement in terms of released fraction of ^{177}Hg isotope is five times higher compared to a static liquid unit at ISOLDE.

A conceptual design of this target has already been proposed during the EURISOL Design Study phase in 2009. The proposed design here makes use of new key elements, as compared to standard ISOLDE targets, such as an electromagnetic pump in order to ensure the circulation of the liquid LBE, an heat exchanger (HEX) to extract the additional power deposited by the primary proton beam impact and a diffusion chamber in which the created droplets will fall and the isotopes diffuse out.

The proposed target is currently under manufacturing and integration. Intensive tests must still be carried out before installation for test under beam. At first, the coupling procedure of the target onto the front-end wil be validated and the proper positioning of the magnets around the pipes of the pump will be ensured. At second, tests will be done with an empty target in order to validate the mechanical integrity of the device under different heating conditions. This will validate some of the numerical analyses used to assess the mechanical integrity of the target under different loading cases. In the same time, the control and monitoring system, already tested on a different system, will be validated, giving a feedback on the thermal balance of the loop. Indeed, by knowing the input power, it will be possible to correlate the power losses and compare them to the analytical estimation. Valuable information on the operation of this target will be collected, allowing a better understanding on the thermal behavior of the target. Furthermore, tests will be conducted with LBE by operating the LIEBE target onto the offline front end of ISOLDE. At that point, an evaluation of the pressure losses will be done and the value will be compared to the expected one. Finally, the target will be tested onto the online ISOLDE front end, under proton beam. This will provide valuable information about the release fraction of short-lived species and allow the validation or tuning of the used analytical model.

PERSPECTIVES

The next steps of this project will be the test of the target under beam irradiation. This will be done at CERN-ISOLDE. It will probe the robustness of the concept, as well as highlight possible issues for the operation of such kind of targets. This return of experience will be of major importance, as this will be one of the main information allowing the development of future targets based on similar concepts. It will provide valuable numbers on the release efficiency, that could be used to develop new target with different liquid.

The following steps of this work will be some further improvement of the developed unit. Indeed, this unit is the first prototype and address most of the constraints. However, for example, it is only a single use target which does not make it appropriate for a monthly basis use at ISOLDE. The design should be modified in order to obtain a "series" production target. This also includes minimizing the manufacturing costs and times.

On a longer term, this target concept can be used for the development of targets in other institutes, with different constraints, mainly in terms of geometry. The major two parameters driving the final release efficiency is the time during which the isotopes will be inside the irradiation chamber (where the proton beam impact occurs) and inside the diffusion chamber (where the isotopes diffuse out of the falling droplets). The first time should be minimized while the second one should be maximized. This directly depend upon the loop flow rate and

target dimensions. A possible improvement for a higher gain in the release fraction of short-lived species would be to increase the loop flow rate and simultaneously increase the diffusion chamber height, reducing the time in the irradiation chamber while possibly increasing the time in the diffusion chamber. In the same idea, smaller hole diameters for the grid creating the droplets would allow a significant gain in the final release efficiency. As well, in a few years, even higher beam power is expected. A new HEX design should be developed, based on the proposed one, making use of a different cooling fluid (here water).

This target is a prototype that could be the first one of a series of new type of targets. More and more, the increase of power intensity of the primary beam will lead to the need of liquid materials, solid ones possibly melting as high power is hardly extracted by active cooling of water or air flow type. Loop target types are definitely an answer to the new problematic that will arrive with the foreseen beam power. Furthermore, the need of higher yield of short-lived species is high for physics research. This design could open up the door to new type of physics and possible new nuclear discoveries.

Bibliography

[1] OECD, editor. *Handbook on Lead Bismuth Eutectic Alloy and Lead properties, Materials compatibility, Thermal-hydraulics and Technologies*. Nuclear Science, 2015.

[2] M. Fowler. Modern physics. rays and particles. *http : //galileo.phys.virginia.edu/classes/252/raysandparticles.html*, 2009.

[3] ChemWiki. Nuclear reactions. *http://chemwiki.ucdavis.edu/ Physical Chemistry/ Nuclear Chemistry/ Nuclear Reactions*.

[4] D. Bazin. Symmetrical tin. *Nature*, 486:330–331, 2012.

[5] Y. Blumenfeld, T. Nilsson, and P. Van Duppen. Facilities and methods for radioactive ion beam production. *Physica Scripta*, 2013(T152):014023, 2013.

[6] T. Stora. Recent developments of the CERN-ISOLDE neutron spallation source. *FPRIB. conference, Saha Inst., Kolkata*, 2012.

[7] E.J.A. Bouquerel. *Atomic beam merging and suppression of Alkali Contaminants in Multi Body high power targets*. PhD thesis, Universite Paris XI, 2009.

[8] T. Stora. Radioactive Ion Sources. *Accelerators Physics, CERN Yellow Report CERN-2013-007, contribution to the CAS-CERN Accelerator School: Ion Sources, Senec, Slovakia, edited by R. Bailey*, pages 331–349, 29 May - 8 June 2012.

[9] M. Fujioka and Y. Arai. Diffusion of Radioisotopes from Solids in the Form of Foils, Fibers and Particles. *Nuclear Instruments & Methods*, 186:409–412, 1981.

[10] P. Hurh, K. Ammigan, B. Hartsell, and R. Tschirhart. High Power Target R&D Program at Fermilab. *FERMILAB conference*, 2013.

[11] C. Fazio, F. Groeschel, W. Wagner, K. Thomsen, B.L. Smith, R. Stieglitz, L. Zanini, A. Guertin, A. Cadiou, J. Henri, P. Agostini, Y. Dai, H. Heyck, S. Dementjev, S. Panabianco, A. Almazouzi, J. Eikenberg, A. Letourneau, J.C. Toussaint, A. Janett, C. Perret, S. Joray, J. Patorski, W. Leung, P. Meloni, P. Turroni, A. Zucchini, G. Benamati, J. Konys, T. Auger, A. Gessi, D. Gorse, I. Serre, A. Terlain, J.B¿ Vogt, A. Batta, A. Class, X. Cheng, F. Fellmoser, M. Daubner, S. Gnieser, G. Grötzbach, R. Milenkovic, C. Latge, and J.U. Knebel. The MEGAPIE - TEST project: Supporting research and lessons learned in first-of-a-kind spallation target technology. *Nuclear Engineering and Design*, 238:1471–1495, 2008.

[12] European Commission. Final report of the EURISOL Design Study (2005-2009). Technical report, GANIL, 2009.

[13] E. Noah Messomo, F. Gerick, J. Lettry, M. Lindroos, and T. Stora. EURISOL 100 kw target stations operation and implications for its proton driver beam. *Proceedings of EPAC 2006, Edinburgh, Scotland*, 2006.

[14] T Stora. Operation of a Pb-Bi loop target at CERN-ISOLDE for the EURISOL prototyping phase. *CERN - internal communication*, 2011.

[15] I.E. Idel'Chik. *Handbook of Hydraulic resistance - coefficients of local resistance and of friction*. NTIS, 1966.

[16] W. Van Hoeve, S. Gekle, J. H. Snoeijer, M. Versluis, M. P. Brenner, and D. Lohse. Breakup of diminutive Rayleigh jets. *Physics of Fluids*, 22, 2010.

[17] A. Leipertz. Spray and Atomization. *Workshop Clean I.C. Engines and Fuels, Louvaine-la-Neuve*, 2005.

[18] S. Castrillon Escobar, R. Meignen, N. Rimpert, and M. Gradeck. Secondary breakup in the context of fuel coolant interactions (fci). *Workshop Société Française de Thermique, Paris*, 2014.

[19] E. Fiorini. Neutrino in Physics and Astrophysics. *International Journal of Modern Physics D*, 22:1360003 (9 pages), 2013.

[20] J. Lettry, R. Catherall, G. Cyvoct, P. Drumm, A. H. M. Evensen, M. Lindroos, O.C. Jonsson, E. Kugler, J. Obert, J.C. Putaux, J. Sauvage, K. Schindl, H. Ravn, and E. Wildner. Release from ISOLDE molten metal targets under pulsed proton beam conditions. *Nuclear Instruments and Methods in Physics Research Section B: Beam Interactions with Materials and Atoms*, 126:170–175, 1997.

[21] P. Bricault, R. Baartman, M. Dombsky, A. Hurst, C. Mark, G. Stanford, and P. Schmor. TRIUMF-ISAC target station and mass separator commissioning. *Nuclear Physics A*, 701(1-4):49–53, 2002.

[22] M. Paul, A. Arenshtam, S. Halfon, D. Kijel, M. Tessler, L. Weissman, D. Berkovits, Y. Eisen, I. Eliyahu, M. Friedman, G. Feinberg, A. Kreisel, I.Mardor, G. Shimel, A. Shor, and I. Silverman. A high-power liquid-lithium target (LiLiT) for neutron production. *Journal Radioanal Nuclear Chemistry*, 305:783–786, 2015.

[23] Ansys software, Release 15.0, and Ansys User's Manual. Inc swanson analysis system. 2015.

[24] PTC MathCad Software, Release 15.0, and MathCad User's Manual. Mathsoft ptc. 2015.

[25] L. Rayleigh. On the instability of jets. *Proceedings - London Math. Soc.*, s1-10:4–13, 1878.

[26] E. John Finnemore and J. B. Franzini. *Fluid Mechanics with Engineering Applications*. Mc Graw Hill, 2002.

[27] J. Benlliure. *Spallation reaction in Applied and Fundamental Research, Chapter of the EuroSchool Lectures on Physics with Exotic Beams, Vol. II*, volume 700 of the series Lecture Notes in Physics pp 191-238. Springer, 2006.

[28] V. Martin. Particle Physics. In *Lecture given at the Mesons and Baryons conference*, 2012.

[29] M. Brunglinghaus. Nuclear fission. *European Nuclear Society, http://www.euronuclear.org/info/encyclopedia/n/nuclear-fission.htm*, 2013.

[30] P.G. Hansen. Experiments with beam of rare isotopes: A fifty year perspective 1951-2001. *Nuclear Physics News*, 11:31–33, 2001.

[31] T. Ohnishi, T. Kubo, K. Kusaka, A. Yoshida, K. Yoshida, M. Ohtake, N. Fukuda, H. Takeda, D. Kameda, K. Tanaka, N. Inabe, Y. Yanagisawa, Y. Gono, H. Watanabe, H. Otsu, H. Baba, T. Ichihara, Y. Yamaguchi, M. Takechi, S. Nishimura, H. Ueno, A. Yoshimi, H. Sakurai, T. Motobayashi, T. Nakao, Y. Mizoi, M. Matsushita, K. Ieki, N. Kobayashi, K. Tanaka, Y. Kawada, N.Tanaka, S. Deguchi, Y. Satou, Y. Kondo, T. Nakamura, K. Yoshinaga, C. Ishii, H. Yoshii, Y. Miyashita, N. Uematsu, Y. Shiraki, T. Sumikama, J. Chiba, E. Ideguchi, A. Saito, T. Yamaguchi, I. Hachiuma, T. Suzuki, T. Moriguchi, A. Ozawa, T. Ohtsubo, M. A. Famiano, H. Geissel, A. S. Nettleton, O. B. Tarasov, D. P. Bazin, B. M. Sherrill, S. L. Manikonda, and J. A. Nolen. Identification of 45 New Neutron-Rich Isotopes produced by In-Flight Fission of a 238U Beam at 345 MeV nucleon. *Journal Physics Society Japan*, DOI:10.1143/JPSJ.79.073201, 2010.

[32] I. Augustin, H. Eickhoff, K. D. Gross, W. F. Hennin, D. Kraemer, and G. Walter. *FAIR Baseline Technical Report, Executive summary*. H. H. Gutbrod (eds.), 2006.

[33] M. Thoennessen. Plans for the facility for rare isotope beams. *Nuclear Physics A*, 834:688c – 693c, 2010.

[34] M. J. G. Borge. Isolde highlights and the hie-isolde project. In *EPJ Web of Conferences*, volume 66, page 11005. EDP Sciences, 2014.

[35] L. Popescu. Nuclear-physics applications of myrrha. In *EPJ Web of Conferences*, volume 66, page 10011. EDP Sciences, 2014.

[36] H. L. Ravn. Experiments with intense secondary beams of radioactive ions. *Physics Reports*, 54:201–259, 1979.

[37] E. Bouquerel, R. Catherall, M. Eller, S. Marzari, T. Stora, and Isolde collaboration. Purification of a zn radioactive ion beam by alkali suppression in a quartz line target prototype. *Europeen Physics Journal*, 150:277–280, 2007.

[38] J. Emsley. *Nature's Building Blocks: An A-Z Guide to the Elements*. Oxford University Press, 2011.

[39] P. Van Duppen. Isotope separation on line and post acceleration. *The Euroschool Lectures on Physics with Exotic Beams*, 700:37–77, 2006.

[40] U. Koster. Intense radioactive-ion beam produced with the ISOL method. *The European Physical Journal A*, 15:255–263, 2002.

[41] G. D. Alton, J. R. Beene, and Y. Liu. Criteria for Selection of Target-Materials and Design of High-Efficiency-Release Targets for Radioactive Ion Beam Generation. *Physics Division*, 438:190–209, 1999.

[42] A. D. Pasternak and D. R. Olander. Diffusion in Liquid Metals. *AIChE Journal*, 13:1052 – 1057, 1967.

[43] T. Antonakakis, C. Maglioni, and V. Vlachoudis. Closed form solutions of the heat diffusion equation with a gaussian source. *International Journal of Heat and Mass Transfer*, 62:314–322, 2013.

[44] E. Noah Messomo. Hydrodynamics of ISOLDE liquid metal Targets. In *ISOLDE Workshop and Users Meeting, CERN*, 2007.

[45] E. Noah Messomo, L. Bruno, R. Catherall, J. Lettry, and T. Stora. Hydrodynamics of ISOLDE liquid metal Targets. *Beam Interactions with Materials and Atoms*, 266:4303–4307, 2008.

[46] P. G. Bricault, M. Dombsky, J. Lassen, and F. Ames. Progress in Development of ISOL RIB Ion Sources and Targets for High Power. *Cyclotrons and Their Applications 2007, Eighteenth International Conference, Giardini Naxos, Italy*, pages 499–504, 2007.

[47] T. M. Mendonca, R. Hodak, V. Ghetta, M. Allibert, D. Heuer, E. Noah Messomo, S. Cimmino, M. Delonca, A. Gottberg, M. Kronberger, J. P. Ramos, C. Seiffert, and T. Stora. Production and release of ISOL beam from molten fluoride salt targets. *Nuclear Instruments & Methods in Physics Research, Section B: Beam Interactions with Materials and Atoms*, 329:1–5, 2014.

[48] C. Latge, F. Groeschel, P. Agostini, M. Dierckx, C. Fazio, A. Guertin, Y. Kurata, G. Laffont, T. Song, K. Thomsen, W. Wagner, and K. Woloshun. MEGAPIE Spallation target: irradiation of the first prototypical spallation target for future ADS. *OECD International Conference on Technology and Components on Accelerated Driven Systems*, Karlsruhe , 15-17 Mars 2010.

[49] C. Latge, M. Wohlmuther, Y. Dai, D. Gaviller, A. Gessi, A. Guertin, B. Hammer, S. Heinitz, J. Henry, M. Konstantinovic, R. Lindau, C. Fazio, S. Maloy, J. Neuhausen, S. Saito, K. Park, D. Shumann, K. Thomsen, A. Türler, and W. Wagner. MEGAPIE: the world's first high-power liquid metal spallation neutron source. *Conference ThEC13 CERN Geneva (Suisse)*, 2013.

[50] CES Selector Software. Release 15 and CES Selector User's Manual and Granta Material intelligence. 2014.

[51] *Net Positive Suction Head for Rotodynamic Pumps. A volume in The Europump Guides to Advanced Pumping Technology*, volume ISBN:978-1-85617-356-8. Elsevier, 1999.

[52] S. E. Haaland. Simple and explicit form for the friction factor in turbulent pipe flow. *Fluids engineering*, 105:89–90, 1981.

[53] A. Ferrari, P. R. Sala, A. Fasso, and J. Ranft. FLUKA: a multi-particle transport code. *CERN*, INFN:SLAC–R–773, 2005.

[54] F.P. Incropera, D.P. DeWitt, T.L. Bergman, and A.S. Lavine. *Fundamentals of Heat and Mass Transfer*. Wiley, 2005.

[55] L.C. Carraz, S. Sundell, H.L. Ravn, M. Skarestad, and L. Westgaard. High-temperature carbide targets for fast on-line mass separation of alkali and noble gas elements. *Nuclear Instruments & Methods*, 158:69–80, 1979.

[56] R. Kirchner. On the release and ionization efficiency of catcher-ion-source systems in isotope separation on-line. *Nuclear Instruments and Methods in Physics Research Section B*, 70:186–199, 1992.

[57] L. B. Loeb. *The Kinetic Theory of Gases*. McGraw Hill, 1934.

[58] B. Eichler, C. Frink, G. Hermann, and N. Trautmann. Fast volatilization of some lanthanide and actinide elements from titanium surfaces. *Fresenius Z Anal Chem*, 335:656–662, 1989.

[59] R. Kersevan. Molflow software developed at CERN, Molflow User's guide. 2015.

[60] Y. H. Mori and T. Mochizuki. Explicit Expressions for Volume of drops release from submerged nozzles: their derivation from semiempirical implicit correlations. *Int. J Multiphase Flow*, 18:141–144, 1992.

[61] Boundless. Basic equations and parabolic path. *https://www.boundless.com/physics/textbooks/boundless-physics-textbook/ two-dimensional-kinematics-3/ projectile-motion-42/basic-equations-and-parabolic-path-226-10952/.*

[62] Normal distribution. Wolfram mathworld. *http://mathworld.wolfram.com/.*

[63] Autodyn module, Ansys software, Release 15.0, and Ansys User's Manual. Inc swanson analysis system. 2015.

[64] D. Houngbo, L. Popescu, P. Schuurmans, M. Delonca, R. Losito, C. Maglioni, T. Stora, P. Bricault, and J. Vierendeels. CFD analysis and optimization of a liquid lead-bismuth loop target for isol facilities. *Nuclear Instruments & Methods Section A*, 777:202–210, 2015.

[65] P. Boogerd, H. J. Verbeek, M. Stuivinga, and A. C. Van der Steen. General Shock wave Equation of state for solids. *Journal of Applied Physics*, 78:5335–5344, 1995.

[66] J. Peng, C. Hu, Y. Li, L. Zhang, and F. Jing. Determination of Parameters of Steinberg-Guinan Constitutive model with Shock Wave Experiments. *International Journal of Modern Physics B*, 22(09-11):1111–1116, 2008.

[67] F. Cezard, A. Pasco, R. Mauduit, and G. Dumenil E. Wenner. *Formulaire de Biologie, Chimie, Physique, Mathématiques*. Dunod, 2011.

[68] CFX module, Ansys software, Release 15.0, and Ansys User's Manual. Inc swanson analysis system. 2015.

[69] S. Marcuzzi. Essai de perçage au Laser LIEBE - Présentation des résultats de métrologie. In *EDMS 1291668 - May 2014*. CERN - internal report.

[70] A. D. Putorti, Jr. D. Everest, and A. Atreya. Simultaneous Measurements of Drop Size and Velocity in Large-Scale Sprinkler Flows Using Particle Tracking and Laser-Induced Fluorescence. *European Particle Accelerator Conference (EPAC), Portland, Oregon*, 04:1807–1809, 2003.

[71] R. A. Granger. *Fluid Mechanics*. Dover publications, Inc., 1995.

[72] Swagelok Product. *https://www.swagelok.com.fr/products/fittings.aspx.*

Appendix A

LBE properties and material compatibility

The thermo-mechanical properties of Lead Bismuth Eutectic (LBE) are presented in the upcoming tables as well as its material compatibility. Here are only presented the compatibility of flowing LBE. Data with stagnant LBE can be found in [1].

Property, parameter	**SI Unit**	**Correlation**	**Temperature range (K)**	**Estimated error ±**
Melting temperature	K	$T_{melt} = 397.7$	n/a	0.6
Latent heat of melting	$kJ.\ kg^{-1}$	$Q_{melt} = 38.6$	n/a	0.2
Boiling temperature	K	$T_{boil} = 1\ 943$	n/a	10
Latent heat of boiling	$kJ.\ kg^{-1}$	$Q_{boil} = 854$	n/a	2.0
Saturated vapour pressure	Pa	$P_s = 11.1.10^9.exp^{-22552/T}$	508 - 1 943	50 %
Surface tension	$N.m^{-1}$	$\sigma = (437.1 - 0.066.T).10^{-3}$	429 - 1 400	5.0 %
Density	$kg.m^{-3}$	$\rho = 11096 - 1.3236.T$	403 - 1 300	0.8 %
Sound velocity	$m.s^{-1}$	$u_{sound} = 1773 + 0.1049.T - 2.873.10^{-4}.T^2$	403 - 1 300	-
Bulk modulus	Pa	$B_s = (35.18 - 1.541.10^{-3}.T - 9.191.10^{-6}.T^2).10^9$	403 - 605	0.05 %
Isobaric specific heat	$J.kg^{-1}.K^{-1}$	$C_p = 159 - 2.72.10^{-2}.T + 7.12.10^{-6}.T^2$	403 - 605	7 %
Dynamic viscosity	$Pa.s$	$\eta = 4.94.10^{-4}.exp^{754.1/T}$	400 - 1 100	5 %
Electric resistivity	$\Omega.m$	$r = (86.334 + 0.0511.T).10^{-8}$	403 - 1 100	6 %
Thermal conductivity	$W.m^{-1}.K^{-1}$	$\lambda = 3.61 + 1.517.10^{-2}.T - 1.741.10^{-6}.T^2$	403 - 1 100	5 %

Table A.1: Summary of the recommended correlations for main thermophysical properties of molten LBE (P $\approx$ 0.1 MPa [1])

Table A.2: Fe-Cr steels in flowing LBE [1]

Material	T (°C)	ΔT	Time (hours)	[O] (%wt.)	OCS	Loop	LBE volume (litres)	Flow rate (m/s)	Oxide thickness/ dissolution depth (microns)	Remark 1	Remark 2	Ref.
D-9 tube	460	300	1000	$3\text{-}5 \times 10^{-6}$		CU-1M (IPPE)	60	1.9	0		Weight gain (mg/mm^2): 0.00	[Li, 2001]
D-9 tube	550	300	1000	$3\text{-}5 \times 10^{-6}$		CU-1M (IPPE)	60	1.9	12		Weight gain (mg/mm^2): 0.009	[Li, 2001]
D-9 tube	460	300	2000	$3\text{-}5 \times 10^{-6}$		CU-1M (IPPE)	60	1.9	5		Weight gain (mg/mm^2): 0.002	[Li, 2001]
D-9 tube	550	300	2000	$3\text{-}5 \times 10^{-6}$		CU-1M (IPPE)	60	1.9	26		Weight gain (mg/mm^2): 0.013	[Li, 2001]
D-9 tube	460	300	3000	$3\text{-}5 \times 10^{-6}$		CU-1M (IPPE)	60	1.9	4		Weight gain (mg/mm^2): 0.006	[Li, 2001]
D-9 tube	550	300	3000	$3\text{-}5 \times 10^{-6}$		CU-1M (IPPE)	60	1.9	24		Weight gain (mg/mm^2): 0.002	[Li, 2001]
1.4970	300	170	1116, 2000	$1\text{-}2 \times 10^{-6}$	He-20%H_2 PbO	Cu-1M(IPPE) Preoxidated	60	2				[Barbier, 2001]
1.4970	470	170	1116	$1\text{-}2 \times 10^{-6}$	He-20%H_2 PbO	Cu-1M (IPPE) Preoxidated	60	2			Weight gain: 0.01	[Barbier, 2001]
1.4970	470	170	2000	$1\text{-}2 \times 10^{-6}$	He-20%H_2 PbO	Cu-1M (IPPE) Preoxidated	60	2			Weight gain: 0.04	[Barbier, 2001]
1.4970	300	170	3116	$1\text{-}2 \times 10^{-6}$	He-20%H_2 PbO	Cu-1M (IPPE) Preoxidated	60	2	<1	Oxidation		[Barbier, 2001]
1.4970	470	170	3116	$1\text{-}2 \times 10^{-6}$	He-20%H_2 PbO	Cu-1M (IPPE) Preoxidated	60	2	<1	Oxidation	Weight gain: 0.02	[Barbier, 2001]
1.4970	420	180	2000, 4000	1×10^{-6}		IPPE	60	1.3	<1			[Müller, 2002]
1.4970	550		2000	1×10^{-6}		Prometey	60	0.5	30		Nodules	[Müller, 2002]
1.4970	550		4300	1×10^{-6}	ArH_2 + PbO	Prometey	60	0.5	15		Pb-Bi infiltration	[Müller, 2004]
1.4970	550		7200	1×10^{-6}	ArH_2 + PbO	Prometey	60	0.5	15 + 15		No LBE infiltration and growing of new oxide layer underneath	[Müller, 2004]
1.4970	600	180	2000	1×10^{-6}		IPPE	60	1.3	30		Nodules	[Müller, 2002]
1.4970	600	180	4000	1×10^{-6}	ArH_2 + PbO	IPPE	60	1.3	-100	Dissolution		[Müller, 2004]
316L	420	180	2000, 4000	1×10^{-6}		IPPE	60	1.3	<1	Oxidation		[Müller, 2002]
316L	550		2000	1×10^{-6}		Prometey	60	0.5		Oxidation	Nodules	[Müller, 2002]

Table A.3: Fe-Cr steels in flowing LBE *(cont.)* [1]

Material	T (°C)	ΔT	Time (hours)	[O] (%wt.)	OCS	Loop	LBE volume (litres)	Flow rate (m/s)	Oxide thickness/ dissolution depth (microns)	Remark 1	Remark 2	Ref.
316L	550		4000	1×10^{-6}	ArH_2 + PbO	Prometey	60	0.5	15	Oxidation	Gap between spinel and magnetite	[Müller, 2004]
316L	550		7200	1×10^{-6}		Prometey	60	0.5	5	Oxidation	New oxide layer	[Müller, 2004]
316L	600	180	2000	1×10^{-6}		IPPE	60	1.3	-200	Dissolution		[Müller, 2002]
316L	400		1500	3.1×10^{-10}-7.3×10^{-8}	Mg +Ar/H_2	LECOR	60	1		Dissolution	1.9×10^{-3} μm/h	[Fazio, 2003]
316L	550	150	1000	2×10^{-9}	H_2/H_2O		22.	2	-100	Dissolution	Erosion started	[Kondo, 2005]
316L-tube	460	300	1000	$3\text{-}5 \times 10^{-6}$		CU-1M (IPPE)	60	1.9	0		Weight gain(mg/mm^2): 0.00	[Li, 2001]
316L-tube	550	300	1000	$3\text{-}5 \times 10^{-6}$		CU-1M (IPPE)	60	1.9	7		Weight loss (mg/mm^2): 0.001	[Li, 2001]
316 tube	460	300	2000	$3\text{-}5 \times 10^{-6}$		CU-1M (IPPE)	60	1.9	3		Weight loss (mg/mm^2): 0.002	[Li, 2001]
316L-tube	550	300	2000	$3\text{-}5 \times 10^{-6}$		CU-1M (IPPE)	60	1.9	18		Weight gain(mg/mm^2): 0.019	[Li, 2001]
316 tube	460	300	3000	$3\text{-}5 \times 10^{-6}$		CU-1M (IPPE)	60	1.9	4		Weight gain (mg/mm^2): 0.00	[Li, 2001]
316L-tube	550	300	3000	$3\text{-}5 \times 10^{-6}$		CU-1M (IPPE)	60	1.9	21		Weight gain(mg/mm^2): 0.00	[Li, 2001]
316L rod	460	300	1000	$3\text{-}5 \times 10^{-6}$		CU-1M (IPPE)	60	1.9	0		Local corrosion No surface treat. Weight gain (mg/mm^2) 0.002.	[Li, 2001]
316L rod	550	300	1000	$3\text{-}5 \times 10^{-6}$		CU-1M (IPPE)	60	1.9	1		Local corrosion No surface treat. Weight gain (mg/mm^2) 0.01.	[Li, 2001]
316L rod	460	300	2000	$3\text{-}5 \times 10^{-6}$		CU-1M (IPPE)	60	1.9	0		Local corrosion No surface treat. Weight loss (mg/mm^2): 0.002.	[Li, 2001]
316L rod	550	300	2000	$3\text{-}5 \times 10^{-6}$		CU-1M (IPPE)	60	1.9	2		Local corrosion No surface treat. Weight gain (mg/mm^2) 0.00.	[Li, 2001]
316L rod	460	300	3000	$3\text{-}5 \times 10^{-6}$		CU-1M (IPPE)	60	1.9	0		Local corrosion No surface treat.Weight gain (mg/mm^2): 0.000.	[Li, 2001]

Appendix B

Procedure of operation of the LIEBE target - at start and stop

B.1 Introduction

The LIEBE target will be first tested on the off-line pump stand and front end reproduction available at ISOLDE before to be installed in the on-line front end. This will allow a full characterisation of the target, including an estimation of the beam current on stable species as well as response in temperature of the target assembly. This is mandatory as, once the target installed on-line in the front end, the operators are blinds and can only refer to the off-line calibration.

Consequently, the target developed should be compatible with both the off-line and on-line front ends, and should allow to be used at least two times.

The planned procedure for the operation of the LIEBE target off-line and on-line is described hereunder.

B.2 Off-line operation

The LIEBE target must be tested on the off-line front end before to be installed in the on-line ISOLDE front end.

Before to enter in details in the procedure of test, one should remind some constraints linked to the use of Lead Bismuth Eutectic (LBE);

- The reaction of LBE with oxygen being highly reactive, the LBE should be kept under controlled atmosphere at all time once it is inside the LBE loop. Indeed, the oxide in the loop should be minimized.
- The loop of LBE should be emptied after the off-line testing as the LBE should not be kept in a solid state in the loop. Indeed, as a proper control of the heating inside the loop seems complicated to achieve, there would be a risk of break up of the loop.

Taking into account these constraints and based on the proposed design, the procedure would happen as follow:

1. Filling of the filling tank: in a glove box, under a controlled atmosphere. The filling tank will be opened up to its opening and will be then closed tight under this controlled atmosphere (Figure B.1).

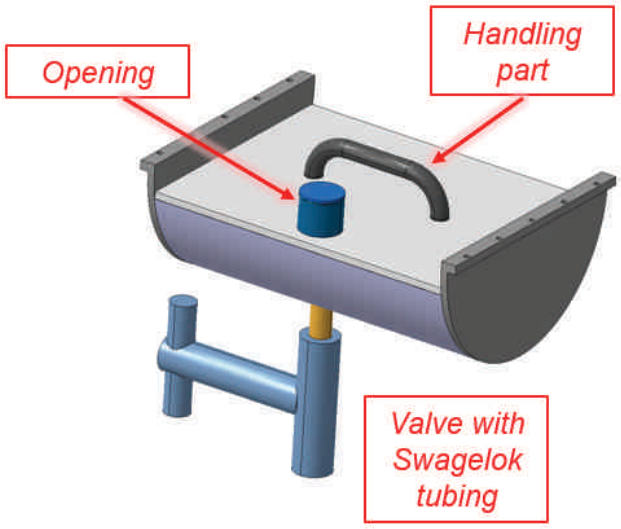

Figure B.1: Filling tank.

2. The LBE will be left to solidify in the filling tank. Two of these tanks will be prepared in the same time, the first one will be used for the off-line testing while the second one will be installed for the on-line testing.

3. Coupling of the filling tank with the main loop, valve closed. The filling tank will then be fixed to the vessel while the opening used for the installation of the tank will be kept open for the side one and closed for the upper one.

4. Coupling the target to the front end and putting the main LBE loop under vacuum through the front end. Then, the valve can be opened while the LBE is still completely solidify. At that stage, the full loop is under vacuum and the LBE has not seen any oxygen.

5. Closing the vessel opening in Titanium and putting the vessel under vacuum thanks to the vacuum valve.

6. Putting the vessel under a low pressurized gas (of 200 mbar) by using the same vacuum valve. At that stage, a fast testing of the leak detection system can be done by increasing the pressure applied over the defined limit.

7. The alignment of the pump part should be done.

8. Then, the pump part can be coupled. During this phase, the water connection of the LBE will be coupled as well.

9. The two control panels (one for the main loop target and one for the pump) will then be coupled by hand and a check of the different readings should be done. At that stage, it is also advised to check that the magnet parts are well positioned compared to the pump pipes of the loop while the loop is still cold.

10. The system is now ready to be used. The heating of the full loop can be started up to 200 °C while the ion source will be heated up as well.

11. Once the target is at the desired temperature, with the Heat Exchanger (HEX) included so that there is no cold point in the loop, checking the different temperatures and pressures (vacuum and leak pressure) and start the heating of the filling tank.

12. When the filling tank will be hot enough, the LBE should melt and go inside the loop. The desired level will be confirmed with the level meter installed at the bottom of the diffusion chamber. One could expect that some "block" of LBE will remain inside the filling tank due to the non homogeneous heating of it. Indeed, the heating and filling of the tank will happen simultaneously as the valve is opened. Consequently, the "inside part" of LBE could take longer to be melted. This should not be an issue as long as the heating is maintained for long enough.

13. When this is done, a visual inspection can be done on the pump part to ensure that no deformation occurred (no deformation are expected).

14. The magnets will then be advanced to be positioned around the pump pipes of the target and after a new control of positioning, the pump and the HEX will be both started simultaneously. Indeed, no proper thermal equilibrium can be reached without the contribution of both elements.

15. The target will then be operated at each defined working temperature. For each points, the corresponding applied power will be noted as well as the HEX parameters (flow rate that should be fixed, inlet and outlet temperatures) as well as the different thermocouples readings and pressure sensors. A mass scan will be done as well for each temperature.

16. Once the off-line testing will be done, the pump will be stopped and the magnets will be removed from their position.

17. Then the full pump part will be uncoupled and thus, the water connections will be opened as well (however, the connection installed will have an automatic closing system so that no water will be put into the front end).

18. The loop should be kept at 200 °C while the upper part of the vessel will be opened to allow the access of the emptying system (Figure B.2).

19. The loop should be then pressurized with noble gases (more than 1 bar in order to be in over pressure compared to the atmosphere) in order to vent it.

20. The screw will then be opened and the LBE will get out of the loop. The temperature of the target will then be reduced till it is possible to put a new screw. During the all time, the over pressurized gas will be applied.

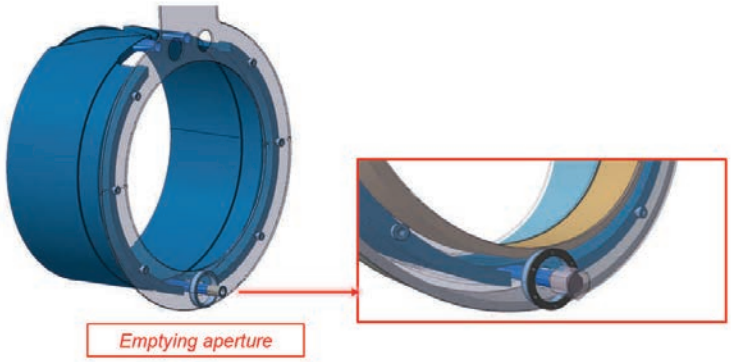

Figure B.2: Emptying elements.

21. Then the valve on the back of the target will be closed, the opening at the bottom of the vessel will be closed back as well and the side and upper openings will be opened in order to allow the access to the filling tank valve.

    At that stage, it is obvious than the vessel will be under atmospheric pressure and not anymore under the low pressurized gas.

22. The target should be now prepared for the on-line run. To do so, the first thing to do will be to install a new filling tank full of solidify LBE (the one that has been prepared in the same time than the first one). To do so, the target will be installed on the off-line front end again, and pressurized noble gas will be injected into the loop of LBE. The connection between the tank and the loop will then be cut just under the valve and the new filling tank and valve will be installed instead and fixed thanks to a Swagelok valve connector [72].

    This system has been used before with LBE and proved is feasibility up to 200 °C.

23. Once this is done, the target is ready to go on-line.

B.3 On-line operation

The on-line operation of the LIEBE target will be very similar to the one of the off-line. The main differences will occur for the installation of the unit that should be done remotely for most of the operation.

Considering the complexity of the target itself, it has been decided to make some of the target coupling by hand. However, after irradiation, all the operations needed for the uncoupling of the target should be done remotely.

The procedure of installation of the LIEBE target will be as follow:

1. Coupling of the main loop target with:

    - the valve of the filling tank opened,
    - the loop under controlled atmosphere (over pressure of noble gas),

- the vessel under a low pressure gas.

2. Pump part of the target brought manually and coupled to its support. In the same time, the coupling of the water connections will be done automatically. A validation of the position should be done at that stage in order to ensure the proper positioning of the magnets regarding to the pump pipes.

3. Once the position is validated, the pump part should be locked in position.

4. Then, the two connectors patch should be plugged manually (one patch per element: the main loop part and the pump part).

5. The water connector at the back of the pump trolley should be plugged manually. At that stage, the full target is ready to be used following the steps explained in the previous part.

After the end of the run, the target will not be emptied as the planned procedure for this cannot be done remotely.

The stopping and uncoupling of the target on the ISOLDE front end will be done as follow:

1. Putting the temperature of the loop at 200 °C,

2. Stopping the pump and the HEX,

3. Removing the magnets from around the pump pipes thanks to the actuator,

4. Go with the ISOLDE robot and uncouple the two connectors panels that should then be positioned on their "fake connector panel" on the front end,

5. Removing the ISOLDE robot and go with the Telemax robot. The Telemax robot should disconnect the water connection behind the pump trolley and pull back the water pipes that should be stored outside the Faraday cage,

6. The Telemax robot will then unlocked the trolley from the support and pull back the pump trolley. By doing that, the water connection between the trolley and the main loop target will automatically be disconnected,

7. The last step will be done by sending back the ISOLDE robot to disconnect the main loop part of the target and store it on the shelf.

Appendix C

Experimental results - plots of velocity over the time for different grids

The plots of the velocity of the droplets out of the grid versus the time are presented for three different grids (0.6 mm, 0.8 mm and 1 mm inter axis distance spacing) tested during the shower campaign test presented in Chapter 4.

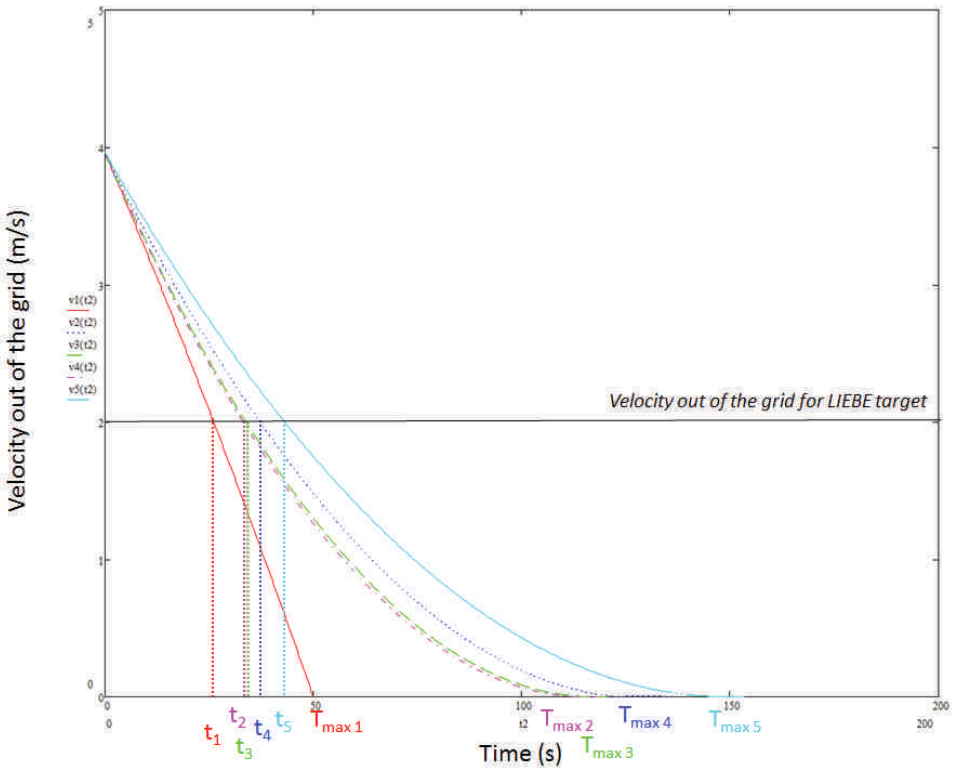

Figure C.1: v=f(t) - for each shower - 0.6 mm inter axis spacing

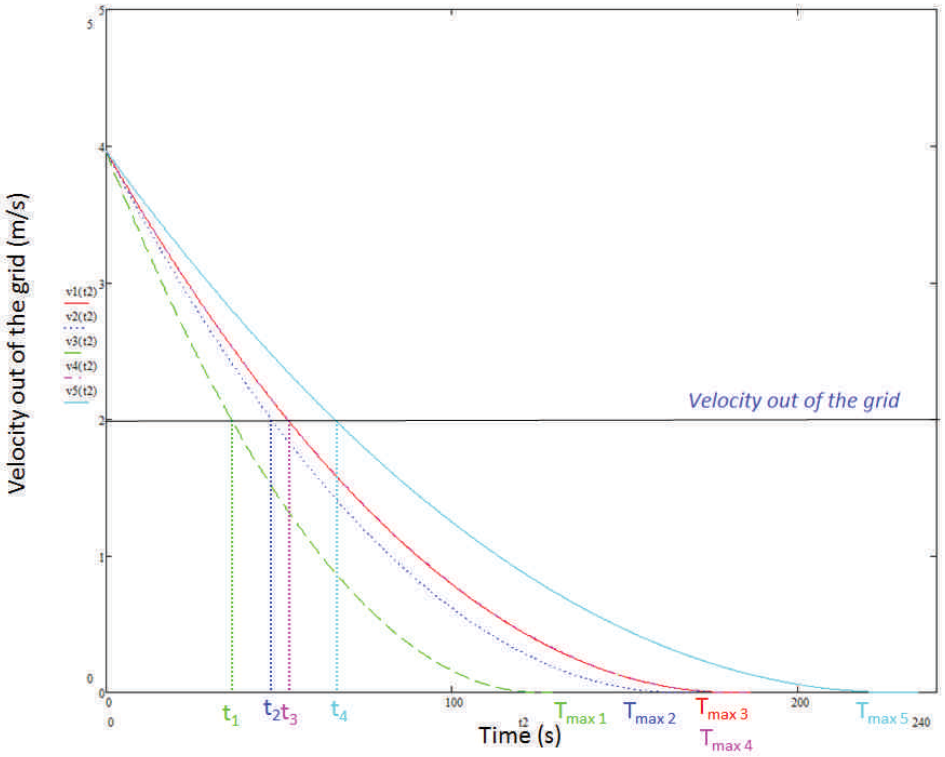

Figure C.2: v=f(t) - for each shower - 0.8 mm inter axis spacing

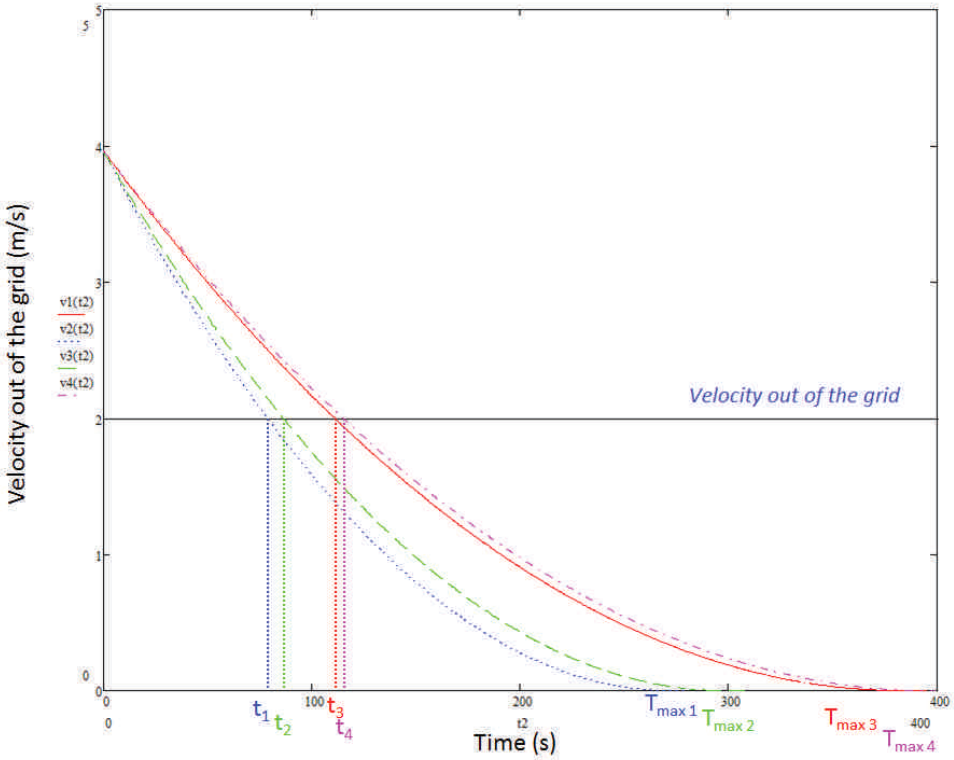

Figure C.3: v=f(t) - for each shower - 1 mm inter axis spacing

Document réalisé avec LaTeX et :
le style LaTeX pour Thèse de Doctorat créé par S. Galland — http://www.multiagent.fr/ThesisStyle
la collection de paquets `tex-upmethodology` — http://www.arakhne.org/tex-upmethodology/

Résumé :

De plus en plus, la puissance des faisceaux primaires envoyés sur les cibles augmente jusqu'à atteindre plusieurs centaines de kiloWatt, créant ainsi de nouvelles problématiques et de nouveaux défis. De nouveaux concepts de cibles ont ainsi vu le jour. Parmi eux, une boucle liquide utilisant du Plomb Bismuth Eutectic (LBE) comme matériau de cible, et dans lequel un échangeur de chaleur et une pompe sont intégrés, a été proposée durant la phase de développement du projet EURISOL. Ce concept prévoit de plus de transformer le liquide irradié sous forme de gouttes de manière à faciliter l'extraction des isotopes créés et ainsi d'augmenter la production d'isotopes à court temps de demi-vie. Cette thèse présente le développement de ce design. Un prototype a été développé et sera testé sous faisceau de protons à ISOLDE au Cern, Genève. Plusieurs outils analytiques pour l'étude et la conception de cible haute puissance sont proposés, prenant en considération divers paramètres de design. Ces outils peuvent être utilise pour d'autres cibles haute puissance et permettent un dimensionnement simple de ce genre de cible. De plus, un design innovant d'échangeur de chaleur est présenté, permettant d'extraire une puissance constante pour différentes températures de LBE. Le design proposé est validé grâce à divers outils numériques et analytiques. De plus, des tests expérimentaux ont été réalisés pour valider la faisabilité de douche. Des gouttes de 400 μm ont été obtenues. La cible proposée est la première combinant l'utilisation d'une chambre de diffusion où la douche est créée, avec une pompe et un échangeur de chaleur. Les concepts avancés peuvent être utilisés pour le développement de cibles similaires dans d'autres instituts.

Mots-clés : Cible haute puissance, Isotopes á court temps de demi-vie, cible ISOL

Abstract:

More and more, the power of primary beam sent onto targets increases until reaching several kilo Watts of magnitude, inducing new problematic and challenges. Consequently, the need of new target design arises and leads to new conceptual design proposal. Amongst them, a concept of Lead Bismuth Eutectic (LBE) loop target making use of an heat exchanger (HEX) and a pump has been proposed during the European project EURISOL Design Study. This concept proposed an improvement in terms of release efficiency of short-lived species by transforming the irradiated liquid into droplets shape. This thesis presents the development of this target design proposal. A prototype target has been developed and will be tested under proton beam at ISOLDE at Cern, Geneva. Several analytical tools for the study of this kind of targets are proposed, taking into account different design parameters. These tools can be applied for other high power target concept and allow an easy dimensioning of this kind of targets. As well, an innovative heat exchanger is developed, allowing to extract constant power out of the target for different LBE temperature. The proposed target design is validated thanks to different numerical and analytical tools while experimental tests have been conducted in order to assess the droplet formation feasibility. These tests prove that a shower of droplets of 400 μm is possible. The developed target is the first one combining a diffusion chamber where a shower is created combined with a pump and a HEX. The concepts of this design could be applied for similar targets that could be developed in other facilities.

Keywords: High power target, Short-lived isotopes, ISOL target

SPIM

■ École doctorale SPIM - Université de Technologie Belfort-Montbéliard
F - 90010 Belfort Cedex ■ tél. +33 (0)3 84 58 31 39
■ ed-spim@univ-fcomte.fr ■ www.ed-spim.univ-fcomte.fr

utbm
université de technologie
Belfort-Montbéliard